IMPROVED GAS EXCHANGE CHARACTERIZATION OF TWO-STROKE ENGINES TO DEVELOP ROBUST EMISSIONS CONTROL SYSTEMS

A Dissertation

by

ABDULLAH UMAIR BAJWA

Submitted to the Office of Graduate and Professional Studies of
Texas A&M University
in partial fulfillment of the requirements for the degree of

DOCTOR OF PHILOSOPHY

Chair of Committee,	Timothy J. Jacobs
Committee Members,	Jerald A. Caton
	Mark A. Patterson
	Jorge L. Alvarado
Head of Department,	Andreas A. Polycarpou

December 2020

Major Subject: Mechanical Engineering

ABSTRACT

Gas exchange processes in two-stroke internal combustion engines, commonly referred to as scavenging, are responsible for removing exhaust gases from the combustion chamber and preparing the fuel-oxidizer mixture that undergoes combustion and thus converts the chemical energy of the fuel into mechanical work. Scavenging is a complicated phenomenon because of the simultaneous introduction of fresh gases into the engine cylinder through the intake ports and the expulsion of combustion products from the previous cycles through the exhaust ports. A non-negligible fraction of the gaseous mixture that is trapped in the cylinder at the conclusion of scavenging is composed of residual gases from the previous cycle. This can cause significant changes to the combustion characteristics of the mixture by changing its composition and temperature, i.e. its thermodynamic state. Thus, it is essential to have accurate knowledge of the thermodynamic state of the post-scavenging mixture to be able to reliably predict and control engine performance, efficiency, and emissions. Of particular import is the trapped equivalence ratio, as it is a good predictor of engine-out NO_x emissions and can be used as a control parameter for ensuring emissions compliance.

Unfortunately, it is not practical to directly measure the trapped residual fraction (which is needed to calculate the trapped equivalence ratio) outside of the laboratory setting. To overcome this handicap, simple scavenging models that estimate this fraction based on some economically measurable engine parameters can be used. This project

studies various simple scavenging models using a one-dimensional *GT-Power* model of a large-bore, natural gas fueled, two-stroke engine; highlights their shortcomings, and proposes an improved multi-stage, two-zone simple scavenging model that can produce accurate estimates of the trapped mixture composition for such engines. The simulation results are directly validated by conducting scavenging experiments to calculate the trapped mixture composition. CO_2 is used as a tracer for combustion products to study scavenging performance of the engine, and fuel - as a part of a pre-mixed fuel-air mixture - is used as a tracer for fresh charge to experimentally study the trapping performance of the engine.

DEDICATION

I dedicate this to my parents for always supporting me and, by making uncountable personal sacrifices, letting me pursue my dreams; my siblings for being a constant source of encouragement – my brother, Khizer, by being someone who I could always look up to for guidance and my sister, Amna, by her generosity of spirit; my grandparents, especially my late Nano (maternal grandmother), for teaching me life lessons that I rely on every day as I try to tread the winding road of life; Nissa, my betrothed, for lending me motivation whenever I have found myself lacking in it; and lastly, the great, late Greg Beshouri (AETC) for his selfless mentorship.

ACKNOWLEDGMENTS

First and foremost, I would like to express my profound gratitude and thanks to Dr. Tim Jacobs for his unrelenting and purposeful support, for his candid and encouraging advice, for his professorial humor, and most importantly for him being an exemplary educator, whose foremost priority has always been the academic development of his students. Over the last five years, from my first conversation with him in the 'Advanced Thermodynamics' class to date, as I near the end of my PhD program amidst a pandemic, Dr. Jacobs has been a constant source of encouragement, inspiration, and guidance; thanks to which my graduate experience has been one I'll cherish for the rest of my life.

I would also like to pay my most respectful compliments to Dr. Mark Patterson for his steadfast support and motivational guidance throughout my PhD. His friendly, unassuming and approachable nature, his candid feedback based on thorough, incisive review of my work, and his words of overall encouragement made my graduate journey much more rewarding and gratifying than what it would've been in the absence of his sincere, overseeing mentorship.

My research committee members, Dr. Jerald Caton and Dr. Jorge Alvarado are acknowledged for volunteering their valuable time and energy to adjudicate my project and for their feedback during and after my preliminary defense, which has helped me

better direct my research efforts and (hopefully) produce a better quality work product. I am also grateful to Dr. Lesley Wright for reviewing my thesis and for agreeing to participate in my final defense.

I owe a great debt of gratitude to my colleagues at the Advanced Engine Research Lab. I am thankful to my seniors, Dr. Alireza Mashayekh and Jacob Hedrick, for showing me the ropes when I was starting off at the lab, and my peers, Tim Kroeger, Taylor Linker, Jeff Brown, Kevin Wallace, Jacob Nowlin, and Forrest Pommier, for their collegiality and help with my research.

Lastly, the Pipeline Research Council International (PRCI) is acknowledged for its support – both financial and technical – during the course of the project. All members of the PRCI project team are thanked for participating in the monthly update meetings and sharing their valuable feedback. Special thanks to Gary Choquette for his support throughout the project both in the form of technical advice and project management.

FUNDING SOURCES

Pipeline Research Council International

This work has been made possible by funding from the Pipeline Research Council International (Contract No. PR-457-17201) as a part of their support for research efforts on pipeline engines. The contents of this dissertation are solely the responsibility of the authors and do not necessarily represent the official views of the Pipeline Research Council International.

NOMENCLATURE

A	Area
AMP	Air manifold pressure
AMT	Air manifold temperature
aEPO	After exhaust port opening
aTDC	After top dead center
BDC	Bottom dead center
BMEP	Brake mean effective pressure
bTDC	Before top dead center
CAD	Crank angle degrees
CI	Confidence interval
DR	Delivery ratio
EMP	Exhaust manifold pressure
EPC	Exhaust port closing
EPO	Exhaust port opening
GTP	GT-Power
IC	Internal combustion
IMEP	Indicated mean effective pressure
IPO	Intake port opening
IPC	Intake port closing
m	Mass

M	Molecular weight
MAE	Mean absolute Error
NAAQS	National ambient air quality standards
NDIR	Non-dispersive infrared
P	Pressure
PD	Perfect displacement
PM	Perfect mixing
R	Ideal gas constant
SCF	Short-circuiting fraction
SE	Scavenging efficiency
ST	Spark timing
t	Time
T	Temperature
TC	Thermocouple
TDC	Top dead center
TE	Trapping efficiency
TER	Trapped equivalence ratio
TRF	Trapped residual fraction
UHC	Unburned hydrocarbons
x	Displacement ratio or mass fraction
y	Short-circuiting fraction or mole fraction
η	Efficiency

γ	Specific-heat ratio
θ_{PM}	Angle of start of PM stage
pc	Mean manifold pressure

Subscripts:

a	Air
b	Burned
c	Cylinder
del	Delivered
exh	Exhaust
f	Fuel
isent	Isentropic
r	Residual
short	Short-circuited
stoic	Stoichiometric
trap	Trapped
u	Unburned

TABLE OF CONTENTS

Page

LIST OF FIGURES

Page

LIST OF TABLES

Page

1. INTRODUCTION

1.1. Background and Motivation

This section describes the motivation behind conducting the current study, the complicated nature of gas exchange in two-stroke engines which makes emissions estimations difficult for such engines, and the changing environmental regulatory landscape that has necessitated the need for improving our understanding of gas exchange in two-stroke engines and the development of better control methods for emissions management.

1.1.1. The Two-Stroke Cycle

Based on the number of 'strokes' needed to complete an engine cycle, internal combustion (IC) engines can broadly be divided into two and four-stroke cycle engines. Each journey of the piston in the cylinder from one extreme to the other constitutes a stroke; and a combination of strokes that results in the execution of the four essential processes needed for sustainable production of work by an IC engine – induction, compression, expansion, and exhaust – comprises a cycle. Two-stroke engines perform all of these four tasks in two trips of the piston from one extreme to another (two strokes), whereas four-stroke engines need four trips (four strokes). Two-stroke engines are able to complete a cycle in two strokes because they, unlike their four-stroke counterparts, have simultaneous intake and exhaust processes. The working principles of two-stroke engines are discussed in detail in the following sections.

Two-stroke engines, because of their inherent simplicity of design and operation, have fascinated engine designers since the pre-industrial revolution days. All internal combustion engine designs prior to Otto's four-stroke cycle (1876) were based on a two-stroke cycle. Some examples of these engines are Huyghen's gun-powder fueled engine (1680), Robert Street's engine that ran on vaporized turpentine (1794), and the French Lenoir Engine (1860) which used 'town gas' (a mixture of hydrogen and carbon monoxide) as fuel [1]. Having a power stroke every cycle provides the opportunity to generate higher specific power (power per unit weight or volume) compared to four-stroke cycle based engines, and the relatively lower number of moving parts makes these engines more reliable. Because of these advantages, two-stroke engines have continued to flourish over the past century despite having shortcomings associated with their gas exchange processes, which are the subject of this research. Figure 1 provides a snapshot of the progress - as quantified by thermal efficiency, brake mean effective pressure (BMEP) which is a measure of the work produced, and specific power - two-stroke engines have made during the twentieth century.

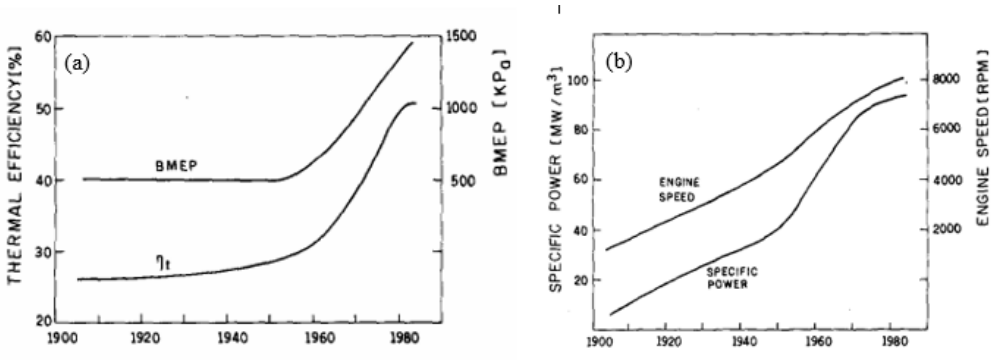

Figure 1: Development of (a) large diesel and (b) small SI two-stroke engines. [2]

Some common two-stroke engine applications include power tools, mopeds, recreational vehicles (snowmobiles, jet skis, etc.), military vehicles (tanks, unmanned aerial vehicles), prime movers for turbomachinery, and marine uses (small boats to mega ships). Two-stroke engines have seen a surge in interest in recent times [3, 4, 5, 6] because of their suitability for use in automotive applications as engine downsizing and powertrain hybridization gain popularity. Such engines are an attractive prospect for these automotive applications because of their high power densities and good high-load performance.

1.1.1.1. **Scavenging in Two-Stroke Engines**

The gas exchange process in two-stroke engines which prepares the combustible mixture that is burned to harness the chemical energy of fuel and produce mechanical work is very different from that in four-stroke engines. Unlike the four-stroke cycle, in a two-stroke cycle, the intake and exhaust processes are not disjoined, but they take place simultaneously for the majority of the gas exchange period. In other words, the overlap period between intake and exhaust valve/port open portion is significantly longer in two-stroke engines. This concurrent intake and exhaust process is commonly referred to as scavenging. For ported two-stroke engines, like the one being studied in this project, the opening and closing of cylinder ports is controlled by the piston edge as it uncovers and recovers them, respectively during its reciprocating motion.

After combustion, as the piston moves away from the top dead center (TDC) during the power stroke, it uncovers the exhaust ports first, followed by the intake ports. The initial portion of the gas exchange process that starts at exhaust port opening (EPO) is known as blowdown. During blowdown, there is a strong rush of high pressure combustion products out of the cylinder and into the exhaust manifold, which results in a sharp drop in the cylinder pressure and a steep rise in the exhaust manifold pressure. Blowdown continues until the cylinder pressure and the exhaust pressure equilibrate; this normally happens around intake port opening (IPO). At IPO, fresh incoming air, or air-fuel mixture, is pushed into the cylinder through scavenging ports, which are the inlets to the cylinder and are, therefore, commonly referred to as just intake ports. The intake flow is driven either by an external pressurizing device or by the bottom surface of the piston as the piston is moving away from TDC. Figure 2 shows the cross section of the two-stroke, piston-scavenged engine being studied in the current project as the piston is moving through bottom dead center (BDC). The volume on the underside of the piston, known as the scavenging chamber or the stuffing box, is filled with freshly inducted charge which is being pushed to the engine cylinder through the intake ports. After BDC, the piston reverses direction and moves towards TDC, closing the intake ports first followed by the exhaust ports.

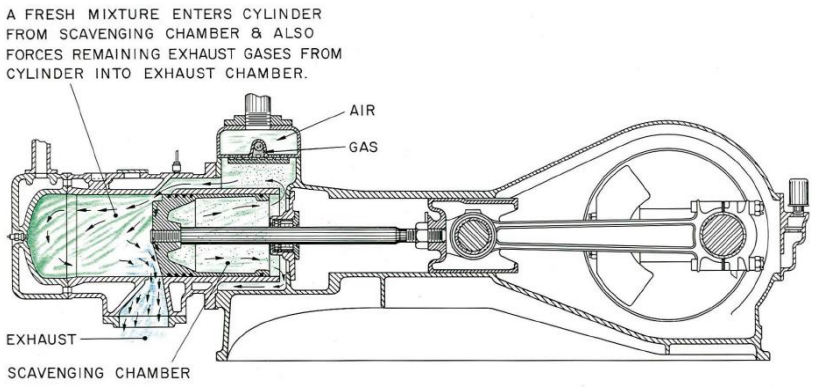

Figure 2: Cross sectional view of a cross-scavenged two-stroke Ajax E-565 engine during scavenging. [7]

In four-cycle engines, the piston sweeps the combustion chamber during dedicated and (mostly) disjoined intake and exhaust strokes to draw in fresh charge and positively displace combustion gases out through the exhaust ports. In contrast to this, two-cycle engines rely on the incoming air jet to act as a 'fluid piston' [8] to 'scavenge' the combustion products and provide fresh oxidizer. As will be discussed later, the fluid does not always act as a perfect piston because of air-residual-gas mixing. Owing to this gas exchange method, an out-of-cylinder pumping apparatus is necessary in two-stroke engines to provide the relatively large rates of mass flow needed across the engine ports (or valves)[1]. Even though pressurizing devices like turbo and super-chargers are sometimes used in four-stroke engines to improve their volumetric efficiency, external pumping apparatus are not essential for engine operation the way they are for two-stroke engines.

[1] Since the engine studied in this research is a ported one, henceforth, for the sake of brevity, only 'ports' is used to refer to the cylinder orifices.

Moreover, in a two-stroke cycle, both the removal of combustion products from the previous cycle and the introduction of fresh gases for the following cycle have to be completed in the limited time for which the intake and exhaust ports are open (approximately 1/3 of a cycle for slow speed two-stroke engines as opposed to 1/2 for four-stroke engines). To overcome the handicap of having limited gas exchange time, two-stroke engines employ several creative strategies to aid in the preparation of a trapped mixture having desired composition. The most significant being the gas exchange scheme discussed above, whereby the incoming stream of fresh charge provides reactants for combustion in the next cycle and also expels combustion products from the previous cycle. A fraction of the fresh charge (between 10% and 40% [9, 10]) 'slips' through the exhaust ports without taking part in the compression and combustion processes that follow. This is known as short-circuiting, and is an unavoidable attribute of the two-stroke engine gas exchange process. Because of these gas exchange inefficiencies, the actual specific power improvement realized in two-stroke engines (relative to four-stroke engines) ranges between 20% and 60%, instead of the 100% one would have expected from doubling the power-stroke frequency [1]. Through better flow path designs (port geometries, port positions, piston deflectors, etc.), modern two-stroke engines short-circuit significantly less than their predecessors. Figure 2 illustrates the flow path of the incoming stream for typical cross-scavenged two-stroke engines. The looping of the stream towards the cylinder head upon entering the cylinder is brought about by the piston deflector and intake port designs. This is done to direct incoming gases away from the exhaust ports in order to thwart their short-circuiting by delaying

their arrival at the exhaust ports. According to [11], the incoming air stream also has a natural tendency to bend towards the cylinder head because of encountering a ‘variable pilot vortex’ and ‘variable deflect pressure’ pockets.

Based on the location of the ports, two-stroke engine scavenging designs can be divided into three broad categories; namely, cross-scavenged, loop-scavenged, and uniflow-scavenged. The engine discussed above has a cross-scavenged configuration. Figure 3 shows several scavenging path configurations. Different designs have various advantages and disadvantages in terms of scavenging effectiveness, reliability, and operating characteristics associated with them. Some of these differences are discussed in Chapter 2.

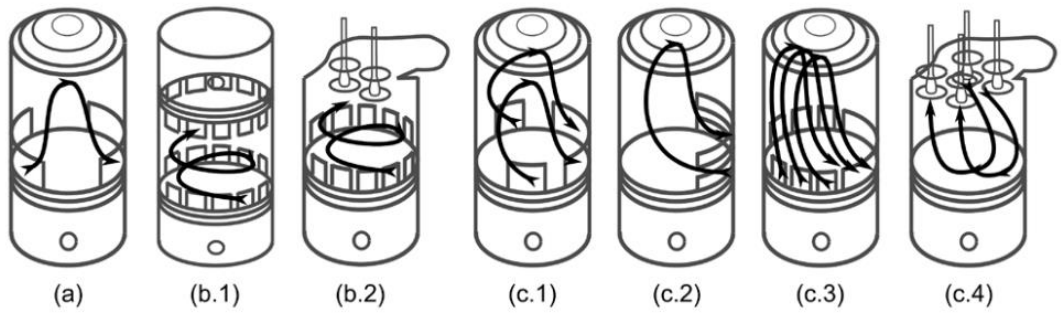

Figure 3: Various two-stroke engine scavenging regimes: (a) cross-scavenged, (b.1) uniflow-scavenged with opposed pistons, (b.2) uniflow-scavenged with overhead exhaust valves, (c.1) loop-scavenged (Schnürle Type), (c.2) loop-scavenged (MAN type), (c.3) loop-scavenged (Curtis Type), (c.4) poppet valved loop scavenged.

A non-negligible fraction (over 50% in some poorly scavenged engines [12] or at low loads [13]) of the gaseous mixture that is trapped in the cylinder at the conclusion of

scavenging is composed of residual gases from the previous cycle, sometimes referred to as 'internal EGR[2]'. The amount of residual gases trapped in two-stroke engines is significantly higher than four-stroke engines [14]. This is because of the absence of a dedicated exhaust stroke and the reliance on the incoming charge to scavenge residual gases. The amount of trapped residual gases can cause significant changes to the combustion characteristics of the mixture by changing its composition and temperature, i.e. its thermodynamic state. This, in turn, affects combustion and through that all aspects of engine operation – performance (torque and power production), emissions, fuel conversion efficiency, cylinder noise, etc.

1.1.1.2. **Two-Stroke Engine Emissions**

A brief discussion of some harmful emissions from two-stroke engines, particularly spark-ignited, two-stroke engines is presented in this section.

A major pollutant species generated by two-stroke engines are unburned hydrocarbons (UHCs). These include all hydrocarbon compounds that are either not oxidized at all, or are partially oxidized during combustion. UHCs can be harmful both for human health and the environment. Many UHCs are highly toxic in nature and some are even carcinogenic. They also contribute towards the formation of photochemical smog as volatile organic compounds, and are regulated as precursors to atmospheric

[2] Internal EGR – exhaust gas recirculation – is a misnomer when used to reference trapped residual gas. Unlike external EGR loops, no residual gas is 'recirculated' back into the cylinder since the trapped residual gas never leaves the cylinder.

ozone under National Ambient Air Quality Standards (NAAQS). Additionally, UHCs, in the form of greenhouse gases like methane from natural-gas fueled engines, can contribute towards global warming. Methane is a very potent greenhouse gas with a global warming potential ranging between 28-36 over a hundred-year window [15]. The global warming potential of CO_2 is 1. Historically, two-stroke engines produced high levels of UHC emissions because of the use of pre-mixed fuel metering systems like carburation, in which the fuel is mixed with air prior to being pushed into the cylinder. As a result, a homogeneous mixture of fuel and air – not just air – slips out through the exhaust ports. Thus, the large UHC emissions were predominantly caused by inefficiencies in the gas exchange, and not the combustion, process. Over the last few decades, UHCs have been reduced significantly by metering fuel directly in the cylinder, through the use of fuel injectors or fuel admission valves, after the gas exchange has concluded. Doing so eliminates the short-circuiting of fuel and, consequently, reduces UHC emissions. Some small two-stroke engines still use carburetors because direct fuel injection is costly.

Another harmful emission species produced from incomplete oxidation of fuel is carbon monoxide (CO), which is the partially oxidized form of carbon. CO emissions are higher at fuel-rich conditions where combustion is inefficient. CO can deteriorate the oxygen carrying capacity of blood and cause breathing complications in humans. Figure 4 qualitatively illustrates how changing the fuel-air equivalence ratio affects CO and hydrocarbon (HC) emissions. HC emissions increase at very lean conditions because

engines become unstable under highly diluted operation and start to misfire and/or partially fire beyond the 'lean limit'. Significant work has been done on reducing UHC and CO emissions [16, 17, 18, 19] in two-stroke engines. The general consensus of such studies is that UHC emissions are primarily a function of the engine's trapping performance, while CO emissions – like in four-stroke engines – are mostly influenced by the fuel-air equivalence ratio, and are nearly unaffected by changes in engine scavenging.

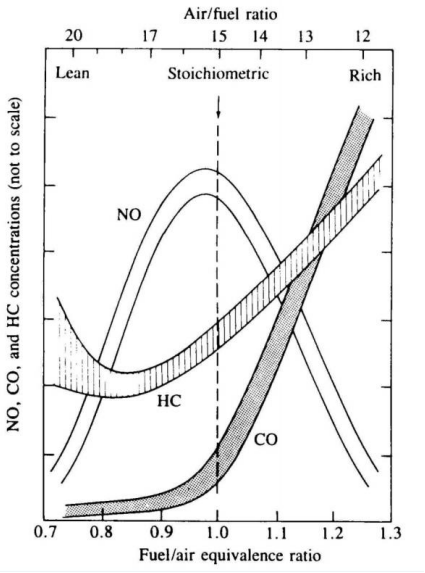

Figure 4: Emissions production at different fuel/air equivalence ratios. [20]

The third major harmful products of combustion in SI two-stroke engines are oxides of nitrogen: NO and NO_2[3], which are normally lumped together as NO_x. The major NO_x species produced in IC engines is NO, which quickly[4] converts to NO_2 upon

[3] There are 7 known oxides of nitrogen (NO, NO_2, NO_3, N_2O, N_2O_3, N_2O_4, and N_2O_5) but only these two are relevant in engine exhaust.
[4] In a matter of minutes, if not seconds.

exposure to oxygen in the atmosphere. NO_2 is a regulated pollutant by the Environmental Protection Agency [21] both directly by NO_2 NAAQS and indirectly through ozone NAAQS, as it is a precursor to atmospheric ozone [22]. NO_x, along with UHCs, is responsible for producing photochemical smog in urban centers and can cause respiratory illnesses. NO_2 can also cause acid rain by reacting with atmospheric moisture to produce nitric acid.

Two-stroke engines have inherently low NO_x emission levels in comparison to similarly-sized four-stroke engines [14, 23, 24, 25]). This advantage results from the poor exhaust removal process in two-stroke engines, which causes relatively large amounts of residual gas to be trapped in the cylinder at the conclusion of the breathing process. This gas acts as a diluent to lower combustion temperatures and as a result, the NO_x emissions [24]; the production of which is strongly dependent on combustion temperatures. It is worth mentioning here that the large trapped residual gas amount could also increase NO_x emissions because the residual gas is hotter than fresh air and increases the compression and combustion temperatures[5]. The literature surveyed, however, suggests that the dilution effect of trapped residual gas overpowers the temperature increasing effect. A secondary reason for the relatively low NO_x emissions is the ability of two-stroke engines to generate the same amount of power as four-stroke

[5] This property of residual gas is sometimes used to induce auto-ignition in two-stroke engines by controlling the amount of trapped residual gases. This is referred to as 'controlled auto-ignition' [69] or 'active radical combustion' [99] and improves combustion stability.

engines but at significantly lower mean effective pressures because of their higher firing frequency [26].

The concentration of available oxygen also plays an important role in determining the NO_x concentration. The equivalence ratio of the trapped mixture is a good measure of combustion temperatures. The highest combustion temperatures are found slightly rich of stoichiometric, but because there is a dearth of oxygen at rich operating conditions, the peak NO_x level falls slightly lean of stoichiometric where the temperatures are fairly high and there is plenty of oxygen feedstock available to produce NO.

In addition to these emissions, other harmful emissions like aldehydes, which fall under the category of hazardous air pollutants, oxides of sulfur (SO_x), and particulate matter can also be found in trace amounts in two-stroke engine exhaust. Some 'fugitive' gases having unburned fuel can also leak into the engine's crank-case across the piston rings, and eventually be released into the atmosphere.

1.1.1.3. **Integral Natural Gas Compressor Engines**

The research for the current project is being done for use in large-bore, two-stroke, natural gas fueled, integral compressor engines. A brief discussion of the role of these engines in the energy distribution infrastructure of the USA and their operational

requirements is in order, so as to better understand the associated emissions control challenges and to provide context for the goals of the project.

Natural gas as a fossil fuel has been gaining popularity in recent decades and is currently the largest single source of electricity generation in the USA. 34% (1,468 Billion kWh) of USA's current energy needs are being met by burning natural gas, and the share of natural gas is projected to rise to 39% by 2050 [27]. Even though the major reason for the rise in natural gas consumption has been the availability of affordable natural gas ever since the shale gas revolution of the 1990s, another factor that has made natural gas an enticing option compared to other fossil fuels is its ability to burn in a relatively clean fashion. Natural gas produces 53 kg of CO_2 to generate one MBtu (1.05 GJ) of energy, compared to 71.3 kg for gasoline, 73.2 kg for diesel, and 97.5 kg for coal (lignite) [28]. A lot of interest has been shown by the engine research community in studying the performance of natural gas fueled engines as they offer significant improvements not only in CO_2 emissions, which are not directly regulated, but also in carbon monoxide and particulate matter emissions [29], which are directly regulated in the USA. Thus, it is important to ensure that the natural gas infrastructure, of which integral compressor engines are an essential component, is able to reliably and cleanly provide natural gas to its ever-increasing clientele.

Integral compressor engines use natural gas as a fuel to drive reciprocating compressors that transport natural gas through distribution pipelines. Internal

combustion engines first appeared on the natural-gas transportation scene in the 1880s when they replaced steam engines as the principal prime mover for compressors. The integral compressor engine design was first introduced in 1909 [30]. In this design, the power cylinders and the compressor cylinders were connected to the same crank-shaft, often through an articulated connecting rod. Ever since, these engines have flourished because of their robust and self-sufficient design, and have become critically important for the natural-gas extraction and distribution system of the USA.

Engines located in remote gas fields and compressor stations are vital for extracting natural gas and ensuring its uninterrupted flow to all consumption sites in the country. The median age of compressor station engines in the USA is 45 years and about 5,600 such spark ignited engines are currently in operation, generating over 6,800 MW [31]. Due to their extensive footprint, it is financially unfeasible to replace the current fleet with newer, potentially cleaner and more efficient engines. Thus, engine retrofits are the most popular means of improving the performance and emissions of these engines. Figure 5 shows a map of the pipeline distribution network of the USA, which spans over 5 million km. Compressor stations are located every 50 to 100 miles (depending on the elevation changes of the pipe segments) to compensate for flow pressure losses during gas transmission.

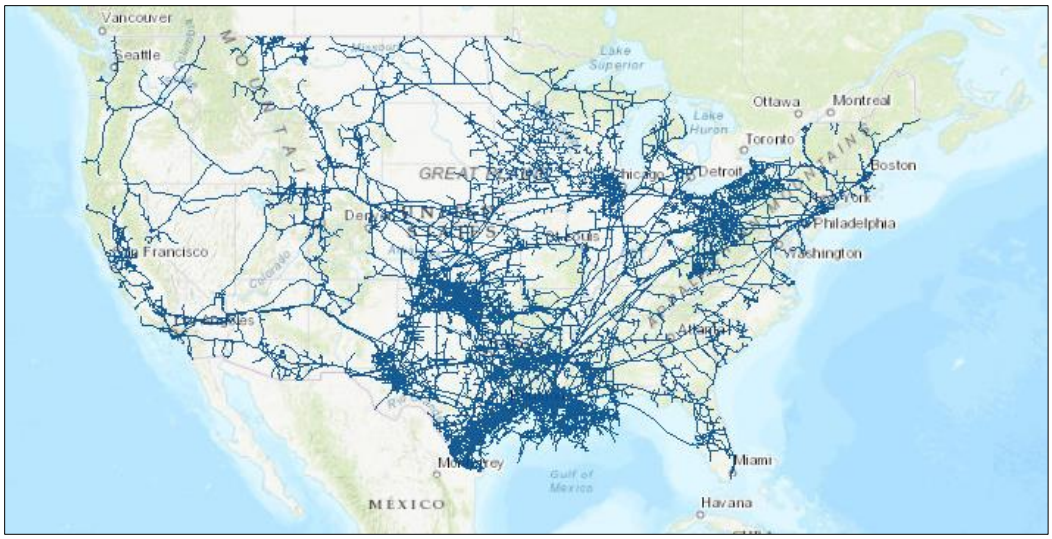

Figure 5: Map showing natural gas pipelines in the USA. [28]

Figure 6(a) shows the cross-section of one of the most popular such engines - the Cooper-Bessemer GMV series of engines - which was produced continuously for over 55 years in the twentieth century, starting in 1937 [30]. The GMV engine is considered to be one of the most successful integral-compressor engines ever built. It has made invaluable contributions to not only the US, but the global energy sector. The characteristic 'vee-angle' configuration of the engine's power cylinders with horizontal compressor cylinders was first introduced in 1937. Over the next fifty years, the basic structure – cylinder configuration, bore, stroke, kinematics – of the engine stayed mostly the same but through retrofits in the gas exchange apparatus, the fuel conversion efficiency was increased from 25% to 37%. A snapshot of this improvement is presented in Figure 6(b). Over 2,500 GMV engines are still in operation today. Since their production came to a halt, various third party improvements in the gas exchange and fuel metering systems have been made to lower their emissions and ensure compliance with

new regulations, e.g. improved air delivery methods [32], pre-combustion chambers [33], electronically controlled ignition systems [34], and high-pressure direct fuel injection systems [35].

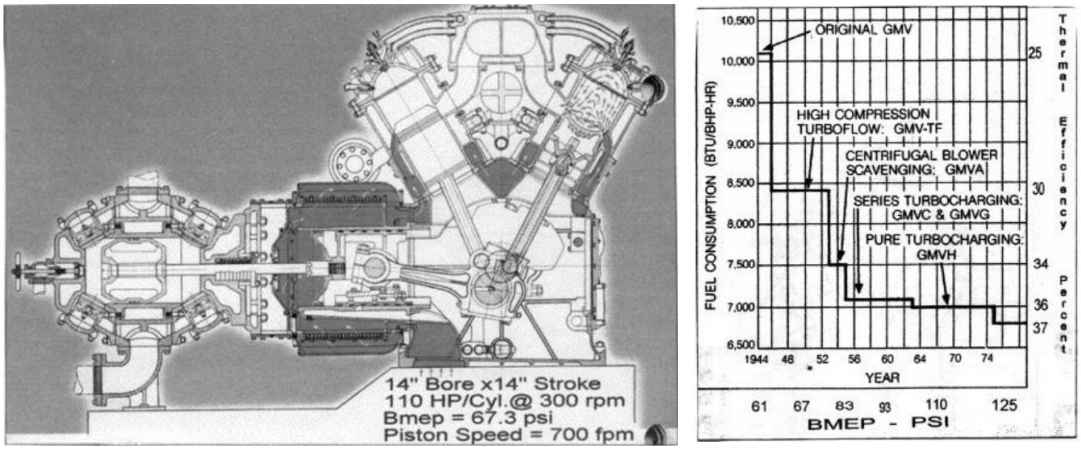

Figure 6: (a) A cross-section of the GMV integral compressor engine and (b) improvements in the GMV engine over the years. [30]

Natural gas integral compressor engines normally operate at fairly lean conditions (fuel-air equivalence ratio of less than 0.7) and are almost always direct-injected. As a result, emissions like UHC and CO are low, and can be kept within regulatory limits by using relatively simple and inexpensive after-treatment technologies like catalytic converters. However, as emissions regulations become more stringent, new NO_x reduction strategies are needed to ensure emissions compliance. After-treatment devices like three-way catalytic converters (sometimes also referred to as non-selective catalytic converters) cannot effectively be used for such engines because their NO_x conversion efficiency is very low at the lean conditions these engines operate at. The converters perform best when the engine exhaust is either close to, or slightly rich of,

stoichiometric[6]. Selective catalytic converters that can operate in the lean region are undesirable because they are expensive, require a regular and precisely controlled supply of an ammonia releasing reagent like urea to reduce NO_x to N_2, and operate efficiently only in a narrow exhaust temperature range (522 to 700 K [22]). Therefore, it is preferable to reduce NO_x emissions by manipulating in cylinder combustion to lower NO_x production.

The changing NO_x regulatory environment, operational limitations of lean-burn engines, and their criticality to the natural gas infrastructure necessitate the need to develop robust control strategies to control engine operation in order to keep NO_x emissions within acceptable limits. For the legacy integral compressor engines being studied, NO_x regulations range between 0.5 to 3 g/bhp-hr [31]. The exact limits depend on a multitude of factors, e.g. the history of the engine (is it a 'new source' or has it been 'grandfathered' in?), the applicable local and federal policies, and the location of the engine with regards to where and how far can its emissions be carried offsite by the wind (NO_x transport) [22]. As was shown in Figure 4, NO_x has a strong dependence on fuel-air equivalence ratio, which makes the equivalence ratio of the trapped mixture, the trapped equivalence ratio (TER), a great candidate to be an engine-out NO_x control parameter. Composition of the trapped mixture, which has fresh gases as well as significant amounts of residual gases, depends on the nature of gas exchange in the

[6] Because of short-circuiting in two-stroke engines, the exhaust gases are diluted. Thus, in order to get stoichiometric exhaust gases, the engine would have to be operated slightly rich.

engine. Thus, reliable estimation of the trapped mixture composition, particularly the trapped residual fraction (TRF), is vital for accurately calculating TER and controlling NO_x emissions. In pursuit of this goal, the current project aims to aid in the development of better emissions control strategies for integral compressor engines by studying the gas dynamics of scavenging for such engines.

1.2. Objective

The goal of the current project is to study gas exchange in cross-scavenged, two-stroke engines to develop a scavenging model that can inexpensively provide reliable estimates of the trapped mixture composition in the form of TRF and TER, which can then be used to control engine operation for emissions compliance.

As will be discussed in Chapter 2, 'state of the art' scavenging models are not sufficiently accurate in their TER and TRF estimations to precisely control engine-out NO_x emissions. This project uses a predictive one-dimensional model of a natural gas, two-stroke engine to investigate some existing simple scavenging models and identify their shortcomings. In conjunction with this, modern high speed CO and CO_2 sensors (along with pressure, temperature, and flow sensors) are used to study the gas exchange characteristics of the engine at different operating conditions. The two major gas exchange characteristics studied are scavenging (the engine's ability to purge the cylinder of combustion products during gas exchange) and trapping (the engine's ability to trap fresh charge delivered during gas exchange). CO_2 is used as a tracer for

combustion products to study scavenging performance of the engine, and fuel, as a part of a pre-mixed fuel-air mixture, is used as a tracer for fresh charge to experimentally study the trapping performance of the engine. Both the computational and experimental results are then used to broaden our understanding of scavenging in two-stroke engines and to develop a new scavenging model for engine control that addresses the shortcomings of existing models.

2. LITERATURE REVIEW

With the goals of this project listed and the need for improved scavenging models briefly discussed in Chapter 1, this chapter takes a deeper look at the current state of scavenging models[7] and how they have been, and continue to be, used to control integral natural gas engine operation.

2.1. Scavenging Models

Before discussing some of the scavenging models found in the literature, a quick discussion of various scavenging terminologies is in order. The efficiency of the charging process determines the properties of the mixture that is trapped at the end of gas exchange and subsequently undergoes combustion. Two metrics commonly used to quantify the quality of the scavenging process are trapping efficiency (TE) and scavenging efficiency (SE). They quantify what fraction of the total delivered charge is trapped at the end of gas exchange and what fraction of this trapped charge is made up of fresh air (or air-fuel mixture), respectively. Scavenging and trapping efficiencies are functions of the total mass of air (or fuel-air mixture) that is delivered every cycle. The delivered mass is generally normalized based on a reference mass value. The resulting dimensionless expression is known as delivery ratio (DR). When the reference mass is calculated using air manifold temperature and pressure values, the resulting delivery

[7] In this and the following sections, unless stated otherwise, 'scavenging models' refers to simple thermodynamic-based, constant volume scavenging models and not the more advanced and computationally expensive gas dynamic-based models.

ratio formulation is known as scavenging ratio. These parameters are mathematically expressed as follows:

$$\text{delivery ratio} = \frac{\text{mass of fresh charge delivered per cycle}}{\text{reference mass}} \quad (1)$$

$$\text{trapping efficiency} = \frac{\text{mass of fresh charge trapped per cycle}}{\text{mass of fresh charge delivered per cycle}} \quad (2)$$

$$\text{scavenging efficiency} = \frac{\text{mass of fresh charge trapped per cycle}}{\text{total mass trapped per cycle}} \quad (3)$$

Different scavenging models having varying levels of accuracy and associated computational costs are used to simulate gas exchange in two-stroke engines. These can broadly be categorized into simplified thermodynamic models or more complex computational fluid dynamic models. The latter are more accurate but come at an additional computational expense, which renders them impractical for direct use in engine control applications.

Simple models are based on the assumption that the scavenging process takes place at a constant volume and discrete pressure values that stay constant during a portion of or the entire gas exchange process. Additionally, there are assumptions about the mechanisms of interaction between incoming and retained gases. These assumptions

state that the fresh gases could either displace the retained gases ‘perfectly’ without entraining in, or mixing with, them; or they could mix ‘perfectly’ with the retained gases to produce a homogenous fresh charge-residual mixture that leaves the exhaust ports. Another idealized gas flow regime is short-circuiting of fresh gases, whereby fresh charge slips out of the exhaust ports with no interaction with cylinder gases. Simple scavenging models’ predictions of the relative contribution of these three interaction modes can result in the exhaust gas composition being either pure air (fresh charge), pure residual products of combustion, or an intermediate mixture of the two. Figure 7 qualitatively illustrates the various idealized gas exchange processes taking place in a two-stroke cycle.

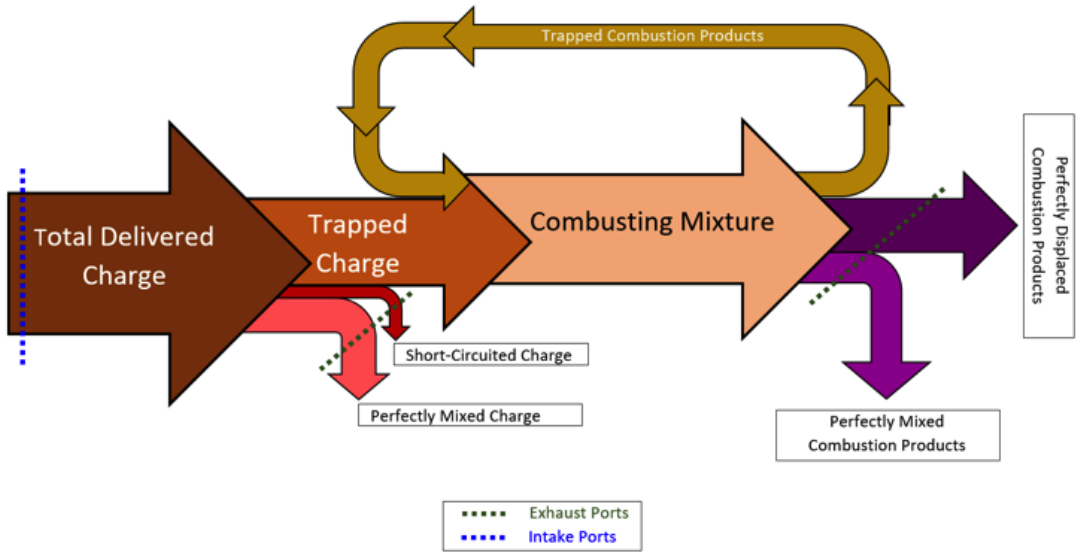

Figure 7: Qualitative illustration of various idealized gas exchange processes in a two-stroke cycle (back-flows have been ignored).

In real engines, the relative contribution of these three interactions (perfect mixing, perfect displacement, and short-circuiting) varies with engine design and operating conditions. In through and cross-scavenged designs, the displacement and mixing modes are dominant, respectively, while loop-scavenged engines have intermediate levels of mixing and displacement. The gas path designs in through-scavenged engines produce better scavenging performance compared to loop and cross-scavenged designs. 'Better' scavenging refers to a higher degree of removal of residual gases during gas exchange, which results in lower TRF and higher SE values. Figure 8 shows normal operating regions for the three designs on a delivery ratio vs. scavenging efficiency map. Because of improved gas flow path designs and better tuning of exhaust and intake systems, the scavenging efficiencies of modern cross-scavenged engines are higher than what is shown in Figure 8. The perfect displacement and mixing modes of gas interaction referenced above form the basis of two of the most popular idealized scavenging models found in the literature, namely the perfect displacement (PD) and the perfect mixing (PM) models. The SE estimates from these models are shown in Figure 8 by the black curves. These models are discussed in detail in the following section.

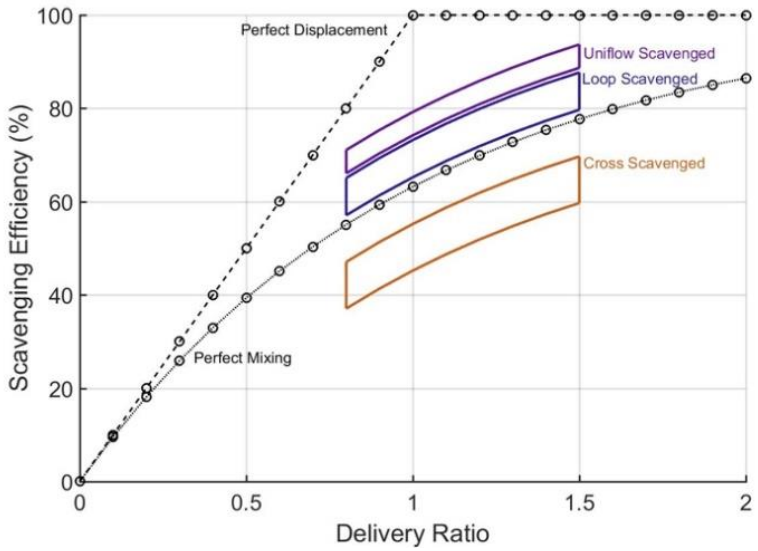

Figure 8: Operating regimes of various scavenging methods. (Recreated from [12])

Simple scavenging models try to simulate the complex flow phenomena taking place during scavenging by either using multiple sub-control volumes called zones, or by assuming that these processes take place in multiple steps called stages[8], or a combination of both. Each zone represents a different mixture of chemical species (e.g. fresh charge, residuals, or a mixture of fresh charge and residuals) and can have different temperatures. Multi-zone models are normally based on visual observations of gas exchange behavior in motored engines where each zone represents some locally observed phenomenon, e.g. (1) Wallace and Cave's two-zone model [8] (Figure 9a) is based on experimental observations of an opposed-piston engine with a high swirl-rate, which causes incoming charge to adhere to the cylinder walls; the resulting model has a

[8] In the literature, the term 'phases' is commonly used for the various scavenging steps. 'Stages' is used here instead to emphasize the time varying nature of the associated processes, and to avoid any confusion with the chemical or physical phase of the fluid.

central un-scavenged core, and (2) Benson's three-zone model [36] (Figure 9b) is based on visual observations of the interaction of fresh charge, mixing, and residual gas zones in loop and cross-scavenged engines.

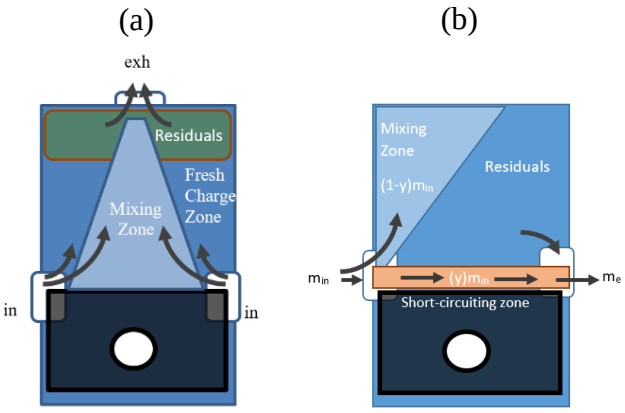

Figure 9: (a) Wallace and Cave's stage/zone concept for an opposed piston engine design. (Recreated from [8]) (b) Benson's three-zone multi-stage model. (Recreated from [36])

Multi-stage models have different temporal stages that represent the transition of one interaction mode to another, e.g. at the beginning of scavenging, the dominant interaction mode between incoming and retained gases could be perfect displacement in which retained gases are being pushed out without mixing. The exiting stream would comprise solely residual gases. In the next stage, there could be perfect mixing between the gases. The exiting gases would then be a mixture of fresh charge and residual gases. A good scavenging model should be able to capture various design-induced flow phenomena taking place in an engine cylinder during gas exchange; and for good scavenging estimates, appropriate models should be selected for the engine being simulated.

2.1.1. Selected Single-Zone Models

In this section, some popular single-zone scavenging models that have been commonly used in the past to predict engine scavenging behavior are discussed. The major assumptions used in the development of each model are also listed. Later in the dissertation, results from these models are used as a baseline to propose a new model that builds upon their strengths and tries to address some of their shortcomings. The models are selected, in part, because of their historical significance and the role they have played in economically modeling scavenging over the years, and, in part, due to the diverse nature of gas flow modes assumed in the models. Thus, making them ripe for conducting a comparative study of different scavenging models. The categorization of single-zone models used is based on Merker and Gerstle's [37] definition of zones, whereby residual gases are not considered a separate zone.

The simplest of the single-zone models are the perfect-mixing and the perfect-displacement models. The perfect displacement model is the first known scavenging model [37]. It assumes that there is no mixing of the incoming and residual gases, and that none of the incoming fresh charge is lost directly through the exhaust ports while there are residual gases still present in the cylinder. This describes the theoretically best possible scavenging performance of a two-stroke engine and serves as an upper bound for scavenging efficiency. The PD model is, however, of little practical use for directly estimating the trapped mixture composition for a real engine. As will be shown later, the PD model can prove to be useful when used in conjunction with other models to

represent those stages in the gas exchange process that involve minimal mixing of incoming and cylinder gases. Two versions of the perfect-displacement model can be found in the literature: the classical isothermal version, which assumes thermal homogeneity between the incoming and outgoing gases, and the non-isothermal PD model [1], which assigns distinct temperatures to the fresh charge and residual streams.

Similarly, the PM model also has two formulations, an isothermal one and a non-isothermal one [1]. Hopkinson's isothermal PM model (developed in 1914) [38] is the classical perfect mixing model which is based on the assumption that incoming and retained cylinder gases mix completely and instantaneously in an adiabatic constant-volume chamber. Moreover, the incoming and outgoing gases behave ideally and have the same temperature, specific heat, and pressure. The scavenging efficiency for this PM model is related to the delivery ratio by the following expression:

$$\mathrm{SE} = [1 - \exp(-\mathrm{DR})] \qquad 4$$

Sher's non-isothermal PM model (developed in 1989) [1, 39] is an improved version of Hopkinson's model. It does not assume thermal homogeneity between incoming and residual gases. The residual gas temperature is assumed to be equal to the average in-cylinder bulk gas temperature at intake port opening. All the remaining assumptions are the same as for the isothermal perfect mixing model. In the resulting scavenging efficiency equation (equation 5), the exponential term from equation 4 is

multiplied by a ratio of the temperatures at the end of scavenging (exhaust port closing, EPC) and blowdown (IPO).

$$SE = 1 - \frac{T_{cyl(EPC)}}{T_{(IPO)}} \exp(-DR) \qquad 5$$

Benson and Brandham's two-stage (displacement-mixing) model (developed in 1969) [40] is also an extension of Hopkinson's isothermal PM model. It includes an initial isothermal perfect displacement stage that pushes out residual gases from the cylinder without any mixing. This is followed by an isothermal PM stage. The relative fraction of the PD mechanism of residual removal is defined by the displacement ratio 'x', which is the fraction of cylinder mass that is perfectly displaced during the first stage of gas exchange. For a well-scavenged engine, x is generally over 0.75. The final scavenging efficiency equation is given below:

$$SE = \begin{cases} DR & DR \leq x \\ [1 - (1 - x)\exp(x - DR)] & DR > x \end{cases} \qquad 6$$

If the displacement fraction is equal to 0, the equation reverts back to the original perfect mixing equation (equation 4).

Wallace and Dang's two-stage (displacement-combined-mixing/short-circuiting) model (developed in 1992) [12] is an extension of Benson and Brandham's model. It has

an additional mode of interaction, or lack thereof, between the incoming and cylinder gases, namely the short-circuiting mode. The authors called their model a two-stage model because the short-circuiting and perfect mixing processes are assumed to be taking place simultaneously; producing, as a result, an exhaust stream that is a combination of short-circuited and perfectly mixed gases. The amount of short-circuiting is defined by a new weighting factor known as the short-circuiting fraction 'y', which is the short-circuited fraction of the incoming air. The non-short-circuited fraction mixes perfectly with the cylinder gases. The final scavenging efficiency equation is given below:

$$\mathrm{SE} = \begin{cases} \mathrm{DR} & \mathrm{DR} \leq \mathrm{x} \\ [1 - (1 - \mathrm{x})\exp\{(1 - \mathrm{y})(\mathrm{x} - \mathrm{DR})\}] & \mathrm{DR} > \mathrm{x} \end{cases} \qquad 7$$

If the short-circuited fraction is equal to 0, the equation reverts back to Benson and Brandham's model (equation 6).

2.2. Scavenging-Based Emissions Control Strategies

Engine emissions control systems can either be open-looped or closed-looped. Closed-loop systems are more reliable than open-loop ones because they use real time feedback of the control parameter, which for the current study would be NO_x emissions, to control engine operation.

Closed-loop control strategies have been successful in the automotive sector through the use of 'lambda sensors' in the exhaust system. Lambda sensors measure

exhaust oxygen concentration and use the mass of injected fuel to estimate the equivalence ratio of the combusting mixture. The equivalence ratio is originally set by knowing the mass flow rate of air entering the engine (measured using a mass air flow sensor; generally hot wire anemometers) and the engine speed. The injection of fuel is controlled accordingly to get the desired equivalence ratio mixture. The equivalence ratio can then be used to estimate NO_x, CO, and UHC emissions. Prior to this control method, known as the mass air flow method, open-loop approaches that estimated the mass of air using engine speed and throttle angle (alpha-n approach), or intake manifold pressure and engine speed (density-n approach) were used for port and direct injected four-stroke engines, respectively [41]. The open-loop approaches rely on close adherence of engine operation to previously made maps, which makes them unreliable under off-design operation. Air-fuel ratio based closed-loop control approaches that rely on exhaust oxygen concentration feedback cannot be implemented in two-stroke engines because, unlike four-stroke engines, the gas exiting the exhaust ports has significant amounts of short-circuited air that dilutes the exhaust stream. Therefore, making it infeasible to directly estimate TER from lambda sensor measurements.

Closed-loop emissions control systems that rely on direct NO_x emission measurements are rarely used for integral compressor engines because of practical and financial limitations. Currently available emissions analysis equipment is expensive, sensitive in nature, and requires regular servicing and calibration for reliable performance. These traits make closed-loop control systems impractical for use in

integral compressor engines at the present, as most of the engines are located in remote places and are exposed to harsh environments. For these reasons, open-loop systems that indirectly estimate emissions are usually used in integral compressor engines. Such systems, commonly known as parametric emissions monitoring systems or PEMS [42], are discussed in the following section.

2.2.1. TER-Based Emissions Control

As was discussed in Chapter 1, TER is an important metric of the trapped mixture composition because it is a good predictor of engine-out emissions, most notably NO_x emissions. Figure 10 [43] is a general operating map for lean-burn natural gas engines. It shows the effects of changing engine spark timing and TER on parameters like engine stability, NO_x emissions, thermal efficiency, and engine knock. The engine is unstable at very lean operating conditions. Even though not explicitly shown in Figure 10, very rich engine operation is also not desirable because it leads to increased UHC and CO emissions, and poor fuel conversion efficiency. All of these parameters have to be within reasonable limits during engine operation. Thus, it is important to have model-based control systems that can accurately estimate TER over a wide range of engine operation. This can be achieved by having a thorough understanding of the underlying physics of the mixture preparation process and basing upon it the scavenging models used to predict control parameters like TER.

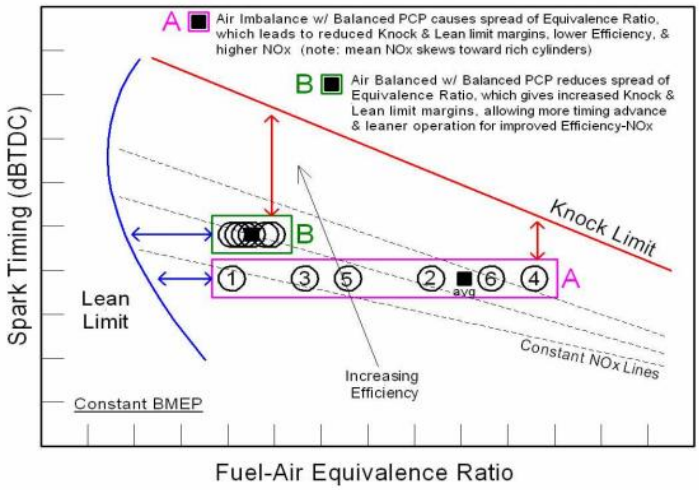

Figure 10: Operating envelope of a lean-burn two-stroke engine. [43]

Parametric open-loop emissions control systems used in two-stroke engines rely on scavenging models, like the ones discussed in section 2.1.1., to control engine operation for emissions compliance. The inputs needed for simple scavenging models generally include air and fuel flow rates; and manifold pressures and temperatures. Most of these are commonly measured in field engines, with the exception of air flow, which is sometimes estimated by the density-n approach using lookup tables. The models estimate the trapping efficiency of the engine at a given operating point. Then, measured air flow data is used to estimate the amount of air that is not short-circuited, i.e. it is trapped. Knowledge of the trapped mass alone is not sufficient to accurately calculate TER because residual gases in the cylinder have to be accounted for as well. This is again done by relying on scavenging models to provide an estimate for the engine's scavenging efficiency. In integral compressor engine jargon, such approaches that use trapped equivalence ratio estimates to control engine emissions are commonly referred

to as TER-based engine control methods [44]. Since these tools can only be as accurate as the TER estimates from the scavenging models, it is critical to have reliable SE and TE estimates from scavenging models,which historically has not always been the case. To compensate for inaccuracies in scavenging models, empirical correction factors are often used to tune scavenging models for different engines. An example of such an equation for scavenging efficiency is given below [41, 45]:

$$\mathrm{SE}_{\mathrm{estimate}} = ([1 - \exp(-\mathrm{DR})] + \mathrm{A})\mathrm{B} \qquad 8$$

'A' and 'B' are correction factors that account for changes in engine specific scavenging characteristics and operating conditions, respectively. The most significant effect of changes in engine operation is from changes in engine speed [44] as scavenging has a strong dependency on engine speed. This is because the phasing of reflected manifold pulses, which affect trapping and scavenging efficiencies, changes significantly with respect to crank angle degrees as the engine speed changes [23, 46]. The basic building block for semi-empirical scavenging models, like equation 8, is generally the non-isothermal perfect mixing model (equation 4). This is because cross-scavenged, integral compressor engines operate close to the perfect-mixing range. The SE calculated from equation 8 can then be used to calculate TE using the functional relationship between TE and SE for the perfect mixing model (equation 9), which can in turn be used to calculate TER using equation 10.

$$\mathrm{TE}_{\mathrm{estimate}} = \frac{\mathrm{SE}_{\mathrm{estimate}}}{\mathrm{DR}} \qquad 9$$

$$\mathrm{TER}_{\mathrm{estimate}} = \frac{\left(\frac{\mathrm{A}}{\mathrm{F}}\right)_{\mathrm{stoich}}}{\mathrm{TE}_{\mathrm{estimate}} \frac{\dot{\mathrm{m}}_{\mathrm{air}}}{\dot{\mathrm{m}}_{\mathrm{fuel}}}} \qquad 10$$

A similar version of the TER estimating approach is given in equation 11. This version has been used in the natural gas engine sector for the past 20 years [31]. Equation 11 also includes ignition timing correction using the correction factor 'c_{IT}' for changes in ignition timing 'ΔIT' from the nominal spark timing. Equation 12 shows the engine/operating point tuning equation (similar to equation 8) used in this method. In this approach, the engine specific offset 'A' is being multiplied instead of being added. The inclusion of the spark timing correction converts the TER estimates into an empirically determined 'virtual sensor' [31] such that the relationship between the values of this 'sensor' and NO_x emissions is a consolidated exponential curve fit for different spark timing cases. To emphasize this pseudo-physical nature of the computed equivalence ratio it is subscripted with 'modified' in equation 11.

$$\mathrm{TER}_{\mathrm{modified,estimate}} = \frac{\left(\frac{\mathrm{A}}{\mathrm{F}}\right)_{\mathrm{stoich}}}{\mathrm{SE}_{\mathrm{estimate}} \frac{\dot{\mathrm{m}}_{\mathrm{air}}}{\dot{\mathrm{m}}_{\mathrm{fuel}}}} + \mathrm{c}_{\mathrm{IT}}.\Delta\mathrm{IT} \qquad 11$$

$$\mathrm{SE}_{\mathrm{estimate}} = [1 - \mathrm{A}\exp(-\mathrm{DR})]\mathrm{B} \qquad 12$$

In equations 10 and 11, the overall air fuel ratio $\left(\frac{\dot{m}_{air}}{\dot{m}_{fuel}}\right)$, which is calculated using the measured fuel and air flowrates, is used to estimate the air fuel ratio and the equivalence ratio of the trapped mixture. TER is different than the overall equivalence ratio because of (1) short-circuiting, and (2) dilution by the trapped residual gases that can have a significant oxygen fraction. For direct-injected, two-stroke engines, the first influence is stronger than the second one and, as a result, the TER is greater (richer) than the overall equivalence ratio. Equation 10 tries to correct for short-circuiting through the use of an estimated TE and equation 11 uses a SE estimate to account for the residual gases. These apparent discrepancies between the two TER estimating methods do not affect the final TER estimates significantly because the correction factors generated through regression fitting of empirical data compensate for the shortcomings in the underlying physics of the two approaches. The basic structure for both the equations (10 and 11) looks similar: the offset 'A' added in equation 8 is also added in equation 11 in the form of the ignition correction timing coefficient, and the pre-exponential multiplier in equation 12 compensates for division by SE instead of the ratio of the corrected SE and DR, i.e. corrected TE, in equation 11.

Another semi-empirical scavenging model was proposed by Tobis et al. [10] using results from tracer (CO_2) based scavenging experiments on a small, high-speed, loop scavenged engine. The model is based on the non-isothermal perfect mixing scavenging model and is capable of estimating SE from the measured overall equivalence ratio for an engine it has been tuned for.

The DR used in scavenging models (equations 9 and 12) can be calculated using the measured air flow rate through the engine. Taylor [45] proposed that the reference mass should be computed at BDC using air density calculated at inlet temperature and exhaust pressure. The resulting expression is shown below. 'N' is the engine speed and 'h' is the absolute humidity of the inlet air.

$$\mathrm{DR} = \frac{\dot{m}_{\mathrm{air,measured\,(dry)}}}{\dot{m}_{\mathrm{air,reference}}} = \frac{\dot{m}_{\mathrm{air,measured\,(dry)}}}{N.V_{BDC}.\rho_{air}} \quad 13$$

$$\rho_{air} = \frac{P_{exh}}{R_{air}.T_{inlet}}\left(\frac{1}{1+1.6h}\right) \quad 14$$

If measured air flow data is not available, it can be estimated from the equations of isentropic gas flow shown below by using air manifold pressure, cylinder pressure, and intake port geometry [47].

$$\frac{dm}{dt} = \frac{C_D A_R p_o}{\sqrt{RT_o}}\left(\frac{p_T}{p_o}\right)^{\frac{1}{k}}\sqrt{\left\{\frac{2k}{k-1}\left[1-\left(\frac{p_T}{p_o}\right)^{\frac{k-1}{k}}\right]\right\}} \quad 15$$

Another version of the mass flow rate equation (equation 16) is used for the cases when the flow is choked.

$$\frac{dm}{dt} = \frac{C_D A_R p_o}{\sqrt{RT_o}}(k)^{\frac{1}{2}}\left\{\frac{2}{k+1}\right\}^{\frac{k+1}{2(k-1)}} \quad \text{when} \quad \frac{p_T}{p_o} \leq \left\{\frac{2}{k+1}\right\}^{\frac{k}{(k-1)}} \quad 16$$

The discharge coefficient 'C_D' accounts for irreversibilities in flow across the ports, which depend on the pressure ratio across the port, the port open area, and the port design. Estimates for these values can be found in the literature [1]. The most reliable means of getting C_D values is direct flow experimentation on the engine being modeled. The discharge coefficients can be different among different engines with similar port design and even among different cylinders of the same engine because of manufacturing differences and varying degrees of degradation from use. Experimental studies [43] for cross-scavenged integral compressor engines have shown that the discharge coefficient values for intake and exhaust ports are around 0.6. Figure 11 shows the discharge coefficient results from an experimental investigation of a GMVH-6 engine. In addition to errors in C_D estimates, pressure-based approaches for mass flow calculations can have errors stemming from imprecise absolute pressure calculations from measured in-cylinder gauge pressure.

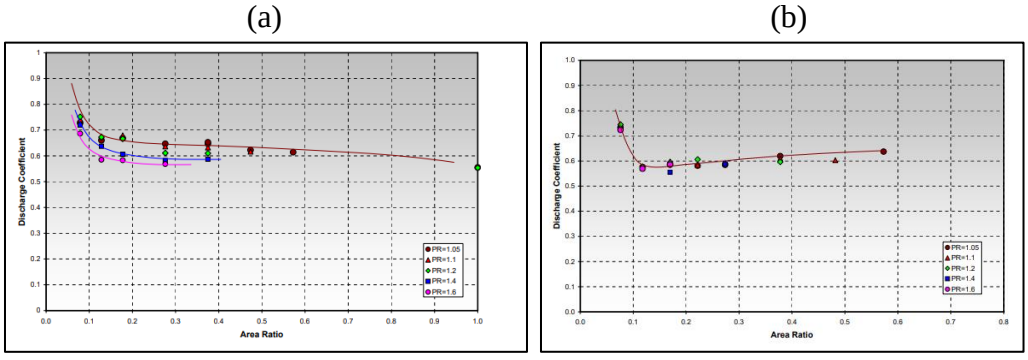

Figure 11: Experimentally measured (a) inlet and (b) exhaust port discharge coefficients for a GMVH-6 engine. [43]

2.3. Experimental Scavenging Measurements

Simulation results can be considered credible only if they have been corroborated by experimental results; that is, they have been validated. Once validated for some important measurable engine properties like cylinder pressure, manifold pressures or temperatures at some operating points, the simulation results can be immensely helpful in studying engine behavior. They can be used to predict engine behavior at other operating points, calculate immeasurable properties (e.g. entropy, enthalpy, etc.), provide high-resolution results for properties that are difficult to measure directly on a time-resolved basis (e.g. mass flow rates across ports, emissions production during a cycle, etc.) and/or spatially-resolved basis (e.g. cylinder temperature, compositional inhomogeneities in the cylinder, etc.). The exact number of validation properties needed for a particular simulation model depends on the level of fidelity expected from the model, and the available measurable properties that carry signatures of variation in the parameter being studied. A parameter considered essential for most engine validation exercises is the cylinder pressure. For the current project, exhaust pressure and air flow will also be used for validation. Because of the importance of experimental data needed for model validation, a brief review of some experimental approaches used for scavenging studies is presented next.

Scavenging is a difficult process to directly measure because direct evidence of the process, which lies in the composition of the trapped cylinder mixture, is difficult to observe, thus, forcing the experimentalist to look for signatures of short-circuiting and

scavenging of residual gases elsewhere. Some indirect but measurable scavenging signatures include engine power, torque, indicated mean effective pressure (IMEP), specific fuel consumption, and emissions. For the same pumping power input, a cylinder that is better scavenged will produce higher engine brake power [1]. These signatures can have different forms. They can be visual flow patterns (velocity fields) obtained through velocimetry experiments (e.g. [48, 49]) or pressure contours obtained from steady state pressure measurements across the cylinder head (e.g. [14, 25]). Such results can be useful when used with the measurable signatures listed above to distinguish 'good' scavenging designs from 'bad' ones.

Experimental scavenging studies can be categorized in multiple ways. First, they can be split between engine-based studies and model-based ones. Engine based studies can be further sub-divided into firing and non-firing studies [1] based on the nature of engine operation; or sampling and non-sampling studies based on the drawing (or lack thereof) of gas samples from the engine. Firing studies are more reliable as they are a more realistic re-creation of actual engine operation, while non-firing studies are less realistic because they are based on the underlying assumption that the effects of combustion on the scavenging process are negligible or, at the very least, consistent over all operating points. Because of this assumption, non-firing studies can provide good qualitative insights into the nature of scavenging but are not well suited for collecting high fidelity quantitative data (SE, TE, DR).

Based on the data collection methodology, experimental techniques can be divided into visual or measurement-based techniques, or a combination of the two [50]. In the studies reviewed, most visual studies were performed on non-firing optically accessible models of the engine (e.g. [11, 48, 49, 51, 52]). Some examples of visual studies on firing two-stroke engines are: [53] which used a Schlieren technique to study scavenging in a Cooper-Bessemer GMV engine, [54] which used Schlieren and Mie-scattering-based flow visualization along with ionization probes to study the effects of scavenging flows on combustion, [55] which used laser Doppler velocimetry (LDV) to study flow through transfer ports in a small two-stroke engine, [56] which used dual seeding to simultaneously image flame propagation and in-cylinder flows using particle tracking velocimetry (PTV), [13] which used Mie scattering and spectrally resolved flame luminosity imaging along with cyclically resolved exhaust HC emissions to study flow and combustion, and [57] which used LDV to study flows through the transfer ports for two different scavenging systems (crankcase vs. blower). Even though optical investigations of fired engines have been common for four-stroke engines since the days of Sir Harry Ricardo (1920s) [58], they have been used in two-stroke engine research only since the 1990s; as is evident from the chronology of the aforementioned references.

Visualization approaches rely on seeding the incoming flow stream with an optically observable tracer, tracking its interactions with the ‘gases’ in the cylinder, and documenting the interactions on either a qualitative or a quantitative basis. The working

fluid used for the studies can either be gaseous or liquid as long as similitude requirements are satisfied. Sher [52] proposed that at least three similarities - Euler, geometric, and Reynolds - need to be satisfied to have a model that accurately captures the fluid mechanics of a real engine. Some tracer species that can be injected in the incoming stream are smoke, silk threads, or sawdust [59] for a gaseous working fluid; and air bubbles, cork powder, aluminum powder, hydrogen bubbles from electrolysis, or colored liquid dye [52] for a liquid substrate. Luminescent tracer particles are used for velocimetry techniques like LDV or particle image velocimetry (PIV).

Another way of characterizing scavenging models is based on the mechanics of the test setup, i.e. is the piston moving or not? Dynamic models (e.g. [48, 25, 50]) are more accurate than static models (e.g. [49, 59]), which treat the flow problem as a steady one. Static tests, which often have the piston locked at BDC position, are used in the early stages of designing a scavenging system. Rizk [59] provides a good classification of various investigation methods used in experimental scavenging studies. A classification diagram from it is shown in Figure 12.

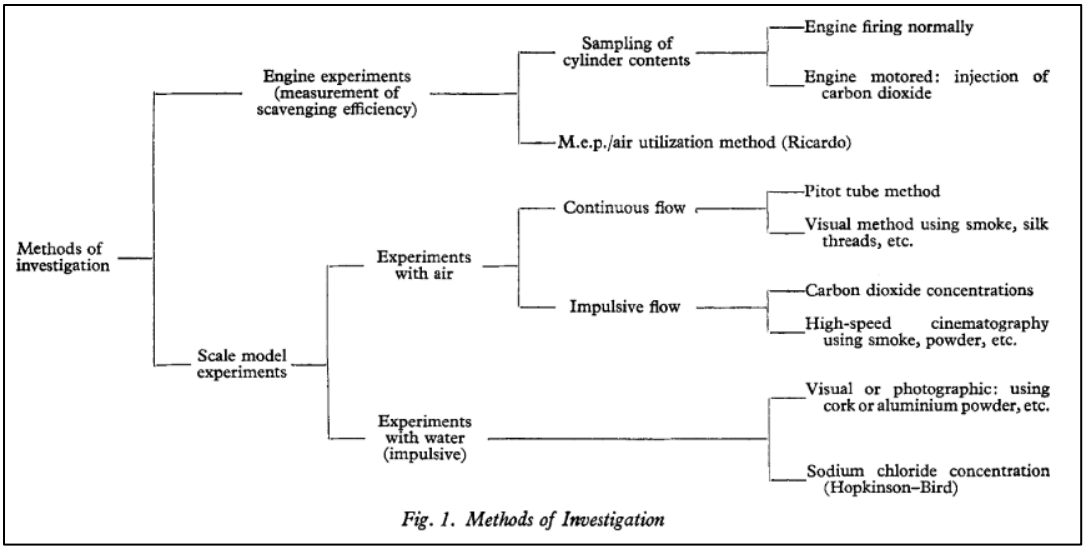

Figure 12: Classification of experimental methods to study scavenging. [59]

One of the most popular means of experimentally studying scavenging during the 1970s and the 80s was qualitative in nature. It was proposed by Jante [25] in 1968 and was extensively used by engine manufacturers to design intake ports so as to minimize short-circuiting and maximize the utilization of incoming air for scavenging. The approach used a manometer comb (Figure 13) to record dynamic pressures at various locations in the cylinder head as the engine (or an engine model) was motored. The dynamic pressures were used to calculate average velocities at different regions and the results were represented on ‘scavenging pictures’, which were equivelocity contour maps at various motoring speeds (Figure 14). Different scavenging designs were used to generate ‘good’ and ‘bad’ velocity maps using measurable parameters like engine power, specific fuel consumption, and emissions. Two examples of typical setups that used this approach are shown in Figure 13.

A good scavenging picture should look similar to Figure 14(a), where the highest velocity region lies on the intake port side. This configuration is considered good because the incoming scavenging gases having high initial velocities and the tendency to mix with the cylinder gases (perfect mixing type interactions) are restricted to the intake port side. The mixing of incoming and cylinder gases is undesirable from the scavenging standpoint as the incoming gases are not effectively displacing the cylinder gases. In a well-scavenged engine, the incoming gases flow along the intake port side wall towards the cylinder head (as the 'scavenging up-current'), losing some of their momentum along the way, and eventually colliding with the head to form a 'stagnation zone'. The gases then move towards the exhaust port side at a relatively slow pace. The slower gases interact with the residual gases in a perfect displacement type mode and scavenge residual gases without mixing in them. Figure 14(b) is an example of a poorly scavenged engine which has high velocity 'tongues' protruding out away from the intake port side wall. Jante described his efficient scavenging flow path criteria as follows, "The scavenging currents must so interact with the piston crown and the cylinder wall that a stable closed rising current is obtained on the wall opposite the exhaust ports, which has its maximum velocity at this wall and near-zero velocities on a line perpendicular to the plane of symmetry and through the cylinder axis."

(a) (b)

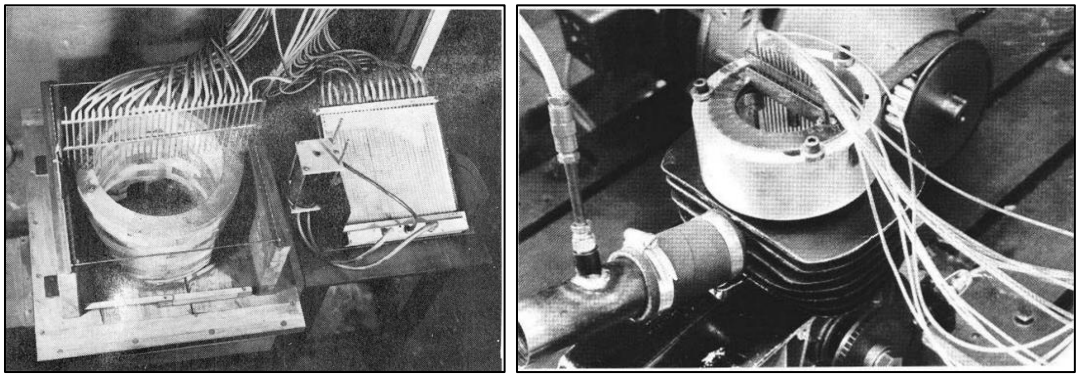

Figure 13: Manometer comb setups to qualitatively study scavenging performance. (a) [25], (b) [50]

(a) (b)

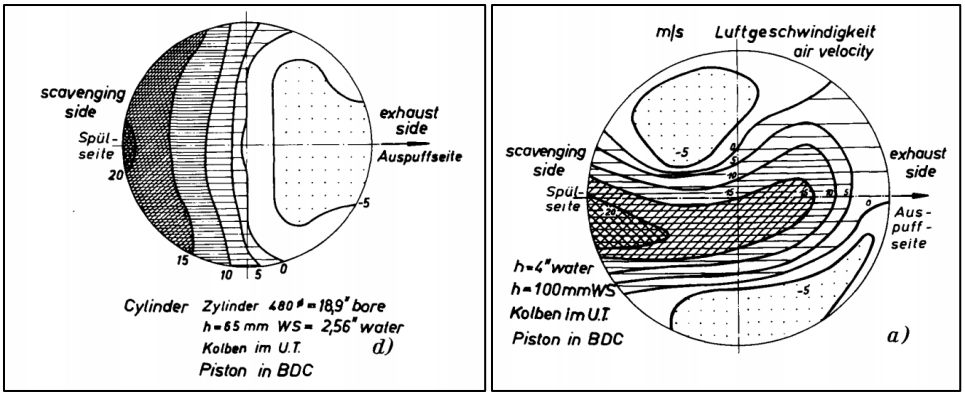

Figure 14: Good (a) and bad (b) scavenging pictures. [25]

An indirect methodology, known as the ‘skip-fire’ technique [60, 61], was proposed in the 1950s to estimate the scavenging efficiency of an engine using ratios of IMEP for cycles that followed a certain number of non-firing cycles. The technique was based on the assumptions that the engine’s combustion efficiency stays constant, its performance (as quantified by IMEP) is proportional to the effectiveness of the scavenging process, and that the engine’s scavenging efficiency is the same for firing

and non-firing cycles. The last assumption was found to be problematic by Tobis et al. [10] who showed that misfiring cycles had considerably (almost 50%) poor scavenging performance compared to normal cycles. The technique is, therefore, not considered reliable and is mentioned here only as a matter of record.

The remaining section discusses the use of tracer species in fired engines to estimate scavenging and trapping efficiencies, as that is the approach used in the current work. Tracer species that represent the concentration of either the burned or fresh gases can be measured in the engine exhaust or in the cylinder. The measurements can be taken continuously throughout the cycle or at specific times of interest during a cycle using an appropriately timed sampling valve.

Species that can be used to track the burned gas concentration should have negligible concentration in the cylinder before combustion, be generated during combustion, homogenize quickly with the cylinder gases, and should be stable enough to be analyzed outside the cylinder. CO [8] and CO_2 [10] are good burned gas tracers for spark-ignited engines [1]. Those species representing fresh charge should be such that they are consumed completely during combustion. Any species sensed in the exhaust would have, therefore, been short-circuited. For rich cases where there is negligible oxygen in the products after combustion, a good tracer for fresh charge is O_2 because almost all of the O_2 in the exhaust comes from the short-circuited stream. The exhaust

O_2 concentration measurements can be used to calculate trapping efficiency using equation 17.

$$TE = 1 - \frac{[O_2]_{exh}}{[O_2]_{atmosphere}} \qquad 17$$

For lean cases, hydrocarbons like monomethylamine (CH_3NH_2), and n-butane (C_4H_{10}) have been used as fresh charge tracers [1]. If fuel is mixed with the air prior to charge induction in the cylinder, fuel can serve as a fresh gas tracer as well for lean burn engines [9]. This approach assumes that 'fuel slip' resulting from combustion inefficiencies is negligible. This is the approach used in trapping efficiency calculations for the current project.

Cylinder sampling of burned gas tracers like CO_2 before and after combustion can be used to calculate SE. The amount of CO_2 in the cylinder before combustion is the sum of CO_2 present in the residual gas from the previous cycle and the CO_2 in the fresh air trapped. If the molecular weights of air, residual gas, and CO_2 are assumed to be the same, the unburned CO_2 concentration is given by equation 18. 'u' and 'b' symbolize unburned and burned gases, respectively. SE can then be calculated using equation 19. For the current project, equation 18 had to be modified slightly to account for the dilution of cylinder CO_2 concentration by the injected fuel. This was needed because the CO_2 concentration could not be precisely measured prior to fuel injection, which is

needed in equation 19. Section 5.2.1. discusses SE calculation in detail and the derivation of the equations used is provided in Appendix A.

$$[CO_2]_u = [CO_2]_b TRF + [CO_2]_{air} SE \quad (18)$$

$$SE = \frac{[CO_2]_b - [CO_2]_u}{[CO_2]_b - [CO_2]_{air}} \quad (19)$$

The trapping efficiency can be calculated using the burned CO_2 concentration in the cylinder if the exhaust CO_2 concentration is also measured. In the absence of any dilution from short-circuiting or residual gases in the exhaust, the exhaust CO_2 concentration should be the same as the burned CO_2 concentration in the cylinder. Any reduction in the observed exhaust concentrations can then be attributed to short-circuiting. This approach can be used to calculate the molar short-circuiting fraction, 'y_{short}' as the following [1]:

$$y_{short} = \frac{[CO_2]_b - [CO_2]_{exh}}{[CO_2]_b - [CO_2]_{air}} \quad (20)$$

TE can be calculated using equation 21. 'ṁ' are mass flowrates and 'M' are molecular weights of the respective subscripted species.

$$TE = 1 - \left(\frac{\dot{m}_{air,del} + \dot{m}_{fuel}}{\dot{m}_{air,del}}\right)\left(\frac{y_{short} M_{air}}{y_{short} M_{air} + (1 - y_{short}) M_b}\right) \quad (21)$$

Previous tracer sampling-based studies [10, 62, 63, 64, 65] have relied on synchronized electromagnetic or cam-actuated sampling valves to draw cylinder and/or exhaust samples at appropriate times during gas exchange, i.e. intermittent sampling. The challenges with such studies are: (1) to obtain representative composition samples because of the heterogeneity of the scavenging mixture, and (2) to obtain sufficient quantities of the samples that they can be analyzed by an emissions analyzer. To overcome this problem, relatively large quantities of samples have to be drawn and averaged over multiple, non-consecutive (every 15^{th} cycle in [10]) cycles to get representative composition data. Consecutive cycles cannot be sampled because of the time needed by the engine to recover from the large (greater than 20% of total engine volume) cylinder gas donation.

The current study uses continuous sampling from the cylinder and exhaust manifold to get crank angle resolved composition data, which is analyzed on a cyclic basis to remove any anomalous, non-representative cycles. Results from the representative cycles are averaged over 300 cycles to get reliable measures of central tendency. This improves the fidelity of the scavenging calculations. There could still be errors because of the stratified nature of cylinder contents, but the good repeatability of results suggests that such errors are most likely minor. Moreover, the measured post-combustion CO_2 concentrations of around 8 vol% are close to the stoichiometric results for methane combustion at an equivalence ratio of around 0.7.

A literature survey of continuous sampling studies yielded only a handful of results. These are listed below:

- [66] used the same high speed CO_2 analyzer as used for the current work on a four-stroke homogeneous charge compression ignition engine to calculate TRF using cycle resolved cylinder CO_2 measurements.

The continuous sampling studies found for two-stroke engines used cycle resolved measurements only in the exhaust:

- [13] used a high-speed flame ionization detector to measure exhaust HC concentration.
- [67] and [68] used high-speed chemiluminescence detectors to measure exhaust NO concentration.
- [69] used high speed exhaust CO_2 measurements along with exhaust O_2 measurements in a valved, automotive type, two-stroke engine to calculate short-circuiting and through that, the trapped equivalence ratio.
- [70] used high and slow speed exhaust CO_2 measurements to calculate short-circuiting for a valved two-stroke engine.

3. EXPERIMENTAL SETUP AND MODELING FRAMEWORK

This section describes the test bench setup for the two-stroke engine being studied, followed by a description of the one dimensional model of the same engine developed on the flow simulator *GT-Power*.

3.1. Engine Test Bench

A single-cylinder, natural gas fueled, naturally aspirated, cross-scavenged, two-stroke, spark ignited engine - the Ajax E-565 - is used to study scavenging. The engine test bed is shown in Figure 15, and engine specifications are provided in Table 1. This particular engine is selected for studying gas exchange in integral-compressor engines because of the similarity in scavenging system designs: most integral-compressor engines have either the Curtis or Schnürle scavenging configurations (Figure 3), which are a mix between loop and cross-scavenged designs. Moreover, the ease of studying and instrumenting a relatively small, single cylinder engine compared to larger multi-cylinder ones makes the engine well-suited for the current study. The biggest differences between the Ajax E-565 and bigger engines like the GMV series discussed in Chapter 1 are in the breathing setup (piston-scavenged vs. turbocharged) and the ignition system (most integral-compressor engines have been retrofitted with pre-combustion chambers).

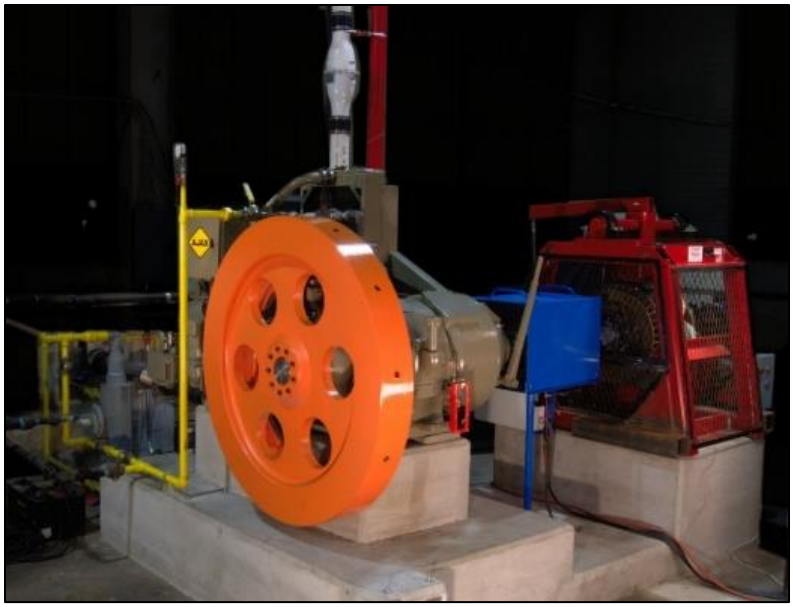

Figure 15: Ajax E-565 engine test bed. (Photograph courtesy of Jacob Hedrick)

Parameter	Units	Value
Bore	cm (in)	21.6 (8.5)
Stroke	cm (in)	25.4 (10)
Displacement	L (in^3)	9.3 (567)
Compression ratio (geometric)	--	8:1
Compression ratio (effective)	--	6:1
Rated continuous power	kW (hp)	29.8 (40)
Rated speed	RPM	525
Rated torque	N.m (ft.lbf)	542 (400)
Spark timing	CAD (bTDC)	11.5
EPO	CAD (aTDC)	120.4
IPO	CAD (aTDC)	138.1
Air induction system	Piston scavenged	
Fuel induction system	1) Fuel admission valve in cylinder head (direct-injected) - or - 2) Fuel delivered in the stuffing box (pre-mixed)	
Scavenging port arrangement	Cross	
Port opening / closing control	Piston edge | symmetric timing diagram about BDC	
Fuel	Natural Gas (95 vol% CH4, 2.2 vol% C2H6, 1.8 vol% N2)	

Table 1: Ajax E-565 specifications.

The current engine is equipped with cylinder and manifold[9] pressure transducers, manifold and coolant temperature sensors, fuel flow meter and a quadrature angular encoder. The exhaust from the engine goes to a 5 gas emissions analyzer (*MEXA-7100D*) that measures CO, CO_2, NO_x, total HC, and O_2 concentrations on a dry basis. Additional high speed CO and CO_2 sensors (made by *Cambustion Ltd.*) are installed for the current study to measure the respective time-resolved cylinder and exhaust concentrations on a wet basis. An air flow meter is also installed on the inlet piping. The meter was not available for the initial experiments that measured cylinder CO_2 concentrations but was available for short-circuiting experiments which used pre-mixed fuel as a tracer for fresh charge.

The engine is coupled to an eddy current dynamometer (Figure 15) via a clutch. The dynamometer is used to load the engine to replicate the angular resistance (torque) that the engine would experience when it is driving a compressor or a pump. The load is set as a percentage of full load, which is defined as the highest torque at which the engine starts to stall at the rated speed of 525 RPM. A third party spark control system (*Altronic NGI-100*), shown in Figure 16, is used to control the spark timing. The system is capable of changing the spark energy and duration but they were held constant for the current project. Recent work by Pommier [71] has looked at some of these ignition system parameters and their effects on engine stability and emissions.

[9] 'Manifold' used loosely herein; the *single*-cylinder engine technically does not have '*mani*'-folds.

Figure 16: Altronic NGI-1000 ignition system installed on the Ajax E-565.

Table 2 shows the test matrix for the test campaign conducted in this study. The spark timings are shown relative to the nominal spark timing (11.5^{o} bTDC); 'R' denotes retarded and 'A' advanced. 10^{o} retarded cases at 100% load could not be run because the engine was very unstable and steady speed operation could not be maintained for data acquisition. At least two experiments were performed at each operating point to ensure repeatability. Data was collected for over 400 consecutive cycles; 300 of which were used during post-processing to get ensemble averaged results. After preliminary data analysis, it was decided that only the twelve operating points highlighted in Table 2 will be used for scavenging analysis. The twelve points represent stable engine operation, which is needed for validating a mean value model like a simple scavenging model. In future work, a stochastic sub-model can be overlaid on the mean value model to account for operating point-specific variability. Most of the experimental results presented herein are for the twelve stable operating points.

Speed (RPM)	350			450			525		
Load	50%	75%	100%	50%	75%	100%	50%	75%	100%
Spark Timing				10R	10R	~~10R~~	10R	10R	~~10R~~
		5R		5R	5R	5R	5R	5R	5R
		0	0	0	0	0	0	0	0
		5A		5A	5A	5A	5A	5A	5A
				10A	10A	10A	10A	10A	10A
Total	4			14			14		

Table 2: Experimental test matrix.

In the following sections, all the sensors used for the project are discussed briefly. Figure 17 shows a schematic of the test setup and lists all the installed sensors.

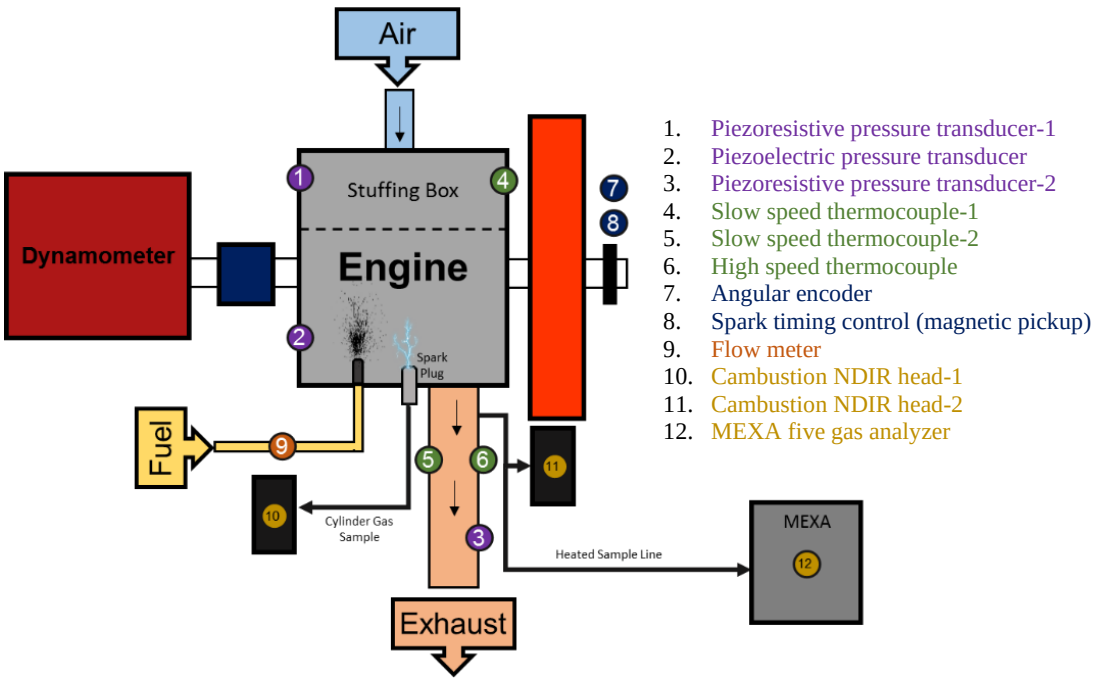

Figure 17: Experimental setup schematic showing installed sensors.

3.1.1. Pressure Measurement

Piezoelectric and piezoresistive pressure transducers made by *Kistler Instrument Corp.* (Figure 18) were used to measure cycle-resolved cylinder and manifold pressures, respectively. The piezoelectric transducer measures change in pressure and has to be pegged to a certain known pressure datum to calculate absolute values, while the piezoresistive transducer measures absolute pressure. For the current study, the piezoelectric transducer readings were pegged at BDC to be 1 atm. The piezoelectric transducer was calibrated in-house using a deadweight calibrator and the piezoresistive transducers were calibrated by the OEM. The piezoresistive transducers have a narrow internal temperature range (0 ^{o}C to 120 ^{o}C) within which they can function safely. They were cooled by pumping water through internal cooling channels to avoid overheating.

(a) (b)

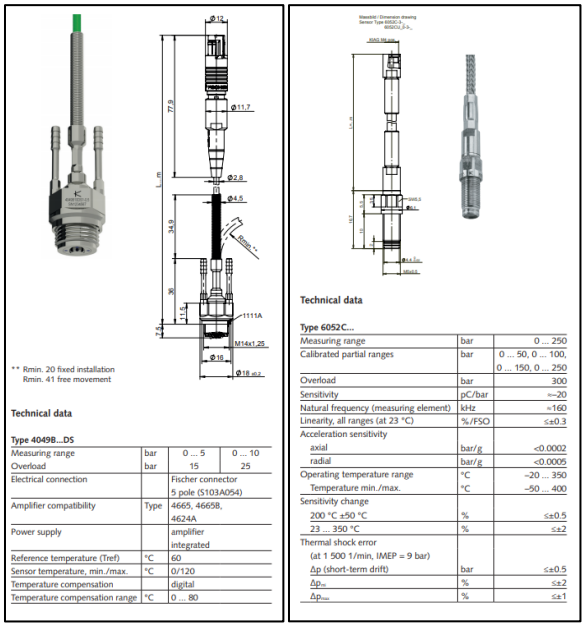

Figure 18: Technical details of the (a) piezoresistive and (b) piezoelectric pressure transducers used. [72]

3.1.2. Temperature Measurement

Intake and exhaust manifold temperatures were measured using k-type thermocouples. Slow speed, commercially available thermocouples with 1/8" probe tips made by *Temprel Temperature Sensors* were used to collect steady state intake and exhaust temperatures. Additionally, a 50 micrometer probe, shown in Figure 19, was used to collect time-resolved exhaust temperature. The sensing element was made by *ANBE, Belgium*. The probe assembly was made in-house. Plaster of Paris, because of its low thermal and electric conductivity, was used as a filler to hold the thermocouple in place. A simple energy balance analysis of the sensing element was performed by assuming steady state heat transfer across it to calculate its response rate. The resulting equation (equation 22) was used with equation 23 [73] to calculate the sensor's time response. Equation 23 is an empirical correlation for convective heat transfer across a sphere for low Reynolds number flows. The subscript 'w' represents the sensor wire properties and 'f' represents the mainstream fluid properties. Using material properties for Inconel-625 at 500 ^{o}C and fluid properties for the exhaust gases at the high speed, high load condition obtained from *GT-Power* simulations, a time constant equal to 10.9 ms was calculated. This corresponds to approximately 34 CAD at 525 RPM. The sensor has an advertised response rate of 2 ms (6.3 CAD at 525 RPM).

$$\tau = \frac{\rho_w c_w D_w}{4h} = \frac{\rho_w c_w D_w^2}{4 k_f Nu} \qquad 22$$

$$Nu = 0.24 + 0.56 Re^{0.45} \qquad 23$$

Figure 19: High speed thermocouple probe.

The fast time response presented some challenges in terms of connecting the sensor to the thermocouple (TC) data acquisition module (*NI-9214*) used for logging slow speed temperature data. The response rate was much faster than the highest time response of the TC module (68 Hz). The module has an inbuilt TC signal conditioning circuit that amplifies the raw voltage signal from the TC and performs cold junction compensation to avoid measurement errors stemming from variations in the cold junction temperature of the thermocouple. In order to log data at high response rates, a signal conditioning circuit was fabricated using the *AD8495* chip manufactured by *Analog Devices*. The circuit amplifies (gain = 100) the millivolt signals from the thermocouple so that they can be registered by the high speed data acquisition module's analog to digital converter. The circuit also provides cold junction compensation. Details of the data acquisition setup are discussed later in this section. All thermocouples were calibrated in an electric thermocouple calibration oven before use. High speed TC calibration results are provided in Appendix D.

3.1.3. Composition Measurement

3.1.3.1. **Slow Speed**

Slow speed exhaust gas composition was measured using a five gas analyzer (*MEXA 7100D*). Exhaust gases were sampled approximately 4” downstream of the exhaust port and were transferred to the analyzer through a heated sample line to avoid condensation. The analyzer measured CO and CO_2 concentrations using a non-dispersive infrared (NDIR) sensor; unburned hydrocarbon concentration using a flame ionization detector (FID) and reported it in ppmC; O_2 concentration using a magnetopneumatic detector (MPD), and NO_x concentration using a chemiluminescence detector (CLD). All sensors were purged before use with air, then zeroed using N_2, and then spanned using sample gases of known concentrations.

3.1.3.2. **High Speed**

In addition to the slow speed exhaust composition measurements, CO and CO_2 concentrations were measured on a crank angle resolved basis using high speed NDIR sensors manufactured by *Cambustion Limited*. Figure 20 shows a schematic of the NDIR sensor, which is capable of producing response times as low as 8 ms (25 CAD at 525 RPM). This is achieved by having a chopper disk rotating at very high speeds (~5000 RPM). The chopper disk has three filters, one for CO and CO_2 each and a reference filter. The filters only allow the respective wavelengths of light (CO or CO_2) emitted from the IR emitter to be sensed by the IR detector. The intensity of the detected light corresponds to the concentration of CO or CO_2 in the sample gas. Figure 21 shows the

setup being used in the lab for measuring cylinder CO and CO_2 concentrations. The sample was obtained through a sampling port in the spark plug, shown in Figure 21(c). Before each run, the analyzer was calibrated using known low and high concentration CO and CO_2 gases.

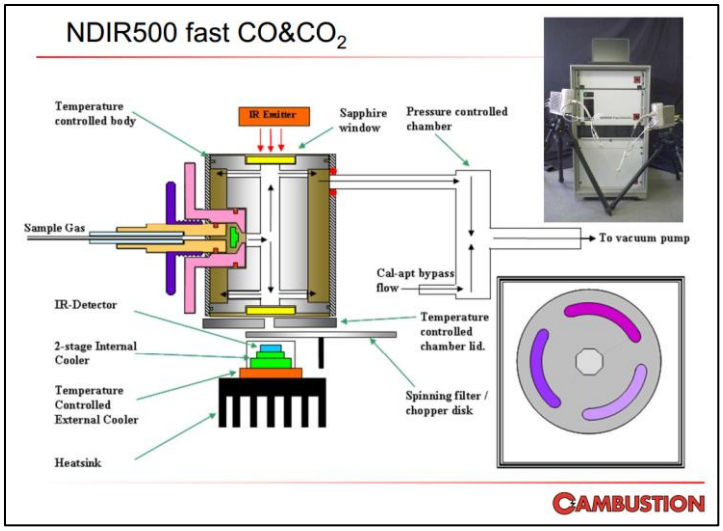

Figure 20: High speed CO/CO_2 analyzer (NDIR-500) schematic. [74]

(a) (b) (c)

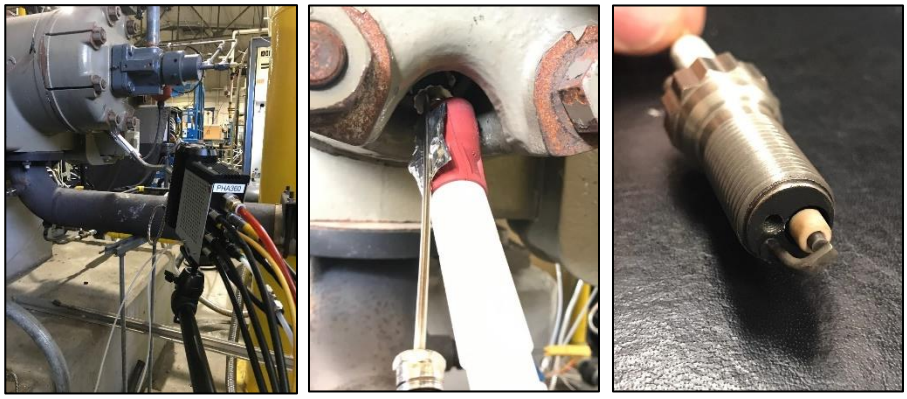

Figure 21: (a) NDIR-500 setup for measuring cylinder CO and CO_2 concentrations, (b) cylinder sampling probe inserted through the spark plug, (c) spark plug sampling port.

3.1.4. Data Acquisition System

Data from all the sensors was recorded by a *National Instruments* data acquisition (DAQ) system. Figure 22 provides a schematic of the DAQ setup with a list of all the sensors connected to their respective DAQ modules. The two high speed modules (*NI-9215*) were used to get high speed data for the 8 listed parameters. Data was collected every quarter crank angle degree, which is the resolution of the quadrature optical encoder (*Dynapar HSD25*) used to measure the angular position of the crankshaft. Angular velocity was calculated by computing the rate (relative to the computer's clock) of angular displacement. In addition to the angular position, the encoder also provided a 'z' or zero signal once every revolution. This signal was later (after adjustment for the thermodynamic loss angle) used to identify the start and end of each cycle. Since both the high speed modules were connected to the same chassis, they were in sync, and synchronized data was acquired for all eight parameters.

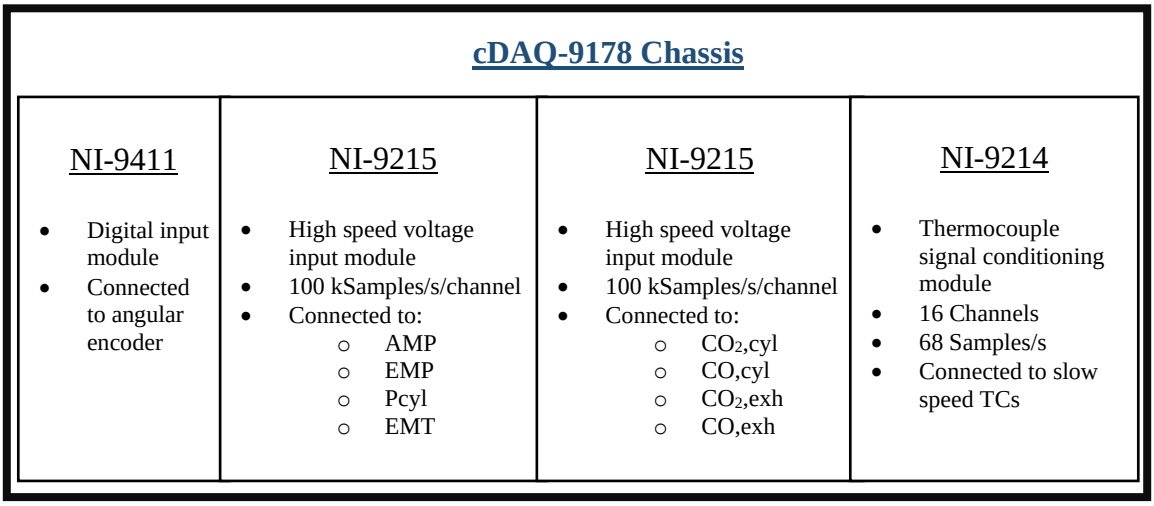

Figure 22: Schematic of the data acquisition system.

A data acquisition program was developed in *MatLab* to acquire data on a cycle-resolved basis using the DAQ setup shown above. Figure 23 shows the basic architecture of the program. It is comprised of two modules: a data recording and a data post-processing module. This approach is adopted to make the data logging process efficient so as to minimize data logging time during experimentation and to preserve the acquired data in its raw form so that no post-logging alterations (e.g. conversion from volts to respective units, pegging cylinder pressure at a certain value and CAD, etc.) are irreversible. The output from the data-logging program is recorded as a function of computer clock time. The analog data is recorded in volts and the encoder data in CAD, RPM, and a binary (0 or 1) z-signal vector.

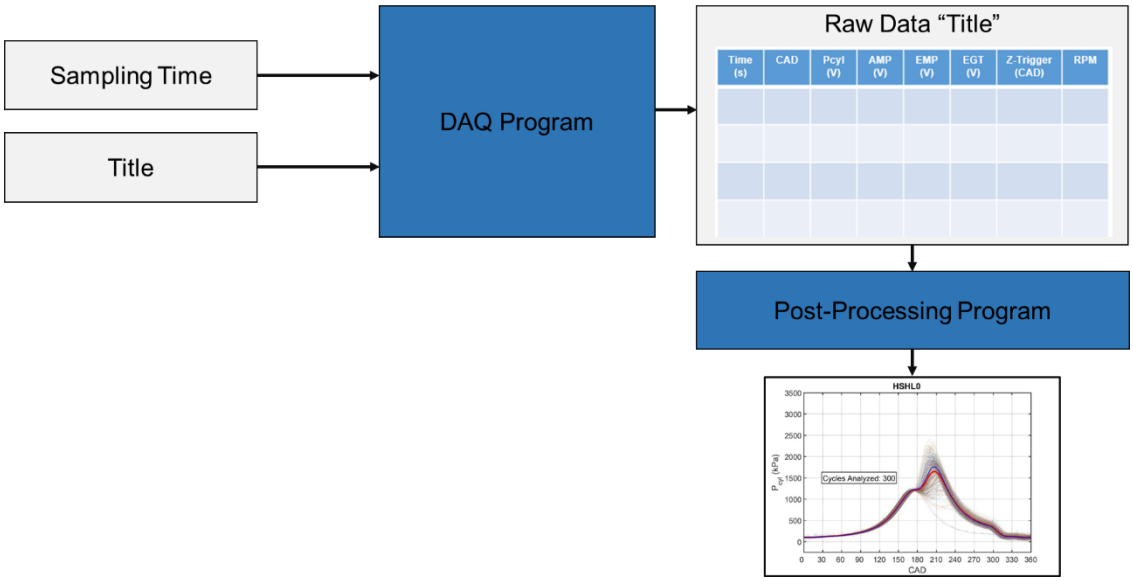

Figure 23: Architecture of the data acquisition and post-processing program.

More details about the experimental setup can be found in [75].

3.2. GT-Power Model

This section describes the *GT-Power* model of the engine. Models in *GT-Power* are constructed by connecting various 'objects' in a suitable arrangement to imitate the actual engine setup. Objects are sub-models that can represent various engine parts, accessories, details of a process, or other parametric specifications of the portion of the model they are linked to. The user provides each object with attributes that represent the system being modeled. The 1D model for the Ajax E-565 is constructed in *GT-Power* by connecting the engine cylinder with the end environments (infinite plenums) through various piping objects as shown in Figure 24.

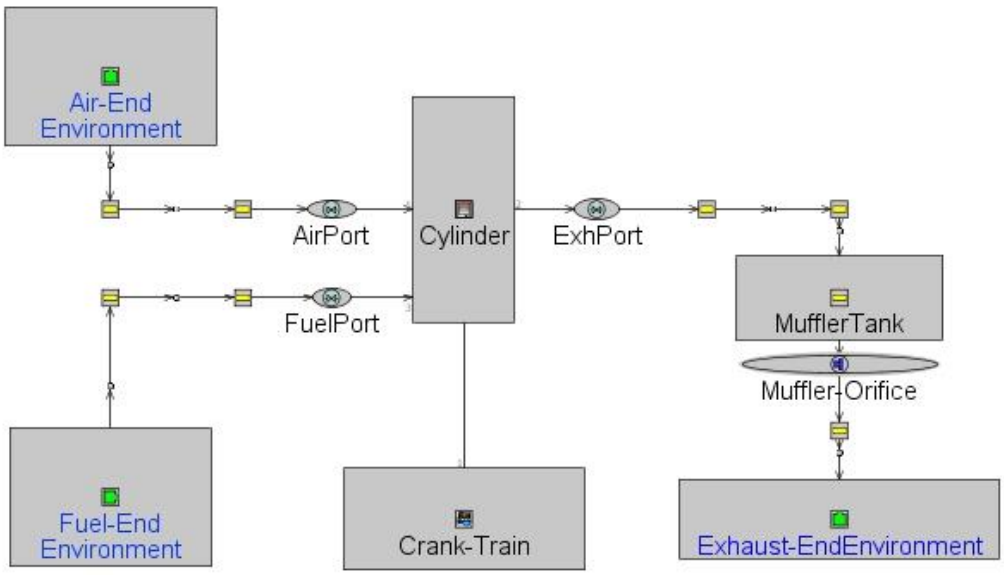

Figure 24: Schematic showing the GT-Power model of the Ajax E-565 engine.

Some salient objects used in the model and their attributes [76] are listed below:

- **Engine cylinder and crank train objects (*EngCyl, EngineCrankTrain*):** Specifies cylinder geometry and models engine kinematics. It needs inputs about engine geometry, speed, wall heat transfer, combustion sub-model, scavenging sub-model, etc.
- **Predictive combustion object (*EngCylCombSITurb*):** Describes the progression of combustion by calculating burn rate using flame propagation parameters (e.g. laminar flame speed, Taylor length scale, turbulence intensity). The model assumes two-zone combustion (burned and unburned zones) and is designed to simulate combustion in homogenous spark ignited engines. It needs inputs about the fuel composition, spark timing, spark size, turbulence parameters, cylinder head and piston crown geometries, fuel composition, wall heat transfer, etc. The model is considered to be predictive because it does not use a user prescribed mass fraction burned function (like the Wiebe function [77] or a sinusoidal function [78]) to determine the burn rate.
- **Engine scavenging object (*EngCylScav or EngCylScavFunction*):** Describes the scavenging behavior of the engine. It needs inputs about scavenging duration and the relationship between residual ratios in the cylinder and exhaust gases. This is discussed further in the next section.
- **End environment object (EndEnvironment):** Provides thermal and pressure boundary conditions to model different fluid reservoirs at a prescribed temperature, pressure, and composition.

The modeling domain includes the entire engine setup downstream of the scavenging chamber. This selection is made to avoid modeling the complicated and highly transient fluttering behavior of the reed valve strips that control the flow of air into the chamber [79]. Experimentally obtained crank angle resolved scavenging chamber pressure is used instead as the upstream boundary condition. The exhaust system is modeled in its entirety, starting from the exhaust header and terminating at the final 'tailpipe' downstream of the muffler. The muffler is modeled by combining a volume and an orifice object. The volume object serves as an expansion chamber (similar to a box silencer) and the orifice object controls the pressure drop realized across the volume object (muffler-tank).

3.2.1. Scavenging Calculations in GT-Power

Residual gas fraction is calculated in *GT-Power* by using a user-defined scavenging function that relates burned gas ratio (residual ratio) in the cylinder and the exhaust. This functional relationship between exhaust and cylinder residual gases can be prescribed in one of two ways: (1) by using the *EngCylScav* object in which tabulated residual gas data is inputted between (0,0)[10] and (1,1), or (2) by using the *EngCylScavFunction* object in which three scavenging parameters; namely, anchor point, transition point, and shape factor are inputted and the object generates a continuous curve between (0,0) and (1,1). Both of these approaches are used herein. The

[10] The coordinates represent (in order) the residual gas fraction in the cylinder and the exhaust.

first approach is used in Chapter 4 and the second one in Chapter 6. Implementation details of the two approaches are discussed as needed in their respective chapters.

During a simulation, burned gases are tracked throughout the cycle. All those molecules are considered burned that have either entered the burned zone during combustion or are present in the cylinder at EPO. The movement of molecules across the burned and unburned zones is governed by the predictive combustion sub-model that calculates the flame entrainment rate. The ratio of the burned molecules to the total retained mass in the cylinder gives the retained residual gas fraction, or the trapped residual gas fraction if the calculations are performed after EPC. Residual fraction in the exhaust is calculated in a similar fashion.

GT-Power uses a modeling approach known as ‘flow-splitting’ to model pressure wave behavior when gases expand or contract across large volume changes. This is relevant for modeling wave dynamics in the exhaust system, which directly impacts scavenging calculations. The one-dimensional simulation tool models these highly three-dimensional expansion phenomena by ‘splitting’ (discretizing) three-dimensional volumes into various flow parts (pipes, shells, elbows, etc.), combining them together in appropriate sequences, and using its 1D solvers to solve the Navier-Stokes equations for flow through the joined parts. Details of the solution method are proprietary but based on publicly available literature, the approach seems similar to Blair’s approach, which treats the exhaust system as “a series of pipes, branches and butted joints” [46].

3.2.2. Model Validation

For the initial set of scavenging simulations, the model was validated only for the standard operating point (525 RPM, standard spark timing and full load - IMEP of 536 kPa) with pre-mixed fuel being delivered along with the incoming air. For later experiments (discussed in Chapters 5 and 6), a direct injection system was used. Validation results for the standard operating point are presented here as a comparison between simulated and experimental cylinder (Figure 25a) and exhaust (Figure 25b) pressure. The mass flows across the cylinder and the retained cylinder mass have been compared to a validated 3D CFD model [80, 81] of the same engine to gauge the accuracy of the 1D model in simulating gas exchange across the engine. These results are shown in Figure 26. The composition of these mass flows (fresh charge vs. residual gas) is not directly validated through experimentation at this point. That is the subject of Chapter 6 where a modified version of the model is used with experimental scavenging results. The partially-validated version of the model discussed here was needed for preliminary analysis of simple scavenging models (discussed in Chapter 4) and to help design scavenging experiments.

(a) (b)

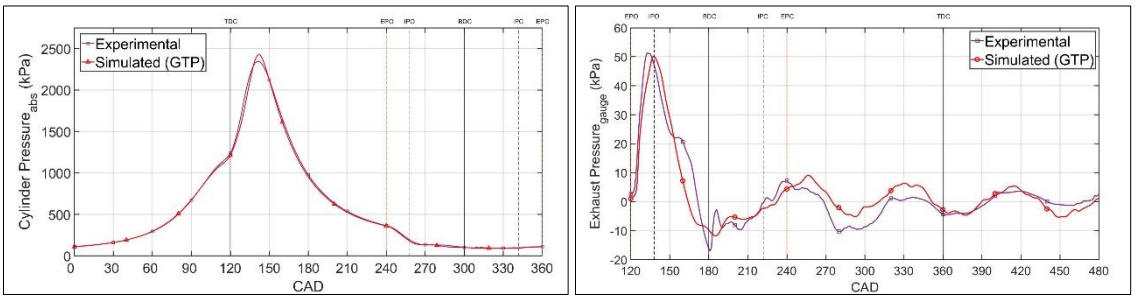

Figure 25: Experimental and GT-Power simulated (a) cylinder and (b) exhaust pressure.

(a)

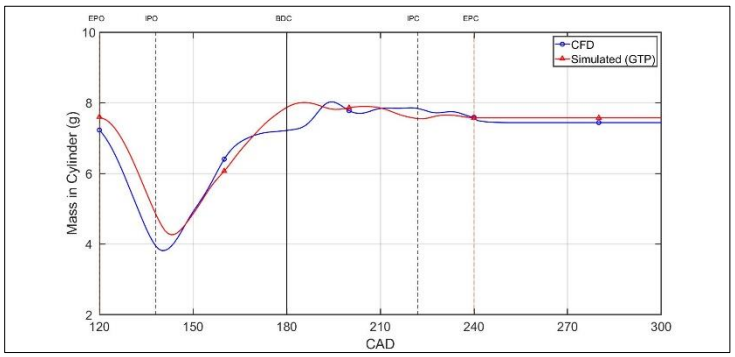

(b) (c)

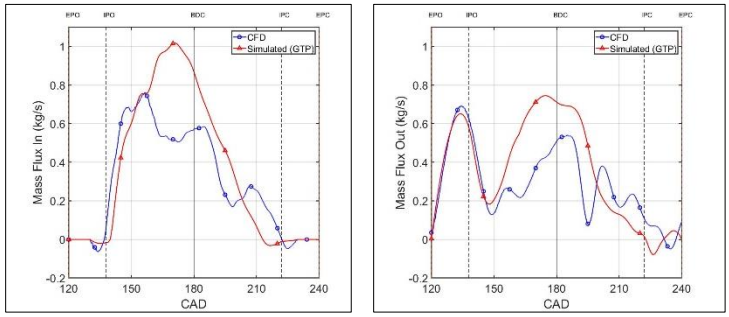

Figure 26: CFD and GT-Power simulated (a) retained mass, (b) mass inflow, and (c) outflow.

4. A NEW SCAVENGING MODEL

An initial set of simulations is run using the *GT-Power* model discussed above to: (1) analyze and compare different currently available simple scavenging models, and (2) propose a new scavenging model that meets the objectives of this research. The proposed model, along with *GT-power's* scavenging model, will be validated by comparing their scavenging estimates to experimental scavenging data in the following two chapters. This chapter presents *GT-Power* simulation results for the initial simulation exercise. An *EngCylScav* object is used with a scavenging curve that falls midway between PM and PD for this analysis.

4.1. Simple Scavenging Model Results

The accuracy of the four single-zone simple scavenging models described in section 2.1.1. is gauged by comparing their TRF estimates to the TRF values predicted by the gas dynamics-based *GT-Power* model for the simulation matrix shown in Table 3. Up to this point, *GT-Power's* scavenging sub-model, which predicts the composition of the cylinder gas (fresh charge vs. residual gas), has not been directly validated through experimentation. This is done in Chapter 6. For the purposes of the exploratory analyses discussed here, the indirectly validated (Section 3.2.2.) sub-model is assumed to be accurate; at least in terms of scavenging trends across various operating points.

Speed (RPM)	350			450			525		
Load	50%	75%	100%	50%	75%	100%	50%	75%	100%
Spark Timing	5R	5R	5R	5R	5R	5R	5R	5R	5R
	0	0	0	0	0	0	0	0	0
	5A	5A	5A	5A	5A	5A	5A	5A	5A
Total	9			9			9		

Table 3: Simulation test matrix.

The results are presented in the format shown in Figure 27. The background is color coded for the three engine speeds and for each speed, results are presented for different loads and spark timings. The first nine cycles (yellow background) are the 350 RPM cases, followed by the nine 450 RPM (pink background), and 525 RPM (green background) cases. For each speed, the first three cases are at the standard spark timing, followed by three at retarded, and at advanced spark timing cases. At each spark timing point, low load is simulated first, followed by the medium, and high load.

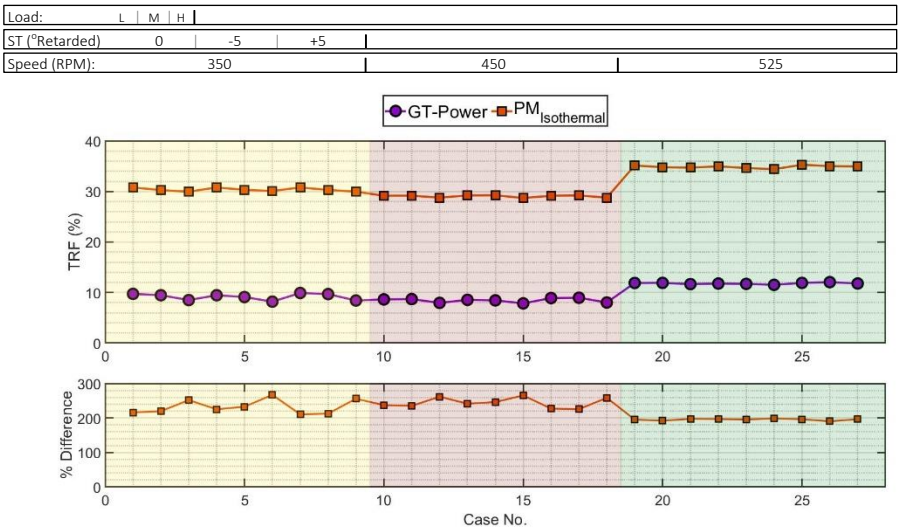

Figure 27: Isothermal perfect mixing model performance.

TRF results for the four simple-scavenging models and the associated absolute percentage difference (compared to *GT-Power*) are shown in Figure 27 to Figure 30. All models produce significantly different results compared to *GT-Power* results.

Figure 27 shows the performance of Hopkinson's model. TRF estimates are consistently higher (by approximately 200%), but the trends are consistent with the *GT-Power* results. The differences are attributed to:

1. The inherently poor residual-gas-purging nature of the perfect mixing process. The fresh and residual gases mix instantaneously at the onset of scavenging to form a homogeneous mixture; thus, disregarding the high-SE sub-processes where residual gases escape the cylinder with no, or very little, mixing with the fresh gases.
2. The assumption that the incoming and residual gases are at the same temperature. This results in an over-estimation of the residual mass, because in actual engine operation the residual gases are at a significantly higher temperature (and lower density) than the fresh gases, which are approximately at ambient temperature.

Figure 28 shows the results for Sher's non-isothermal PM model. TRF is still being overestimated compared to the *GT-Power* model, but the differences reduce from around 200% to less than 50%, and close agreement is achieved at high speeds. This improvement results from the use of a better residual temperature approximation, i.e. cylinder bulk gas temperature at IPO, instead of intake air temperature. The major source

of difference in these results is the lack of a high scavenging efficiency stage (e.g. a PD stage). A secondary source of the difference could be the choice of the residual gas temperature.

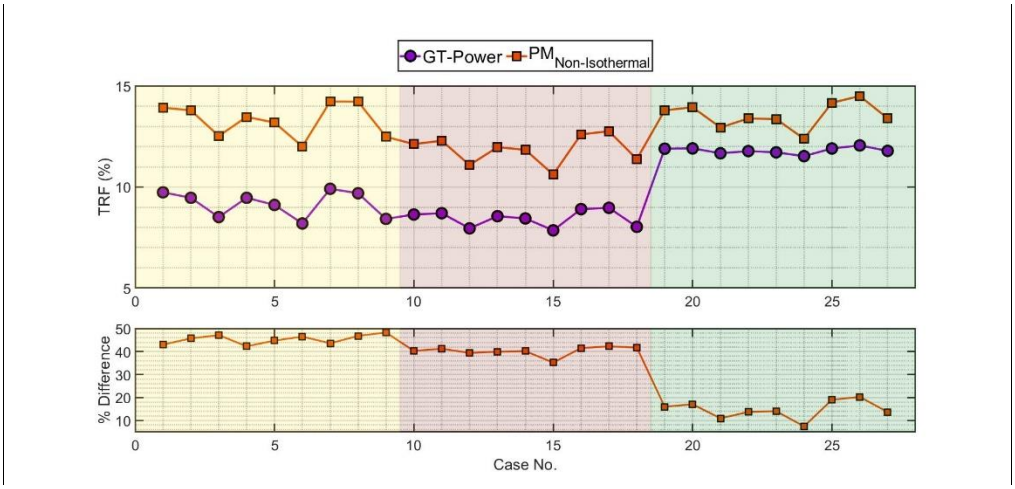

Figure 28: Performance of the non-isothermal perfect mixing model.

Figure 29 shows the results of Benson and Brandham's perfect-displacement-perfect-mixing model using two displacement ratios (x = 0.85 and 0.9). The results improve significantly compared to the isothermal perfect mixing model with maximum difference values of 30%. This approach holds promise because by selecting appropriate PD fraction values for various operating cases, acceptable levels of accuracy in SE results can be obtained for all operating points. The model does show a lack of resolution in capturing the variations in TRF at a given speed as spark timings and loads change. This lack of resolution is attributed to the inability of the isothermal scavenging models to account for variations in residual gas temperature, which is a strong function of engine load and spark-timing.

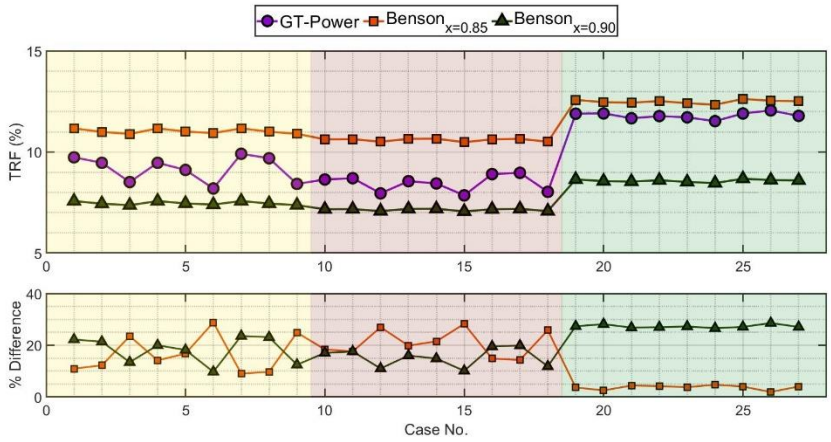

Figure 29: Performance of Benson and Brandham's single-zone two-stage model.

Figure 30 shows the results of Wallace and Dang's model for two different short-circuiting fractions (y = 0.1, y = 0.2) at a constant displacement fraction value (x = 0.85). Adding a short-circuiting stage increases the amount of trapped residuals and thus, lowers the scavenging efficiency of the engine. Since the PM-based single-zone models are over-predicting the TRF for this particular engine, introducing short-circuiting would further deteriorate the results. Similar to Benson and Brandham's model, the inadequacies of this model lie in its inability to capture the effects of variations in residual gas temperature.

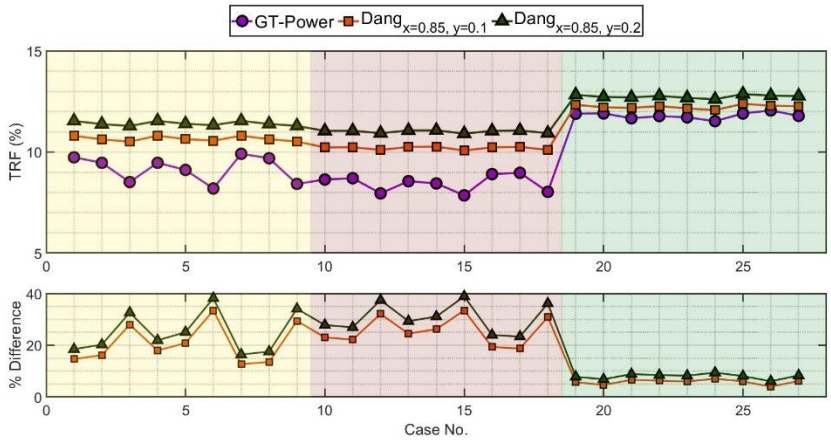

Figure 30: Performance of Wallace and Dang's single-zone two-stage model.

4.2. A New Simple Scavenging Model

From the comparative exercise discussed in section 4.1, the following conclusions can be drawn about the attributes that an accurate multi-stage simple scavenging model should possess:

1. A single-stage model by itself cannot accurately estimate SE for all operating cases.
2. At least two stages, one with high SE characteristics (PD) and one with low SE characteristics (PM or short-circuiting) are needed to accurately estimate SE.
3. A tunable weighting factor for each of these stages is needed to account for variations in engine behavior at different operating conditions. In a robust scavenging model, the relative contribution of different stages should not vary significantly in the absence of irregular changes in engine breathing behavior.
4. The isothermal assumption between the incoming and exiting gases desensitizes the scavenging models to variations in SE that stem from changes in engine

operating parameters which substantially change the cylinder gas temperature. A well-resolved scavenging model should not assume thermal homogeneity between incoming (air) and exiting (residual) streams.

Previous scavenging studies can provide some guidance regarding the selection and sequencing of the high and low SE phases needed for an accurate scavenging model. CFD results of gas exchange processes in cross-scavenged two-stroke engines [82] show that during scavenging on the intake side hemi-cylinder, phenomena similar to perfect mixing takes place initially when high velocity and turbulent fresh gases enter the cylinder and blend with the cylinder gases. This is followed by a perfect displacement type stage as the fresh gases slow down and become less turbulent. Blair [83] and Jante [25] also talk about there being an initial PM-type stage during scavenging and a delayed PD-type stage, during which incoming gases that have slowed down displace cylinder gases instead of mixing in them. Visual observations from Boyer [53] also confirm the existence of turbulent jets of incoming fluid and laminar streamlines of exiting gases. LDV-based observations of incoming flows for a crank-case scavenged engine by Miles et al. [57] also report a strong initial rush of turbulent gases through the transfer ports because of the high crank-case pressure.

In light of these findings, a three-stage model is proposed that attempts to overcome shortcomings of the previous models. This model, referred herein as the *hybrid model*, assumes that the gas exchange process in two-stroke engines takes place in three stages. These three stages (shown in Figure 31) are discussed below.

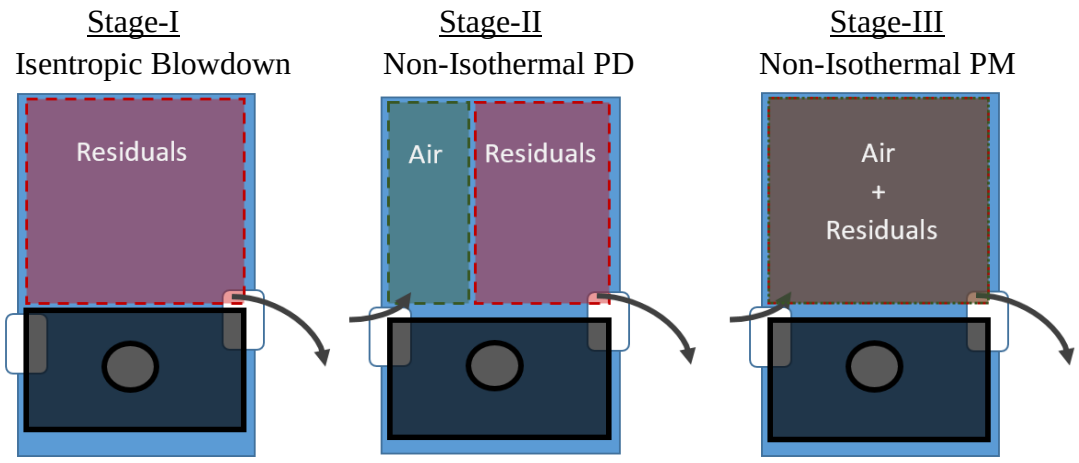

Figure 31: Three stages of the hybrid scavenging model.

Stage-I: Isentropic Blowdown (A – B)

This stage replicates the blowdown process; during which, only the exhaust ports are open, no air enters the cylinder, and the entire cylinder volume is occupied by combustion products. The pressure of the cylinder gases isentropically decreases from the cylinder pressure at exhaust to a lower pressure value. This pressure is assumed to be equal to the mean manifold pressure 'p_c', which is the average of the mean exhaust and intake manifold pressures. Subsequent scavenging processes take place at this pressure. The end-of-stage residual gas mass is lower than the initially trapped mass and so is the density of the cylinder gases. The temperature of the residual gases decreases, and the final temperature 'T_{isent}' is calculated using isentropic ratios for ideal gases as follows:

$$T_r(B) = T_{isent} = T_r(A)\left(\frac{P(B)}{P(A)}\right)^{\frac{\gamma-1}{\gamma}} = T_{EPO}\left(\frac{p_c}{P_{EPO}}\right)^{\frac{\gamma-1}{\gamma}} \qquad 24$$

The specific heat ratio 'γ' is assumed to be constant for all the gases. The decrease in cylinder pressure, temperature, and retained mass during stage-I is shown in Figure 32, Figure 33, and Figure 34, respectively by the process A-B. The process lines are vertical because the blowdown is assumed to be instantaneous. The following are assumed during this stage:

- Process takes place in a constant volume cylinder with volume equal to trapping volume (V_{trap}).
- Cylinder walls are adiabatic.
- Cylinder volume is occupied only by combustion products.
- Cylinder gases behave ideally and have a constant specific heat ratio.
- Gases undergo instantaneous isentropic expansion from P(EPO) to p_c.

The mass of residual gases at the start of this stage is equal to:

$$m_r(A) = \frac{P_{EPO} V_{trap}}{R T_{EPO}} \qquad 25$$

The mass of residual gases at the end of this stage is equal to:

$$m_r(B) = \frac{p_c V_{trap}}{R T_{isent}} \qquad 26$$

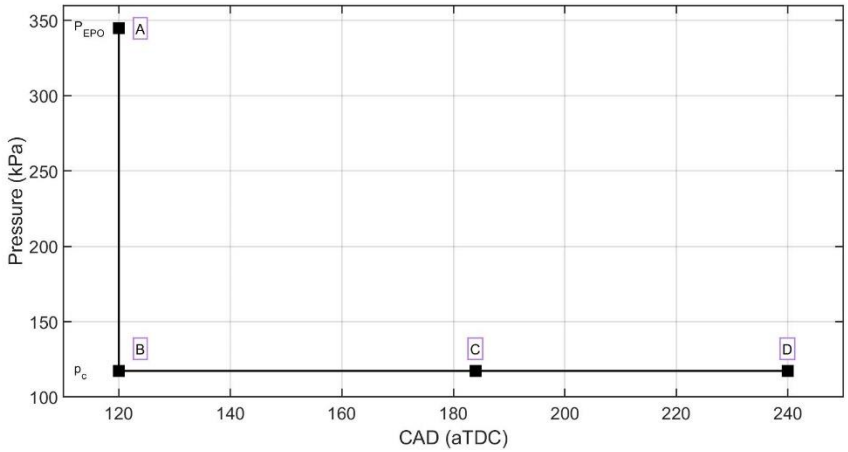

Figure 32: Pressure changes during the three stages of the scavenging process simulated by the hybrid model.

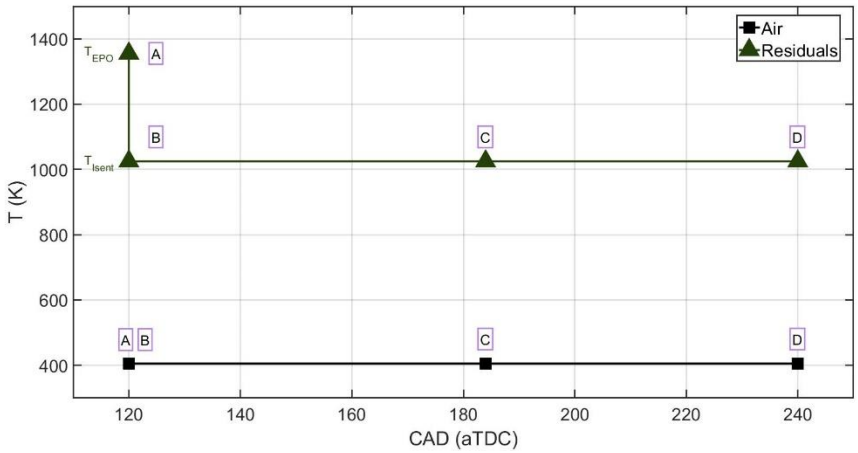

Figure 33: Temperature changes during the three stages of the scavenging process simulated by the hybrid model.

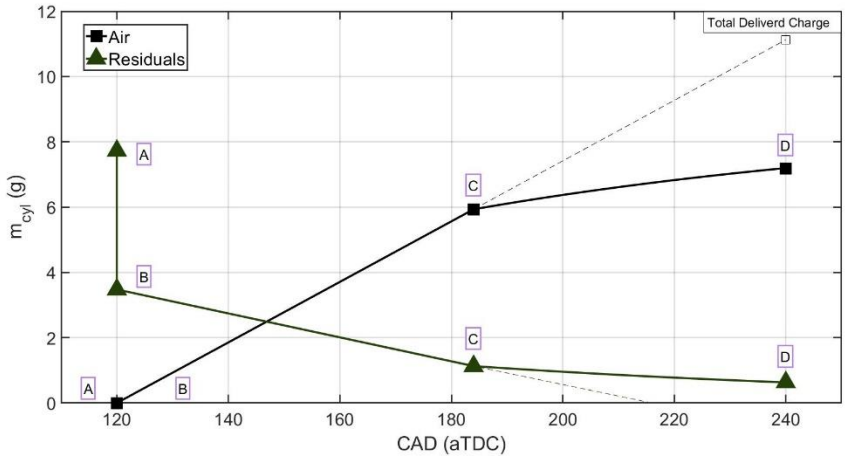

Figure 34: Retained mass changes during the three stages of the scavenging process simulated by the hybrid model.

Stage-II: Non-Isothermal Perfect Displacement (B – C)

Stages II and III model the scavenging process. During stage II, fresh air at intake conditions (AMT) enters the constant volume cylinder and perfectly displaces residual gases, which are at a higher temperature (T_{isent}). Because of the perfect displacement assumption, the two gases do not mix at all. The cylinder pressure stays constant during this stage, as can be seen in Figure 32. The average cylinder bulk gas temperature, however, decreases because as the relatively hot residual gases leave the cylinder and the relatively cold fresh charge enters the cylinder, the mass fraction of hot residual gases retained in the cylinder decreases and that of the cooler air increases. The change in retained residual and fresh charge mass can be seen in Figure 34. The increase in the amount of air mass in the cylinder is simply the total mass delivered ($\dot{m}_{in}t$). The decrease in residual mass is linear because of the perfect displacement assumption. The following are assumed during this stage:

- Process takes place in a constant volume cylinder (V_{trap}).
- Cylinder walls are adiabatic.
- Cylinder volume is occupied by combustion products and incoming air.
- Air is entering the cylinder at a constant mass flow rate ($\dot{m}_{in}$) and temperature (AMT).
- Residual gases are at a constant temperature (T_{isent}).
- Cylinder gases behave ideally.
- All cylinder gases have the same molecular weight and specific heat.
- No heat or mass transfer takes place between the fresh and residual gases.

This stage follows the non-isothermal PD model of Heywood and Sher [1]. The mass of residual gases at the end of this stage is equal to:

$$m_r(C) = m_r(B) - \frac{T_a}{T_{isent}} \dot{m}_{in} t_{B \to C} \qquad 27$$

Stage-III: Non-Isothermal Perfect Mixing (C – D)

At the conclusion of the non-isothermal PD stage, the non-isothermal PM stage commences and lasts until the end of scavenging (EPC). The choice of the angular position at which the PM stage starts is somewhat arbitrary. This position is represented by 'θ_{PM}'. The freedom to control the duration of the PD stage gives the model an additional degree of freedom which is similar to the choice of PD and short-circuiting fractions in Benson's and Wallace's isothermal models, respectively. θ_{PM} acts as a

tuning knob and can be used to get the final thermodynamic state at point D to match the *GT-Power* results at EPC. The test for the robustness of this model will be to produce accurate estimates for state D with minimal changes in θ_{PM}. It will be shown in the results section that the model performs well on this count.

During stage-III, it is assumed that all gases in the cylinder (air and residuals) mix perfectly to form a homogenous mixture that exits the cylinder at a constant pressure and flowrate. This stage is based on Sher's non-isothermal perfect mixing model, and assumes the following:

- Process takes place in a constant volume cylinder (V_{trap}).
- Cylinder walls are adiabatic.
- Cylinder volume is occupied by a homogenous mixture of combustion products and air.
- Air is entering the cylinder at a constant mass flow rate ($\dot{m}_{in}$) and temperature (AMT).
- Cylinder gases behave ideally.
- All cylinder gases have the same molecular weights and specific heats.

Cylinder gases mix ideally to form a mixture that is at the temperature:

$$T_{mixture} = \frac{m_r}{m_r+m_a} T_{isent} + \frac{m_a}{m_r+m_a} T_a \qquad 28$$

During this stage, the reduction in the mass of residual gases is non-linear because the decrease is being governed by the non-isothermal PM model; according to which, the residual mass decreases exponentially. If the scavenging process is made infinitely long, the retained residual mass would eventually decrease to zero. The mass of residual gases at the end of this stage - the trapped residual mass - is equal to:

$$m_r(D) = m_r(C)\exp\left(-\left[\frac{\dot{m}_{in}RT_a}{p_c V_{trap}}\right]t_{C\to D}\right) \qquad 29$$

Figure 35 illustrates the combined effects of all the gas-gas interactions during the three stages, and compares the process to the corresponding *GT-Power* process for the same operating point. Figure 35(a) compares the mixture temperature and Figure 35(b) compares the residual gas fraction. It can be seen in Figure 35(b) that the cylinder is initially completely filled with residual gases. During the blowdown process (A-B), even though the mass of residual gases decreases, the mass fraction of the combustion products in the cylinder remains unity as there is no other gas; namely, air in the cylinder. When air enters the cylinder during stages II and III, the residual gas fraction decreases. This decrease is linear and rapid during the PD stage, and exponential and slow during the PM stage.

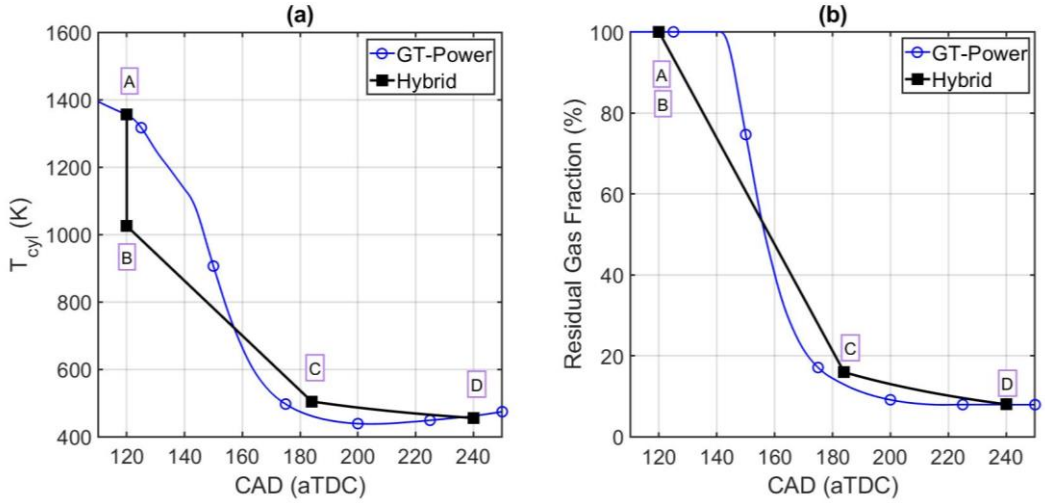

Figure 35: Cylinder mixture (a) temperature and (b) residual gas fraction results from the hybrid and GT-Power models.

4.3. Testing the New Simple Scavenging Model

The proposed hybrid model is run with boundary conditions extracted from *GT-Power* results, as was done for other scavenging models in section 4.1. The resulting trapped mixture composition and state estimates are compared against *GT-Power* results to gauge the accuracy of the new model; assuming, for the time being, that the *GT-Power* scavenging results are accurate. Some of the results of this exercise are presented here. A more comprehensive discussion can be found in [84, 85].

Baseline Case: For the baseline case, the hybrid model is tuned for the arbitrarily selected medium speed high-load standard-spark-timing case (case-12), and is run for all 27 cases without changing the model setup. A summary of the boundary and initial conditions used is as follows:

- $P(A) = P(EPO)$
- $T_r(A) = T(EPO)$
- $P(B) = P(C) = P(D) = P(EPC) \sim pc$
- $T_a(B) = T_a(C) = T_a(D) = AMT$
- $T_r(B) = T_r(C) = T_r(D) = T_{isent}$
- $\theta_{PM} = 64^o$ after exhaust port opening (aEPO)

With these inputs, satisfactory results are obtained for the low and medium speed cases. The high speed results do not correlate as well. The unsatisfactory high speed results are discussed in the next section. Figure 36 to Figure 39 present the trapped mixture composition results using this baseline model and the *GT-Power* model. It can be seen that the differences in predicting the trapped residual mass (Figure 36), the trapped air mass (Figure 37), and the trapped residual fraction (Figure 38) are consistently below 5% for all cases discussed in this section. The results shown in these three figures are presented in Figure 39 in a consolidated fashion to summarize the differences between the hybrid model and the *GT-Power* model results.

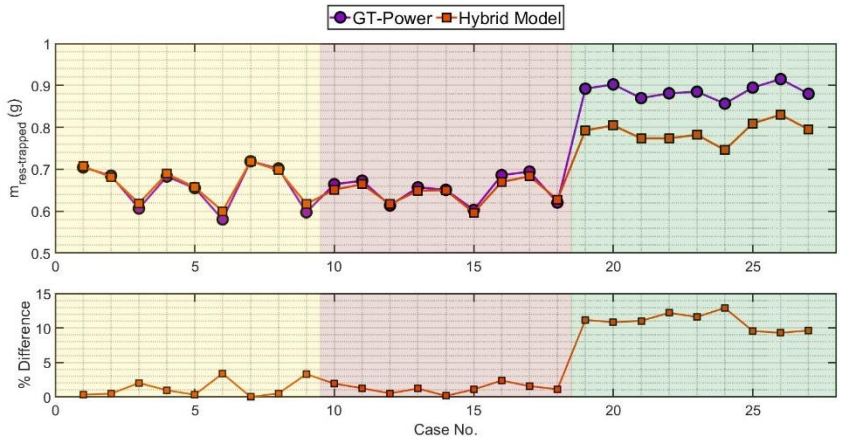

Figure 36: Hybrid model estimated trapped residual mass compared to GT-Power results for the baseline case.

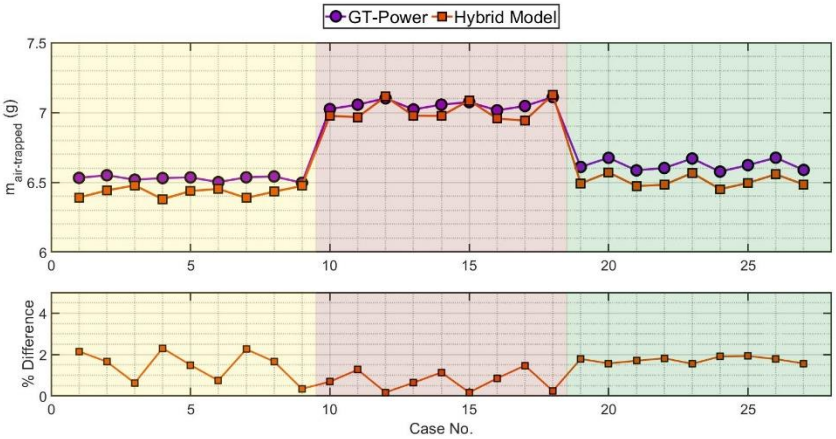

Figure 37: Hybrid model estimated trapped air mass compared to GT-Power results for the baseline case.

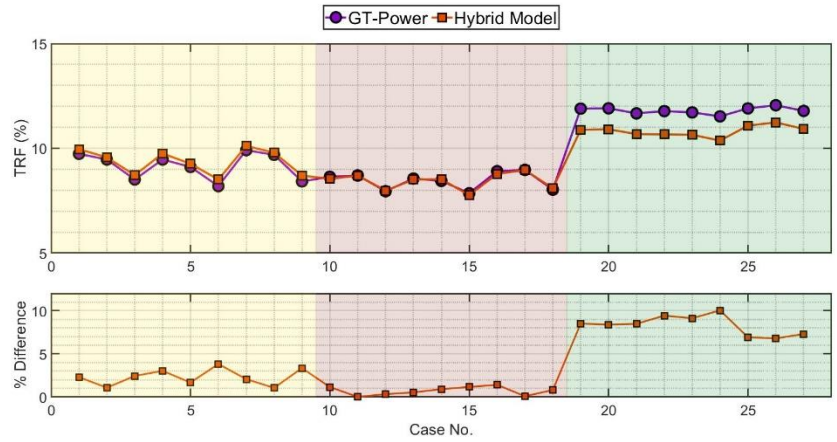

Figure 38: Hybrid model estimated trapped residual fraction compared to GT-Power results for the baseline case.

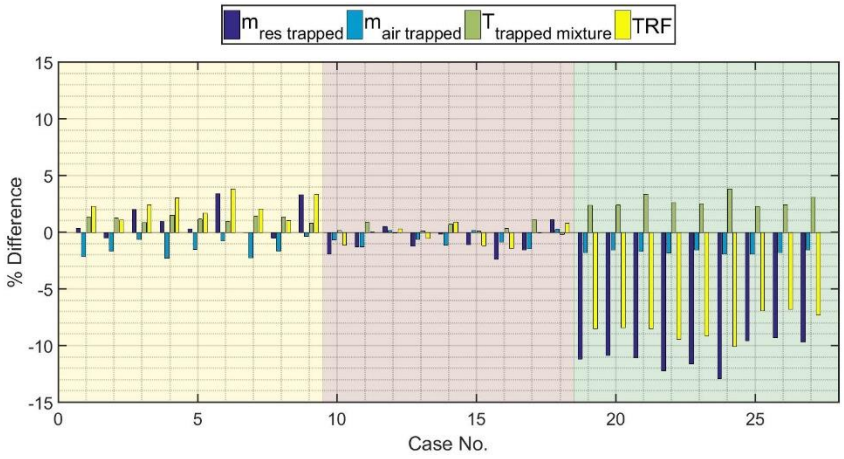

Figure 39: Comparison of hybrid model and GT-Power results for the baseline case.

High Speed Correction: The high engine speed results (cases 19 to 27) show very large differences in trapped residual mass. *GT-Power* simulated trapped residual mass is significantly higher than the low speed cases; probably because of there being less time available for scavenging. It can be seen in Figure 36 that the hybrid model

under-predicts the mass of trapped residuals. The mass of trapped air, however, is being estimated with reasonable accuracy (Figure 37). The under-estimation of the trapped residual mass at high speeds results in an under-estimation of TRF (Figure 38). The overestimation of the trapped mixture temperature in Figure 39 is the result of under-estimations in the cooler trapped air mass estimates overpowering the under-estimations in the hotter residual mass estimates.

To correct the trapped residual mass results, the duration of the high-SE PD stage is reduced by 6 degrees, i.e. θ_{PM} is advanced from 64^o aEPO to 58^o aEPO. This should increase the final trapped residual mass since less residual gases will be removed during stages II and III. To implement this change, the hybrid model is re-run with the following boundary and initial conditions. The only parameter value that is different from the baseline case is that of θ_{PM}.

- P(A) = P(EPO)
- T_r(A) = T(EPO)
- P(B) = P(C) = P(D) = P(EPC)~ pc
- T_a(B) = T_a(C) = T_a(D) =AMT
- T_r(B) = T_r(C) = T_r(D) =T_{isent}
- θ_{PM} = 58^o aEPO

These changes increase the trapped residual mass for all the cases – increasing the differences for the low and medium speed cases and decreasing them for the high speed

cases. The results are shown in Figure 40. The increased differences for the low and medium speed cases are expected. The desired high speed improvement in the results is of significance.

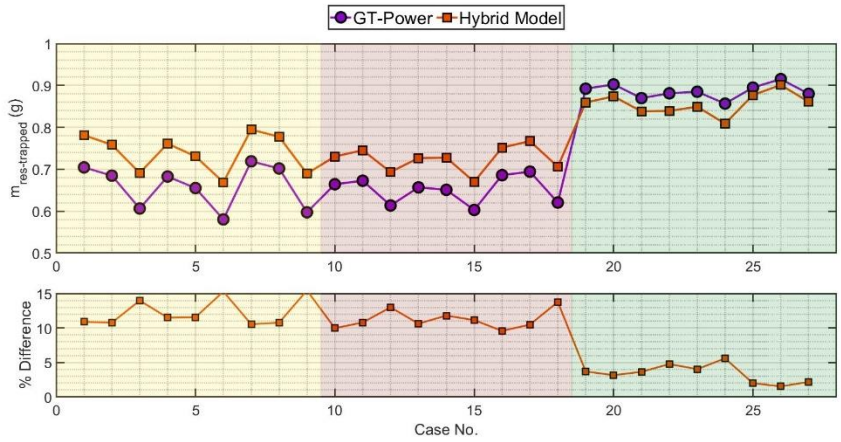

Figure 40: Hybrid model estimated trapped air mass compared to GT-Power results after high speed correction.

Figure 41 provides a summary of the differences in the trapped mixture property estimates from this run of the hybrid model. The results show that the TRF estimates are acceptable for the high speed cases after the θ_{PM} correction. The over-estimated mixture temperatures result from the under-estimated trapped air mass. Figure 41 should be seen together with Figure 39 to analyze the performance of the hybrid model for the entire simulation matrix. This is shown in Figure 42 in which the tuned portions of the two figures have been stitched together.

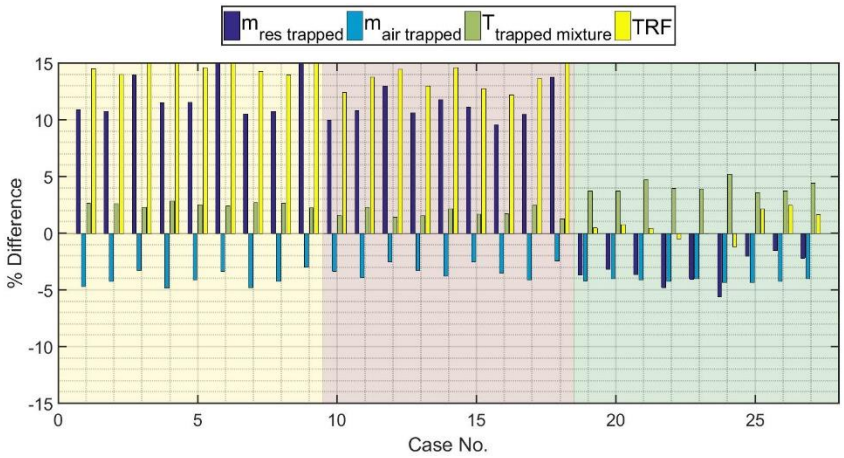

Figure 41: Comparison of hybrid model and GT-Power results after high speed correction.

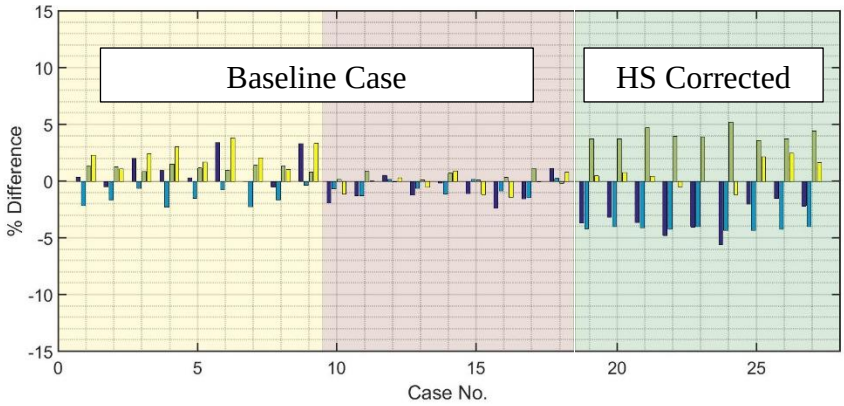

Figure 42: Comparison of hybrid model and GT-Power results using the baseline configuration for cycles 1 to 18, and the high speed corrected configuration for cycles 19 to 27.

It can be concluded that in the absence of any extraordinary changes in engine gas flow behavior, as was the case at high speeds, the hybrid model needs to be tuned only for one operating condition and it will produce acceptable results for all similar operating points. The results also show that the TRF estimates are noticeably sensitive to changes in θ_{PM}, suggesting that it can be used as an effective tuning knob. The

effectiveness of this knob will prove to be inadequate in the next chapter when experimental trapping and scavenging efficiency results are used to test the hybrid model. A second tuning knob (the short-circuiting fraction) will thus be introduced to extend the model's range.

5. EXPERIMENTAL RESULTS AND SCAVENGING MODEL IMPROVEMENT

This section presents experimental scavenging results along with discussions of the methods used to calculate them from measured data. The simple scavenging model proposed above (the hybrid model) is then used to simulate the experimental results, but the model, in its originally proposed form, fails to produce satisfactory results at some operating points. It is, therefore, modified to improve its performance. The modifications and the final results are also presented in this chapter. Slow speed experimental results (fuel flow rate, intake/exhaust temperature, etc.) are not reported here. They are provided in Appendix C, and some sample unprocessed high speed results (crank angle resolved intake/exhaust pressure, exhaust temperature, etc.) are provided in Appendix D.

5.1. High Speed CO_2 Results

Sample high speed CO_2 concentration results are shown for a low and high load case in Figure 43 and Figure 44, respectively. The CO_2 results show good sensitivity and acceptable resolution. A lag between the pressure and the CO_2 concentration data can be seen in the two figures. This is because of transportation delays (or 'sample transit time' [13]) in filling the NDIR analyzer's sampling chamber with gas. The unstable nature of low-load operation is visible in the form of large cyclic variations in the measured parameters in Figure 43. The time constant of the analyzer was calculated to be 0.43 ms and the rise time (10% to 90% of final value) was calculated to be 0.65 ms using cylinder CO_2 curve for a cycle at 525 RPM. This is shown in Figure 45. The time

constant of 0.43 ms corresponds to 1.16 CAD at 450 RPM and 1.35 CAD at 525 RPM, which is an acceptable level of resolution.

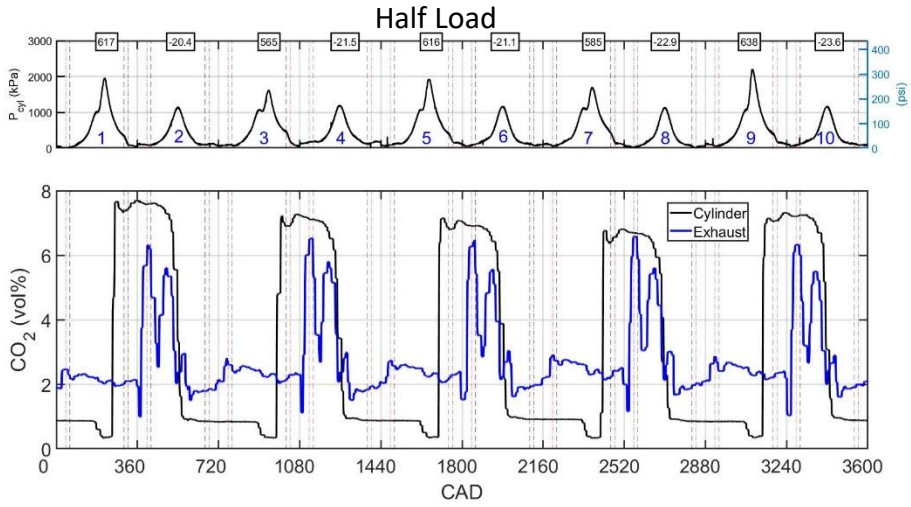

Figure 43: High speed cylinder and exhaust CO_2 concentration for ten cycles at 525 RPM, standard ST, and 50% load. Corresponding cylinder pressures are also shown with their respective IMEPs (in kPa) above them. Vertical dashed lines show exhaust (grey) and intake (red) port event timings.

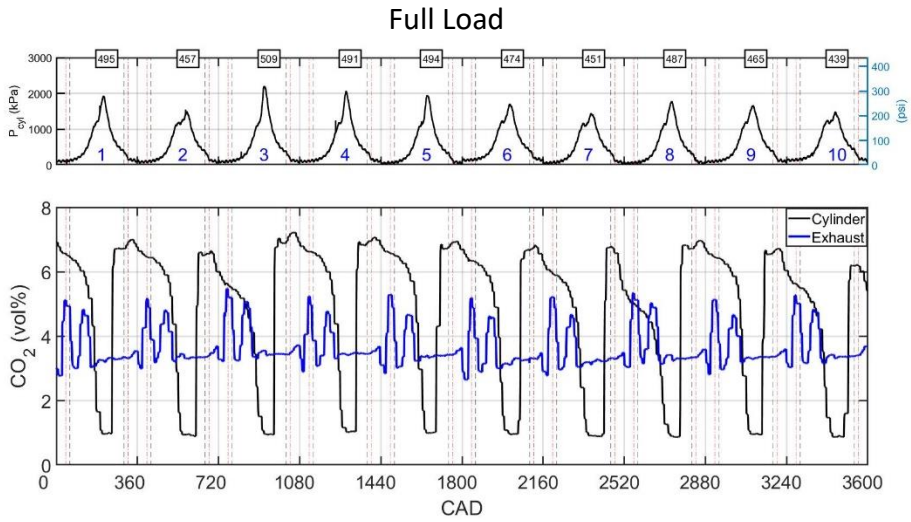

Figure 44: High speed cylinder and exhaust CO_2 concentration for ten cycles at 525 RPM, standard ST, and 100% load. Corresponding cylinder pressures are also shown with their respective IMEPs (in kPa) above them. Vertical dashed lines show exhaust (grey) and intake (red) port event timings.

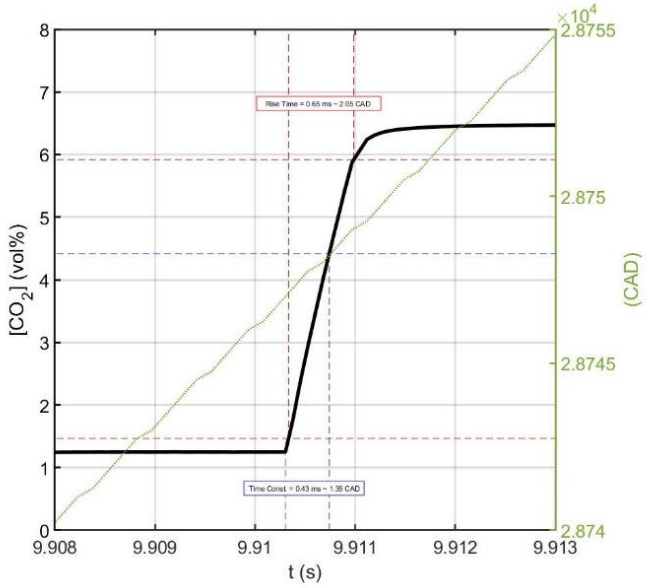

Figure 45: High speed CO_2 analyzer's response time (63% of final value) and rise time (10% to 90% of final value) during combustion calculated from measured cylinder CO_2 concentration curve for a cycle at 525 RPM, 100% load, and standard ST.

Figure 46 shows the ensemble averaged cylinder and exhaust CO_2 concentration for an engine cycle at full load and high speed (525 RPM). The translucent curves illustrate the spread in concentration data at the relatively stable operating point. Additionally, the effects of transportation delay in the form of a crank angle offset can be seen clearly in both the figures. EPO for the engine is 300^o aBDC and standard spark timing is 168.8^o aBDC but because of the offset, concentration rise accompanying exhaust blowdown is observed at 0 ^{o} aBDC and combustion triggered CO_2 concentration rise takes place at 240 ^{o} aBDC. Scripts were developed to account for these offsets while calculating TRF from CO_2 concentration at specific times during the cycle. This is discussed further in the next section. The crank angle offsets in the CO_2 data rendered them unfit for

generating scavenging curves needed for *GT-Power*'s scavenging sub-model discussed in Chapter 3.

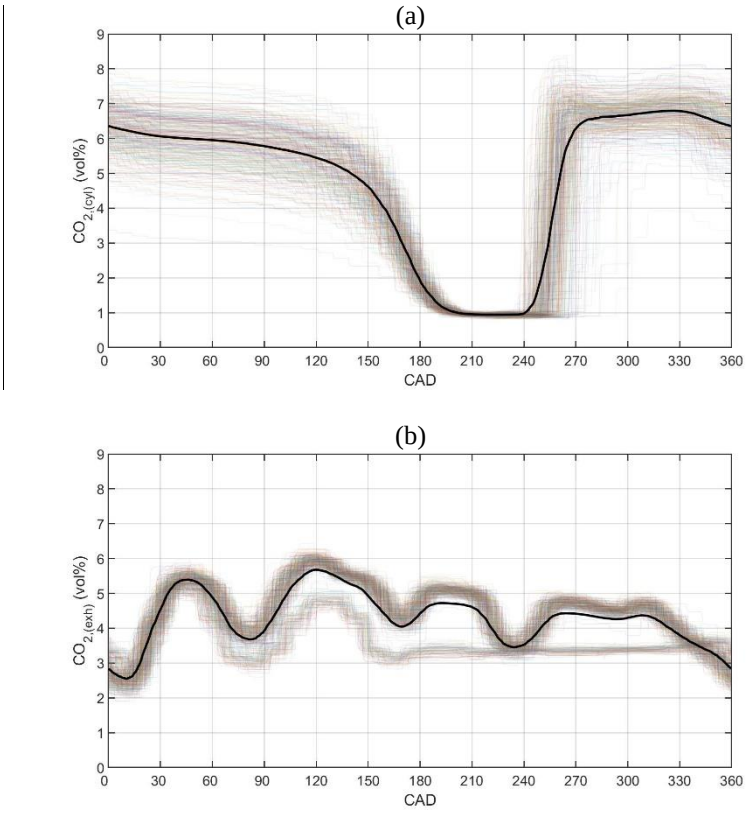

Figure 46: Ensemble averaged high speed (a) cylinder and (b) exhaust CO_2 concentration data at 100% load and 525 RPM. Translucent curves are individual cycles.

The post-combustion CO_2 concentration, averaged over 300 cycles, for the twelve stable operating points studied is shown in Figure 47. The error bars show the spread in the averages over two experimental runs. The data is acceptably repeatable. Post-combustion CO_2 concentration can serve as an indicator of the trapped equivalence ratio if combustion inefficiency effects are ignored. The results suggest that the trapped

mixture becomes leaner as the speed increases and the load decreases. This is discussed in more detail in section 5.3. when TER results are presented.

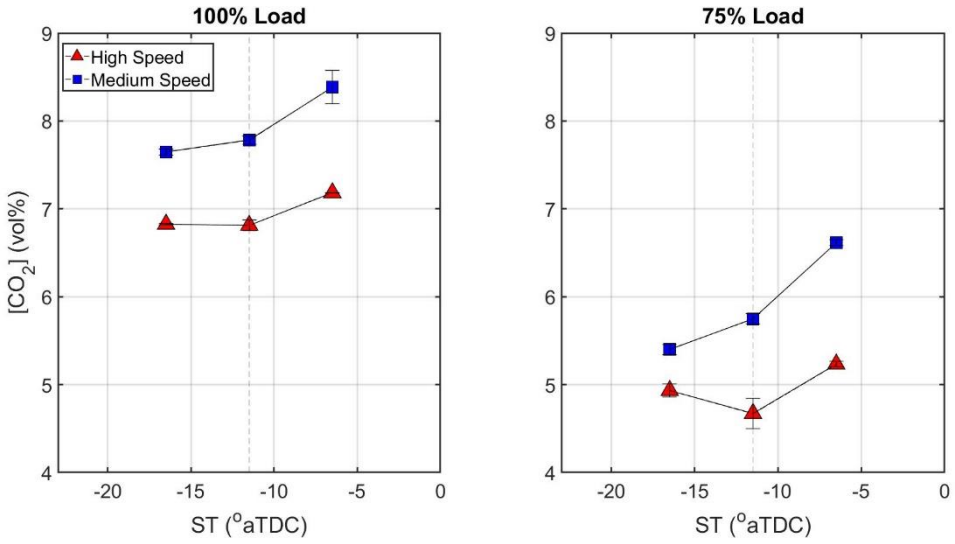

Figure 47: Post-combustion in-cylinder CO_2 concentration at different engine speeds, loads, and spark timings.

Figure 48 shows high speed exhaust CO_2 data for different engine speeds and loads after being adjusted for transportation delays. The purpose of the plots is to illustrate the progression of scavenging in the engine and to see how it changes as the engine speed and load change. Since exhaust CO_2 is being used as a tracer for combustion products, various features of the exhaust CO_2 'wave' can be used to comment on the nature of the scavenging process. The first crest can be attributed to an initial stage where a plug of combusted gases escapes the cylinder during blowdown in a perfect displacement type gas ejection process. It can be argued that the following trough is caused by the arrival of a short-circuited stream in the exhaust. The short-circuited

stream of fresh air dilutes combustion products in the exhaust and thus, produces the observed dip in CO_2 concentration. The second crest probably represents a delayed perfect mixing type scavenging stage, which takes place when the mixture formed on the intake port side hemi-cylinder by the mixing of turbulent incoming gases and residual gases reaches the exhaust. These observations corroborate the choice of various scavenging stages for the scavenging model proposed in Chapter 4.

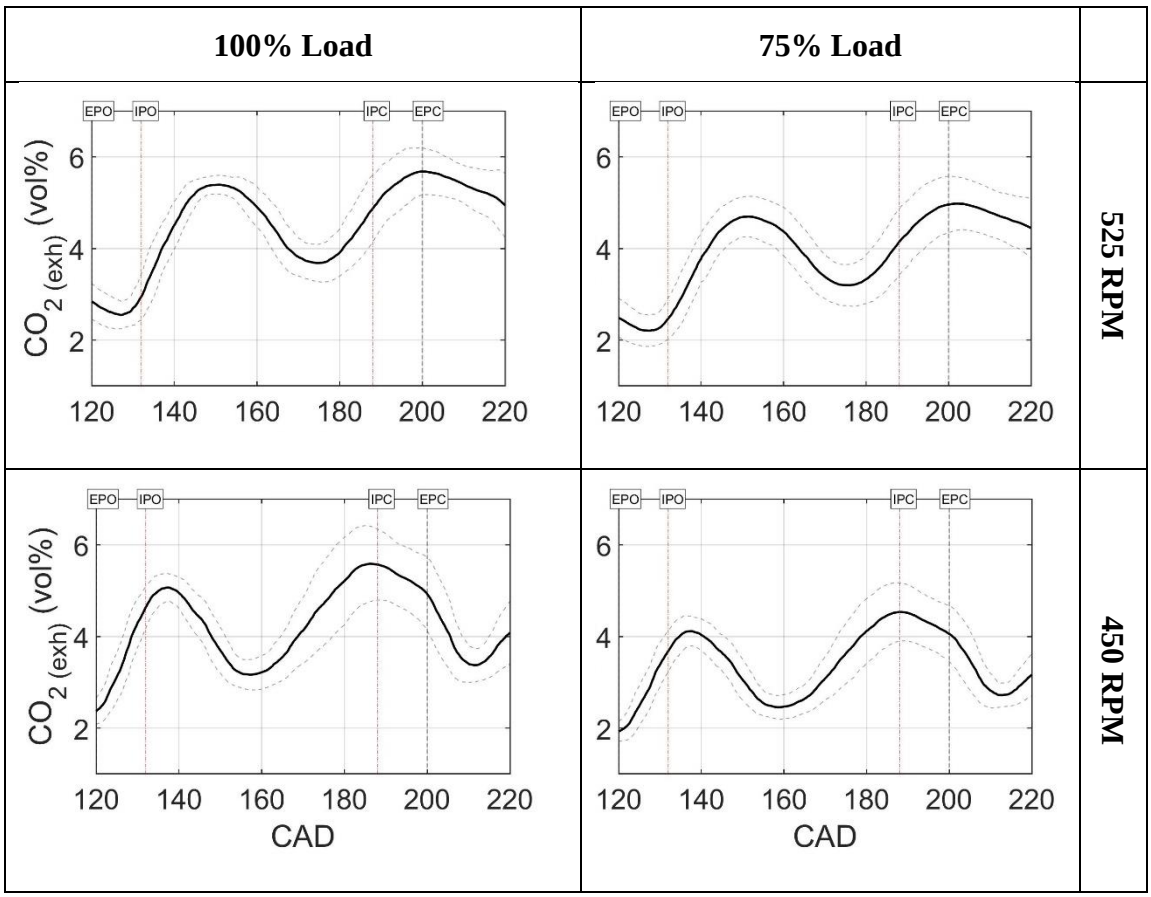

Figure 48: 300 cycle averaged exhaust CO_2 concentration data at standard spark timing for different speeds (rows) and loads (columns).

If the two crests (in order) represent the PD and PM phases and the valley represents short-circuiting, then the results in Figure 48 show that:

1. Scavenging progresses in the following order: PD – short-circuiting – PM. There is probably some overlap between the last two processes.
2. At medium speed (450 RPM), the blowdown and PD phases are shorter and short-circuiting starts earlier compared to the high speed cases.
3. PM and short-circuiting stages dominate at medium speed while the blowdown-PD stage dominates at high speed. The increase in short-circuiting with speed reduction is confirmed by experimental short-circuiting results shown later.
4. The effect of load reduction is an overall decrease in residuals in the exhaust, which could be representative of either poor scavenging (less combustion products leaving the cylinder) or lean combustion (less combustion products being generated). TER results (shown later) support the latter explanation. High-speed exhaust CO_2 measurements in [70] show similar trend with load changes.
5. The effects of changing engine load on scavenging phasing (starting time and duration of the three scavenging modes) are unclear.

The bi-modal exhaust CO_2 wave observed in the present study might be unique to cross-scavenged engines because a similar study conducted on a cylinder-head-valved engine [69] did not show the second peak. This bimodal behavior can be attributed to the existence of an unscavenged ‘island’ on the piston crown surface in cross and loop (Schnürle type) scavenged engines [82] that splits the incoming air jet into the following

two streams: (1) a ‘direct slippage’ stream that slips diametrically across the cylinder during the initial portion of scavenging, and (2) a ‘bypassed air’ stream that flows around the residual gas island; first towards the cylinder head and then out through the exhaust ports during the latter portion of scavenging [82]. The bypassed air stream entrains residual gases during its journey while the direct slippage stream does not interact with them.

5.2. Post-Processing Experimental Data

The raw high speed composition data had to be processed before meaningful conclusions about the scavenging process could be drawn from it. The following sub-sections describe some of the data processing methods used.

5.2.1. TRF Calculation

Trapped residual fraction is calculated from the cylinder CO_2 concentration data by using concentration values before and after gas exchange, as shown in equation 19. Figure 49 shows in-cylinder CO_2 measurements for three consecutive cycles. ‘Cycle N’ is used to discuss the approach used to calculate TRF. Using the labels shown in Figure 49, equation 19 can be represented as equation 30 to calculate TRF. Equation 30 implicitly assumes that the concentration ‘X’ represents the post-EPC and pre-injection CO_2 concentration. Because of the lack of temporal resolution and unreliability of the CO_2 data phasing, the pre-injection CAD value cannot be determined with precision. Therefore, the diluting effects of fuel addition have to be accounted for while using

concentration at X to calculate TRF. The resulting formulation, shown in equation 31, is used to calculate TRF using in-cylinder CO_2 data for each cycle. Cycle resolved TRF values are then averaged for 300 cycles to get TRF for a given operating point. 'y_f' in equation 31 is the mole fraction of fuel in the pre-combustion mixture. The derivation of equation 31 is given in Appendix A. An ambient CO_2 concentration of 400 ppm is used for all TRF calculations. Tobis et al. [10] used Equation 19 in their intermittent sampling study by disabling fuel injection for the cycle for which the pre-combustion CO_2 concentration was to be measured. Thus, avoiding the fuel dilution problem.

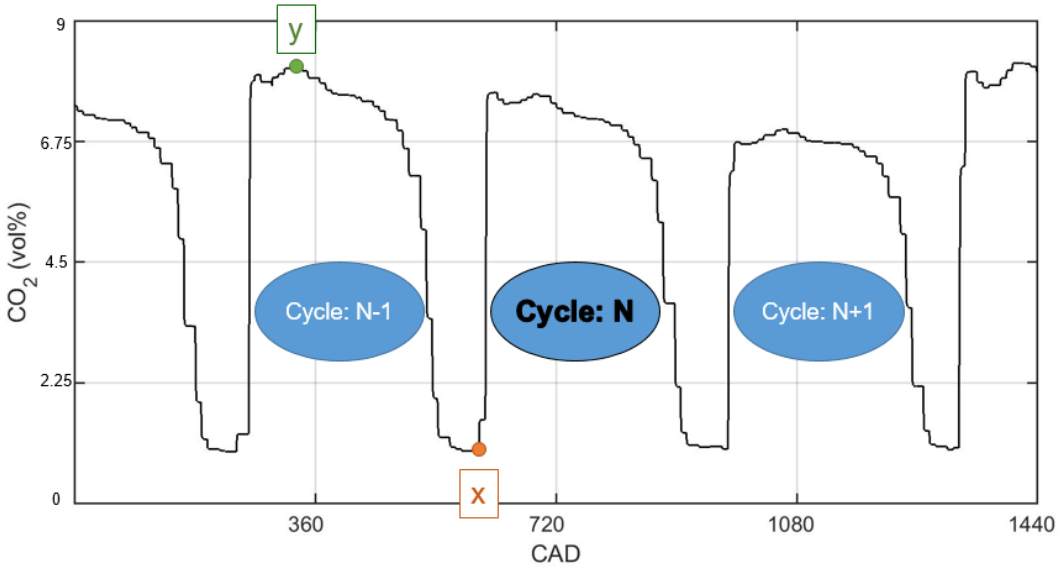

Figure 49: Sample in-cylinder CO_2 data for consecutive cycles.

$$TRF_N = \frac{[CO_2]_X - [CO_2]_{Air}}{[CO_2]_y - [CO_2]_{Air}} \qquad 30$$

$$\mathrm{TRF_N} = \frac{[\mathrm{CO_2}]_\mathrm{X} - [\mathrm{CO_2}]_\mathrm{Air}}{[\mathrm{CO_2}]_\mathrm{y} - [\mathrm{CO_2}]_\mathrm{Air}} + \frac{[\mathrm{CO_2}]_\mathrm{Air}\, \mathrm{y_f}}{[\mathrm{CO_2}]_\mathrm{y} - [\mathrm{CO_2}]_\mathrm{Air}} \quad 31$$

The transportation delays responsible for the lag observed in CO_2 measurements discussed earlier had to be properly accounted for before the data could be used to calculate cycle resolved TRF. This was done by using a post-processing script that linked CO_2 data to corresponding cycles during data analysis. The approach was based on the OEM's recommendations of correcting for the delays empirically using a heuristic approach rather than analytically. Analytic approaches to calculate the transportation delays were discouraged because the delays, owing to the transient nature of sample flows, are not linear.

5.2.2. Accounting for CO_2 Sensor Limitations

During data processing while trying to calculate TRF, it was discovered that for some low expansion pressure cycles, which can be identified from their low IMEP values, the cylinder CO_2 sensor did not sense CO_2 even though combustion had taken place in the cylinder, as evidenced by cylinder pressure, exhaust pressure, and high speed exhaust temperature data. An example of such a cycle is shown in Figure 50 where for cycle-2, no visible rise in CO_2 concentration is observed after combustion. The absence of a combustion signature in the CO_2 data is attributed to the relatively weak nature of combustion that does not produce sufficient CO_2 to homogenously increase the cylinder CO_2 concentration. As a result, for these partially firing cycles the cylinder gas

sample analyzed by the CO_2 sensor does not have high enough CO_2 concentration to indicate the existence of combustion. If larger samples were drawn for these cases, some CO_2 rich strata would have probably made their way to the analyzer and the sensed CO_2 concentration would have indicated combustion. Doing so would have, however, deteriorated the time-response of the analyzer and the removal of substantial amounts of cylinder gas would have affected engine behavior and inhibited continuous sampling.

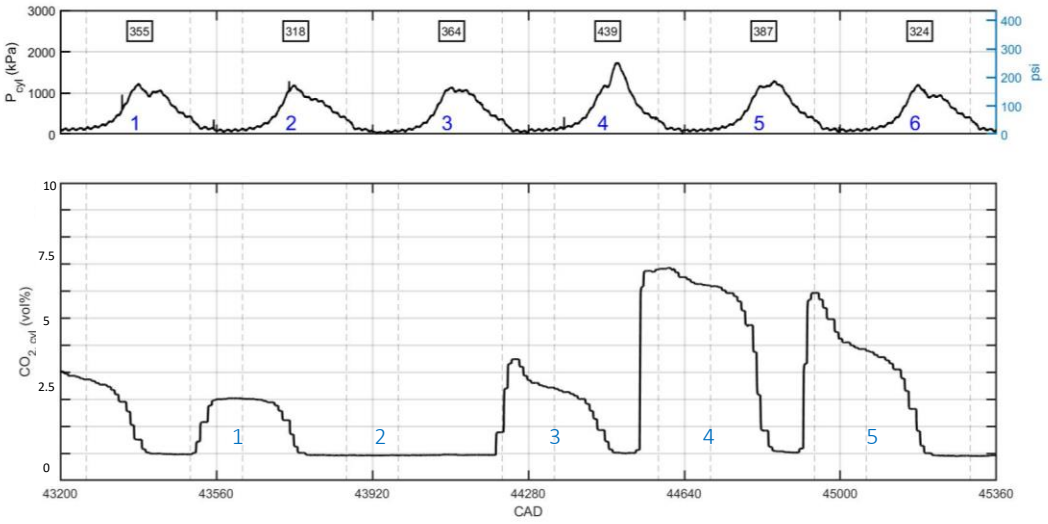

Figure 50: Six consecutive cycles showing cylinder pressure and CO_2 concentration. Cycle-2 represents a partially firing cycle with sensor malfunction.

It is important to discount the effects of such 'sensor malfunction' cycles while calculating TRF because not doing so would, incorrectly, result in small pre-scavenging CO_2 concentration values for the following cycles (cycle-3 in Figure 50), which would in turn increase the TRF value for it to unrealistic levels (over 80%). These cycles, if left uncorrected, can result in significant overestimation of average TRF values. The box

plot in Figure 51 gives an example of the effects of including 'sensor fail' cycles in TRF calculations. The outliers in the last box are cycles with artificially high TRF values because of 'sensor fail' cycles.

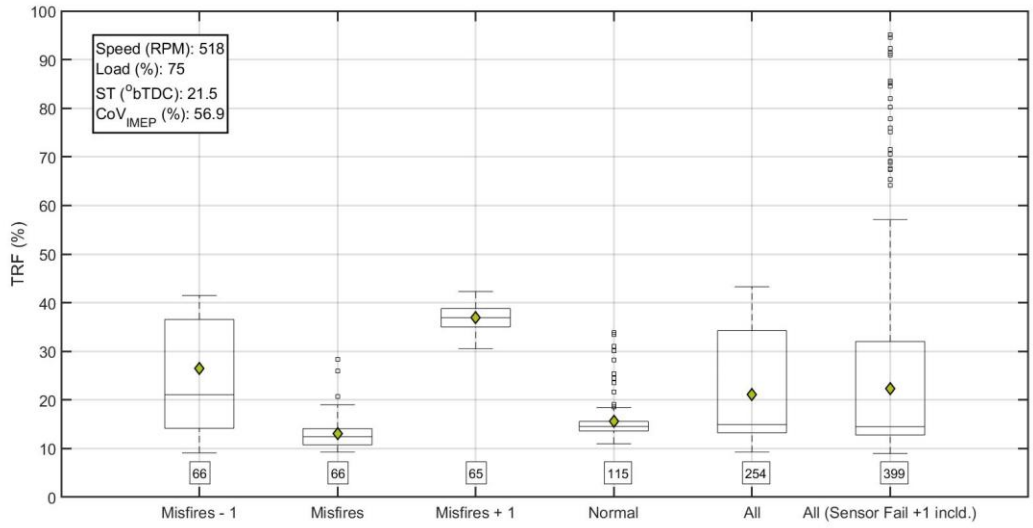

Figure 51: TRF values for different kinds of cycles. Boxes show the interquartile range, diamonds represent the mean, horizontal lines within boxes are the median, and the whiskers are the fences beyond which data points are considered outliers. Numbers below the boxes show the number of cycles for each type.

A methodology was developed to identify and remove such cycles before conducting any analysis. The sensor malfunctioning cycles were termed as weak partial fires and were identified based on the following criteria:

$$\text{Cycle}_N \in [\text{PF}_{\text{weak}}] \text{ if } \{\text{IMEP}_N > 20 \text{ kPa } \& \ [CO_2] \leq 2 \text{ vol\%}\}$$

The other cycle types shown in Figure 51 are listed below. The following characterization should be read together with Figure 52, which provides examples of all of these cycle types on an IMEP-Post CO_2 concentration map.

- Misfiring Cycles (MF): These are the cycles where both the pressure and CO_2 signatures point to the failure of combustion. The IMEP is around 0 kPa and the post-combustion CO_2 concentration is less than 2 vol%, which is selected to be the lower post-combustion CO_2 concentration threshold for firing cycles.
- Pre-Misfiring Cycles (MF-1): As the name suggests, these are the cycles preceding misfiring cycles. TRF is plotted for these cycles to investigate if they influenced the following MF cycle. This topic is the subject of a separate study that can be found in [86] and is not discussed here any further.
- Post-Misfiring Cycles (MF+1): These are the cycles succeeding misfiring cycles. They have unusually high combustion pressures, and as a result, very high IMEPs. This increased combustion pressure is attributed to the burning of a richer-than-usual trapped mixture produced by residual fuel from the preceding misfiring cycle.
- Normal Cycles: These are the remaining cycle; that is, those cycles that are not misfires, partial fires, or post-misfires.
- All Cycles: A set of the four cycle types described above.

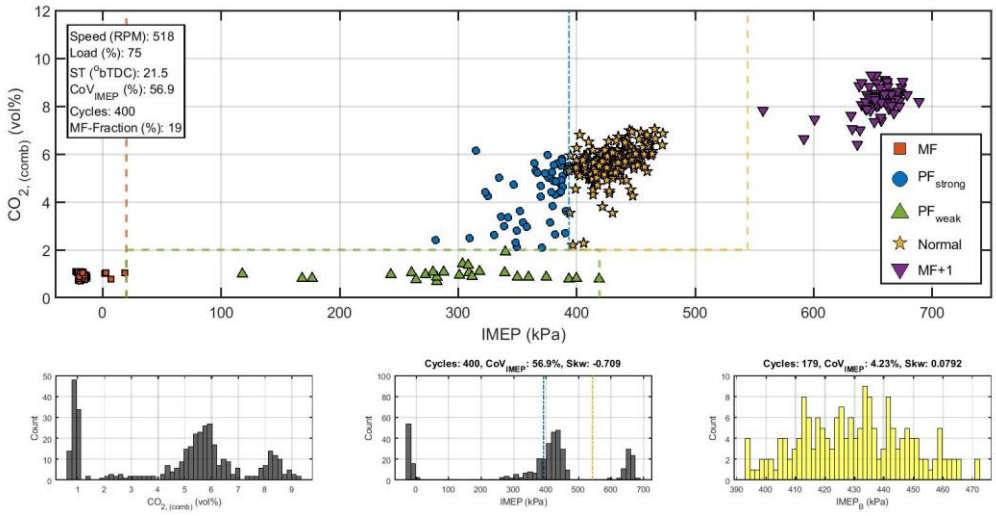

Figure 52: Different kinds of cycles on an IMEP-CO_2 map (top); and histograms showing the distribution of CO_2 (bottom left) and IMEP (bottom center) for all cycles, and IMEP for normal cycles (bottom right) at a moderately unstable operating point.

Weak partially firing cycles are shown in Figure 52 by upward facing triangles for a moderately stable (CoV_{IMEP} = 57%) operating point. For stable operating points (CoV_{IMEP} less than 15%), such cycles are not observed. Figure 53 shows how the fraction of 'analyzer fail' cycles changes as the engine becomes unstable. At very unstable operating points, the fraction of such cycles decreases because approximately half of the cycles are misfires and the remaining half are the MF+1 cycles that have very high IMEPs and produce sensible CO_2 signals. This phenomenon of cycling between MF and MF+1 cycles is sometimes informally referred to as 'four-stroking' [87]. It can also be seen in the low load data shown in Figure 43. The interested reader is referred to [86] for a detailed discussion and analysis of the characterization work presented here.

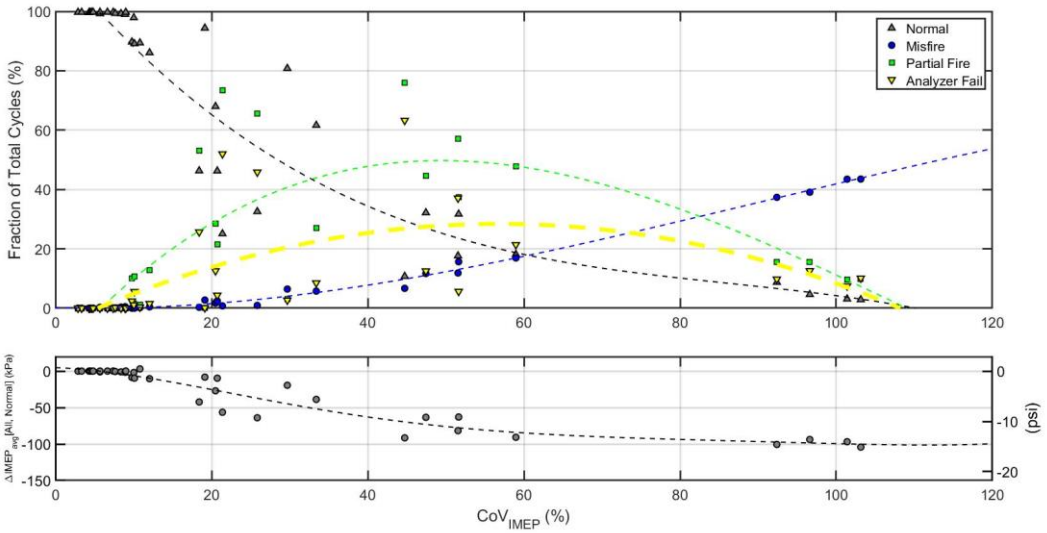

Figure 53: Changes in fraction of different cycle types (normal, misfires, partial fires, and 'analyzer fail' or weak partial fires) as a function of engine stability.

5.2.3. Short-Circuiting Calculation

The short-circuiting fraction is defined as the *total* mass fraction of the incoming air that exits the engine through the exhaust ports during gas exchange. This includes fresh air lost to the exhaust as a pure air stream (i.e. the pure slippage stream) and as a part of a residual-gas-air mixture (i.e. the bypassed air stream). The short-circuiting fraction is calculated using the natural gas fuel as a tracer. The engine is operated at the twelve stable operating points highlighted in Table 2 using the pre-mixed fuel delivery system. Unburned hydrocarbon emissions are measured, and it is assumed that the source of all the emissions is short-circuited methane. The number of methane molecules in the exhaust are then calculated by using measured air flowrate. The molar flow rate of methane in the exhaust is used to calculate the mass of methane exhausted. The short-circuiting fraction is then calculated by comparing the mass of methane exhausted to the

measured mass of fuel inducted. These calculations are shown in equations 32 and 33. Figure 54 shows the total HC results for the twelve operating points using the pre-mixed fueling system. Results from the direct injection system are also shown for reference. HC emissions for the direct injection system, which represent combustion inefficiencies, are negligible compared to those for the pre-mixed system. Nuti et al. [9] demonstrated using exhaust gas chromatography that the majority of the exhausted fuel in a pre-mixed two-stroke engine comes from short-circuiting. It has to be noted that in the current study, the engine was operated on the pre-mixed system only for the short-circuiting calculations. All other validation experiments used direct fuel injection.

$$N_{CH_4,exh} = [HC]_{exh} N_{tot,exh} = [HC]_{exh} \frac{m_{air,in}}{MW_{air}} \quad 32$$

$$x_{short} = \frac{N_{CH_4,exh}\, MW_{CH4}}{m_{fuel,in}} \quad 33$$

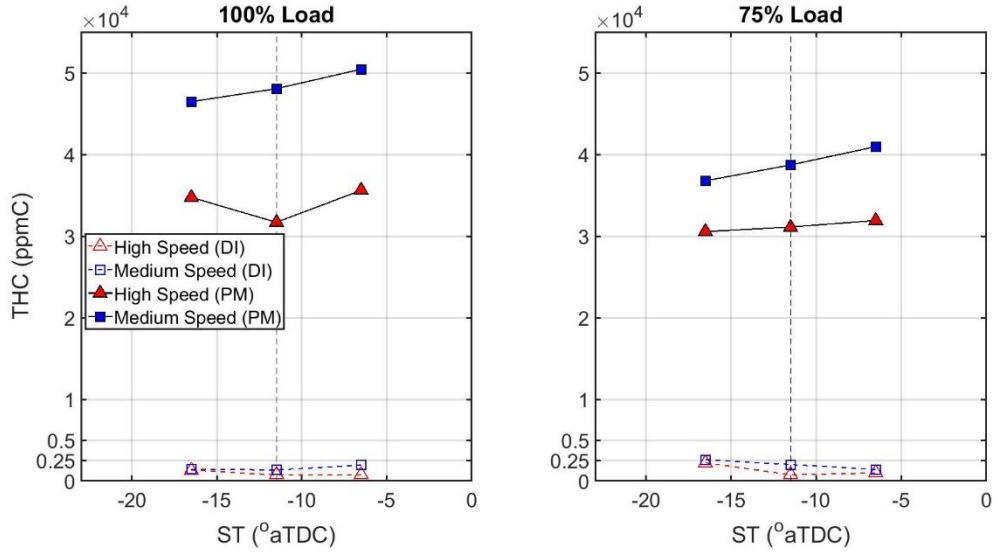

Figure 54: Unburned hydrocarbon concentration in engine exhaust for pre-mixed (PM) and direct-injected (DI) operation.

5.2.4. Air Flow and TER Calculation

Information about the amount of air delivered every cycle is needed to calculate TER and validate the hybrid model. Since an air flow meter was not available for the scavenging experiments, an alternative calculation methodology was needed to calculate the air flow rate.

At first, air flow rate was calculated using equations for gas flow through an orifice using crank angle resolved intake, cylinder, and exhaust pressures. The results were found to be unreliable because of being very sensitive to the choice of datum pressure value used to calculate absolute cylinder pressure. Additionally, the pressure-based calculations were also sensitive to the choice of discharge coefficients used for the intake and exhaust ports. The coefficients used were either obtained from the literature or estimated indirectly from a previous CFD study on the engine [80]; both of which left a lot to be desired in terms of accuracy. Because of these shortcomings, it was decided not to pursue the pressure-based approach. A brief discussion of this approach is provided in Appendix-E for the record.

Next, an approach was developed to calculate air flow rate using measured exhaust oxygen concentration data and short-circuiting fractions. In this approach, engine exhaust oxygen concentrations are calculated using flow data (short-circuiting fraction, TRF, and mass of fuel), combustion efficiency, and a guessed value of air flow rate. Combustion efficiency results are used to discount the non-combusted fraction of

delivered fuel - the so called 'fuel slip'. A rate of heat release-based approach is used to calculate combustion efficiency because exhaust THC data was found to be unreliable. The calculated O_2 concentration is compared against measured exhaust data and the air flow rate is iteratively changed until the calculated and measured oxygen concentrations match. O_2 is selected for this purpose because it was the most stable of the measured exhaust gases. This can be seen in Figure 55 in which the error bars show the average range (spread) of two sets of O_2 measurements at each operating point. Details of the mass flow calculation method are provided in Appendix-B.

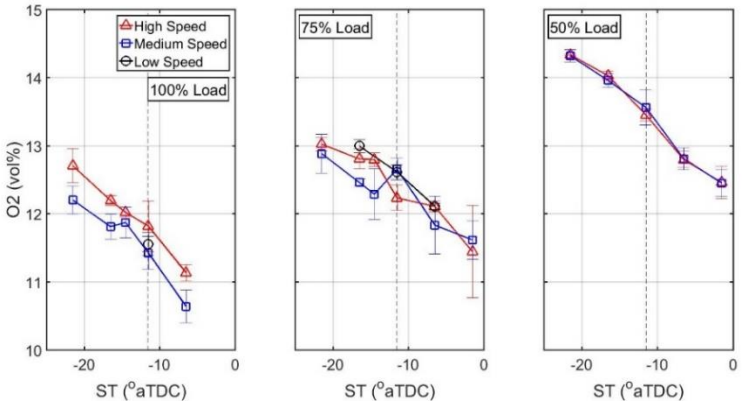

Figure 55: Measured exhaust O_2 concentration at different speeds, loads, and spark timings.

TER is calculated by using the mass of trapped fuel and the mass of trapped air, which is comprised of fresh air that is trapped and air present in the trapped residual gases. This is done by implicitly solving equations 34 and 35 at various values of '$x_{air,res}$'. $x_{air,res}$ is the mass fraction of air in the trapped residual gas. The mass of trapped residual gas is calculated using TRF. Figure 56 shows the results of these

calculations for all data points (including unstable ones). The dashed box marks the 12 stable operating points being studied.

$$CH_4 + \frac{2}{TER}(O_2 + 3.76N_2) \rightarrow CO_2 + 2H_2O + 2(3.76)N_2 + \left(\frac{2}{TER} - 2\right)(O_2 + 3.76N_2) \quad (34)$$

$$TER = \frac{m_{f,non-slipped}}{m_{fresh\ air,trap} + x_{air,res} m_{res,trap}} \left(\frac{A}{F}\right)_{stoich} \quad (35)$$

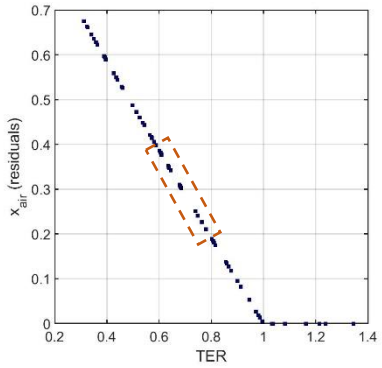

Figure 56: Calculated fraction of air in trapped residual gases as a function of TER.

5.3. Scavenging Results

With the implementation of the scavenging calculation methods discussed above, gas flow across the engine can be completely characterized; that is, the following scavenging parameters can be obtained:

- Delivered air mass
- Short-circuiting fraction (trapping efficiency)
- Trapped air mass

- Delivered fuel mass
- Trapped fuel mass
- Trapped fuel mass that took part in combustion
- TRF (scavenging efficiency)
- Trapped residual mass
- TER
- Total trapped mass

Additionally, the cylinder pressure at EPO is known from experimental measurements, which can be used with the trapped mixture composition to calculate average cylinder temperature at EPO using the ideal gas equation. This temperature is important because the hybrid model assumes the residual stream to be at this temperature during scavenging. Results for these scavenging parameters are presented in this section.

Figure 57 shows TRF results calculated using the technique discussed in section 5.2.1. for the twelve stable operating cases studied. The results show 300 cycle averaged TRF values for each operating point. It can be seen that increasing engine load decreases TRF. This is because of higher expansion pressures at high load that cause more effective removal of residual gases (higher SE). The same reasoning can be extended to the reduction in TRF with retarding spark timings as retarded combustion increases expansion pressures at a given speed and load point. The high expansion pressures also

produce high exhaust blowdown pressures. The change in TRF accompanying speed changes result from the combined effect of the following two competing influences:

1) As the speed increases, rarefaction exhaust waves, sometimes referred to as scavenging pulses, arrive at the exhaust ports around BDC. This is beneficial from a scavenging standpoint because at this point in the cycle, the exhaust ports are maximally open and the cylinder has significant amounts of residual gas present [14]. As a result, the scavenging pulse is utilized more effectively and more residual-rich gas is exhausted. Contrary to this, for the medium speed cases, the pulse arrives earlier in the cycle when the ports are still opening and some of its scavenging improving potential is wasted. Moreover, reflected compression waves, sometimes referred to as plugging or ramming pulses [23], are optimally timed to arrive at the exhaust ports around IPC for the 525 RPM cases, which increases the trapped air mass and thus improves the scavenging efficiency. Since the fixed geometry exhaust system is tuned for the rated speed of 525 RPM, the scavenging performance is better at high speed compared to medium speed.
2) As the engine speed decreases, there is more time available for residual gases to be exhausted and fresh gases to be inducted.

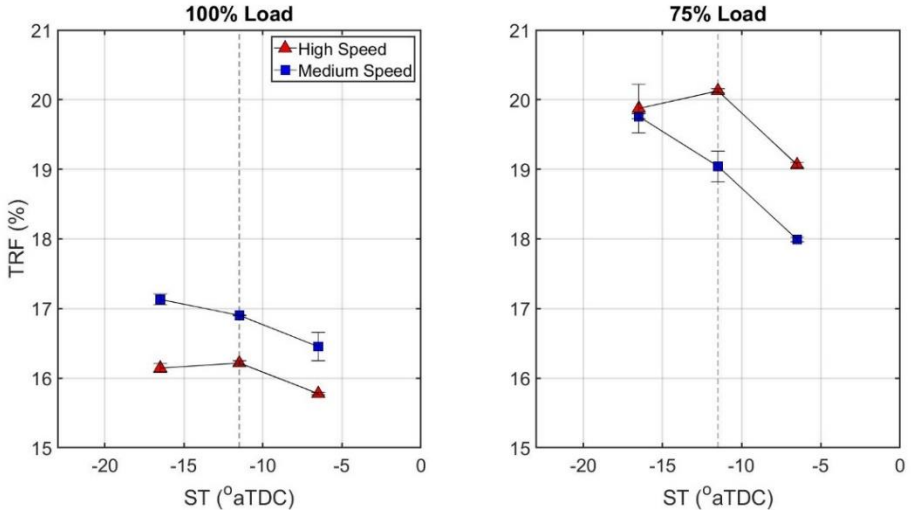

Figure 57: Trapped residual fraction at different engine speeds, loads, and spark timings.

The results indicate that at full load, the former influence (exhaust wave phasing) dominates, which is why TRF decreases as the engine operates at the tuned high engine speed while for the medium load case, the latter influence (time available for scavenging) is dominant and medium speed TRF values are lower. There could be secondary effects from changes in the momentum/turbulent characteristics of incoming air stream at different speeds that could affect mixing of fresh and residual gases.

Figure 58 shows the short-circuiting fraction results for the twelve stable operating points. It can be seen that the engine's trapping performance improves as both engine speed and load increase. The improved trapping at higher speeds can be attributed to (1) there being less time available for incoming air to short-circuit, and (2) optimal phasing of the reflected plugging wave. The wave arrives at the exhaust ports prior to EPC to discourage the efflux of fresh air-rich cylinder gases and to stuff exhaust

manifold gases back in the cylinder. The improved trapping with increasing engine load can be explained by the plugging pulse phasing as well. At higher loads, exhaust temperatures are higher which increases the local speed of sound, causing the reflected plugging pulse to travel faster and arrive slightly earlier at the exhaust ports; thus pushing more air-rich exhaust manifold gases into the cylinder. Spark timing effects can also be explained using plugging pulse phasing. Retarding spark timing also increases exhaust temperature and consequently wave propagation speeds. These exhaust pulse phenomena can be seen in Figure 59 which shows exhaust waves for different speeds, loads, and spark timings stacked vertically. Each increment along the y-axis is 10 kPa and the horizontal dashed lines represent atmospheric pressure for each wave. A more detailed discussion of exhaust wave phasing effects on the scavenging characteristics of the engine can be found in [88].

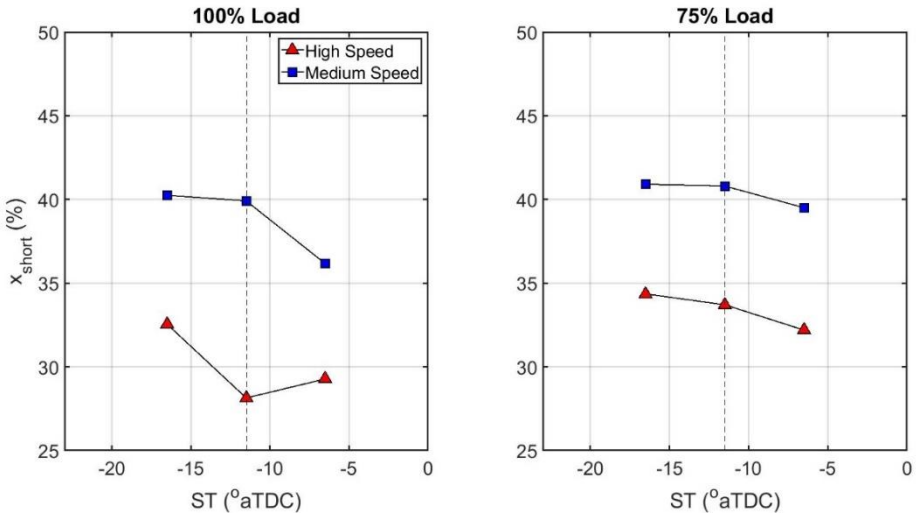

Figure 58: Short-circuiting fraction at different engine speeds, loads, and spark timings.

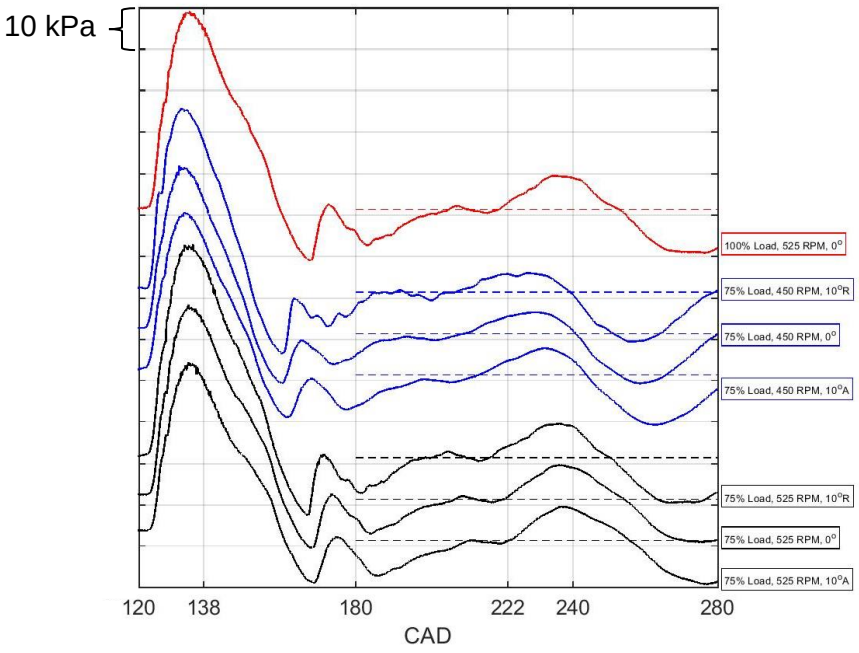

Figure 59: Exhaust pulse phasing for different engine speeds, loads, and spark timings stacked vertically. Dashed horizontal lines represent atmospheric pressure. (EPO: 120 CAD, BDC: 180 CAD, intake port closing (IPC): 222 CAD, EPC: 240 CAD)

Figure 60 shows the mass of fuel that is delivered every cycle and Figure 61 shows the indicated fuel conversion efficiency (product of thermal and combustion efficiencies) of the engine. Fuel mass is calculated from the average mass flow rate and engine speed measured during data collection. Since fuel is injected after EPC, the trapping efficiency of the fuel is 100% and the delivered fuel amount is equal to the trapped fuel mass. Increasing engine load increases fuel consumption because of the need for additional chemical energy to provide more torque.

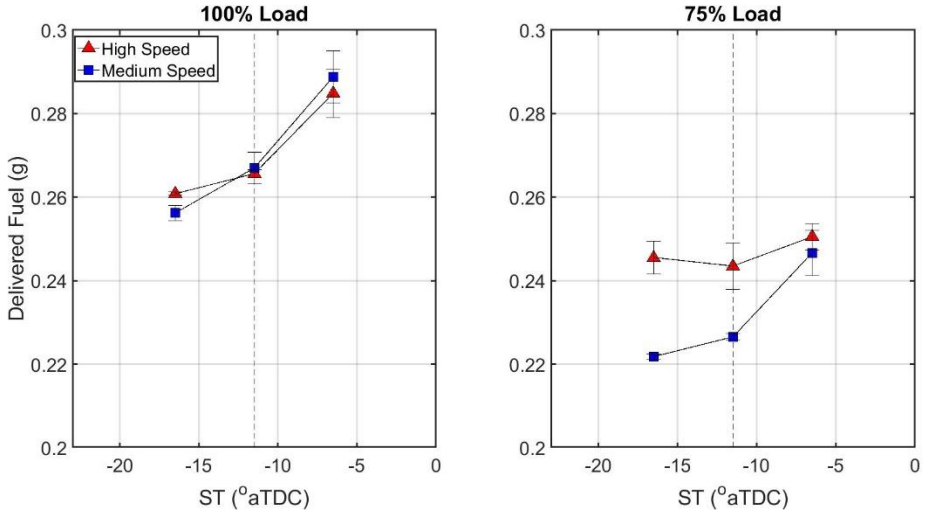

Figure 60: Mass of fuel delivered per cycle at different engine loads, speeds, and spark timings.

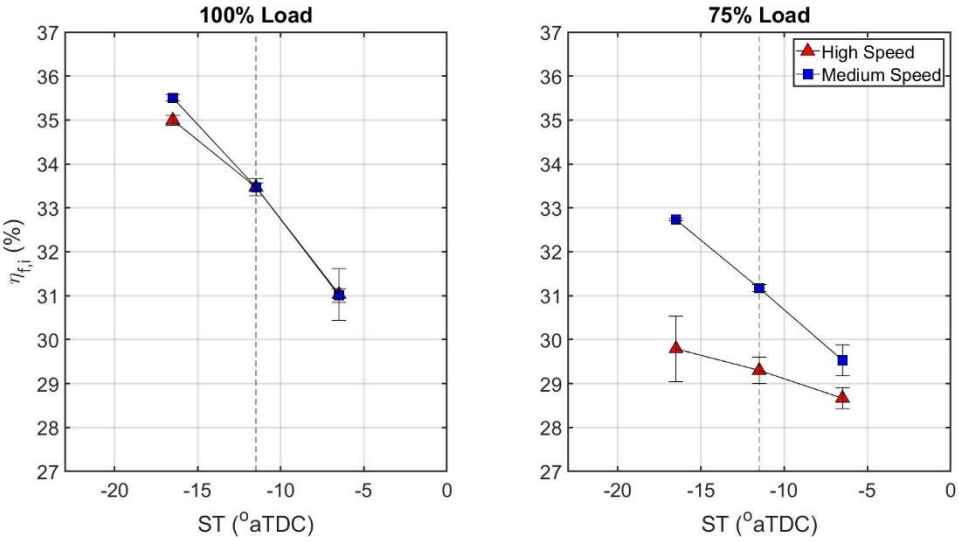

Figure 61: Indicated fuel conversion efficiency at different engine speeds, loads, and spark timings.

As mentioned during the TER calculation section, reliable exhaust hydrocarbon data was not available to calculate combustion efficiency. In lieu of that, rate of heat release analysis was carried out to calculate the net accumulated heat release which was

then used to calculate apparent combustion efficiency using the mass of fuel delivered and its lower heating value. The results are shown in Figure 62. The combustion efficiency results are corroborated by CoV_{IMEP} and misfiring fraction (the fraction of misfires in the recorded data set) results which can be considered as measures of combustion inefficiency (Figure 62, bottom). The engine's combustion efficiency decreases at medium load, particularly for high speed. The effects of these changes along with changes in thermal efficiency are responsible for the observed fuel consumption and fuel conversion efficiency behavior.

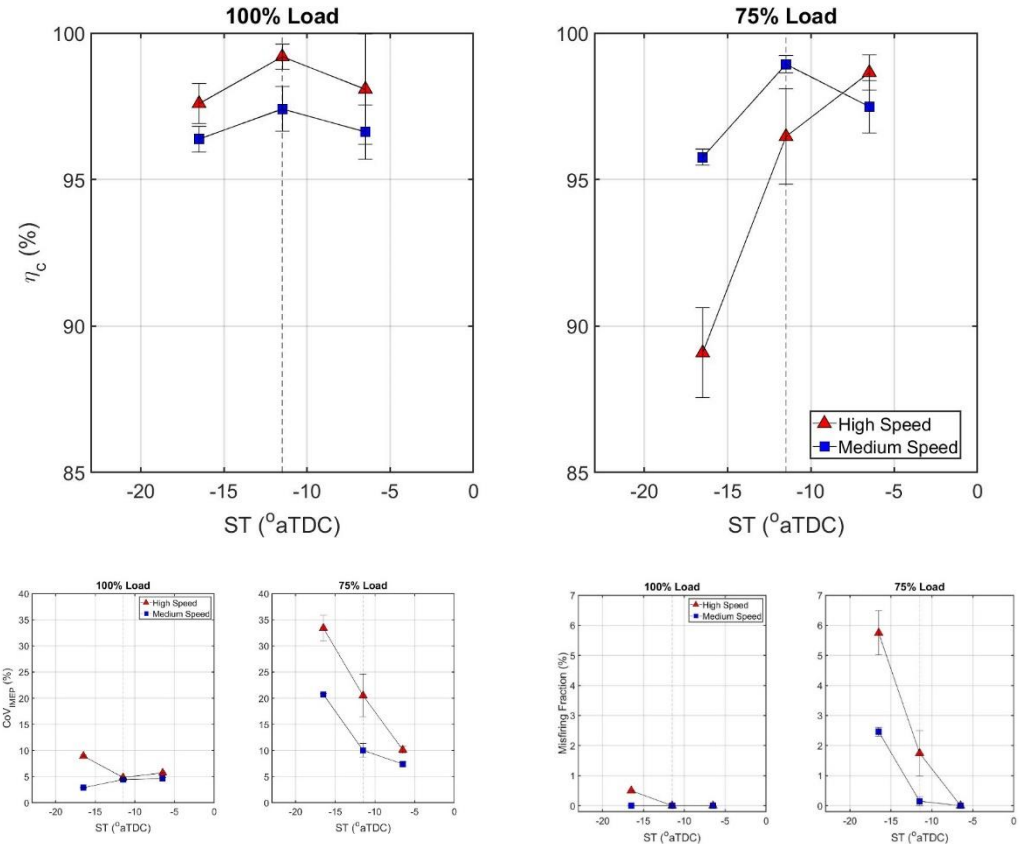

Figure 62: Apparent combustion efficiency (top); and coefficient of variation and misfiring fraction (bottom) at different engine speeds, loads, and spark timings.

Retarding spark timing makes the engine less thermally efficient and as a result, its fuel consumption increases. This is because at retarded spark timings, peak pressures are lower and their location is retarded which results in inefficient utilization of the expansion stroke. The effects of thermal efficiency improvement are less visible in the fuel conversion efficiency plot at medium load because of an accompanying decrease in combustion efficiency, especially at high speed. The decrease in combustion efficiency at medium load also overshadows any fuel conversion efficiency gains that might have resulted from thermal efficiency improvements caused by lean combustion (Figure 47) and high trapped residual fraction (Figure 57) [89]. Improvements in thermal efficiency (if any) because of reduced wall heat losses at high speed are also difficult to discern. The effect of speed on fuel consumption is not significant at full load but at medium load, it decreases as the speed decreases. Improved engine stability at medium speed ($CoV_{IMEP} \sim 10\%$) compared to full speed ($CoV_{IMEP} \sim 20\%$) is responsible for this reduction. Higher trapped residual gas mass at 525 RPM might be responsible for the increased cyclic variability at medium load (Figure 57).

Figure 63 shows the total delivered mass (solid lines) - which includes the mass of delivered fuel and air - and the total trapped mass (dashed lines) - which comprises non-short-circuited fraction of air, delivered fuel, and trapped residuals - per cycle. The short-circuiting results shown above and delivered air results are used to calculate the trapped mass. Delivered air mass has not been shown separately because the total delivered mass shown in Figure 63 mostly (over 95%) comprises air. More air is

delivered as engine speed increases. This is because of the piston scavenged design of the engine, whereby engine speed is directly coupled (via the stuffing box pressure) to the mass of air delivered. The difference between high and medium speed mass becomes more pronounced after trapping because of the higher levels of short-circuiting at medium speed. This can be seen by the large (over 1 g) difference in the trapped mass results in Figure 63.

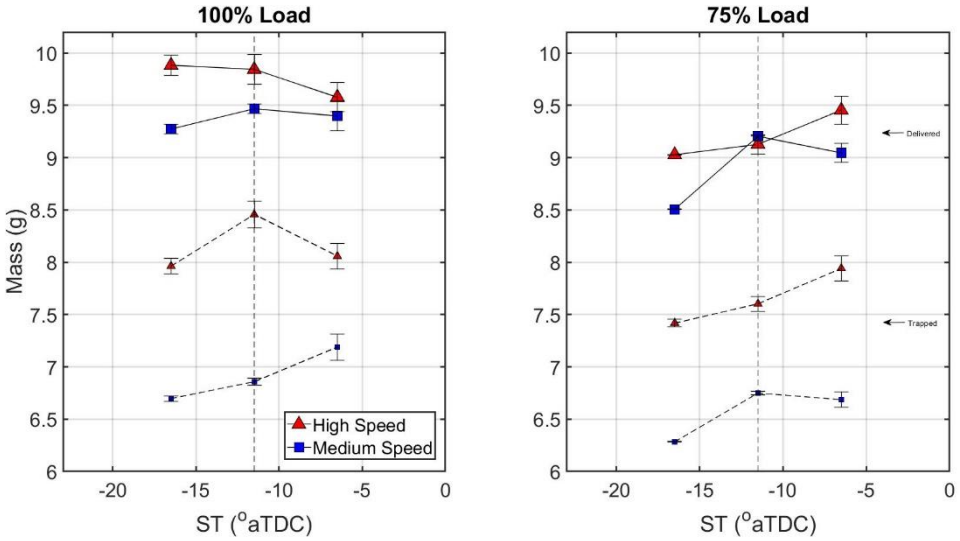

Figure 63: Total delivered (solid lines) and trapped (dashed lines) mass for different loads, speeds, and spark timings.

Figure 64 shows TER values calculated from the trapped fuel, air, and residual gas quantity. It can be seen that the engine runs leaner at high speeds compared to medium speeds. This is because of (1) more air being delivered, and (2) better trapping at high speeds. The effects of scavenging efficiency changes and thermal efficiency improvements from reduced heat transfer are secondary. Decreasing engine load makes

the engine run leaner as well. This can be attributed to: (1) a reduction in the chemical energy demand as less work is being generated, and (2) higher amounts of trapped residuals, which not only provide additional oxidizer but also act as a diluent to lower combustion temperatures and increase the engine's thermal efficiency [89]. The only exception to this trend is the high speed, high load, standard spark timing point, which, incidentally, is the engine's design operating point. At this point, the engine is leaner at full load. The lean low load operation can help explain the reduction in residual gas tracer concentration in the exhaust seen in Figure 48. Richer mixtures at medium speed, which increase mixture reactivity, can help explain the observed engine stability improvements.

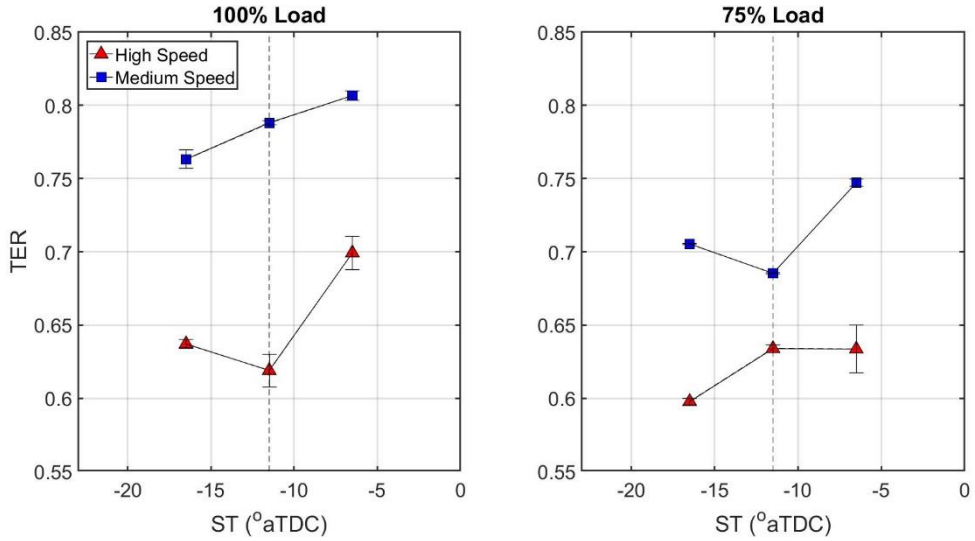

Figure 64: Trapped equivalence ratio at different engine speeds, loads, and spark timings.

Figure 65 shows the average cylinder temperature computed using the calculated trapped mixture mass and measured cylinder pressure at exhaust port opening. The cylinder temperatures trend with TER. Medium speed temperatures are higher because considerably more mass is trapped at high speed even though cylinder pressures at EPO are also slightly higher for the high speed cases (Appendix C).

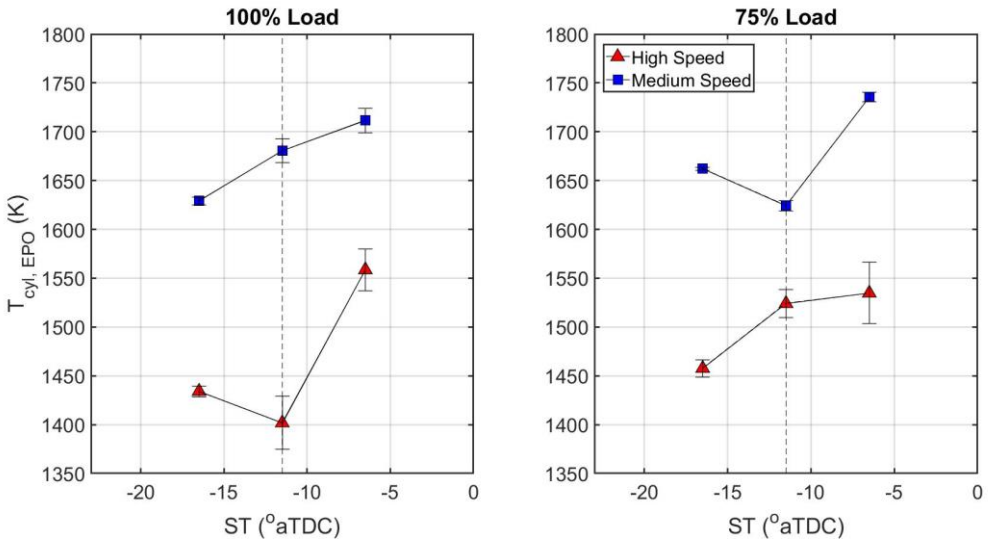

Figure 65: Trapped mixture temperature at EPO for different engine speeds, loads, and spark timings.

Figure 66 shows the relationship between engine-out NO_x emissions and TER for 450 RPM and 525 RPM. An exponential relationship can be seen between the two; that is, as the trapped mixture becomes richer, NO_x emissions increase exponentially. The dashed curves represent exponential curve fits for the two engine speeds. The scatter, especially at 525 RPM, can be attributed to the method used for slow speed emissions data collection. Emissions data were logged manually after being read from the

emissions bench. A closer exponential fit could have probably been achieved by logging the data electronically and averaging it over the data collection period – a capability that was not available at the time of running these experiments but has since been added to the engine test bench. It can be seen in Figure 66 that at a given TER value, more NO_x is emitted at high speed. This can be attributed to higher combustion temperatures at the same load resulting from reduced wall heat losses at high speed.

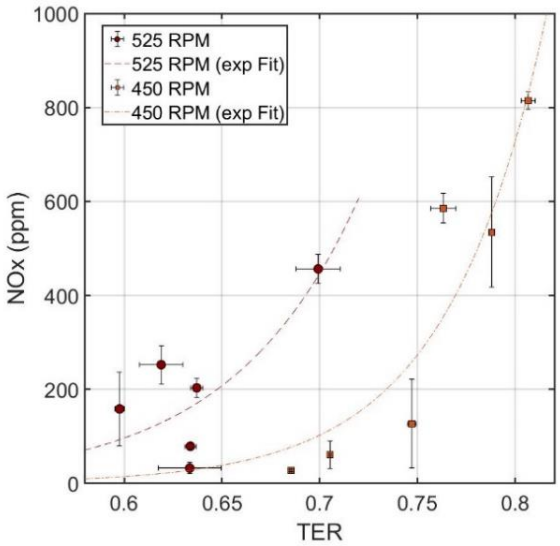

Figure 66: Engine-out NO_x emissions as a function of TER for two engine speeds. Dashed lines are exponential curve fits.

Figure 67 plots the burn duration (10% mfb to 90% mfb) at different engine operating points to illustrate the effects of dilution and flame reactivity on the laminar flame speed and consequently, on the burn duration. Dilution is the addition of a diluent gas, like products of combustion, in the combusting mixture that acts as a heat sink and lowers combustion temperatures. Mixture reactivity is a broad term used to describe a mixture's ability to carry a flame (its 'flammability'). The more reactive a mixture, the

faster is the propagation speed of flames traveling in it. An increase in dilution (as quantified by TRF) decreases the laminar flame speed and elongates burn duration, whereas an increase in mixture's reactivity (as quantified by TER) increases LFS and shortens the burn duration. These trends can be seen in Figure 68 in which burn duration is plotted against TRF and TER. There is a lot of scatter in the plots (particularly in the TER plot) because the burn duration changes calculated from rate of heat release analyses reflect the combined effects of changes in the combusting mixture's thermodynamic state and composition. A more systematic study of dilution and reactivity effects using chemical kinetics to isolate the contribution of each effect is presented in [86].

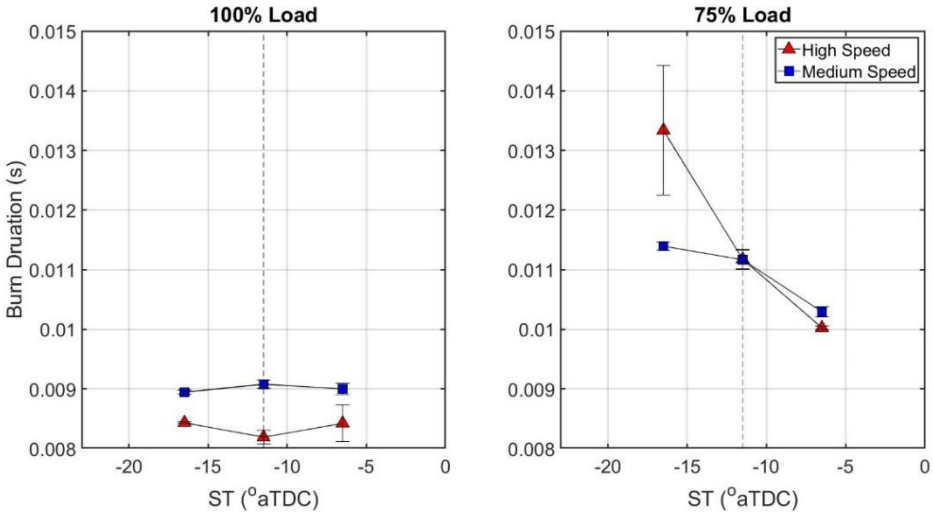

Figure 67: Burn duration (CA10 to CA90) for different engine speeds, loads, and spark timings.

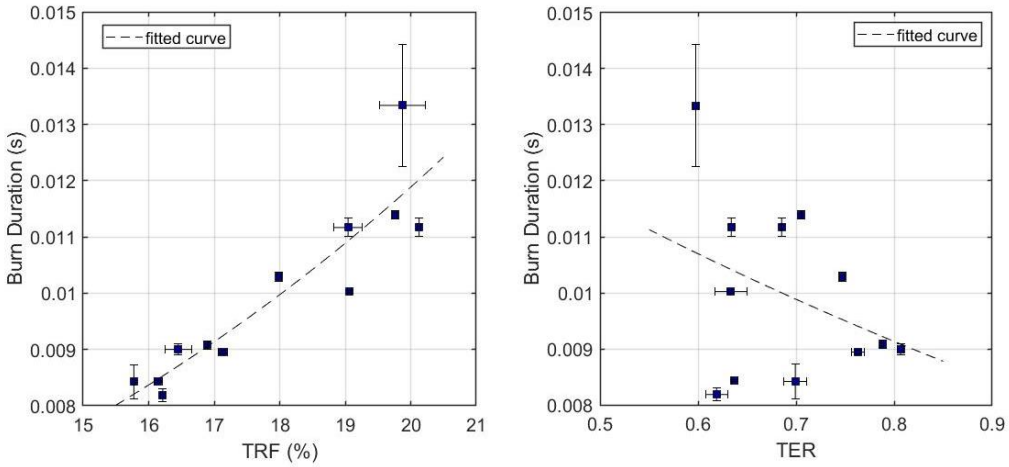

Figure 68: Burn duration as a function of TRF and TER.

Figure 69 shows the delivery ratio at different engine operating points. The delivery ratio is calculated by normalizing the delivered mass by the trapped mass. DR can be considered to be a measure of *excess*[11]air (over what is needed to deliver the trapped mass) that has to be supplied in order to scavenge the engine. An ideally scavenged engine would have a delivery ratio of unity. The quantity above 1 represents the excess air fraction that is needed to prepare the trapped mixture. The results show that the engine's DR decreases with engine speed, confirming that the scavenging process is more efficient at the rated engine speed.

[11] Refers to air needed above what would perfectly scavenge the engine; not to be confused with 'excess air' used in stoichiometry.

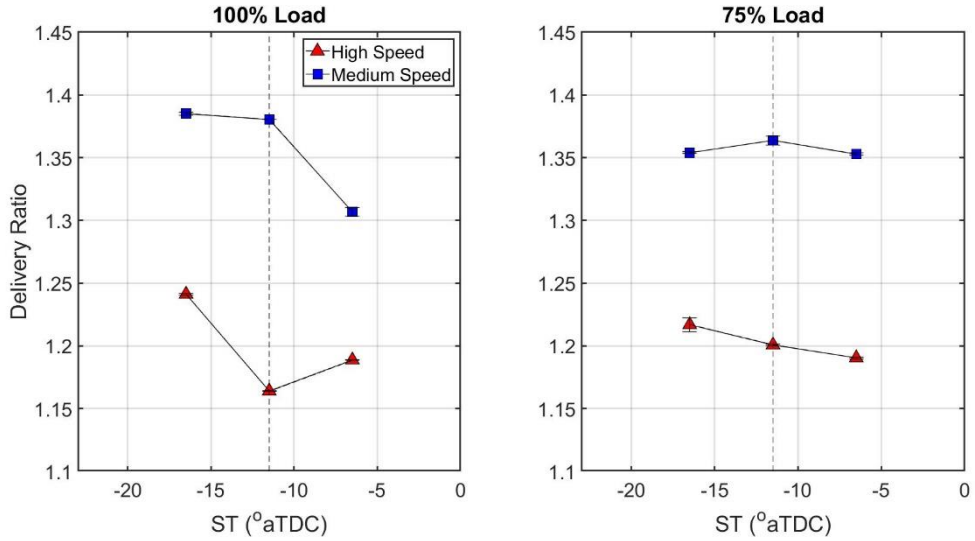

Figure 69: Delivery ratio at different engine speeds, loads, and spark timings.

Figure 70 maps the calculated scavenging and trapping efficiencies on a delivery ratio plot. The dashed lines in Figure 70 represent the scavenging and trapping performance as predicted by the non-isothermal perfect mixing model [38]. It can be seen that both the trapping and the scavenging performance of the engine being studied are better than the PM model predictions. This is a testament to the engine designers who, by optimizing port and piston deflector geometries and harnessing the potential of reflected waves, have improved the gas exchange performance of a cross-scavenged engine beyond the PM threshold; which is no meager task because cross-scavenged engines are notorious for having high short-circuiting and poor scavenging.

The scavenging efficiency of the engine is consistently over 80% and does not have a noticeable trend with delivery ratio, while trapping efficiency increases as the delivery ratio increases. The results show that for the current engine, excess scavenging

air does not significantly improve the residual gas removal process but it does substantially increase short-circuiting. Another way of interpreting the results is that beyond a certain DR threshold, any increase in air delivery does not scavenge additional residual gas, rather the additional air is short-circuited out resulting in a TE decrease.

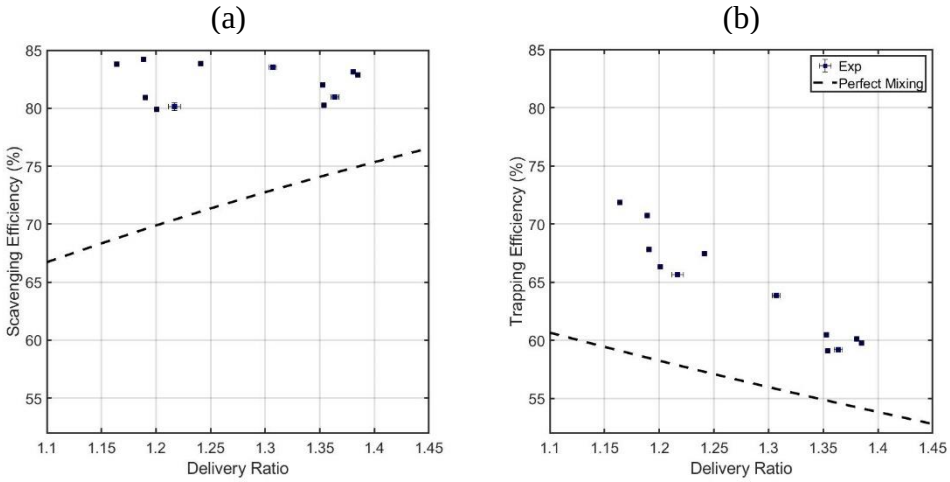

Figure 70: (a) Scavenging and (b) trapping efficiencies as a function of delivery ratio for the twelve stable engine operating points studied.

Figure 71(a) compares the trapped equivalence ratio with the overall equivalence ratio calculated using the delivered mass of fuel and air. The TER in the abscissa does not discount fuel slippage as has been done previously. It can be seen that the overall equivalence ratio is consistently leaner[12] than TER; primarily because of short-circuiting, and secondarily because of dilution by trapped residual air. The effects of the latter influence can be inferred from Figure 71(b) which shows the differences in TER when

[12] Overall ER is leaner that TER by 22% to 37%.

trapped residual air is not included in the calculations. Accounting for residual air results in slightly (4% to 9%) leaner TER values.

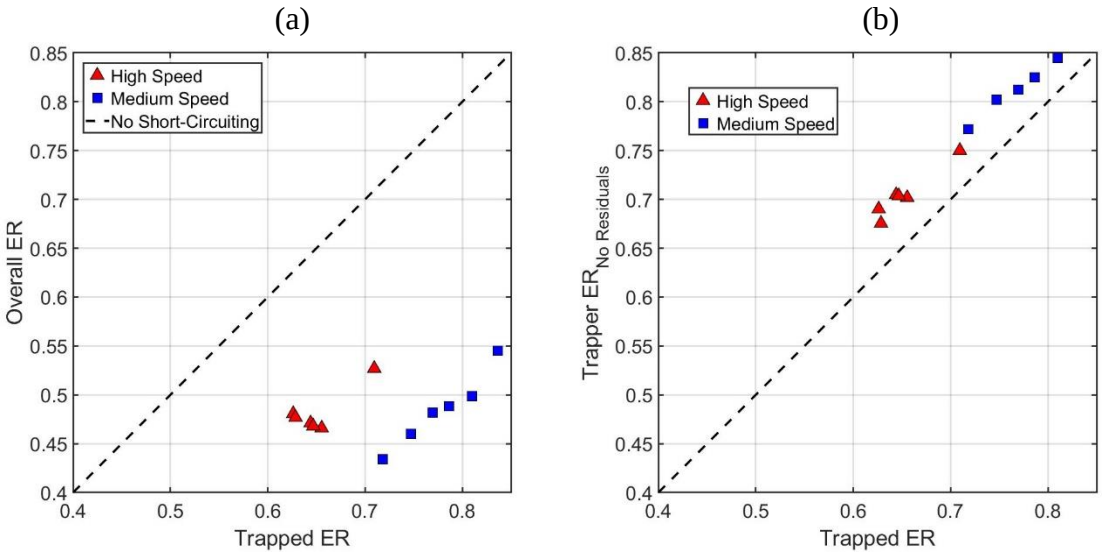

Figure 71: (a) Overall equivalence ratio and (b) trapped equivalence ratio without considering residual air plotted as a function of trapped equivalence ratio. Note: TER in the abscissa is slightly different from what has been presented above in that it is not corrected for combustion inefficiencies.

5.4. Scavenging Model Results

All inputs needed for validating the simple scavenging model are available either directly from experiments or calculated from experimental measurements. These parameters are listed below (calculated parameters are italicized):

- Engine speed
- Fuel flow rate
- *Air flow rate*
- Intake temperature
- Exhaust temperature

- *Residual gas temperature* (approximated as cylinder temperature at EPO)
- Intake pressure (approximated as average intake pressure from IPO to IPC)
- Exhaust pressure (approximated as average exhaust pressure from EPO to EPC)

These parameters are then used to assess the performance of the hybrid model by comparing the estimated and experimentally obtained trapped mixture state values, as quantified by the following parameters (calculated parameters are italicized):

- Cylinder pressure at EPC
- *Cylinder temperature at EPC*
- *Trapped mixture mass*
- *Scavenging efficiency*
- *Trapping efficiency*
- *TER*

In order to calculate the trapped mixture state using the hybrid model, a θ_{PM} point has to be selected. Its value could range between 0^o aEPO, which means all of the post-blowdown gas exchange happens in a PM manner, and 120^o aEPO, which means that the post-blowdown gas exchange happens entirely in a PD manner. To gauge the ability of the model to accurately predict the trapped mixture state, a sensitivity study at four θ_{PM} values - 0 , 40, 60 and 80^o aEPO - is performed for 100% load and standard spark timing cases at high and medium speeds. The results, presented in Figure 72 and Figure 73, respectively, show the changes in cylinder air and residual mass, temperature, pressure, and residual gas fraction during gas exchange (EPO to EPC). The final values of all of

these parameters at trapping are compared to corresponding experimental values, shown by the filled markers at 240 CAD. The only exception to this norm is the temperature sub-plot in which the filled markers at EPC show various experimentally obtained temperatures during or before gas exchange. This is done to show how different exhaust temperature measurements (e.g. peak high speed exhaust temperature and slow speed exhaust temperature) compare to each other.

It can be seen in Figure 72 that: (1) the θ_{PM} sweep produces a healthy spread in the trapped mixture parameters, especially for trapped mass and TRF, which are the two most important parameters in determining TER, and (2) with a θ_{PM} value of 60^{o} aEPO (180^{o} aTDC), the trapped mass and residual fraction estimates are acceptably accurate. These results are encouraging and demonstrate that the scavenging model is capable of accurately predicting scavenging at high speeds if the right θ_{PM} value is chosen. Results for the 450 RPM case (Figure 73), however, are less encouraging. The predicted trapped air mass is too high even when the high-SE PD stage is disabled. As a result, the TER values are too lean even though TRF estimates can be close to experimental values by the happenstance of the trapped air and residual masses being proportionally incorrect. The results suggest that the PM stage, which is the low-SE stage in the model, is not sufficiently inefficient to account for scavenging inefficiencies observed in the real engine at medium speed operation. This problem is not noticed at high speed because there is significantly less short-circuiting (Figure 58), which is majorly responsible for the low trapped air mass.

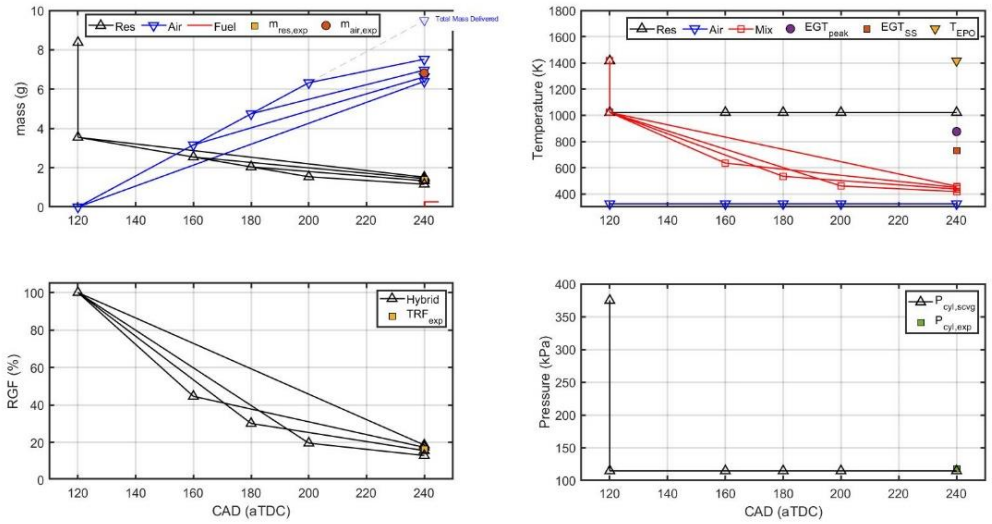

Figure 72: Scavenging estimates for (clockwise) cylinder mass, temperature, pressure, and residual gas fraction for four different θ_{PM} values at standard spark timing, 100% load, and 525 RPM.

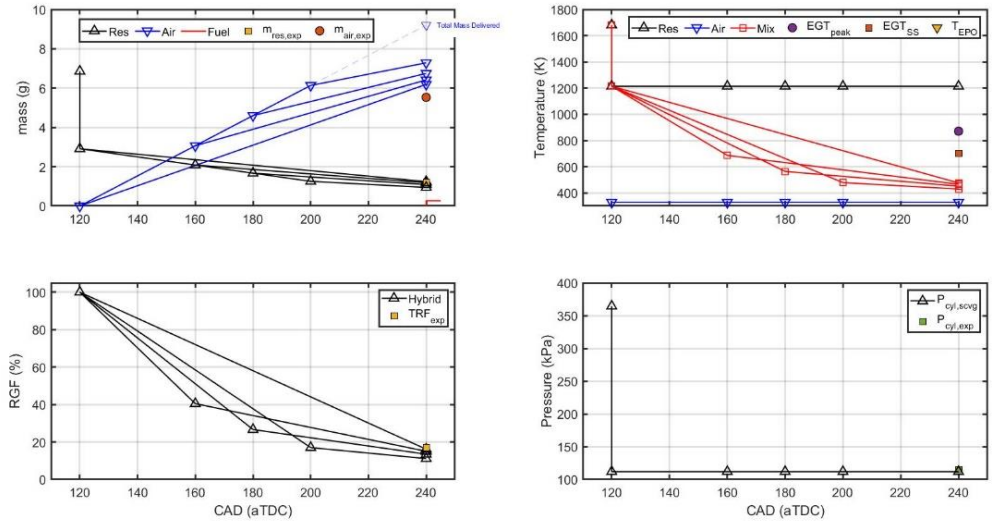

Figure 73: Scavenging estimates for (clockwise) cylinder mass, temperature, pressure, and residual gas fraction for four different θ_{PM} values at standard spark timing, 100% load, and 450 RPM.

5.4.1. Scavenging Model Improvements

To overcome the scavenging model's limitations at low TE points, a short-circuiting zone is added to the model in order to account for the decreased trapping performance. It is assumed that after the initial blowdown stage, a simultaneous perfect displacement and short-circuiting stage takes place, followed by a simultaneous perfect mixing and short-circuiting stage. This is realized by splitting the incoming air stream, which has a constant flowrate and temperature, into two branches: one feeding the perfect displacement or the perfect mixing zone (depending on the stage) and the second branch feeding the short-circuiting zone. The amount of incoming flow going to the short-circuiting stream is defined by the short-circuiting fraction 'SCF', which is a user prescribed input and a second tunable knob for the model. The first one being, θ_{PM}. The model is now a two-zone, three-stage one with the same three stages as before (blowdown, PD, and PM) but the PD and PM stages now have a second zone - the short-circuiting zone. Each of the two non-short-circuiting zones can be modeled exactly as before but by using only the non-short-circuited air flow rate, which is calculated from SCF. Figure 74 shows a schematic of the two-zone model during the perfect mixing stage. The idea of having combined short-circuiting and scavenging stages is borrowed from Wallace and Dang [12] who had a combined isothermal perfect mixing and short-circuiting stage as well, as was discussed previously.

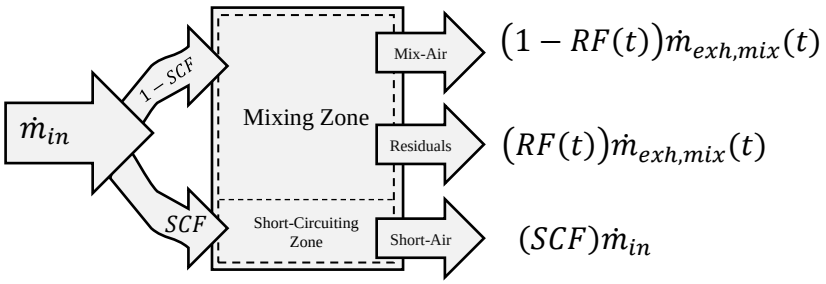

Figure 74: Schematic showing the two scavenging zones during the perfect mixing stage.

The volume of the short-circuiting zone (V_{short}) is determined indirectly during the PD stage by the choice of the θ_{PM} time. It is assumed that no short-circuiting actually takes place during the PD stage. Instead, the short-circuiting zone is primed for air slippage during this stage such that at the end of the PD stage, all residual gases in the short-circuiting zone have been perfectly displaced by fresh air, leaving the fresh air on the verge of slipping out at θ_{PM}. When the PM stage starts, the primed short-circuiting zone starts hemorrhaging air at a constant flow rate (SCF. $\dot{m}_{in}$), temperature (intake temperature), and pressure (average manifold pressure). The start of short-circuiting with the mixing stage is based on the observations from Figure 48, whereby short-circuiting takes place after the initial displacement scavenging process. The following schematic illustrates flow through the short-circuiting zone during the PD and PM stages.

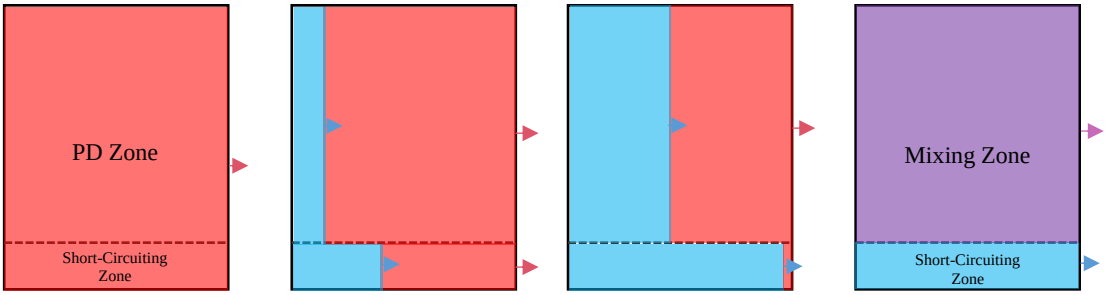

Event: PD(start)	During PD	PD(end) - δt	PM(start) and during
State: [B]	[B] to [C]	Approaching [C]	[C] to [D]

Figure 75: Development of short-circuiting zone over the perfect displacement and perfect mixing stages. Red regions represent combustion products and blue regions represent air.

Mathematically, the PD stage (Process B to C), is represented as:

$$m_{r,cyl}(C) = m_r(B) - \frac{T_a}{T_r}[\dot{m}_{in}SCF + \dot{m}_{in}(1 - SCF)]t_{B\to C} \qquad 36$$

The first term in square brackets represents residuals exhausted from the short-circuiting zone and the second term represents the residuals exhausted from the would-be mixing zone. Air flows into the cylinder during the PD stage are handled similarly (equation 37). The resulting mass in the short-circuiting zone (subscript 'short') is given by equation 38 and its volume by equation 39.

$$m_{a,cyl}(C) = [\dot{m}_{in}SCF + \dot{m}_{in}(1 - SCF)]t_{B\to C} \qquad 37$$

$$m_{\text{short-circuiting zone}}(C) = \dot{m}_{in}(1 - SCF)t_{B\to C} \equiv m_{short} \qquad 38$$

$$V_{short} = \frac{m_{short}(C)RT_a}{p_c} \quad (39)$$

Equations 40 to 43 describe the flow in the mixing (subscript 'mix') and short-circuiting zones during the PM stage.

$$V_{mix} = V_{trap} - V_{short} \quad (40)$$

$$m_{r,cyl}(D) = m_{r,mix} = m_{r,cyl}(C)\exp\left(-\left[\frac{\dot{m}_{in,mix}\ R\ T_a}{p_c V_{mix}}\right] t_{C\to D}\right) \quad (41)$$

$$m_{a,mix}(D) = m_{a,mix}(C)\exp\left(1-\left[\frac{\dot{m}_{in,mix}\ R\ T_a}{p_c V_{mix}}\right] t_{C\to D}\right) \quad (42)$$

$$m_{a,cyl}(D) = m_{a,mix}(D) + m_{a,short}(D) = m_{a,mix}(D) + m_{a,short}(C) \quad (43)$$

In order to limit the degrees of freedom of the scavenging model to one, the SCF value is selected such that the calculated trapping efficiency matches experimental measurements. To avoid any confusion between the two similar sounding parameters, x_{short} and SCF, their definition are restated here. x_{short} is the fraction of the exhaust stream that is made up of fresh air. This includes air leaving the cylinder as a part of a short-circuiting stream as well as air exiting as a residual-gas-air mixture. SCF, on the other

hand, only comprises the fraction of delivered air lost by pure slippage. Consequently, SCF values are smaller than the corresponding x_{short} values.

The revised scavenging model looks similar in its construction to two single-stage multi-zone models developed by Benson and colleagues [36, 40]. These are shown in Figure 76. The proposed model is superior to the first model (Figure 76a) because it does not assume isothermal gas exchange, and it is easier to use than the second model (Figure 76b) because it requires 2 calibration parameters instead of 5.

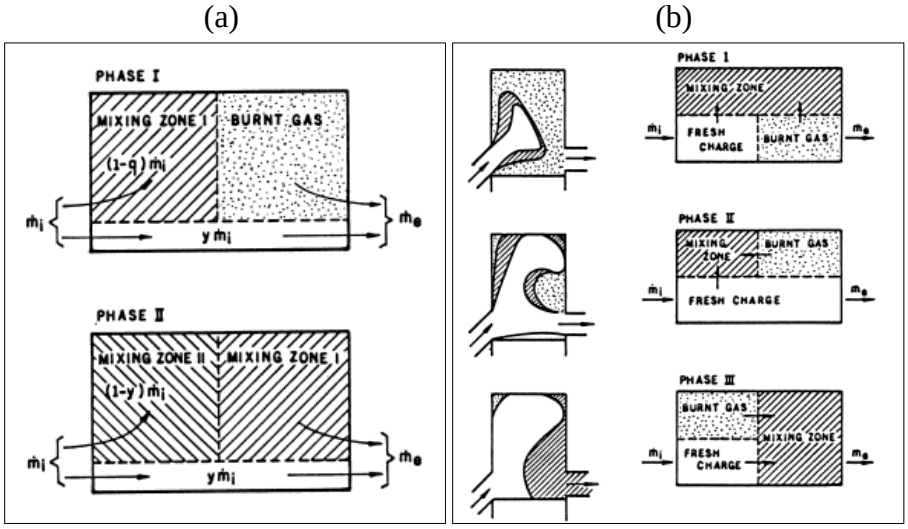

Figure 76: (a) Isothermal two-zone model of Benson and Brandham [40], and (b) non-isothermal three-zone model of Benson [36].

5.4.2. Revised Scavenging Model Results

A sensitivity analysis is performed on the two-zone model prior to using it to estimate trapped mixture state for all operating points. The point selected for this exercise is the 450 RPM, 100% load, standard spark timing point; the same as Figure 73 where the trapped air mass was too low to be estimated by the single-zone model. Figure 77 and Figure 78 show the effects of changing SCF values on the trapped mixture mass, temperature, residual gas fraction, and pressure. Figure 77 is a magnified version of the first quadrant of Figure 78. An SCF sweep from 0% (no short-circuiting) to 100% (no PM, all short-circuiting) is performed at a fixed θ_{PM} point (40^{o} aEPO). The corresponding fractions of non-short-circuiting zone volume are also shown in Figure 77. The big swing in the trapped mixture properties, especially mass, demonstrate that by choosing appropriate SCF and θ_{PM} values, experimental results can be recreated. The quality of these matches for all scavenging parameters of interest will be evaluated next.

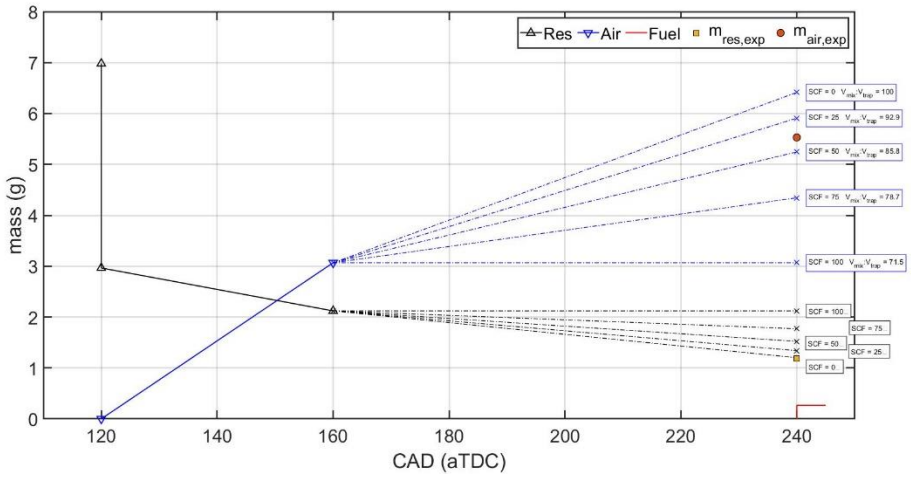

Figure 77: Effect of changing SCF on trapped mass for MS-HL-0.

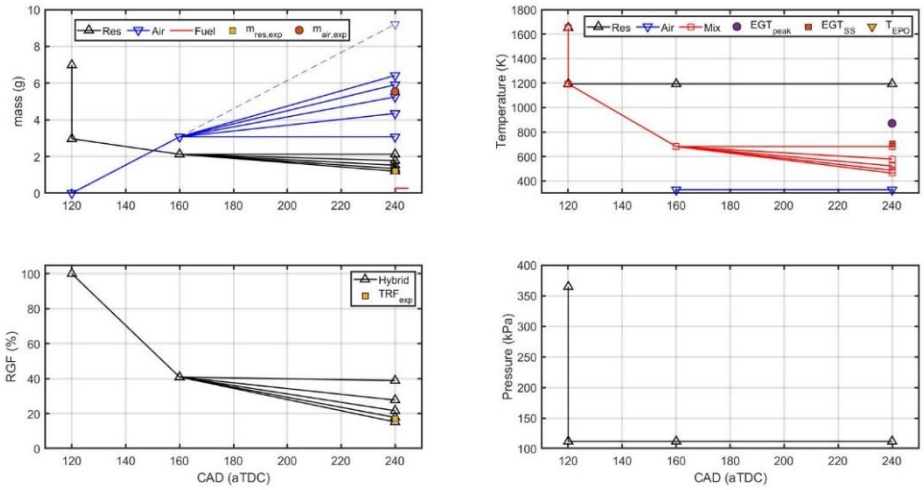

Figure 78: Effect of changing SCF on trapped mass, temperature, residual fraction and pressure at θ_{PM} of 40 °aEPO for 450 RPM, 100% load, and standard ST.

Figure 79 shows the effects of SCF on trapped mixture mass at four different θ_{PM} timings (0, 40, 60, and 80° aEPO). The effects of short-circuiting (decrease in trapped air mass and increase in trapped residual mass) increase as the PM stage is prolonged.

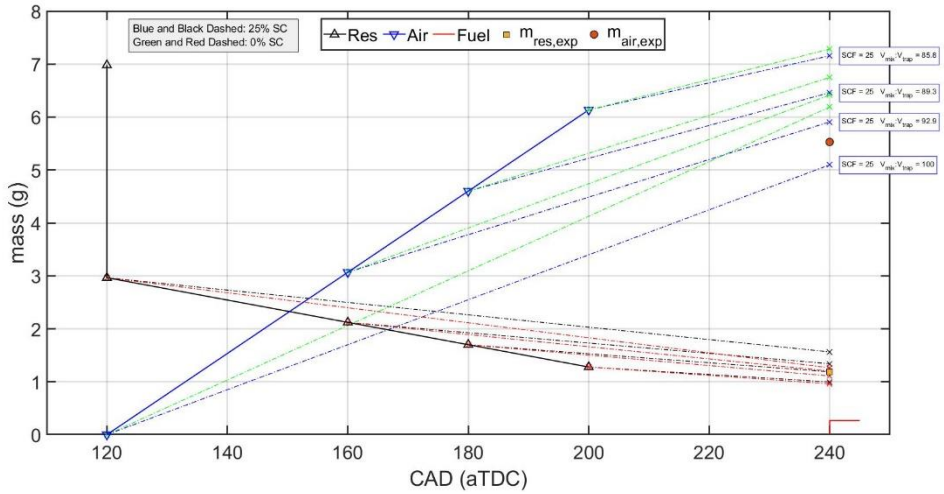

Figure 79: Effect of changing SCF on trapped mass, temperature, residual fraction and pressure at four different θ_{PM} timings for 450 RPM, 100% load, and standard ST. Dashed green and red curves show results for SCF = 0%. Dashed blue and black curves show results for SCF = 25%.

Having demonstrated adequate resolution of the scavenging model, experimental trapped mixture results are estimated by using SCF calculated to match experimental TE values, and adjusting θ_{PM} values to get experimental and estimated trapped air to match. Trapped air mass is selected as the property to tune the model against because of its large influence on the trapped mixture composition. Table 4 lists the final θ_{PM} values that are selected to get good trapped air mass matching, and SCF values that produce good TE matching.

Operating Point	θ_{PM} (CAD aEPO)	SCF (%)
HSHL-5A	45.2	17.4
MSHL-5A	0	17
HSTQL-5A	23	15
MSTQL-5A	0	20
HSHL-0	59	16
MSHL-0	0	18
HSTQL-0	26	15
MSTQL-0	0	20
HSHL-5R	52	15.6
MSHL-5R	18	15.9
HSTQL-5R	40	15.9
MSTQL-5R	0	19

Table 4: θ_{PM} and SCF values used to match trapped air mass.

Figure 80 compares experimental and hybrid model estimated trapping efficiencies. At advanced spark timing and medium speed, TE is overestimated because SCF had to be decreased beyond the calculated values to get the trapped air mass to match. This was needed because the PM stage could not be prolonged any further (θ_{PM} = EPO). The resulting trapped air mass estimates are shown in Figure 81.

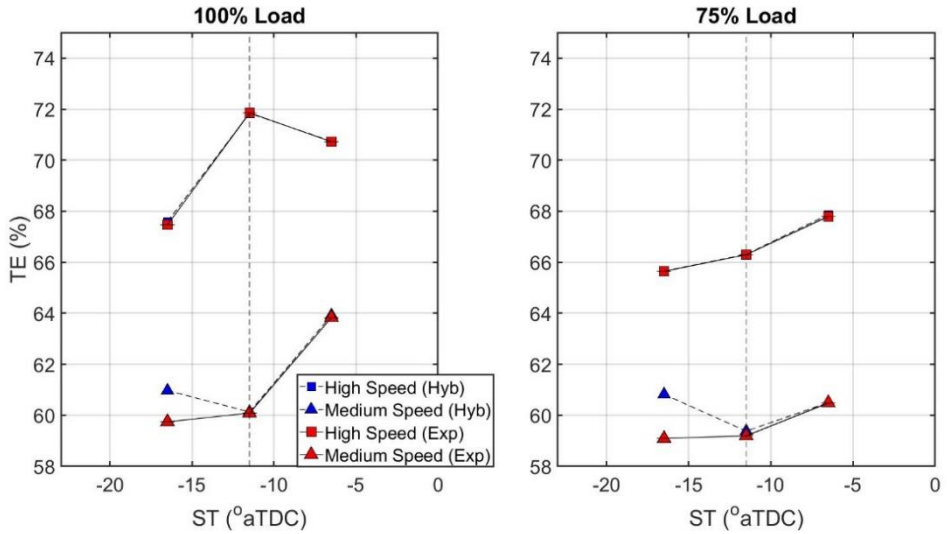

Figure 80: Experimental and hybrid model estimated trapping efficiency at different engine speeds, loads, and spark timings.

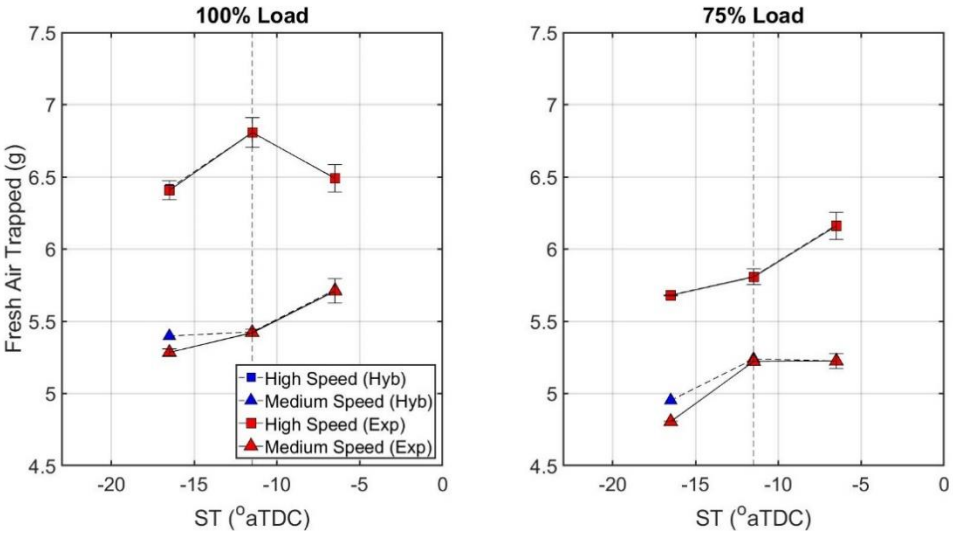

Figure 81: Experimental and hybrid model estimated trapped air mass at different engine speeds, loads, and spark timings.

Figure 82 to Figure 86 compare (in order) the estimated and experimental trapped residual mass, total trapped mass, trapped residual fraction, trapped equivalence ratio, and cylinder pressure at EPC. Overall, the high speed estimates are more accurate

than the medium speed ones. In order to get the trapped air mass to match, errors are introduced in the trapped residual estimates (Figure 82) but the absolute errors are minor (less than 0.3 g).

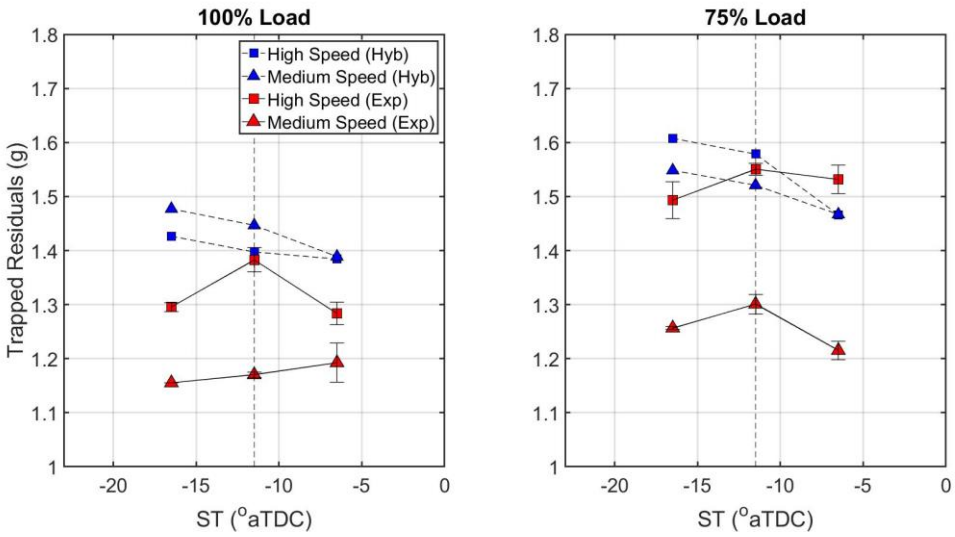

Figure 82: Experimental and hybrid model estimated trapped residual mass at different engine speeds, loads, and spark timings.

The estimated total trapped mass match experimental results satisfactorily (Figure 83). The matching for high speed cases is excellent while that for medium speed cases is not as good; primarily because of errors in trapped residual mass. Because of errors in trapped residual mass, TRF results (Figure 84) have errors as well, especially at medium speed. The results are, however, considered acceptable because of the relatively small contribution of errors in the minor trapped mixture constituent (the residual gases) on the overall trapped mixture state results.

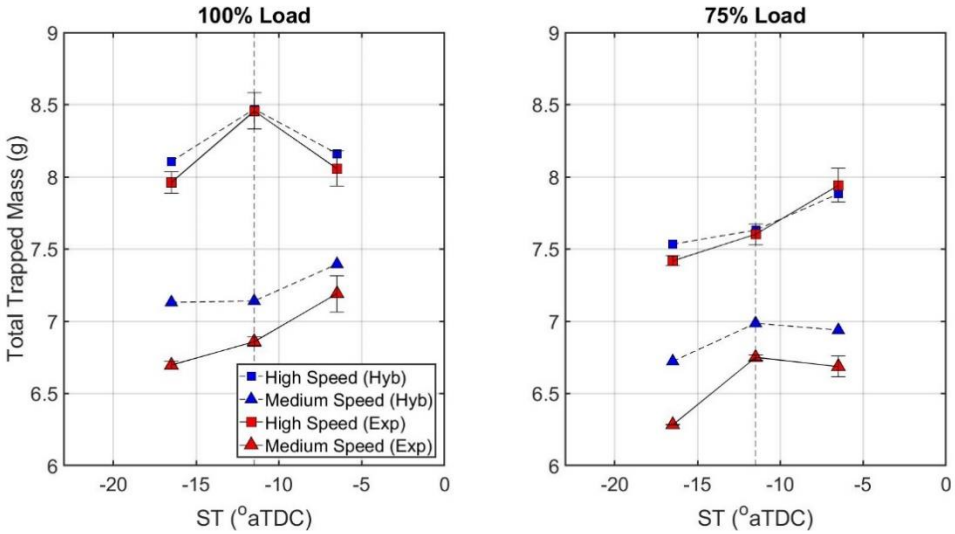

Figure 83: Experimental and hybrid model estimated total trapped mass at different engine speeds, loads, and spark timings.

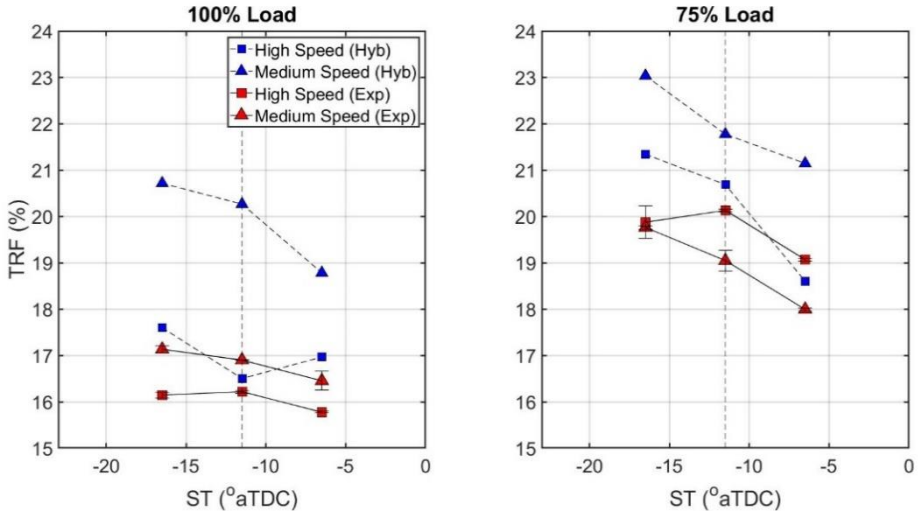

Figure 84: Experimental and hybrid model estimated trapped residual fraction at different engine speeds, loads, and spark timings.

Estimates for the trapped equivalence ratio, which is the main control parameter of interest for the current study, are acceptably accurate (Figure 85). The matching is excellent at high speeds. At medium speeds, TER is slightly under-estimated because of

the over-estimation of trapped residual gas mass. The effects of the over-estimation of TRF are minor because only a small fraction (~25%) of the trapped residuals is composed of air. The remainder is made up of oxidized combustion products. The TER results show that the scavenging model can be used for estimating TER with reasonable accuracy using only out-of-cylinder sensors.

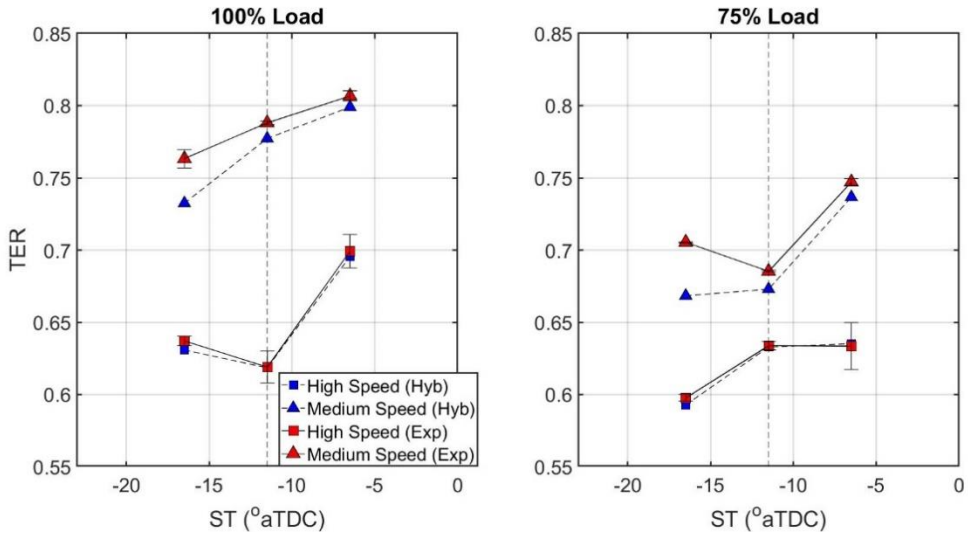

Figure 85: Experimental and hybrid model estimated trapped equivalence ratio at different engine speeds, loads, and spark timings.

For the sake of completeness, estimated and experimental cylinder pressures at trapping are shown in Figure 86. Accurate estimation of cylinder pressure is not critical from an engine control perspective. Estimated cylinder pressures, which are calculated by averaging intake and exhaust pressure during their respective port open periods, are within 6 kPa of the experimental cylinder pressure at EPC, making them an acceptable approximation.

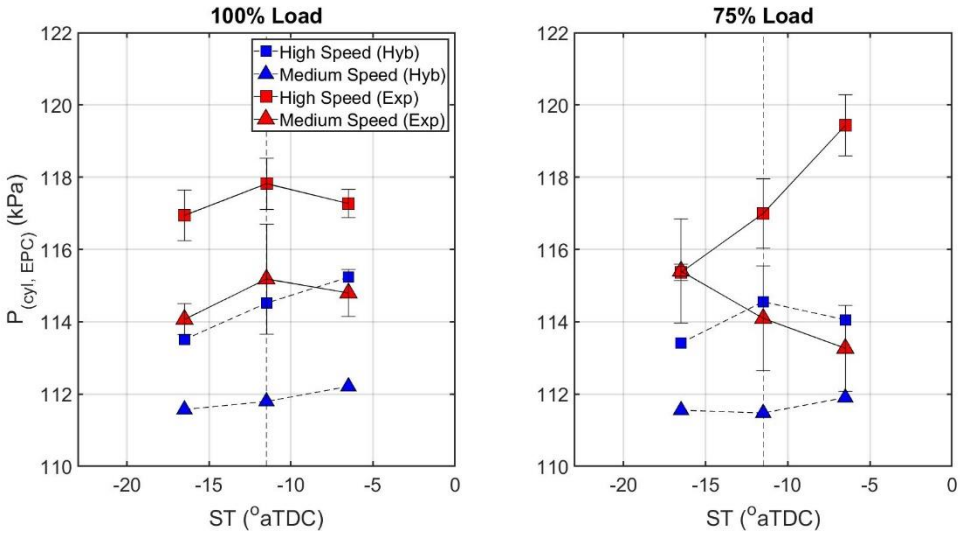

Figure 86: Experimental and hybrid model estimated trapped cylinder pressure at different engine speeds, loads, and spark timings.

Figure 87 shows the θ_{PM} timings used for the validation exercise at different engine operating points and Figure 88 shows the timings as a function of corresponding delivery ratios.

θ_{PM}, which is the length of the PD stage, increases as engine speed and load increase. The results can be used to explain actual scavenging changes at different engine operating points that are being reflected as changes in the duration of the two idealized scavenging stages. The prolonged PD stage at high load can be attributed to a strong blowdown process which removes residuals in a PD type manner. The lengthening of this stage with increasing speed can be attributed to the overall more efficient scavenging at high speed resulting from (1) less time available for mixing and short-circuiting, and (2) favorable reflected exhaust wave timings. These results are in

line with the high speed exhaust CO_2 concentration results shown in Figure 48. The CO_2 exhaust wave results showed a larger PM-short-circuiting hump at medium speeds and a larger PD hump at high speeds. Benson et al. [90] reported similar results from their 1D scavenging modeling work for a loop scavenged engine when they said, "At low speeds the scavenge [*sic*] process is a combination of mixing and displacement, whilst at high speeds it tends to displacement." The longer PM stage at the medium speed cases can provide a secondary explanation for the improved engine stability at these speeds. The primary explanation being their high TER. A long PM stage implies that the post-scavenging (trapped) mixture is hotter, which increases the likelihood of successful ignition by decreasing the ignition delay.

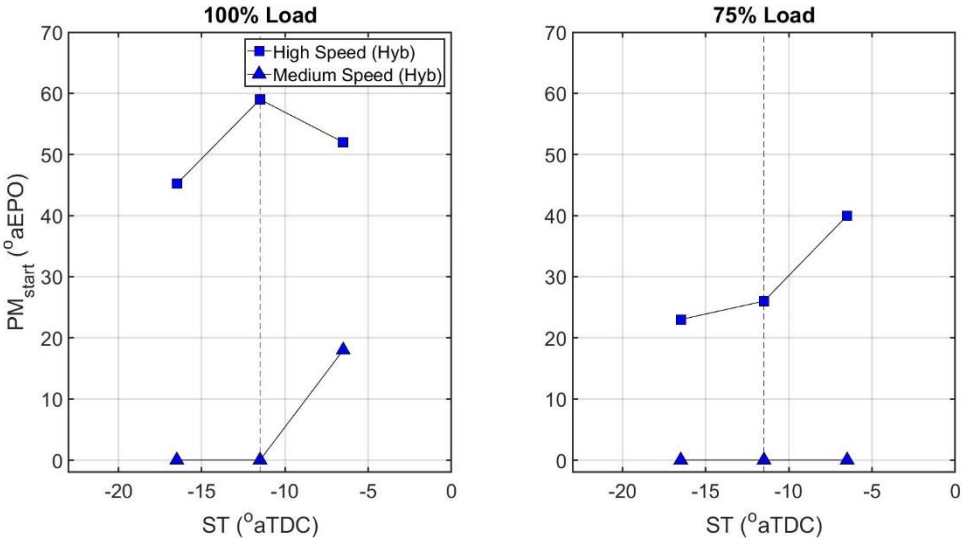

Figure 87: Hybrid model estimated θ_{PM} timings at different engine speeds, loads, and spark timings.

As the delivery ratio (fraction of excess scavenging air) increases, scavenging becomes less efficient and as a result, PD stage shrinks. This can be seen in Figure 88. The θ_{PM} trends are consistent with Blair and Ashe's computational work [83] where they used a two-stage (PD followed by PM) model.

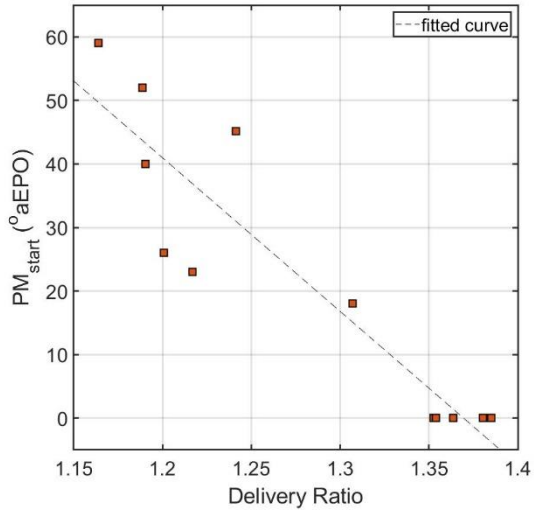

Figure 88: Hybrid model estimated θ_{PM} timings as a function of delivery ratio.

Lastly, results from the scavenging model are used to illustrate the difference in total fresh air loss during gas exchange (x_{short}) compared to the fraction that is lost as a pure short-circuiting stream (SCF). The comparison is presented in Figure 89 as a mass fraction of the total exhaust flow. Almost half of the exhausted air is lost to pure short-circuiting and the remainder is lost as an air-residual mixture. These numbers are similar to those reported by Dedeoglu [51] from a visualization study for a motored engine in which 13% and 41% of the delivered air were, respectively, lost to pure short-circuiting and short-circuiting and mixing.

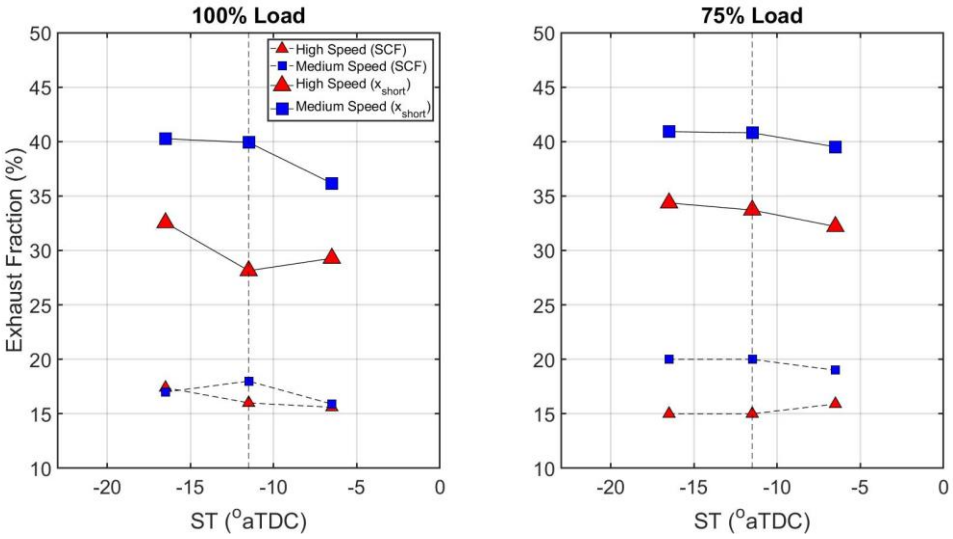

Figure 89: Experimental x_{short} and hybrid model estimated SCF at different engine speeds, loads, and spark timings.

6. GT-POWER RESULTS

The *GT-Power* model presented in Chapter-4, upon which the original hybrid scavenging model was based, is modified to simulate direct-injected engine operation at the four standard spark timing operating points from the scavenging study test matrix (Table 2). The nomenclature used to reference the four cases studied is of the following form: xS-yL-0, where x can be high (H) or medium (M) speed, y can be high (H) or three quarters (TQ) load, and 0 refers to the standard spark timing (11.5^{o} bTDC).

The simulation results are presented in this chapter to assess the ability of flow simulation models to simulate gas flow in two-stroke engines and the suitability of using such models for tuning the hybrid model for engines where experimental cylinder CO_2 concentration data is not available. Of particular interest is to investigate the *GT-Power* model's ability to capture interactions between fresh and retained cylinder gases. These interactions determine the trapping and scavenging performance of the engine, as quantified by scavenging and trapping efficiencies, respectively.

6.1. Modeling Methodology

Air flow across the cylinder is governed by gas dynamic phenomena taking place between the engine cylinder, intake, and exhaust systems. Composition of the trapped mixture formed at the end of gas exchange, however, depends on gas dynamics as well as the interactions between fresh and retained gases. The nature of these interactions is

prescribed by *GT-Power's* scavenging sub-model objects *EngCylScav* or *EngCylScavFunction*. As mentioned in Chapter 3, the *EngCylScavFunction* object generates a scavenging curve using the following three user prescribed parameters: (1) transition point[13], (2) anchor point[14], and (3) shape factor[15], whereas the *EngCylScav* object needs tabulated residual fraction values.

For an accurate two-stroke model, both the gas dynamic results (e.g. mass of air delivered and trapped) and scavenging results (e.g. TRF and TER) should match experimental measurements. These criteria are used to test the performance of the *GT-Power* model. Three modeling approaches are tested. The first two approaches use the model's entire domain as was described in Chapter 3, that is, everything downstream of the scavenging chamber, including the exhaust system. Experimentally measured time-resolved scavenging chamber pressure serves as the upstream boundary condition and atmospheric pressure is used as the downstream end-of-exhaust boundary condition. The third approach was implemented after the results from the first two approaches were found to be unsatisfactory. This approach restricts the modeling domain to the engine cylinder and uses experimental time-resolved exhaust pressure for the downstream boundary condition. The first two approaches present a more comprehensive setup of the engine and need one less experimental boundary condition compared to the third

[13] This is the cylinder residual fraction when PD type of scavenging ends.
[14] This is the cylinder residual fraction when exhaust residual fraction is 0.5.
[15] A parameters that defines the shape of the scavenging curve generated through (1,1), transition point, anchor point, and (0,0).

approach. The difference between the first two approaches is the choice of the scavenging curves. Approach I uses arbitrary scavenging profiles while approach II uses scavenging profiles derived from hybrid model results.

The *GT-Power* model is tuned to try and satisfy the testing criteria mentioned above. Table 5 provides a summary of the tuning parameters used. It also lists the operating points for which the parameters are changed and the approaches to which the respective parameters are applicable. Most of these 'knobs' are interconnected and have to be turned in a complementary manner to minimize overall error. A brief description of how some of these parameters are tuned is presented below:

- Exhaust system parameters: Exhaust system geometry (muffler tank dimensions, pre/post-muffler piping dimensions) and wall temperatures have strong effects on the scavenging behavior of the engine. These effects can be sensed as changes in TRF, exhaust pressure wave phasing and amplitude, and trapped air mass. The dimensions are adjusted while staying close to actual dimensions to get good exhaust wave matching. After initial tuning for HS-HL-0, no changes are made across different operating points.
- Fuel flow rate: This is controlled by adjusting the fuel metering valve opening to ensure that sufficient chemical energy is available to achieve required IMEPs. The fuel valve opening is adjusted for almost all operating points.
- Combustion parameters: Combustion parameters that govern flame initiation (flame kernel growth multiplier and initial spark size) and propagation (Taylor

length scale multiplier and turbulent flame speed multiplier) are adjusted to phase the release of chemical energy appropriately so as to get peak and expansion pressures to match experimental results. The initial spark size is held constant across all operating points and minor adjustments are made to the Taylor length scale multiplier for some cases.

- Wall heat transfer: For some of the operating points, the cylinder wall heat transfer multiplier is adjusted between 0.9 and 1.2 to improve the pressure curve matching.

Tuning Parameter	Operating Points	Applicable to Approaches
Intake port discharge coefficients	HS-HL-0	I, II, III
Exhaust port discharge coefficients	Multiple	I, II, III
Scavenging parameters	All	I, II, III
Exhaust system dimensions and wall temperature	HS-HL-0	I, II
Spark size	HS-HL-0	I, II
Flame kernel growth multiplier	HS-HL-0	I, II
Taylor length scale multiplier	Multiple	I, II
Turbulent flame speed multiplier	HS-HL-0	I, II
Wall heat transfer coefficient multiplier	Multiple (minor changes)	I, II, III
Fuel flow rate	All	I, II, III

Table 5: Tuning parameters used in the GT-Power model.

6.2. Approach I: Using Arbitrary Scavenging Profiles

This approach serves as a baseline assessment of the *GT-Power* model's accuracy. In this approach, the exhaust discharge coefficient and scavenging sub-model parameters are adjusted to match the mass of air delivered and trapped, while allowing the mass of the trapped fuel and residuals to float. The expectation is that if the model is accurate, the simulated mixture composition (as quantified by TRF and TER) would also

match experimental results. The results that follow show that this is not the case. The modeling domain for this approach includes the exhaust system.

6.2.1. Validation

The principal parameter used for validating *GT-Power* simulation results is the in-cylinder pressure. This is done by comparing average experimental pressure and simulated pressure traces. These results, shown in Figure 90, exhibit excellent matching between experimental and simulated results. The translucent black curves in the figures represent the $\pm$ 1 standard deviation envelope for experimental measurements.

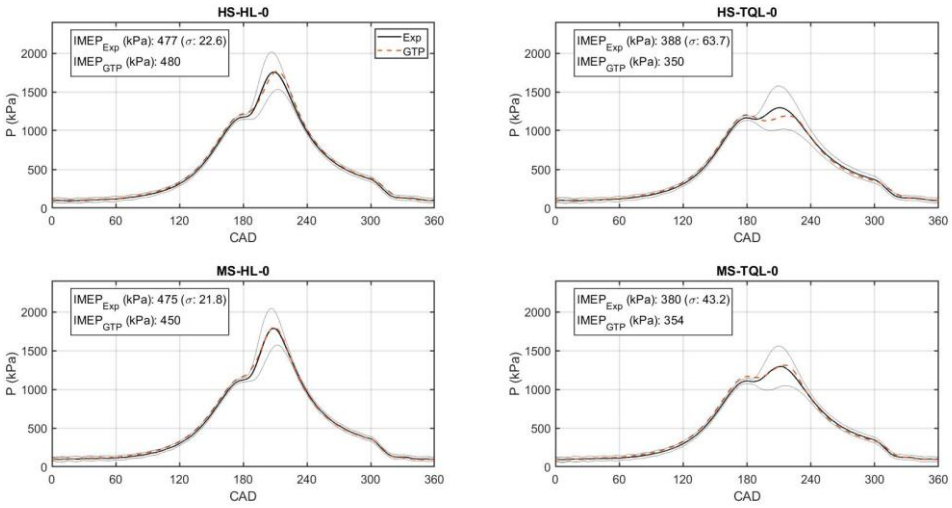

Figure 90: Experimental and GT-Power simulated cylinder pressure at standard spark timing for different speeds and loads (Approach I).

In addition to the cylinder pressure, emphasis is given to having reasonable simulated exhaust pressure. Correctly modeling various exhaust wave features is

important because they directly impact mass flow calculations across the exhaust port. Figure 91 shows the simulated and experimental exhaust waves from EPO to EPC for the standard spark timing cases. The model successfully captures the macro-features of the exhaust wave; namely, the blowdown incident wave, the reflected expansion wave with sub-atmospheric pressures following the blowdown wave, and the reflected compression wave around IPC (222 CAD). Some of the micro-features like the small compression wave around 170 CAD are not captured. Overall, the simulated exhaust pressure results are deemed acceptable.

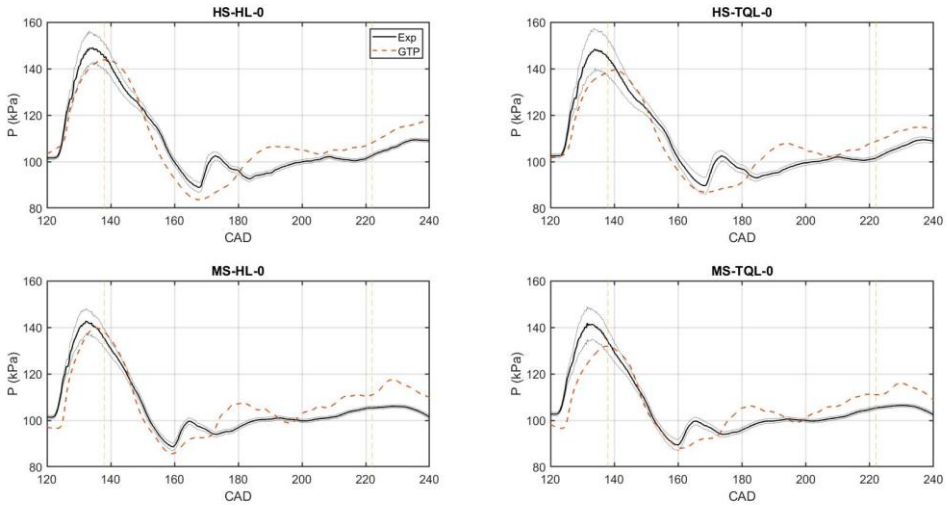

Figure 91: Experimental and GT-Power simulated exhaust pressure from EPO to EPC at standard spark timing for different speeds and loads (Approach I).

Lastly, the air flow parameters mentioned earlier are matched by tuning the exhaust discharge coefficient and scavenging parameters. The results are shown in Figure 92 and Figure 93 for the mass of air that is delivered and trapped, respectively.

The results are acceptable for all four cases. The resulting trapping efficiency results, shown in Figure 94, also match reasonably well with experimental data.

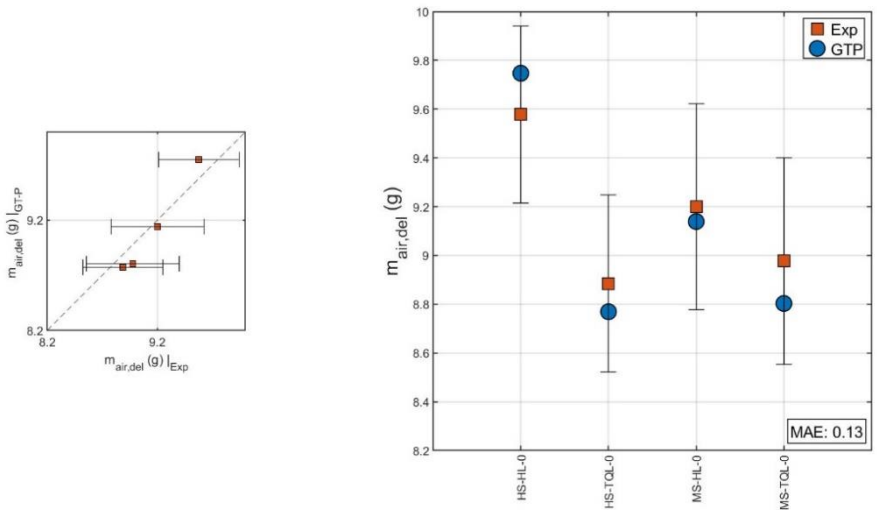

Figure 92: Experimental and GT-Power simulated mass of air delivered per cycle at different speeds and loads at standard spark timing (Approach I).

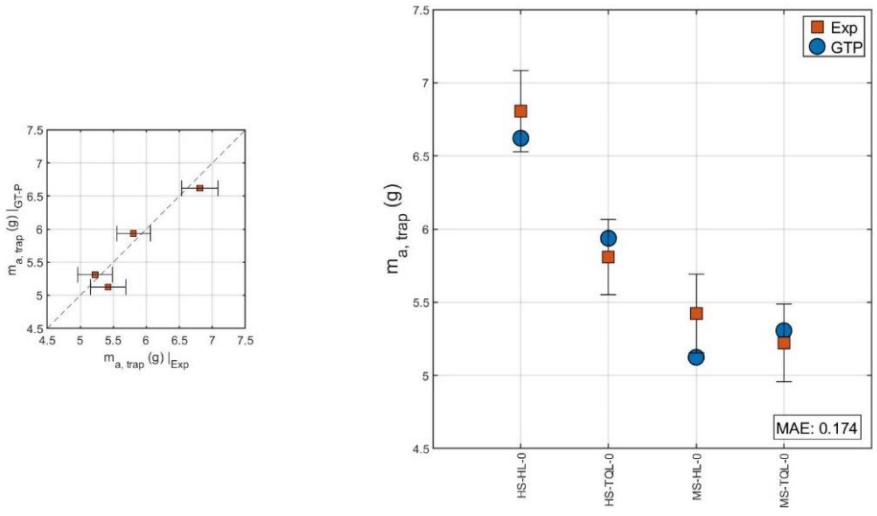

Figure 93: Experimental and GT-Power simulated mass of air trapped per cycle at different speeds and loads at standard spark timing (Approach I).

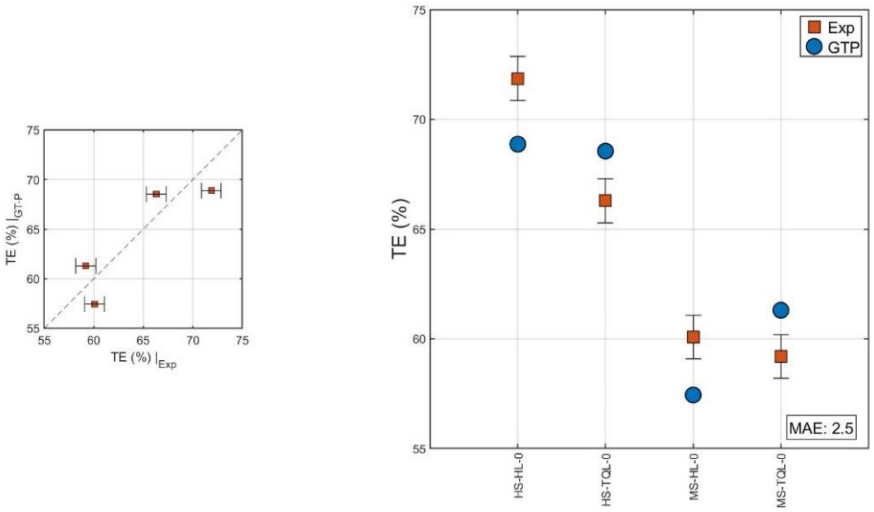

Figure 94: Experimental and GT-Power simulated trapping efficiency at different speeds and loads at standard spark timing (Approach I).

6.2.2. Scavenging Results

In this section, scavenging results from the *GT-Power* model using approach I are presented. The scavenging parameters presented represent the composition of the trapped mixture. Unlike the validation results (Figure 90 to Figure 94), the model is not tuned to achieve good matching for these parameters.

The dashed curves in Figure 95 illustrate the scavenging profiles produced as a result of the tuning exercise discussed above. 'Experimental' scavenging curves are also shown for reference. These are curves generated by using residual fractions from the validated hybrid model results presented at the end of Chapter 5. Exhaust and cylinder residual fractions at the four discrete states calculated in the hybrid model are connected using straight lines to generate the so called 'experimental' or hybrid scavenging curves.

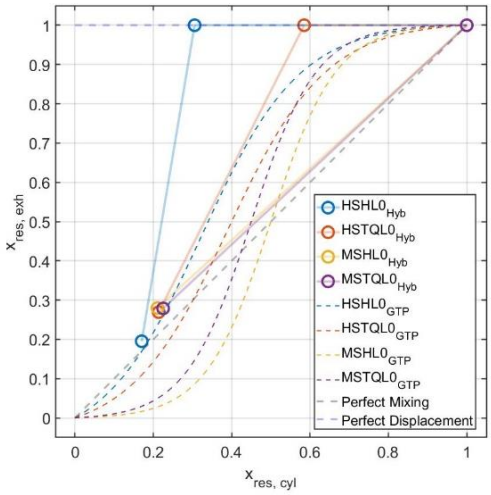

Figure 95: Scavenging profiles used in approach I and the corresponding curves from the validated hybrid scavenging model.

Scavenging curves generated on a continuous basis by Mattarelli et al. [91] for a loop scavenged engine using a CFD model are shown in Figure 96. The general shape of the 'experimental' curves generated by the simple scavenging model (Figure 95) looks reasonable when compared to the CFD generated curves.

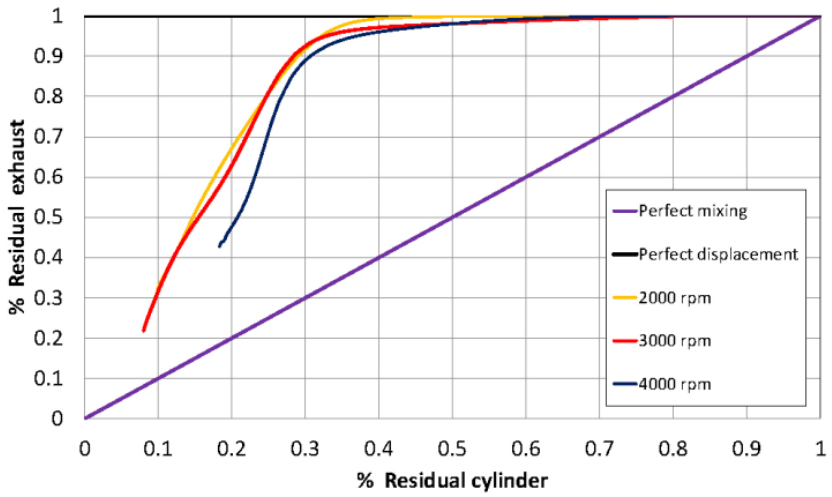

Figure 96: Scavenging curves generated from a CFD model of a loop-scavenged two-stroke engine [91].

Figure 97 and Figure 98, respectively, show the trapped mass of fuel and residual gases. Figure 99 shows the TRF and Figure 100 shows the TER, which is the most consequential composition metric from an emissions controls perspective. The error bars affixed to the experimental markers represent uncertainties in the measurement system. Appendix F presents a brief description of the uncertainty analysis used to calculate the height of the bars. The results show that even though the simulated values are in the same range as the experimental data, there are non-negligible errors in the scavenging parameter results. Whether these errors are acceptable for control applications depends on the sensitivity of the parameter being controlled for (e.g. NO_x) to changes in the control variable (e.g. TER), and the accuracy requirements of the application. For NO_x controlling purposes, the errors in TER are likely unacceptably high because of the exponential TER-NO_x relationship and stringent NO_x regulatory requirements. Table 6 lists the mean absolute errors (MAE) for the results presented here.

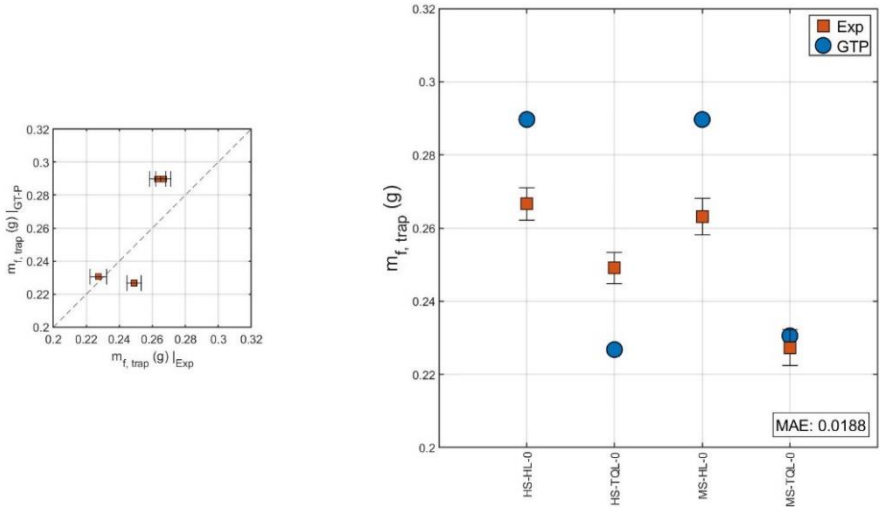

Figure 97: Experimental and GT-Power simulated mass of fuel trapped every cycle at different speeds and loads at standard spark timing (Approach I).

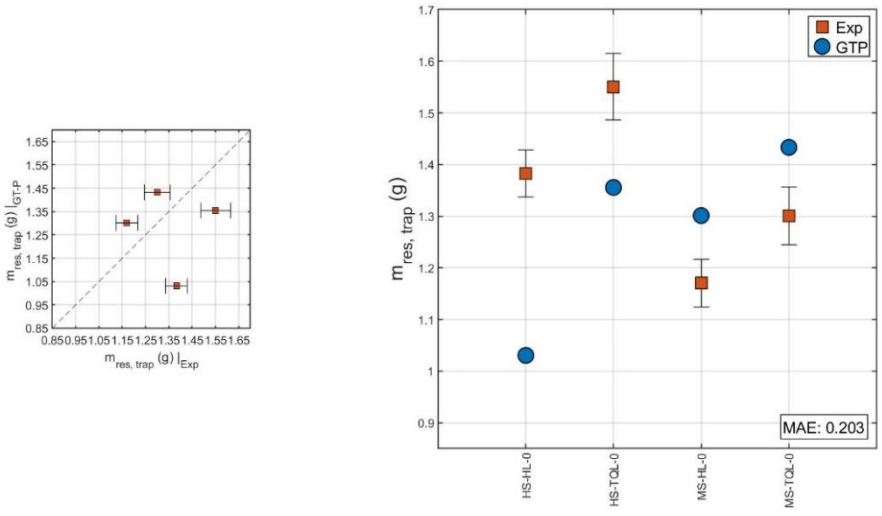

Figure 98: Experimental and GT-Power simulated trapped residual gas mass at different speeds and loads at standard spark timing (Approach I).

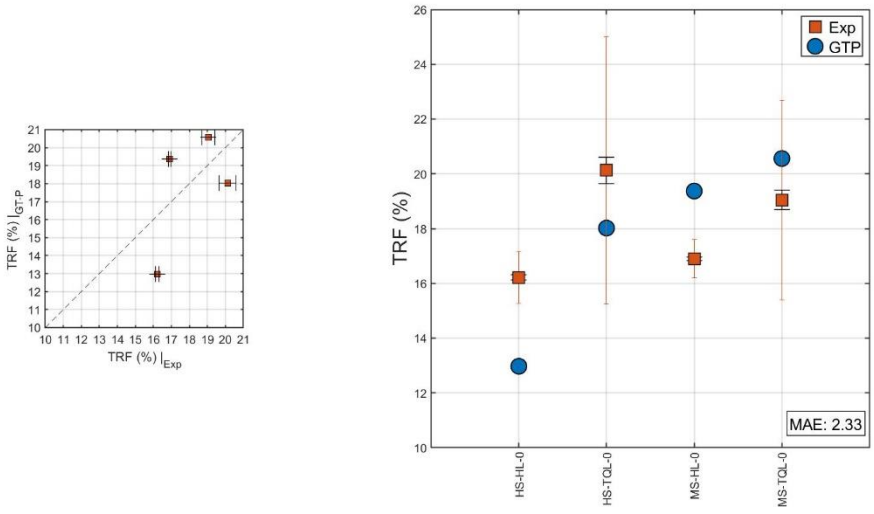

Figure 99: Experimental and GT-Power simulated trapped residual fraction at different speeds and loads at standard spark timing. Tall error bars show ± 1 SD bands; short bars show 95% CI (Approach I).

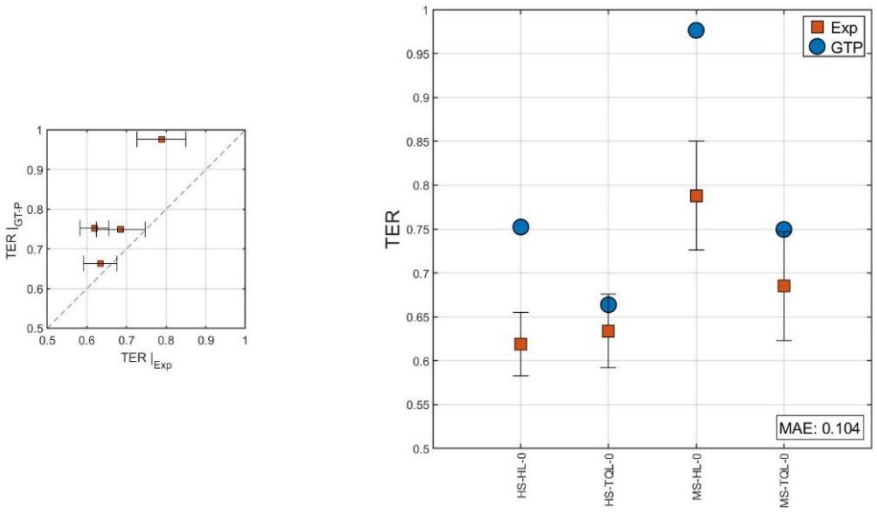

Figure 100: Experimental and GT-Power simulated trapped equivalence ratio at different speeds and loads at standard spark timing (Approach I).

Parameter	Mean Absolute Error
$m_{air,delivered}$	0.13 g
$m_{air,trap}$	0.17 g
$m_{fuel,trap}$	0.019 g
$m_{res,trap}$	0.203 g
TE	2.5%-pts
TRF	2.33%-pts
TER	0.104

Table 6: Mean absolute error for GT-Power simulated parameters (Approach I).

6.3. Approach II: Using Hybrid Scavenging Profiles

Next, the same model is used with the 'experimental' scavenging curves generated from the validated hybrid model. The curves, shown in Figure 101, are extrapolated to (0,0) from the state D (end of PM-short-circuiting stage) residual fraction point to make them compatible with *GT-Power's EngCylScav* object. The extrapolated segments are represented by the dashed lines. Everything else is the same as the foregoing model.

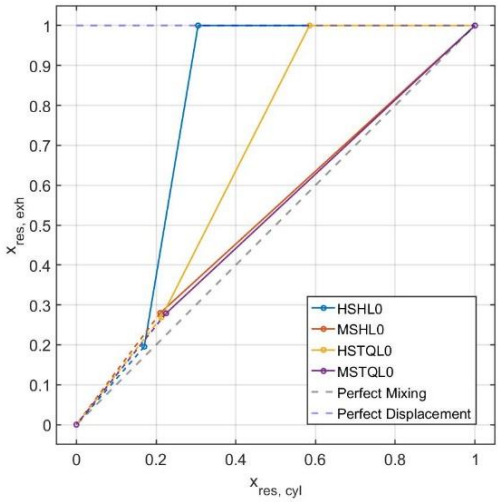

Figure 101: 'Experimental' scavenging profiles generated from the hybrid model. Dashed curves are extrapolated segments (Approach II and III).

6.3.1. Validation

In this approach, only the cylinder and exhaust pressures are used for validation. Since the air flow is not explicitly tuned to match experimental results, it is not considered a validation parameter. Figure 102 shows the simulated and experimental cylinder pressure traces and Figure 103 shows the exhaust pressures. The pressure curves are considered to be acceptable.

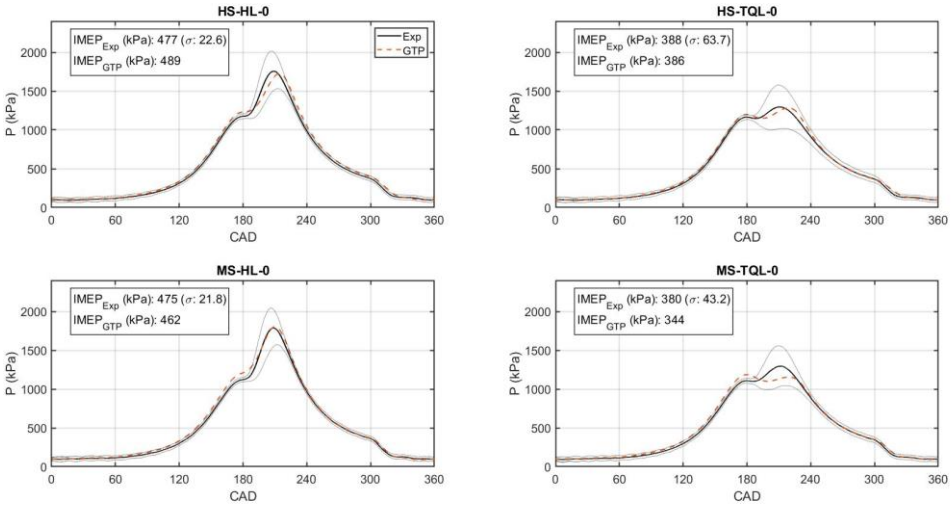

Figure 102: Experimental and GT-Power simulated cylinder pressure at standard spark timing for different speeds and loads (Approach II).

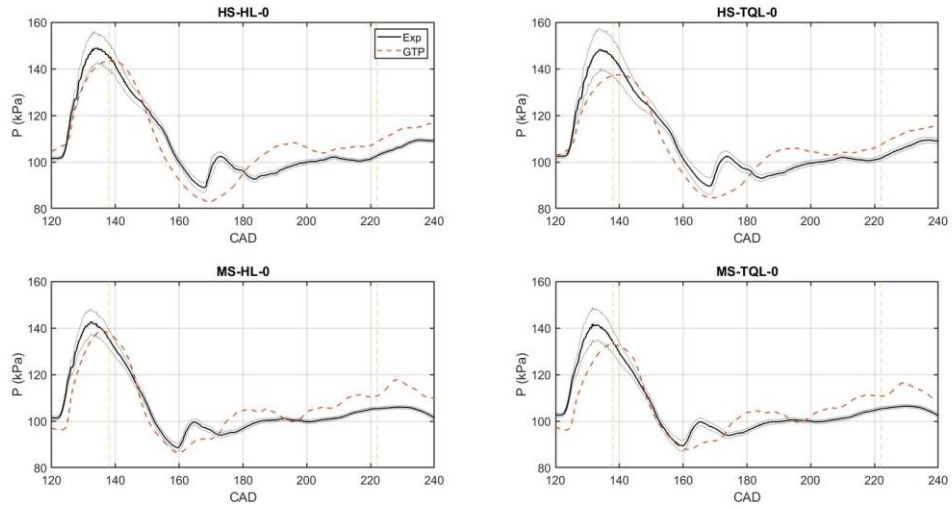

Figure 103: Experimental and GT-Power simulated exhaust pressure at standard spark timing for different speeds and loads (Approach II).

6.3.2. Scavenging Results

Results of using this approach are shown in Figure 104 to Figure 109. Results from approach I are also shown for reference (small circles) and the mean absolute errors for the two sets of simulated results are also printed. It is seen that using the hybrid scavenging curves slightly increases the error in delivered and trapped air estimates, whereas TER estimates improve significantly (Figure 109). If TER is considered to be the measure of the model's ability to accurately simulate scavenging, using scavenging profiles extracted from experimental results improves the model's accuracy. However, if the accuracy defining metrics are the delivered and trapped air mass (i.e. trapping efficiency), approach I produces better results. That said, neither of the two approaches produce satisfactory results as TRF estimates have high errors (MAE > 2.3%-pts) for both. The significance of this limitation is discussed in Section 6.5.

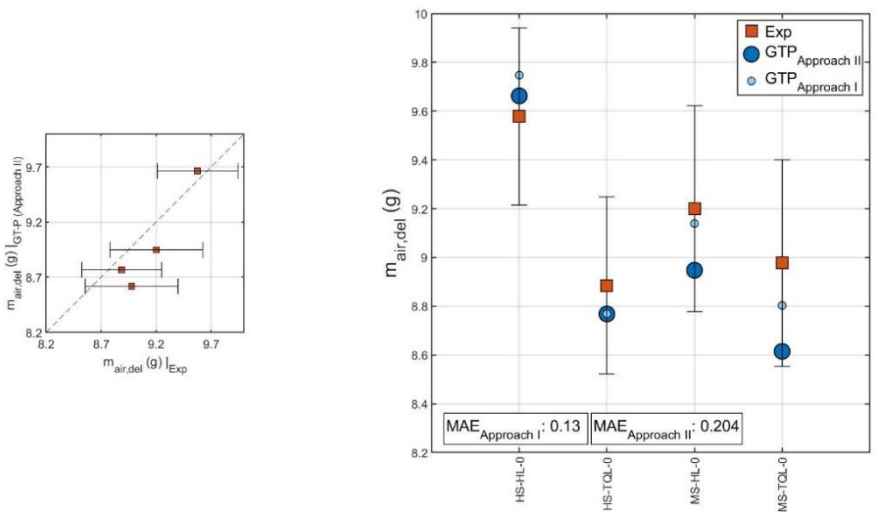

Figure 104: Experimental and GT-Power simulated mass of air delivered per cycle at different speeds and loads at standard spark timing (Approach II).

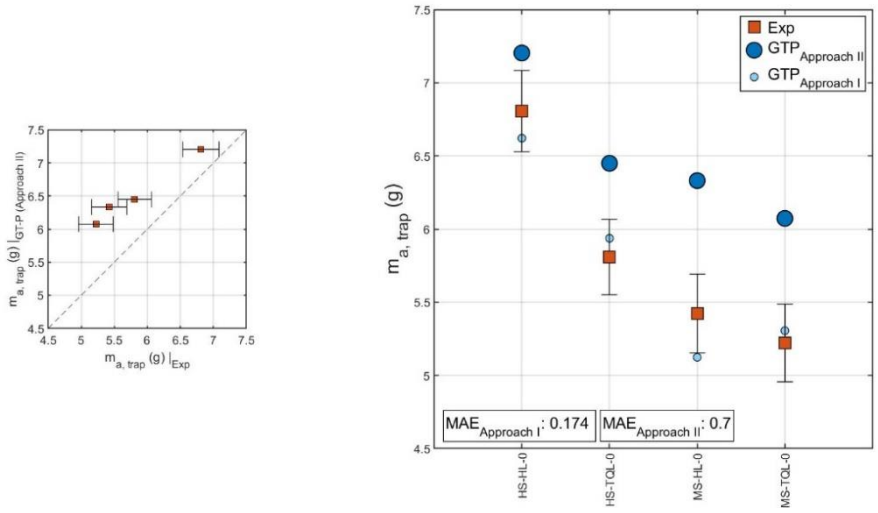

Figure 105: Experimental and GT-Power simulated mass of air trapped per cycle at different speeds and loads at standard spark timing (Approach II).

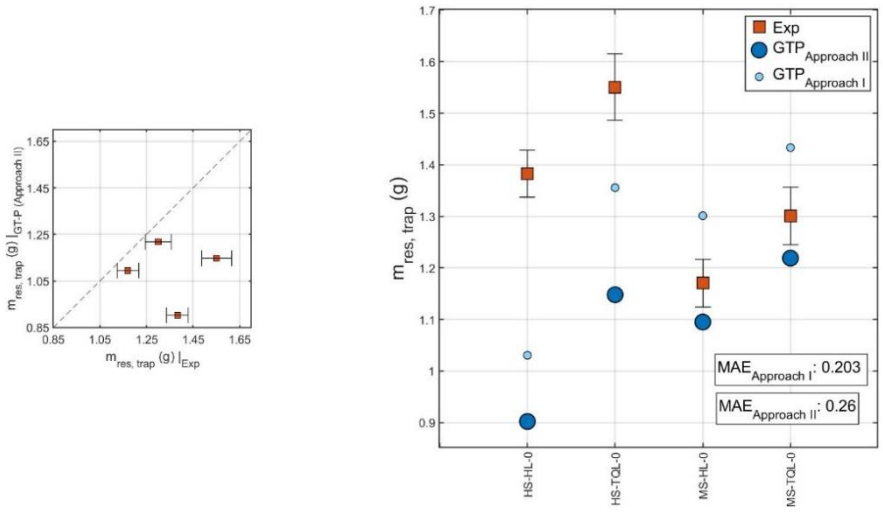

Figure 106: Experimental and GT-Power simulated trapped residual mass at different speeds and loads at standard spark timing (Approach II).

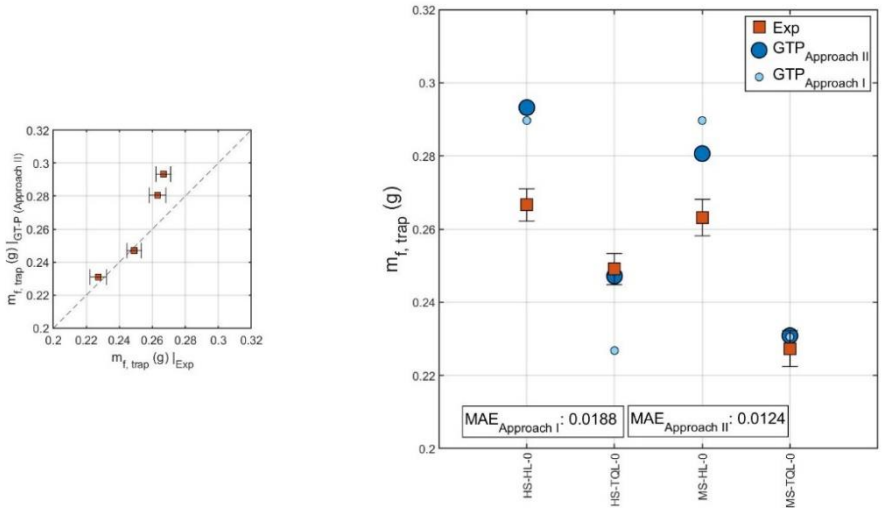

Figure 107: Experimental and GT-Power simulated trapped fuel mass at different speeds and loads at standard spark timing (Approach II).

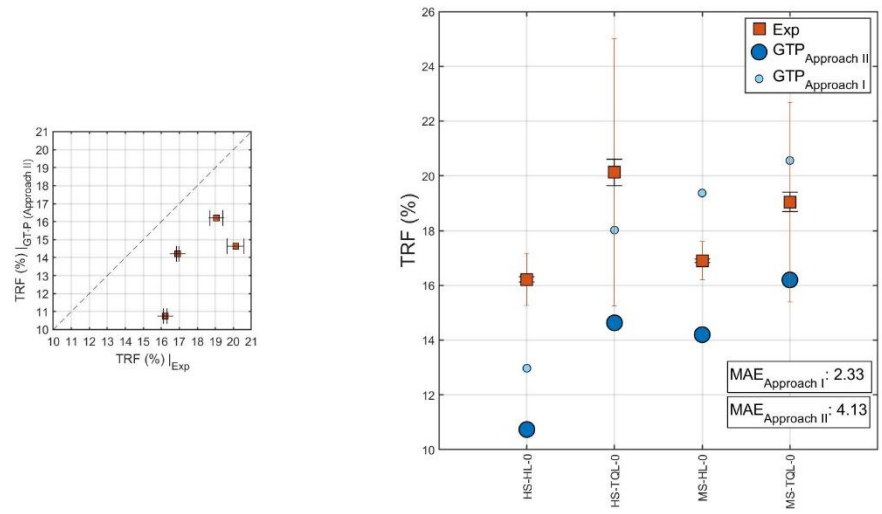

Figure 108: Experimental and GT-Power simulated TRF at different speeds and loads at standard spark timing. Tall error bars show ± 1 SD bands; short bars show 95% CI (Approach II).

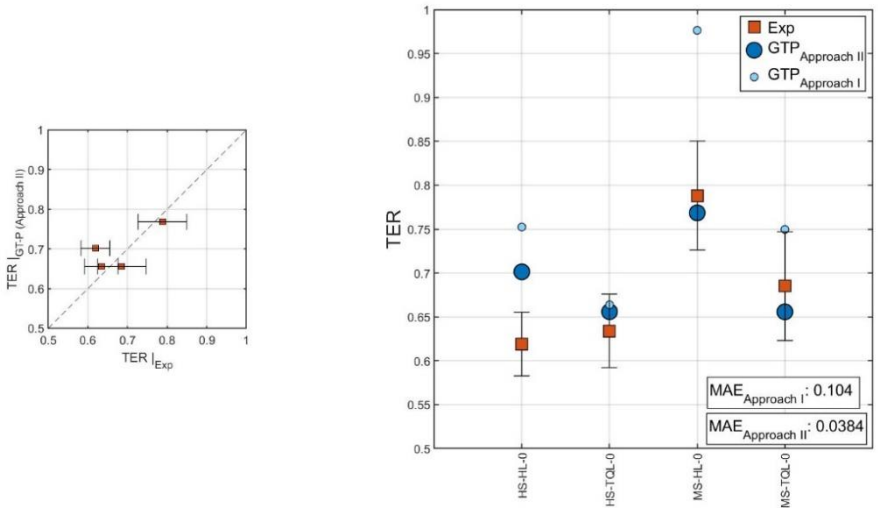

Figure 109: Experimental and GT-Power simulated trapped equivalence ratio at different speeds and loads at standard spark timing (Approach II).

6.3.2.1. How Scavenging Profile Changes Affect Trapping

The foregoing results show that changing the scavenging profile can have significant effects on the scavenging results. To help explain the mechanisms of these changes, the MS-HL-0 case is used as an example as it has the most pronounced change in the trapped air mass. The two scavenging profiles (extracted from Figure 95 and Figure 101) are reproduced in Figure 110. As stated earlier, everything else stays the same between the two model versions.

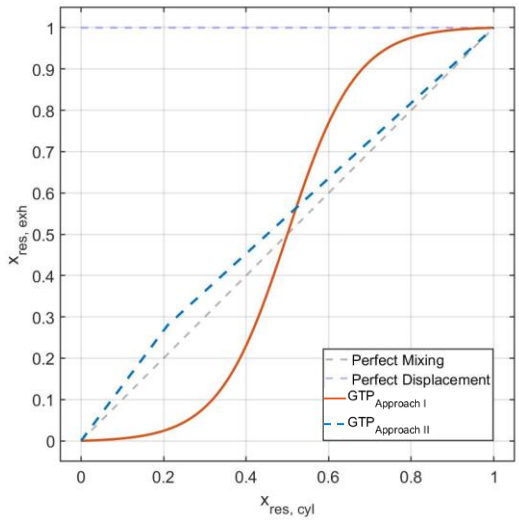

Figure 110: Scavenging profiles used for MS-HL-0 analysis while matching for air flow (Approach I) and when using hybrid model results (Approach II).

These scavenging profiles dictate the residual gas fraction in the engine cylinder and the exhaust. The resulting fractions are shown in Figure 111 from EPO to EPC. After EPO (during blowdown), the exhaust residual fraction increases to 100% and the cylinder residual fraction stays constant at 100% as no fresh gases have entered the cylinder up to this point. This corresponds to the top right corner (1,1) of Figure 110. After IPO (138 CAD), fresh air dilutes the cylinder mixture and as a result, the cylinder residual fraction starts to decrease (going from right to left in Figure 110). The corresponding decrease in exhaust residual fraction is dictated by the respective scavenging curves. The 'S' shaped curve (Approach I) keeps the exhaust fraction steady in the beginning, and then lets it drop rapidly owing to the rapid descent of the scavenging curve. The two scavenging curves intersect around an exhaust residual fraction value of 0.58. Below this point, the 'Approach I' curve is to the right of the

'Approach II' curve, that is, for the same exhaust residual fraction, the cylinder residual fraction is higher for approach I of the model. Since the exhaust residual fraction falls in this region (0 to 0.58) during the latter half of gas exchange for both the cases, the resulting TRF is higher for approach I (19.4% vs 14.2%). A consequence of this is that for approximately the same delivered air and fuel mass, a richer trapped mixture is needed with the approach I profile to produce almost the same IMEP as approach II. This is achieved by reducing the amount of trapped air (5.1 g vs 6.3 g) and increasing TER (0.98 vs 0.77).

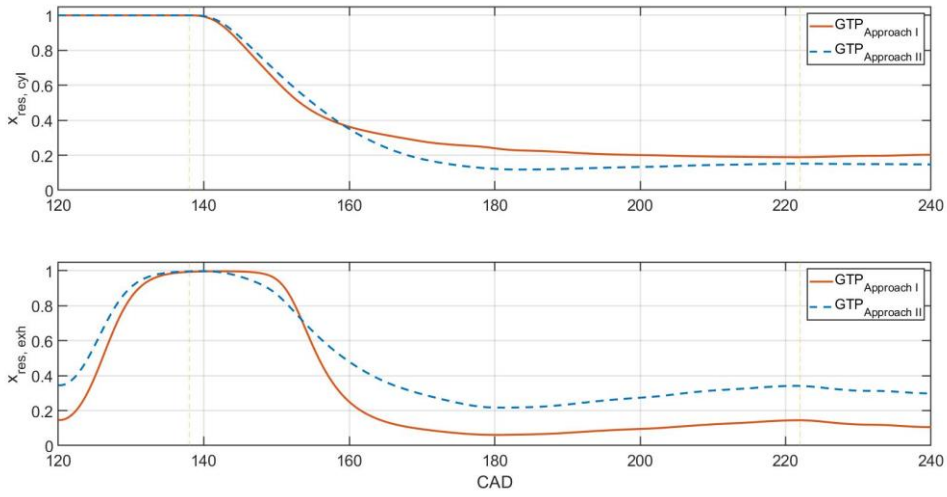

Figure 111: Residual gas fraction in the cylinder (top) and exhaust (bottom) at MS-HL-0 for the two scavenging profiles from Figure 110.

An analysis of the sensitivity of scavenging parameters to changes in scavenging curve shape is presented in Appendix G. The results show that scavenging parameters are highly sensitive to changes in the scavenging curve shape, especially if those changes move the anchor point.

6.4. Approach III: Using Hybrid Scavenging Profiles with 'Three Pressure Analysis'

Since neither of the two foregoing approaches that calculated pressure at the exhaust ports using gas dynamic-based methods produced satisfactory scavenging results, it was postulated that the failure of the model to precisely replicate the exhaust pressure wave might be responsible for the inaccuracies. To test this theory, *GT-Power's* 'three pressure analysis' simulation method was used. This method uses three user prescribed time-resolved pressures, namely, intake pressure, cylinder pressure, and exhaust pressure, to calculate the flow across the cylinder and the fuel burning rate in the cylinder. To implement this method, the predictive combustion and exhaust sub-models were removed and replaced by experimental cylinder and exhaust pressures, respectively. Everything else stayed the same as approach II, including the scavenging profiles. Table 5 lists the tuning parameters used in this analysis.

6.4.1. Validation

The 'three pressure analysis' solver in *GT-Power* tries to recreate experimental cylinder pressure curves by solving conservation laws within the bounds prescribed by pressure boundary conditions, scavenging sub-model, heat transfer sub-model, fuel flow rate, port discharge coefficients and other secondary constraints. The resulting cylinder pressure curves, shown in Figure 112, match well with their experimental counterparts. The underlying burn rate results that produce the excellent cylinder pressure matching

are shown in Figure 113 as apparent rates of heat release. Not surprisingly, they match heat release rates calculated from experimental pressure data very closely.

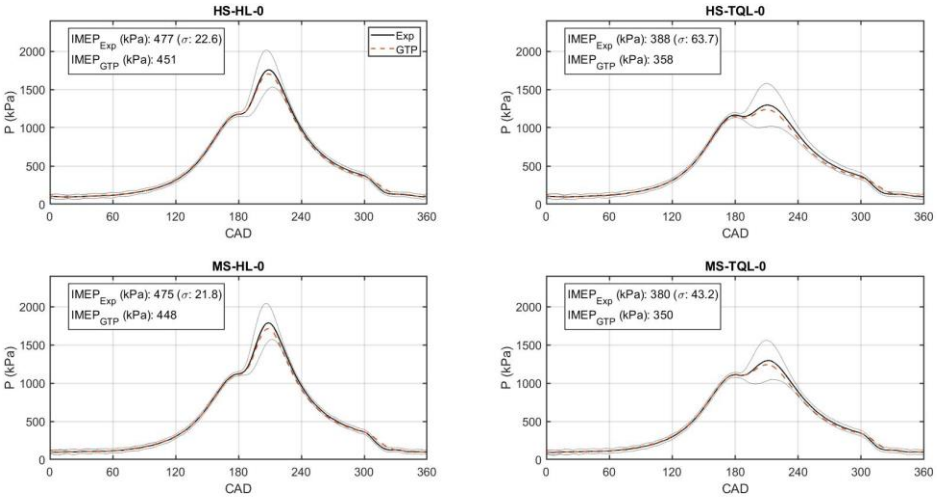

Figure 112: Experimental and GT-Power simulated cylinder pressure at standard spark timing for different speeds and loads (Approach III).

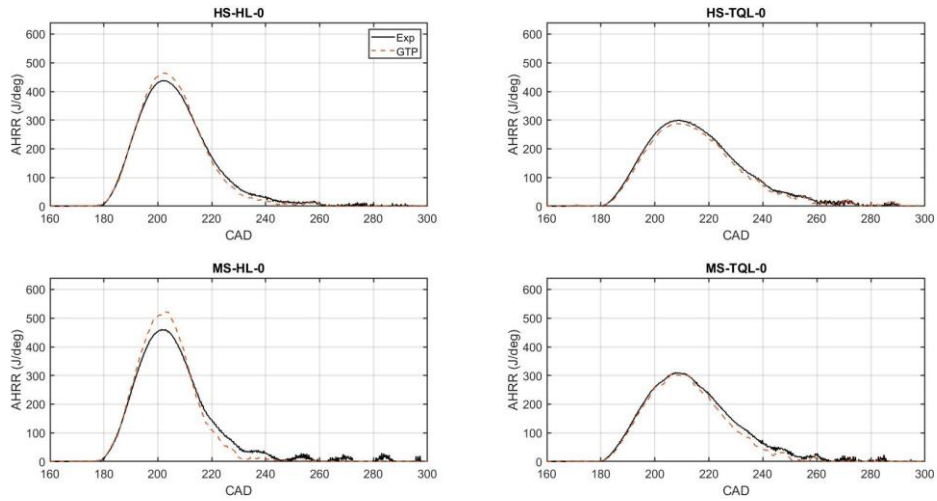

Figure 113: Experimental and GT-Power simulated apparent rates of heat release at standard spark timing for different speeds and loads (Approach III).

Similar to approach I, the mass of air trapped is used as a secondary validation parameter but unlike approach I, the mass of air delivered is allowed to float. The simulated trapped air mass results, shown in Figure 114, match experimental results reasonably well.

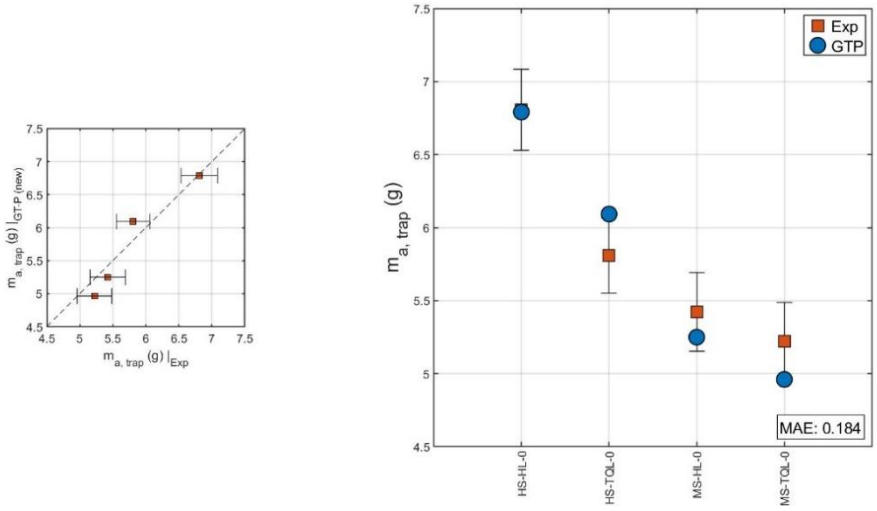

Figure 114: Experimental and GT-Power simulated mass of air trapped per cycle at different speeds and loads at standard spark timing (Approach III).

6.4.2. Scavenging Results

Results using the 'three pressure analysis' approach are shown in Figure 115 to Figure 122. Except for the mass of delivered air and mass of trapped fuel, all other results match experimental results very well.

The delivered air results (Figure 115) have a mean absolute error of 0.65 g, which translates to a percentage error of 7%. This is not ideal but can reluctantly be

considered acceptable. The errors in mass of air delivered lead to an MAE of 4.2%-pts in the trapping efficiency.

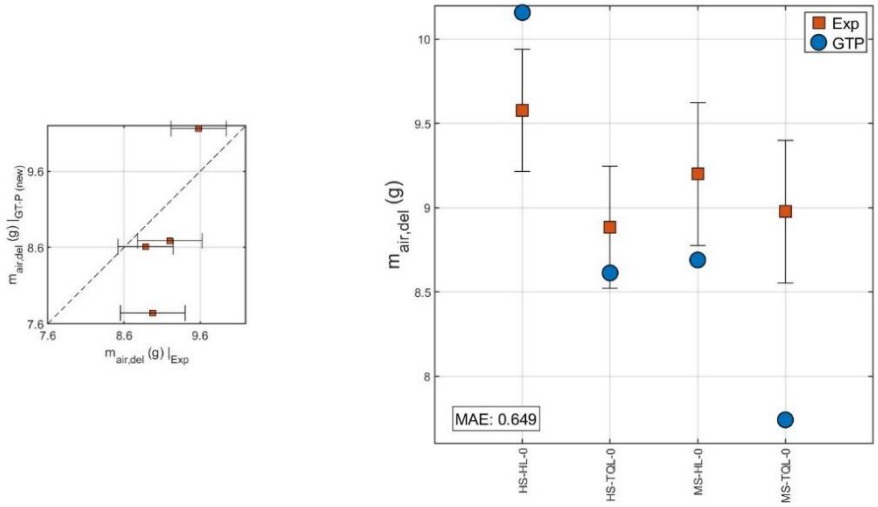

Figure 115: Experimental and GT-Power simulated mass of air delivered per cycle at different speeds and loads at standard spark timing (Approach III).

The 0.0136 g MAE in trapped fuel results (Figure 116) translates to a 5% error, which is acceptable. The simulated trapped fuel is consistently lower than experimental results; probably because the simulated expansion pressures in Figure 112, and resultantly the IMEPs, are also lower. The pressures are still, however, within the acceptable range of cyclic variability. The effects of mismatched combustion and/or thermal efficiencies are most likely negligible because the fuel conversion efficiency results have excellent matching, as can be seen in Figure 117.

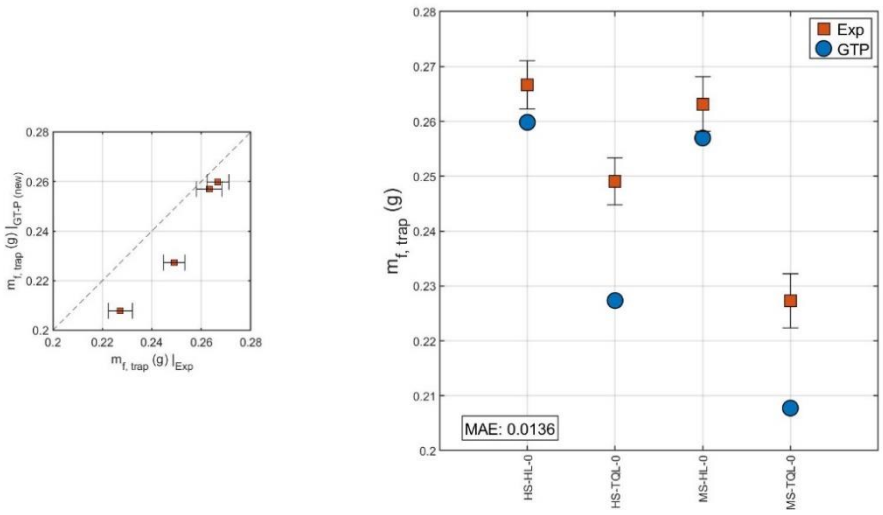

Figure 116: Experimental and GT-Power simulated trapped fuel mass at different speeds and loads at standard spark timing (Approach III).

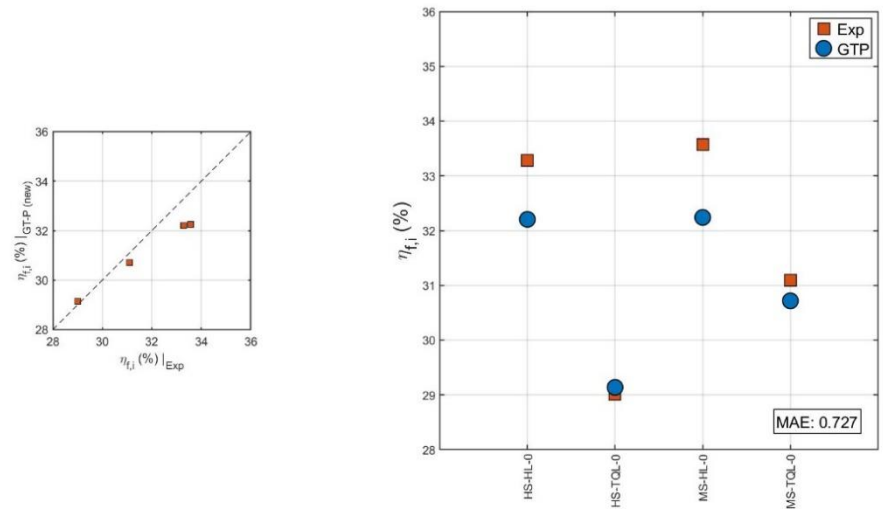

Figure 117: Experimental and GT-Power simulated fuel conversion efficiency at different speeds and loads at standard spark timing (Approach III).

The trapped residual mass and trapped residual mass fraction results shown in Figure 118 and Figure 119, respectively match experimental results very well, as evidenced by the low MAEs of 0.05 g and 0.35%-pts.

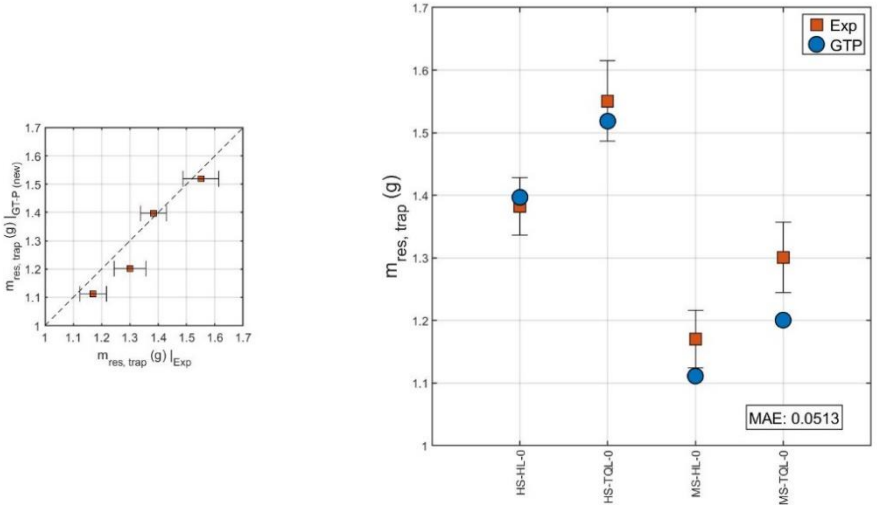

Figure 118: Experimental and GT-Power simulated trapped residual mass at different speeds and loads at standard spark timing (Approach III).

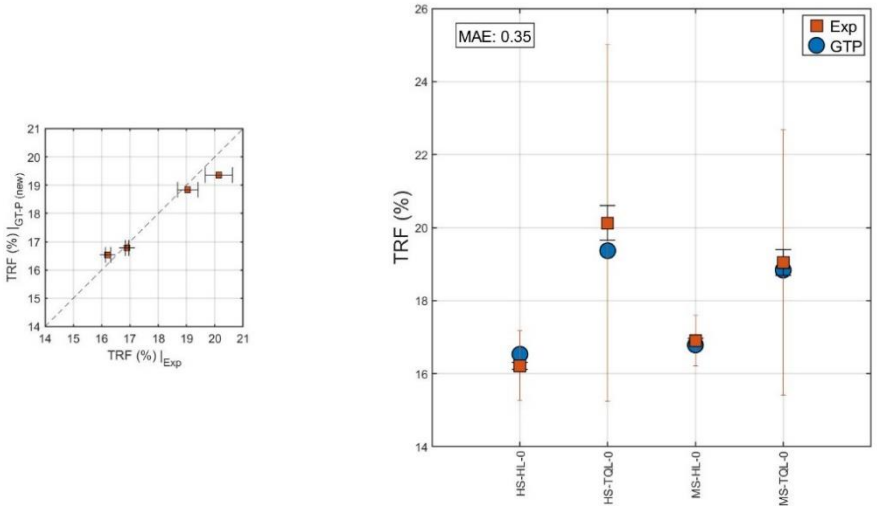

Figure 119: Experimental and GT-Power simulated trapped residual fraction at different speeds and loads at standard spark timing (Approach III).

The TER results shown in Figure 120 are also acceptable as all of the estimates are within the uncertainty bounds.

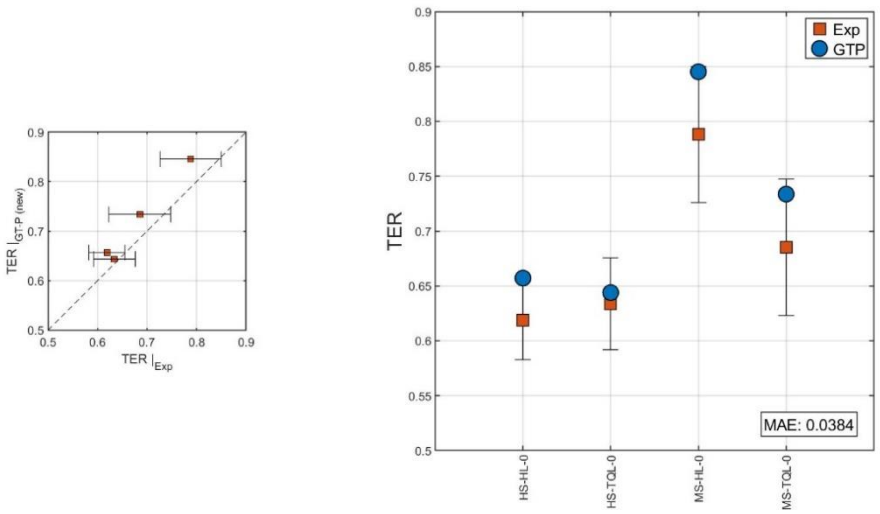

Figure 120: Experimental and GT-Power simulated trapped equivalence ratio at different speeds and loads at standard spark timing (Approach III).

As additional examples of the good quality of *GT-Power* results generated using approach III, the average cylinder gas temperature at EPO, and high-speed exhaust temperature are compared to experimental results in Figure 121 and Figure 122, respectively. Reasonably good matching is achieved for both.

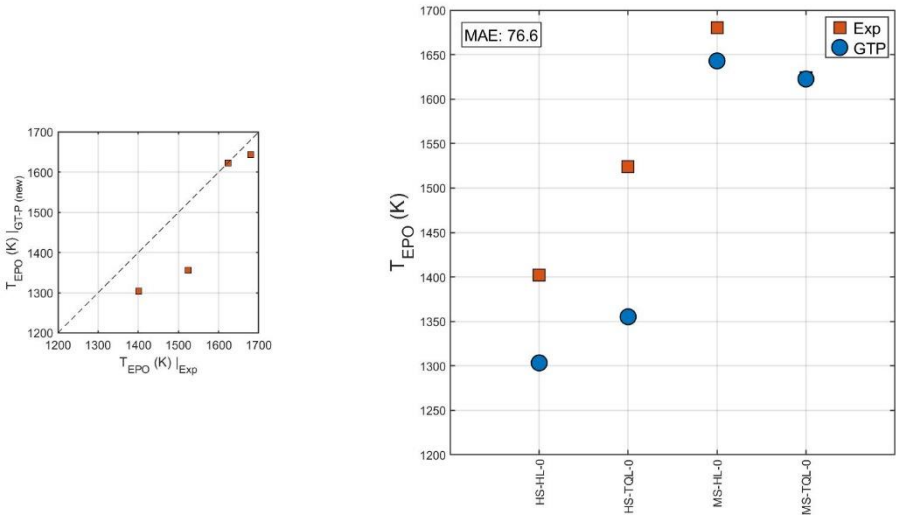

Figure 121: Experimental and GT-Power simulated average cylinder temperature at exhaust port opening for different speeds and loads at standard spark timing (Approach III).

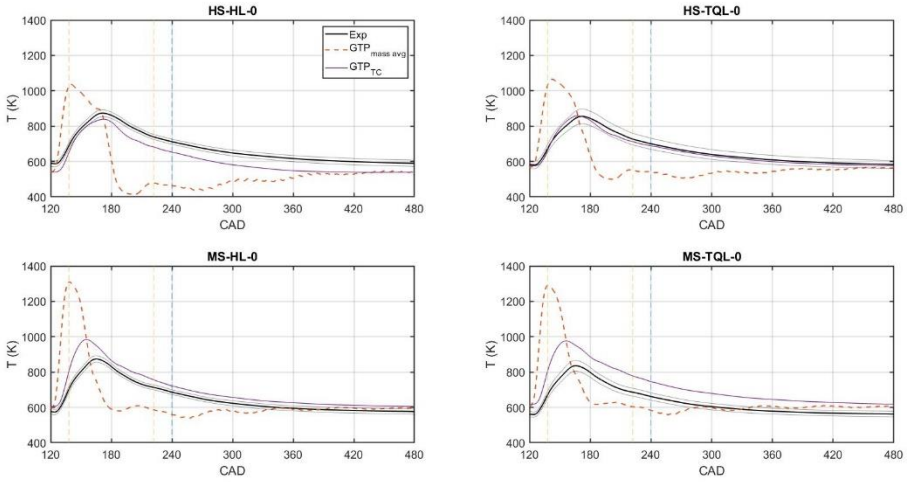

Figure 122: Experimental and GT-Power simulated exhaust temperature (mass averaged and thermocouple - TC - object calculated) at standard spark timing (Approach III).

6.5. Discussion of Results

The unsatisfactory scavenging results obtained using approaches I and II, and the improvement in simulated results using approach III point to the fact that even seemingly minor errors in exhaust pressures can have significant adverse effects on the scavenging results. The approaches that used simulated exhaust pressures could not simultaneously ensure accurate trapping and scavenging efficiency estimations. For acceptable trapping estimates, TRF results had a mean absolute error of 2.3%-pts, and for acceptable TER estimates, TE results had a mean absolute error of 8.8%-pts, whereas, the 'three pressure analysis approach' that used experimental exhaust pressure boundary conditions yielded MAEs of 0.038 for TER, 0.35%-pts for TRF, and 4.2%-pts for TE. Table 7 compares the MAEs among the three simulation approaches. The results obtained from approach III are acceptable and hint at the suitability of using *GT-Power* to tune the hybrid model for emissions control in engines for which in-cylinder CO_2 concentration data is not available to calculate scavenging parameters.

Parameter	Mean Parameter Value	Approach I MAE	Approach II MAE	Approach III MAE
$m_{air,delivered}$ (g)	9.16	0.13	0.20	0.65
$m_{air,trap}$ (g)	5.81	0.17	0.7	0.18
$m_{fuel,trap}$ (g)	0.25	0.019	0.012	0.0136
$m_{res,trap}$ (g)	1.35	0.203	0.26	0.05
TE (%)	64.4	2.50	8.8	4.2
TRF (%)	18.1	2.33	4.13	0.35
TER	0.68	0.104	0.038	0.038

Table 7: Mean absolute errors for GT-Power results.

A second aspect of the simulation approach that warrants further discussion is the means of prescribing the engine's scavenging behavior, that is, providing a functional relationship between exhaust and cylinder residual fractions. Such continuous relationships are difficult, if not impossible, to obtain experimentally using currently available sampling techniques. The limitation stems from the non-linear sampling delay induced offsets seen in the high-speed CO_2 data (Chapter 5), and the lack of time resolved exhaust mass flow rate data. The latter can, however, be calculated using simple flow models [67, 70] or orifice flow calculations using experimental pressures (Appendix E). Optical scavenging studies with firing engines might be able to generate the required residual fraction data.

Simple models like the hybrid model can provide some useful information about the scavenging profiles but cannot precisely generate the resolved continuous data needed by *GT-Power's* scavenging sub-model. Any curves extrapolated from the limited experimental residual gas data available will be susceptible to errors stemming from the shape of the connecting curves; as can be seen from the appended sensitivity analysis results. Results from validated CFD models can potentially be used to generate scavenging curves for use in *GT-Power* (e.g. [91]). This would, however, be an additional expense to scavenging investigations, thus, making it an unattractive option. A new approach is, therefore, needed to simulate scavenging in 1D flow simulation models. This approach should be able to accurately model both scavenging and trapping performance of the engine, as well as be easily implementable using experimental data

without needing an intermediate CFD model. The hybrid scavenging model proposed in the previous chapters can be one potential solution.

Additional *GT-Power* results that were not necessary for the discussion at hand but can provide useful information to the interested reader about the modeling abilities of the platform are provided in Appendix G.

7. SUMMARY AND CONCLUSIONS

Gas exchange in a large-bore, single-cylinder, cross-scavenged, two-stroke engine was studied computationally using a 1D flow simulator (*GT-Power*) and experimentally using tracers for residual and short-circuited gases. The study was motivated by the need for improving trapped mixture composition estimation tools (i.e. simple scavenging models) to have the accuracy needed for reliably controlling engine-out emissions, particularly NO_x emissions.

As a first step, a semi-validated *GT-Power* model was used to study five existing scavenging models to gauge their performance and identify modeling assumptions that negatively impacted the models' predictive abilities. The models, selected based on their unique traits after an extensive literature review, are listed below:

- Perfect displacement model (isothermal)
- Perfect mixing model (isothermal and non-isothermal)
- Benson and Brandham's two-stage (displacement-mixing) model
- Wallace and Dang's two-stage (displacement-mixing/short-circuiting) model

Results from this comparative study helped establish a modeling baseline and provided a list of attributes that an accurate scavenging model should possess. The following is an abridged version of this list:

- The model should have at least two stages, one with high SE characteristics (PD) and one with low SE characteristics (PM or short-circuiting).
- A tunable weighting factor for each of these stages is needed to account for variations in engine behavior at different operating conditions. In a robust scavenging model, the relative contribution of different stages should not vary excessively in the absence of extraordinary changes in engine breathing behavior.
- The isothermal assumption between the incoming and exiting gases desensitizes scavenging models to variations in SE stemming from changes in engine operating parameters that substantially change the residual gas temperature.

To substantiate the computational findings, an experimental test campaign was conducted at three different speed, load, and spark timing settings. CO_2 was used as a tracer for combustion products to study scavenging performance of the engine, and fuel, as a part of a pre-mixed fuel-air mixture, was used as a tracer for fresh charge to study the trapping performance of the engine. CO_2 concentration was measured in the engine cylinder and the exhaust on a time-resolved basis using high speed NDIR analyzers. Major findings from the experimental investigation are as follows:

- By comparing the exhaust CO_2 concentration 'waves' at different operating points, it was noted that scavenging takes place in three phases: an initial perfect displacement type stage, followed by a short-circuiting, and a perfect mixing type stage. The PM and short-circuiting stages are dominant at medium speed while the PD stage dominates at high speed.

- Engine speed and load changes have the strongest effects on the trapping and scavenging performance of the engine; spark timing effects are less significant.
- Changes in measured scavenging and trapping efficiencies at different operating points result from a combination of influences, e.g. (1) reduced time for gas exchange at high speed, (2) higher expansion and scavenging pressures at high load and retarded spark timing, and (3) phasing of the reflected scavenging and plugging pulses in the exhaust relative to BDC and EPC, respectively.
    - Most pronounced operating point induced changes in scavenging efficiency result from changing engine load: at higher loads, the engine scavenges better (has lower TRF).
    - Most pronounced operating point induced changes in trapping efficiency result from changing engine speed: at higher speeds, a larger fraction of the delivered air is trapped.
- For the stable operating points studied, the trapped equivalence ratio ranged between 0.6 and 0.8, highlighting the lean burn nature of the engine.
    - The engine runs leaner at high speeds because of more air being delivered, and better trapping efficiency. The effects of scavenging efficiency changes and thermal efficiency improvements from reduced heat transfer are secondary.
    - Decreasing engine load makes the engine run leaner as well. This can be attributed to: (1) a reduction in the chemical energy demand as less work is being generated, and (2) higher amounts of trapped residuals, which not

only provide additional oxidizer but also act as a diluent to lower combustion temperatures and increase the engine's thermal efficiency.

- Engine-out NO_x emissions increase exponentially with TER, and at a given TER value, more NO_x is emitted at high speed. This can be attributed to higher combustion temperatures resulting from reduced wall heat losses at high speed.
- The scavenging and trapping efficiencies of the engine are higher than the corresponding non-isothermal perfect mixing model estimates. This demonstrates the optimized nature of the gas flow path design of the engine, which has gone through multiple design iterations.

Based on the desired scavenging model attributes listed earlier and preliminary experimental results, a three-stage, two-zone, simple scavenging model (named the hybrid model) was proposed as a control solution for emissions management. The model simulates scavenging as a three-stage process: an initial isentropic blowdown stage, followed by non-isothermal perfect displacement and perfect mixing stages. During the latter two stages, the model has two zones: a main zone where either PD or PM scavenging takes place, and a short-circuiting zone through which fresh charge 'slips' out without interacting with the main zone gases. Two tunable parameters prescribe the length of the PD stage and the size of the short-circuiting zone in the model.

The hybrid model was tuned to match experimental results and based on the quality of the matching, it was concluded that the model can estimate the trapped equivalence ratio with an acceptable degree of accuracy. Accurate TER estimation is important

because there exist well-established dependencies between NO_x emissions and TER levels which make TER a reliable control parameter. The tuning exercise also provided the following insights about the nature of scavenging in the engine at different operating points:

- Length of the PD stage increases as engine speed and load increase. The shorter PD stage at medium speed results in a correspondingly longer PM stage.
- By comparing x_{short} (total fresh air loss fraction during gas exchange) and SCF (fresh air loss fraction only because of air slippage), it was found that almost half of the exhausted air was lost to pure short-circuiting (‘direct slippage’) and the remainder was lost as an air-residual mixture (‘bypassed air’-residual mixture).

After establishing the suitability of the hybrid model for predicting trapped mixture composition, thereby making it a promising emissions control solution, the *GT-Power* model was updated and a simulation test campaign was conducted to gauge the scavenging modeling capabilities of such platforms. This was done with the hopes of discovering an economical way of tuning the hybrid model for engines where high speed CO_2 concentration data is not available. Initially, simulations were run with the modeling domain spanning from the intake ports to the end of the exhaust system. The simulation results using this approach failed to simultaneously produce accurate predictions for trapping and scavenging efficiencies. For acceptable trapping estimates, TRF results had a mean absolute error of 2.3%-pts, and for acceptable TER estimates, TE results had a mean absolute error of 8.8%-pts. The shortcoming was believed to have

arisen from the seemingly small errors in the simulated exhaust pressure waves. Thereafter, experimentally measured time-resolved exhaust pressures were used as the engine exhaust boundary condition with *GT-Power's* 'three pressure analysis' solver. Doing so significantly improved the modeling predictions and brought down the errors in TRF and TER estimates to 0.35%-pts and 0.038, respectively.

Despite the encouraging *GT-Power* results, there are implementation challenges associated with using its scavenging sub-model. The sub-model requires a functional relationship between cylinder and exhaust residual fractions, which is difficult to obtain experimentally. The model was also found to be very sensitive to the shape of the prescribed scavenging curve. A new approach is, therefore, needed to model scavenging in 1D flow simulation models. This approach should be able to accurately model both scavenging and trapping performance of the engine, as well as be easily implementable using experimental data without needing an intermediate CFD model. The hybrid model proposed could potentially provide one such approach.

8. FUTURE WORK

The following is a list of recommendations that, if pursued, can pave the way for the implementation of the hybrid model on field engines and improve its reliability.

8.1. Testing the Hybrid Model to Control NO_x

Use the tuned hybrid model with the Ajax E-565 engine being studied to predict, in real time, the trapped equivalence ratio at stable operating points. Use the TER estimates to predict NO_x emissions and compare the predictions with measured emissions data. Also, compare the NO_x predictions with those from the 'corrected TER' method [31] predictions. The corrected TER approach is the predominant NO_x control method for integral compressor engines. Recent work done by Linker [92] has already mapped the engine for this method.

8.2. Implementing the Hybrid Model in a 'White-Box' Thermodynamic Model

Based on the implementation limitations of *GT-Power's* scavenging curve-based approach, the hybrid model was proposed as a potential solution. To test the accuracy of the hybrid model, it would have to be coded into *GT-Power* to calculate the purity of the exhaust gas. Unfortunately, because of *GT-Power's* 'black box' architecture, this is not possible. Moreover, since the scavenging sub-model results affect all subsequent calculations (e.g. TRF estimates affect combustion characteristics), it cannot be implemented a-posteriori in *GT-Power*, either. This limits the direct testing of the hybrid

model in *GT-Power*-based engine simulations. It is thus recommended that the model be included in an in-house developed thermodynamic model of the engine that can be easily modified to calculate its scavenging and trapping behavior. Implementing the hybrid model in a thermodynamic simulation will allow for its inexpensive validation and tuning for engines where high speed CO_2 concentration data is not available. This can be done by tuning the hybrid model parameters until other simulated parameters (exhaust emissions, cylinder pressure, etc.) match experimental measurements. Recent work by Wallace [93] on thermodynamic modeling of the engine being studied can potentially provide the white box modeling platform needed.

8.3. Adding a Stochastic Sub-Model

All the work done thus far has been for steady state operation, but cyclic variations are part and parcel of engine operation, e.g. during startup and shutdown [94], during a 'hot gas event'[16] [95], or at an unstable operating point [86]. A stochastic sub-model can be overlaid on the mean value hybrid model to account for cyclic variability, and to control emissions under unsteady operation. The characterization work briefly discussed in section 5.2. can aid in the development of the stochastic sub-model by identifying 'normal' cycles and treating all the remaining cycles as the source of cyclic variability. The normal cycles can be treated as the signal and the remaining cycles as noise.

[16] Periods of significant fuel composition variability, particularly in reference to times of high ethane and/or propane concentration.

8.4. Studying Fuel Composition Variability Effects

The combustion characteristics (ignition delay, laminar flame speed, etc.) of natural gas fuel can vary significantly because of fluctuations in the composition of the gas being extracted. This lack of fuel composition control can cause the engine's operational and, as a result, its emissions characteristics to change significantly [95, 96, 97]. The fuel composition variation problem has become more pronounced in the last decade, ever since the popularization of hydro-fracking to extract tightly bound gas from shale formations. Recent works by Fieseler [98] and Linker [97] have used chemical kinetics-based methods in *GT-Power* to predict NO_x emissions from an integral compressor engine running on different composition natural gas fuels. These works can be extended to a model of the engine being studied; be it the *GT-Power* model discussed in this dissertation or a thermodynamic model developed as per Recommendation 8.3. Such a study will help test the hybrid model's capabilities for non-standard fuel compositions.

9. REFERENCES

[1] J. B. Heywood and E. Sher, The Two-Stroke Cycle Engine, Philadelphia: Taylor and Francis, 1999.

[2] D. T. Brown, "A History of the Sulzer Low-Speed Marine Diesel Engine," Sulzer Bros., 1984.

[3] E. G. Groff, "Automotive Two-Stroke-Cycle Engine Development in the 1980-1990's," *SAE Technical Paper*, no. 2016-01-0177, 2016.

[4] R. Osborne, J. Stokes, T. Lake, P. Carden, J. Mullineux, H.-L. R., J. Evans, M. Heikal, Y. Zhu, H. Zhao and T. Ma, "Development of a Two-Stroke/Four-Stroke Switching Gasoline Engine-the 2/4SIGHT Concept," *SAE Technical Paper*, no. 2005-01-1137, 2005.

[5] L. D. Pugnali and R. Chen., "Feasibility Study of Operating 2-Stroke Miller Cycles on a 4-Stroke Platform Through Variable Valve Train," *SAE Technical Paper*, no. 2015-01-1974, 2015.

[6] R. E. Herold, M. H. Wahl, G. Regner, J. U. Lemke and D. E. Foster, "Thermodynamic Benefits of Opposed-Piston Two-Stroke Engines," *SAE Technical Paper*, no. 2011-01-2216, 2011.

[7] A. I. Works, Ajax E-42 and EO-30 Manual, Corry, Pennsylvania, 1996.

[8] F. J. Wallace and P. R. Cave., " Experimental and Analytical Scavenging Studies on a Two-Cycle Opposed Piston Diesel Engine," *SAE Technical Paper,* no. 710175, 1971.

[9] M. Nuti and L. Martorano., "Short-Circuit Ratio Evaluation in the Scavenging of Two-Stroke SI Engines," *SAE Technical Paper,* no. 850177, 1985.

[10] B. J. Tobis, R. Meyer, J. Yang, D. D. Brehob and R. W. Anderson, "Scavenging of a Firing Two-Stroke Spark-Ignition Engine.," *SAE Transactions,* pp. 535-546, 1994.

[11] S. Ishihara and K. Nakashima, "Analysis of Scavenging Flow in Cross-Scavenged Two-Stroke Engine," *SAE Technical Paper,* no. 2007-32-0033, 2007.

[12] D. Dang and F. J. Wallace, "Some Single Zone Scavenging Models for Two-Stroke Engines," *International Journal of Mechanical Sciences,* no. 34(8), pp. 595-604, 1992.

[13] T. D. Fansler, D. T. French and M. C. Drake, "Individual-Cycle Measurements of Exhaust-Hydrocarbon Mass from a Direct-Injection Two-Stroke Engine," *SAE Transactions,* no. 980758, pp. 946-966, 1998.

[14] G. P. Blair, Design and Simulation of Two-Stroke Engines, Warrendale, PA: Society of Automotive Engineers, 1996.

[15] "Inventory of U.S. Greenhouse Gas Emissions and Sinks," U.S. Environmental Protection Agency, 2018.

[16] R. U. K. Gustafsson, G. P. Blair and B. I. R. Jonsson, "Reducing Exhaust Emissions and Increasing Power Output Using a Tuned Exhaust Pipe on a Two-Stroke Engine," *SAE Technical Paper,* no. 2001-01-1853, 2001.

[17] R. U. Gustafsson, "A Practical Application to Reduce Exhausts Emissions on a Two-Stroke Engine with a Tuned Exhaust Pipe," *SAE Technical Paper,* no. 2006-32-0054, 2006.

[18] F. L. Watson and G. Hong., "Application of Exhaust Pipe Restriction Technique to a Small Two-Stroke Engine," *SAE Technical Paper,* no. 2007-32-0032, 2007.

[19] G. Zsiga, R. Kerres, M. Bach and K. Fuoss, "Potential of Expansion Chamber Exhaust Pipes for Two-Stroke Powered Tools," *SAE Technical Paper,* no. 2010-32-0011, 2010.

[20] J. B. Heywood, Internal Combustion Engine Fundamentals, New York: McGraw-Hill Science, 1988.

[21] "Nitrogen Oxides (NOx): Why and How They are Controlled.," Clean Air Technology Center. (U.S. Environmental Protection Agency), 1999.

[22] "Availability and Limitations of NOx Emissions Control Resources for Natural Gas Fired Reciprocating Engine Prime Movers Used in the Interstate Natural Gas Transmission Industry," Innovative Environmental Soultions Inc. and Optimized Technical Solutions, 2014.

[23] G. P. Blair, "Design and Simulation of Engines: A Century of Progress," *SAE Technical Paper,* no. 1999-01-3346, 1999.

[24] G. Yamagishi, T. Sato and H. Iwasa, "A Study of Two-Stroke Cycle Fuel Injection Engines for Exhaust Gas Purification," in *Automotive Engineering Congress and Exposition*, Detroit , 1972.

[25] A. Jante, "Scavenging and Other Problems of Two-Stroke Cycle Spark-Ignition Engines," *SAE Transactions,* pp. 1803-1824, 1968.

[26] E. G. Groff, "Automotive Two-Stroke-Cycle Engine Development in the 1980-1990's.," *SAE Technical Paper,* no. 2016-01-0177, 2016.

[27] "Annual Energy Outlook 2019," U.S. Energy Information Administration, Washington D.C., 2019.

[28] "U.S. Energy Information Administration," (https://www.eia.gov/tools/faqs/faq.php?id=73&t=11).

[29] C. S. Weaver, "Natural Gas Vehicles-A Review of The State of the Art," *SAE Technical Paper,* no. No. 892133., 1989.

[30] M. J. Helmich, "Cooper-Bessemer Type GMV Integral-Angle Gas Engine-Compressor," ASME and Knox County Historical Museum, Mount Vernon, Ohio, 2006.

[31] G. Beshouri, T. J. Jacobs and G. Choquette, "The Impact of Varying Fuel Speciation on Engines Using "Virtual Sensor" Air/Fuel Ratio Controls," in *Dessau Gas Engine Conference* , Dessau-Roßlau, 2019.

[32] M. Toema, P. Watts, H. Mathews and G. Beshouri, "Overcoming Turbocharger Limitations for Low BMEP Two-Stroke Large Bore Gas Engines: A Technical Analysis and Case Study," in *ASME ICEF*, Chicago, 2019.

[33] D. J. Simpson and D. B. Olsen., "Precombustion Chamber Design for Emissions Reduction from Large Bore NG engines," *Journal of Engineering for Gas Turbines and Power,* no. 132.12, p. 122802, 2010.

[34] D. B. Olsen and B. D. Willson., "The Effect of Retrofit Technologies on Formaldehyde Emissions from a Large Bore Natural Gas Engine," *Energy and Power Engineering*, no. 3.04: 574, 2011.

[35] D. B. Olsen, B. D. Mastebergen and B. Willson, "Investigation of the Fuel Injection Process for Large Bore Natural Gas Engines," *Gas Machinery Conference ,* 2001.

[36] R. S. Benson, "A New Gas Dynamic Model for the Gas Exchange Process in Two Stroke Loop and Cross Scavenged Engines," *International Journal of Mechanical Sciences,* no. 19(12), pp. 693-711, 1977.

[37] G. P. Merker and M. Gerstle, "Evaluation on Two Stroke Engines Scavenging Models," *SAE Transactions,* pp. 604-627, 1997.

[38] B. Hopkinson, "The Charging of Two-Cycle Internal-Combustion Engines," *Journal of the American Society for Naval Engineers,* pp. 974-985, 1914.

[39] E. Sher, "Modeling the Scavenging Process in the Two-Stroke Engine-An Overview," *SAE Technical Paper,* no. 890414, 1989.

[40] R. S. Benson and P. T. Brandham., "A Method for Obtaining a Quantitative Assessment of the Influence of Charging Efficiency on Two-Stroke Engine Performance," *International Journal of Mechanical Sciences,* no. 11.3, pp. 303-312, 1969.

[41] G. D. Bourn, J. W. Gingrich and J. A. Smith, "Advanced Compressor Engine Controls to Enhance Operation, Reliability and Integrity," Southwest Research Institute, San Antonio, 2004.

[42] D. Olsen, P. Puzinauskas, N. Sabey and B. Wilson, "Improved Cyclic Pressure-Based PEMS Model," Pipeline Research Council International, Fort Collins, 2002.

[43] G. D. Bourn, F. A. Phillips and R. E. Harris, "Technologies to Enhance the Operation of Existing Natural Gas Compression Infrastructure - Manifold Design for Controlling Engine Air Balance," Southwest Research Institute, San Antonio, 2005.

[44] G. Choquette, G. Beshouri, B. Goffin, J. Millott, G. Arney and J. McCarthy, "Diagnostics for Reciprocating Engines and Compressors," in *Gas Machinery Conference,* Pittsburgh, 2017.

[45] C. F. Taylor, Internal Combustion Engine Theory and Practice, MIT Press, 1985.

[46] R. U. K. Gustafsson, G. P. Blair and B. I. R. Jonsson, "Reducing Exhaust Emissions and Increasing Power Output Using a Tuned Exhaust Pipe on a Two-Stroke Engine," *SAE Technical Paper,* no. 2001-01-1853, 2001.

[47] J. A. Caton, An Introduction to Thermodynamic Cycle Simulations for Internal Combustion Engines, John Wiley & Sons, 2015.

[48] K. M. Ingvorsen, K. E. Meyer, J. H. Walther and S. Mayer, "Turbulent Swirling Flow in a Dynamic Model of a Uniflow-Scavenged Two-Stroke Engine," *Experiments in Fluids,* vol. 1748, no. 55.6, 2014.

[49] K. M. Ingvorsen, K. E. Meyer, J. H. Walther and S. Mayer, "Turbulent Swirling Flow in a Model of a Uniflow-Scavenged Two-Stroke Engine," *Experiments in Fluids,* vol. 1494, no. 54.3, 2013.

[50] G. P. Blair, "Studying Scavenge Flow in a Two-Stroke Cycle Engine," in *SAE Off-Highway Vehicle Meeting*, Milwaukee, 1975.

[51] N. Dedeoglu, "Scavenging Model Solves Problems in Gas Burning Engine," *SAE Transactions,* no. 710579, pp. 1930-1941, 1971.

[52] E. Sher, "Investigating the Gas Exchange Process of a Two-Stroke Cycle Engine With a Flow Visualization Rig," *Israel Journal of Technology*, pp. 127-136, 1982.

[53] R. Boyer, D. Craig and C. Miller, "A Photographic Study of Events in a 14-in. Two-Cycle Gas Engine Cylinder," *Transactions of ASME,* pp. 97-108, 1954.

[54] S. C. Bopp, B. J. Cousyn, R. M. Green and P. O. Witze, "Experimental Study of the Scavenging and Combustion Processes in a Two-Stroke Cycle Research Engine," *SAE Transactions* , no. 920183, pp. 245-260, 1992.

[55] M. Ekenberg and B. Johansson., "Scavenging Flow Velocity in Small Two-Strokes at High Engine Speed," *SAE Technical Paper,* no. 951789, 1995.

[56] A. Cairns and C. G. W. S. ", "Cyclically Resolved Simultaneous Flame and Flow Imaging in a SI Engine," *SAE Transactions,* no. 2000-01-2832, pp. 2017-2035, 2000.

[57] P. C. Miles, R. M. Green and P. O. Witze., "In-Cylinder Gas Velocity Measurements Comparing Crankcase and Blower Scavenging in a Fired Two-Stroke Cycle Engine," *SAE Transactions,* no. 940401, pp. 599-618, 1994.

[58] P. C. Miles, "The History and Evolution of Optically Accessible Research Engines and Their Impact on Our Understanding of Engine Combustion," in *ASME ICEF Technical Conference*, Columbus (IN), 2014.

[59] W. Rizk, "Experimental Studies of the Mixing Processes and Flow Configurations in Two-Cycle Engine Scavenging," *Proceedings of the Institution of Mechanical Engineers,* pp. 417-437, 1958.

[60] R. R. Booy, "Evaluating Scavenging Efficiency of Two-Stroke Cycle Gasoline Engines," *SAE Technical Paper*, no. 670029, 1967.

[61] P. M. Ku and T. F. Trimble, "Scavenging Characteristics of a Two-Stroke-Cycle Engine as Determined by Skip-Cycle Operation," *Journal of Research of the National Bureau of Standards,* vol. 57.6, pp. 325-331, 1956.

[62] T. Asanuma and S. Yanagihara, "Gas Sampling Valve for Measuring Scavenging Efficiency in High-Speed Two-Stroke Engines," *SAE Transactions,* pp. 420-433, 1962.

[63] A. Kannappan, "A New Method for Evaluating the Scavenging Performance of Two-Stroke Diesel Engines," *SAE Technical Paper*, no. 640370, 1964.

[64] C. R. Nelson, "Determination of Two-Cycle Gasoline Engine Scavenging Efficiency by a Gas Sampling Technique," University of Wisconsin (MS Thesis), Madison, 1957.

[65] H. Z. Foudray and J. B. Ghandhi., "Scavenging Measurements in a Direct-Injection Two-Stroke Engine," *SAE Transactions*, no. 20034381, pp. 2195-2204, 2003.

[66] H. Wu, N. Collings, S. Regitz, J. Etheridge and M. Kraft, "Experimental Investigation of a Control Method for SI-HCCI-SI Transition in a Multi-Cylinder Gasoline Engine," *SAE International Journal of Engines*, no. 2010-01-1245, pp. 928-937, 2010.

[67] P. V. Puzinauskas, D. B. Olsen and B. D. Willson, "Mass Integration of Fast-Response NO Measurements from a Two-Stroke Large-Bore Natural Gas Engine," *International Journal of Engine Research* , vol. 4.3, pp. 233-248, 2003.

[68] M. Ioannou, G. Papalambrou, N. P. Kyrtatos, D. Larsson, S. Matlok and S. Mayer, "Crank-Angle Resolved NOx Measurements from a Specific Engine Cylinder of a Large Marine Two-Stroke Engine," *Journal of Marine Engineering & Technology*, vol. 13(2), pp. 12-20, 2014.

[69] Y. Zhang, M. Ojapah, A. Cairns and H. Zhao, "2-Stroke CAI Combustion Operation in a GDI Engine with Poppet Valves," *SAE Technical Paper*, no. 2012-01-1118, 2012.

[70] Y. Zhang and H. Zhao, "Measurement of Short-Circuiting and its Effect on the Controlled Autoignition or Homogeneous Charge Compression Ignition Combustion in a Two-Stroke Poppet Valve Engine," *Proceedings of the Institution of Mechanical Engineers. Part D: Journal of Automobile Engineering* , vol. 226.8, pp. 1110-1118, 2012.

[71] F. Pommier, "A Fundamental Study of Spark Ignition for a Large-Bore Single Cylinder Natural Gas Engine," Texas A&M University (MS Thesis), College Station, 2020.

[72] "Data Sheets," Kistler Instrument Corp..

[73] D. C. Collis and M. J. Williams., "Two-Dimensional Convection from Heated Wires at Low Reynolds Numbers," *Journal of Fluid Mechanics,* no. 6.3, pp. 357-384, 1959.

[74] "NDIR-500 User Manual," Cambustion Limited, Cambridge, UK.

[75] A. U. Bajwa and T. J. Jacobs, "Residual Gas Fraction Estimation Based on Measured Engine Parameters (Phase-III Report)," Pipeline Research Council International , 2020.

[76] "Engine Performance Application Manual," Gama Technologies, 2017.

[77] J. I. Ghojel, "Review of the Development and Applications of the Wiebe Function: A Tribute to the Contribution of Ivan Wiebe to Engine Research," *International Journal of Engine Research,* pp. 297-312, 2010.

[78] C. R. Ferguson, Internal Combustion Engines - Applied Thermosciences, New York: Wiley, 1986.

[79] A. Mashayekh, T. Jacobs, M. Patterson and J. Etcheverry., "Prediction of Air–Fuel Ratio Control of a Large-Bore Natural Gas Engine Using Computational Fluid Dynamic Modeling of Reed Valve Dynamics," *International Journal of Engine Research*, vol. 18, no. 9, pp. 900-908, 2017.

[80] A. U. Bajwa, A. Mashayekh, M. Patterson and T. Jacobs, "Interactions Among 3D, 1D and 0D Models for Natural Gas Fueled Two-Stroke SI Engines," in *THIESEL*, Valencia, 2018.

[81] A. S. Mashayekh, "Study of Conjugate Heat Transfer of a Spark-Ignited Natural Gas Engine Cylinder," Texas A&M University (Doctoral Dissertation), College Station, 2017.

[82] D. Malicke, M. Patterson and K. Ashraph, "Applying Advanced Computer Modeling To Improve Emissions And Combustion Efficiency In Large Bore 2 Cycle Engines," in *Gas Machinery Conference*, Nashville, 2011.

[83] G. P. Blair and M. C. Ashe., "The Unsteady Gas Exchange Characteristics of a Two-Cycle Engine," *SAE Transactions*, 1976.

[84] A. U. Bajwa, M. Patterson, T. Linker and T. J. Jacobs, "A New Single-Zone Multi-Stage Scavenging Model for Real-Time Emissions Control in Two-Stroke Engines," in *ASME ICEF*, Chicago, 2019.

[85] A. U. Bajwa and T. J. Jacobs, "Residual Gas Fraction Estimation Based on Measured Engine Parameters (Phase-II Report)," Pipeline Research Council International, 2019.

[86] A. U. Bajwa, T. Linker, M. A. Patterson, G. Beshouri and T. J. Jacobs, "A Study of Cyclic Combustion Variations at Lean SI Engine Operation Using High-Speed In-Cylinder CO2 Measurements," in *THIESEL*, Valencia, Spain, 2020.

[87] T. D. Fansler and M. C. Drake., Flow, Mixture Preparation and Combustion in Direct-Injection Two-Stroke Gasoline Engines. (Chapter 2 in: Flow and Combustion in Reciprocating Engines), Berlin: Springer, 2008, pp. 67-136.

[88] A. U. Bajwa, M. A. Patterson and T. J. Jacobs, "Using Gas Dynamic Models to Improve Exhaust System Design for Large-Bore Two-Stroke Engines," *International Journal of Engine Research,* 2020.

[89] J. A. Caton, "The Thermodynamic Characteristics of High Efficiency, Internal-Combustion Engines," *Energy Conversion and Management,* no. 58, pp. 84-93, 2012.

[90] R. S. Benson, P. C. Baruah and B. Whelan., "Simulation Model for a Crankcase-Compression Two-Stroke Spark-Ignition Engine Including Intake and Exhaust Systems.," *Proceedings of the Institution of Mechanical Engineers,* vol. 189, pp. 167-175, 1975.

[91] E. Mattarelli, C. A. Rinaldini and T. Savioli., "Port Design Criteria for 2-Stroke Loop Scavenged Engines," *SAE Technical Paper,* no. 2016-01-0610., 2016.

[92] T. Linker and T. J. Jacobs, "Variable Fuel Effects on Legacy Compressor Engines, Phase V - Engine Control Enhancement," Pipeline Research Council International, 2020.

[93] K. L. Wallace, "Thermodynamic Cycle Simulation of a Large Bore, Single Cylinder, 2-Stroke, Natural Gas Engine for Predicting Emissions of Oxides of Nitrogen," Texas A&M Univerity (MS Thesis) , College Station , 2020.

[94] G. Beshouri and B. Goffin, "Starting Damage on Legacy Pipeline Engines," Pipeline Research Council International , 2018.

[95] T. Linker and T. J. Jacobs, "Variable Fuel Effects on Legacy Compressor Engines, Phase IV - Predictive NOx Emissions Modeling," Pipeline Research Council International, 2019.

[96] J. W. Ladd, D. B. Olsen and G. Beshouri, "Evaluation of Operating Parameters and Fuel Composition on Knock in Large Bore Two-Stroke Pipeline Engines," *Fuel*, pp. 165-174, 2017.

[97] T. Linker, "Predictive NOx Emissions Modeling for a Large Bore, Lean-Burn, Integral Compressor Engine," Texas A&M University (MS Thesis), College Station, 2019.

[98] K. Fieseler, "Simulation Development of a Large Bore Two Stroke Integral Compressor Engine to Study Variable Natural Gas Composition Effects," Texas A&M University (MS Thesis), College Station, 2018.

APPENDIX A: TRAPPED RESIDUAL FRACTION CALCULATION USING CYLINDER CO_2 CONCENTRATION

The following section presents the derivation of the method used to calculate TRF from measured in-cylinder CO_2 concentration data. The method was needed to account for reduction in trapped CO_2 concentration because of fuel injection.

Figure 123 shows the makeup of cylinder gases at three stages: (I) before exhaust port opening, (II) after gas exchange (EPC) but before fuel injection, and (III) after fuel injection but before combustion.

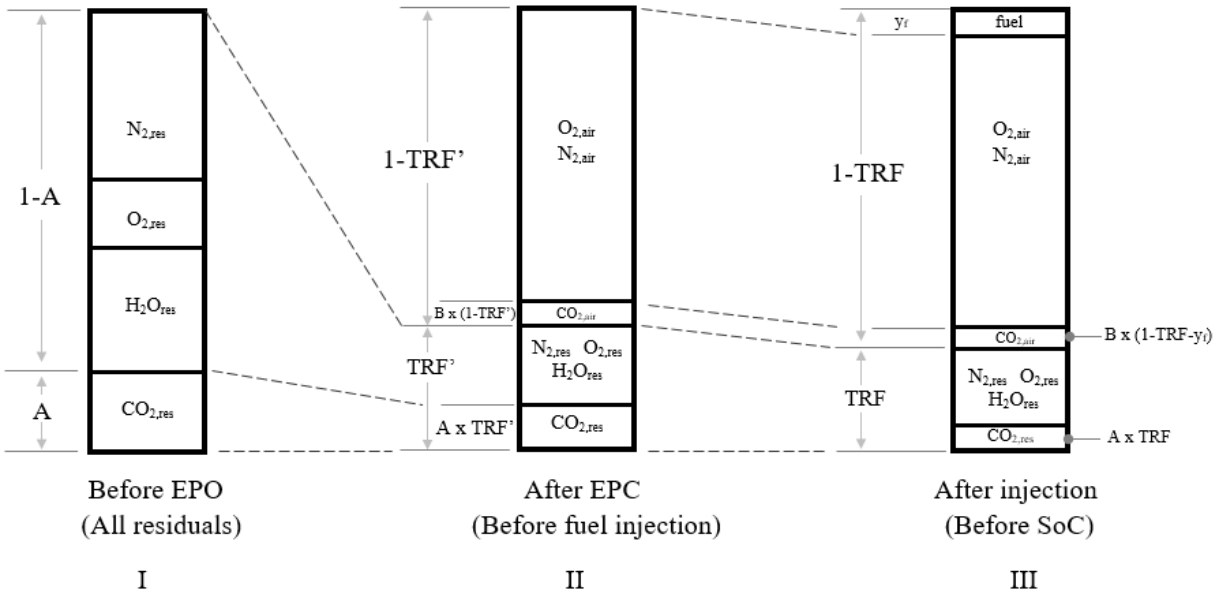

Figure 123: Cylinder concentrations before and after gas exchange.

Known:

- CO_2 concentration after combustion (before EPO): 'A' (from experimental data)
- CO_2 concentration before combustion (after injection): 'X' (from experimental data - Figure 49)
- Concentration of CO_2 in air: B ~ 400 ppm
- Mass of fuel injected (from experimental data)

At II:

$$\mathrm{TRF}' = \frac{\mathrm{m_{res}}}{\mathrm{m_{res}} + \mathrm{m_{air}}}$$

$$\mathrm{y'_{res}} = \frac{\frac{\mathrm{m_{res}}}{\mathrm{MW_{res}}}}{\frac{\mathrm{m_{res}} + \mathrm{m_{air}}}{\mathrm{MW_{mix,II}}}} \approx \mathrm{TRF}'$$

Assuming that the mixture and the residual molecular weights are approximately equal and close to that of air.

$$[\mathrm{CO_2}]_{\mathrm{II}} = \mathrm{X} = \mathrm{A\ x\ TRF}' + \mathrm{B}(1 - \mathrm{TRF}')$$

$$[\mathrm{CO_2}]_{\mathrm{II}} = \mathrm{A\ x\ TRF}' + \mathrm{B} - \mathrm{B\ x\ TRF}'$$

$$\mathrm{TRF}' = \frac{[\mathrm{CO_2}]_{\mathrm{II}} - \mathrm{B}}{\mathrm{A} - \mathrm{B}}$$

At III:

$$\mathrm{TRF} = \frac{\mathrm{m_{res}}}{\mathrm{m_{res}} + \mathrm{m_{air}} + \mathrm{m_{fuel}}}$$

$$\mathrm{y_{res}} = \frac{\frac{\mathrm{m_{res}}}{\mathrm{MW_{res}}}}{\frac{\mathrm{m_{res}} + \mathrm{m_{air}} + \mathrm{m_{fuel}}}{\mathrm{MW_{mix,III}}}} \approx \mathrm{TRF}$$

Assuming that the addition of fuel does not significantly change the mixture's molecular weight.

$$[\mathrm{CO_2}]_{\mathrm{III}} = \mathrm{A\ x\ TRF} + \mathrm{B}(1 - \mathrm{TRF} - \mathrm{y_f})$$

$$[\mathrm{CO_2}]_{\mathrm{III}} = \mathrm{A\ x\ TRF} + \mathrm{B} - \mathrm{B\ x\ TRF} - \mathrm{B\ x\ y_f}$$

$$\mathrm{TRF} = \frac{[\mathrm{CO_2}]_{\mathrm{III}} - \mathrm{B} + \mathrm{B\ x\ y_f}}{\mathrm{A} - \mathrm{B}}$$

$$\mathrm{TRF} = \frac{[\mathrm{CO_2}]_{\mathrm{III}} - \mathrm{B}}{\mathrm{A} - \mathrm{B}} + \frac{\mathrm{B\ x\ y_f}}{\mathrm{A} - \mathrm{B}}$$

Based on the old TRF calculation method (Equation 30) in which it is assumed that the pre-combustion minimum CO_2 concentration (X) does not have any fuel:

$$\frac{[\mathrm{CO_2}]_{\mathrm{III}} - \mathrm{B}}{\mathrm{A} - \mathrm{B}} = \frac{\mathrm{X} - \mathrm{B}}{\mathrm{A} - \mathrm{B}} = \mathrm{TRF}'$$

Therefore,

$$\mathrm{TRF} = \mathrm{TRF}' + \frac{\mathrm{B\ x\ y_f}}{\mathrm{A} - \mathrm{B}} \quad (\mathrm{eq\ A1})$$

$$\mathrm{TRF} - \mathrm{TRF}' = \frac{\mathrm{B\ x\ y_f}}{\mathrm{A} - \mathrm{B}}$$

$$\Delta \mathrm{TRF}(\%\ \mathrm{pts}) = \frac{\mathrm{B\ x\ y_f\ x\ 100}}{\mathrm{A - B}}$$

Where A, B and y_f are in %.

Sample Calculation:

Assume: B = 0.04%, A = 8%, y_f = 5%

$$\Delta \mathrm{TRF}(\%\ \mathrm{pts}) = \frac{0.04\ \mathrm{x}\ 5\ \mathrm{x}\ 100}{8 - 0.04}$$

$$\Delta \mathrm{TRF}(\%\ \mathrm{pts}) = 2.5\ \%\ \mathrm{pts}$$

This shows that there is a potential for introducing significant errors if the reduction in CO_2 concentration because of fuel injection is disregarded.

Solution Method:

Solve iteratively. First, assume that there is no fuel dilution to get TRF'. Use TRF' to calculate trapped mass and mole fraction of fuel in the trapped mixture; plug that into equation (A1) to get TRF. Repeat the process till convergence. Normally requires 2 to 3 iterations.

APPENDIX B: AIR FLOW CALCULATIONS

Exhaust O_2 concentration is calculated using the mass of fuel delivered (m_f), trapped residual fraction (TRF), and short-circuiting fraction (x_{short}). In addition to these parameters, the mass flow of air through the intake ports ($m_{in,net}$) , which is assumed to be equal to the mass flow through the exhaust ports, is needed. Initially, a guessed value is used to seed the iterative process. The main calculation steps for exhausted O_2 are given below. The subscript 'd' in the following equations stands for delivered, 'tot' for total, 'trap' for trapped, 'short' for short-circuited, 'f' for fuel, 'res' for residual gases, 'u' for unburned gases, and 'fresh' for the fresh charge (including injected fuel) delivered during gas exchange and fuel delivery.

$$m_{d,tot} = m_f + m_{in,net} = m_{exhausted} \quad \text{B1}$$

$$m_{fresh,trap} = m_{d,tot}(1 - x_{short}) \quad \text{B2}$$

$$m_{res,trap} = \frac{m_{fresh,trap}.\,TRF}{1 - TRF} \quad \text{B3}$$

$$m_{O_2,short} = [m_{O_2\ \text{in delivered air}}]\ x_{short} \quad \text{B4(a)}$$

$$m_{O_2,short} = \left[m_{in,net}\left(0.21\frac{MW_{O_2}}{MW_{air}}\right)\right] x_{short} = \left[m_{in,net}(0.23)\right] x_{short} \quad \text{B4(b)}$$

$$N_{O_2,u} = \left(\frac{2}{TER} - 2\right) N_f \quad \text{B5}$$

$$m_{O_2,u} = MW_{O_2} N_{O_2,u} \quad \text{B6}$$

$$m_{O_2,\text{exhausted}} = m_{O_2,u}(1 - \text{TRF}) + m_{O_2,\text{short}} \quad \text{B7}$$

$$N_{O_2,\text{exhausted}} = \frac{m_{O_2,\text{exhausted}}}{MW_{O_2}} \quad \text{B8}$$

$$N_{\text{tot,exhausted (dry)}} = \frac{m_{d,\text{tot}}}{MW_{\text{air}}} - N_{H_2O,\text{exhausted}} = \frac{m_{d,\text{tot}}}{MW_{\text{air}}} - 2N_f \quad \text{B9}$$

$$\mathbf{[O_2]_{exh} = \frac{N_{O_2,exhausted}}{N_{tot,exhausted\ (dry)}}} \quad \textbf{B10}$$

Equation (B5) is obtained from the following lean combustion reaction for methane:

$$CH_4 + \frac{2}{\text{TER}}(O_2 + 3.76N_2) \rightarrow CO_2 + 2H_2O + 2(3.76)N_2 + \left(\frac{2}{\text{TER}} - 2\right)(O_2 + 3.76N_2) \quad \text{B11}$$

In equation B7, only a fraction (1-TRF) of the unburned oxygen is assumed to be exhausted. The rest is assumed to stay back in the cylinder as air in the trapped residuals. Figure 124 shows an outline of the algorithm used to calculate air flow rate using measured oxygen data. The major steps followed are summarized below:

1. Guess mass of air delivered
2. Use short-circuiting fraction to calculate mass of trapped air
3. Use TRF to calculate mass of trapped residuals
4. Calculate mass of air in trapped residuals
5. Calculate total trapped air (3+4)

6. Calculate mass of fuel that takes part in combustion (mass of fuel delivered x combustion efficiency)
7. Calculate TER using effective mass of fuel and total trapped air
8. Use lean combustion equation for methane to calculate excess O_2
9. Calculate exhaust O_2 concentration from excess and short-circuited O_2
10. Compare calculated and measured exhaust O_2 concentrations
11. Iteratively change mass of delivered air until the two O_2 concentrations match

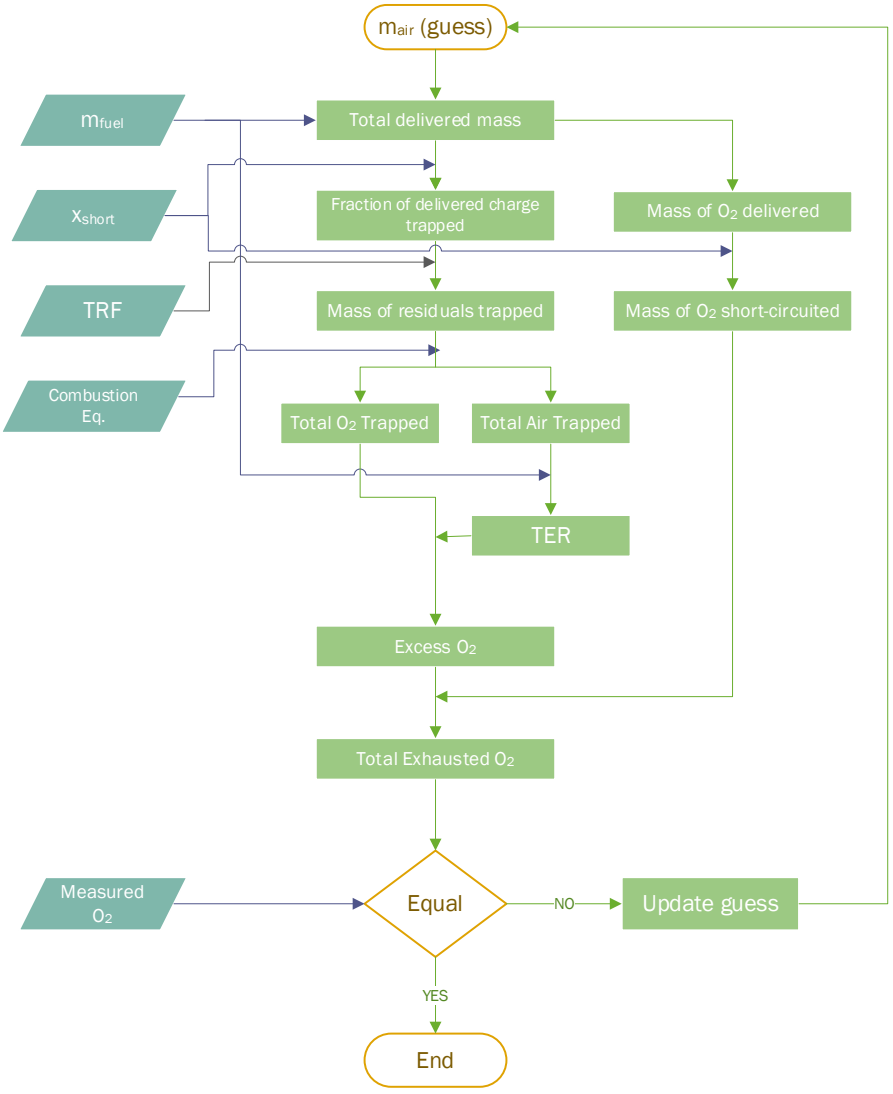

Figure 124: Flowchart showing the air flow rate calculating algorithm.

APPENDIX C: SLOW SPEED EXPERIMENTAL RESULTS

Figure 125 to Figure 132 show the slow speed data (manifold temperatures, fuel flow rate, and emissions) recorded for all tested cases during the scavenging experiments with direct fuel injection. For Figure 125 to Figure 127, the error bars show the difference in recorded data between two experimental runs; while for Figure 128 to Figure 132, the error bars show the maximum and minimum recorded values from two experimental runs. The markers in all the figures show the mean for two experimental runs. Figure 134 to Figure 137 show parameters calculated from high-speed pressure data.

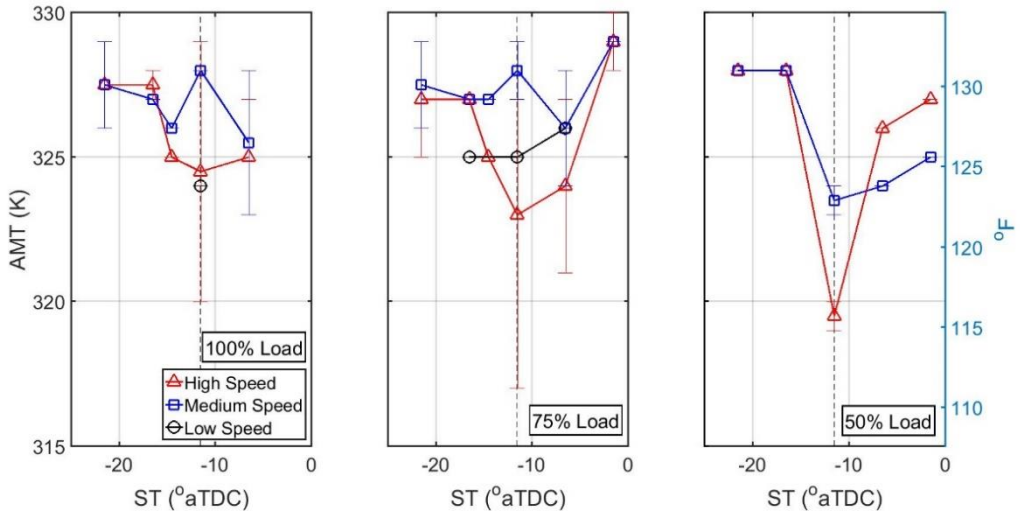

Figure 125: Air manifold temperature at different speeds, loads, and spark timings.

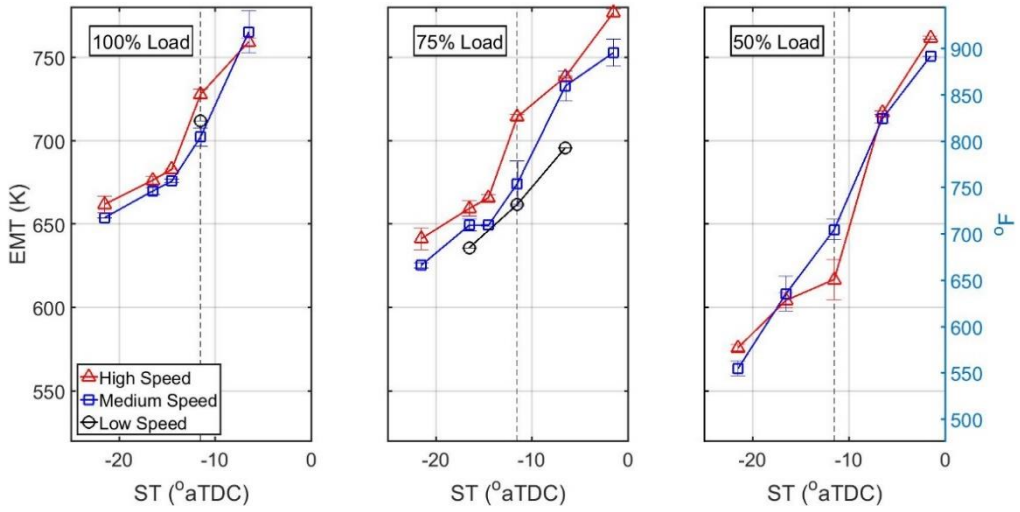

Figure 126: Exhaust manifold temperature at different speeds, loads, and spark timings.

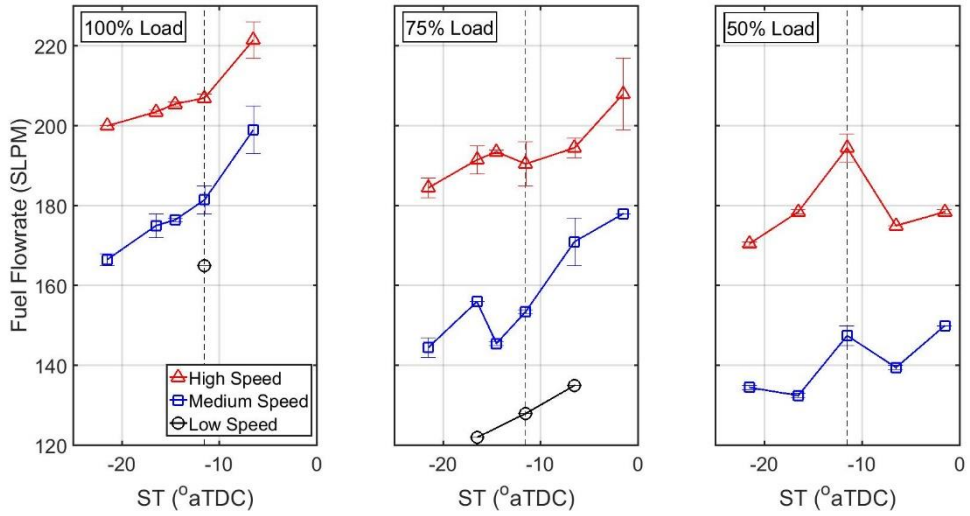

Figure 127: Fuel flowrate at different speeds, loads, and spark timings.

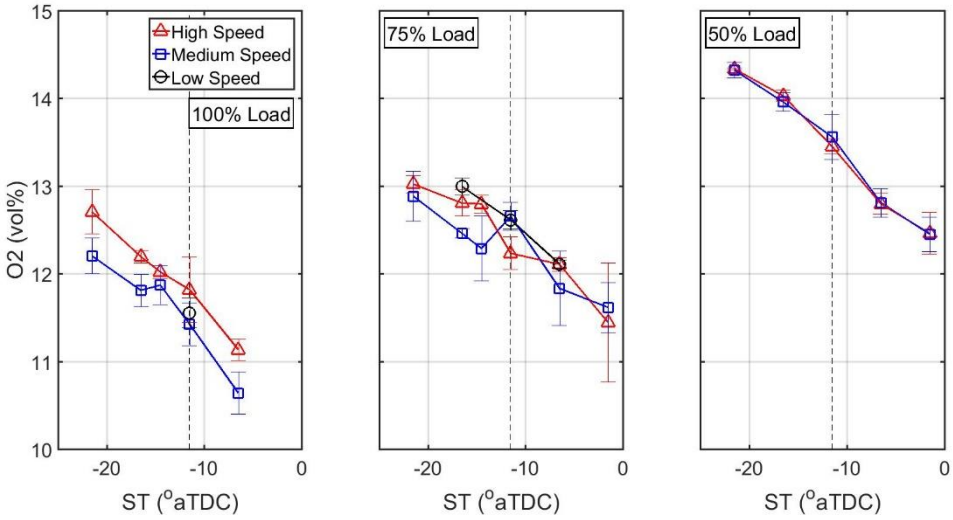

Figure 128: Exhaust O_2 concentration at different speeds, loads, and spark timings.

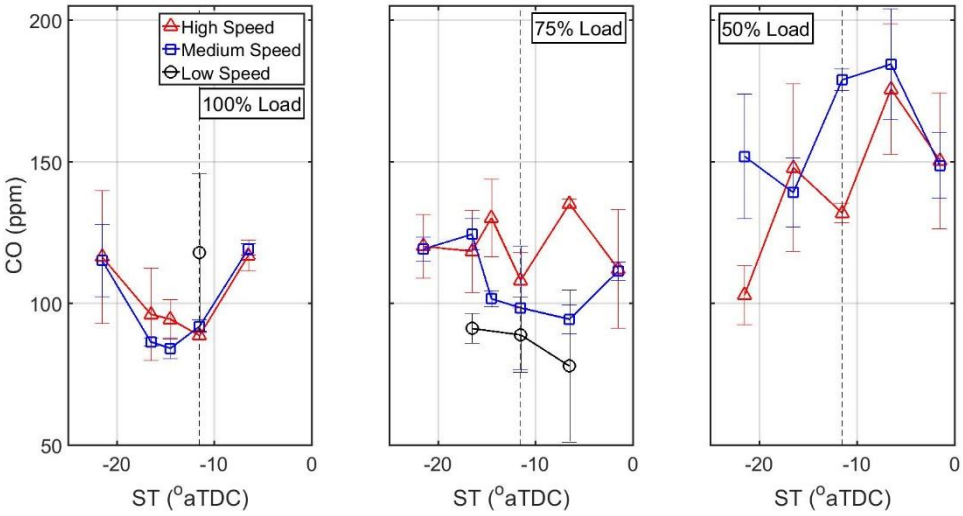

Figure 129: Exhaust CO concentration at different speeds, loads, and spark timings.

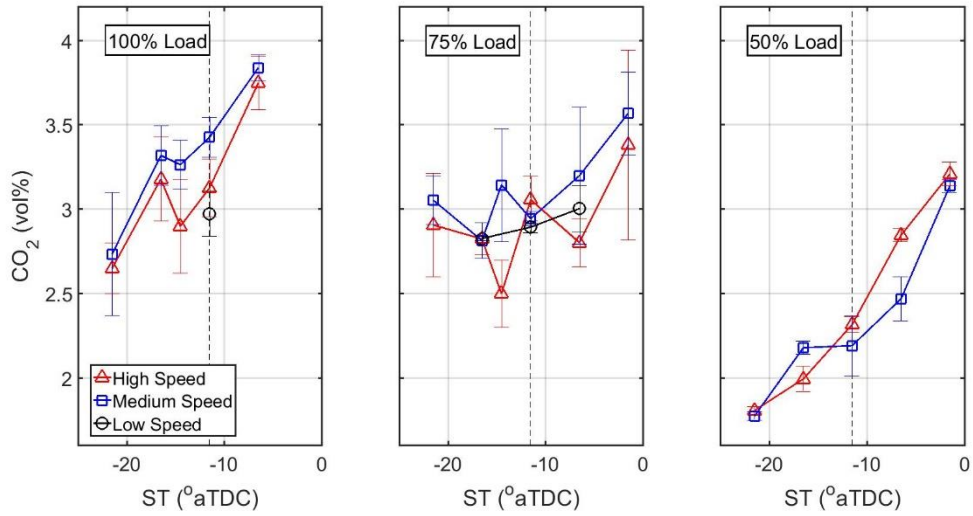

Figure 130: Exhaust CO_2 concentration at different speeds, loads, and spark timings.

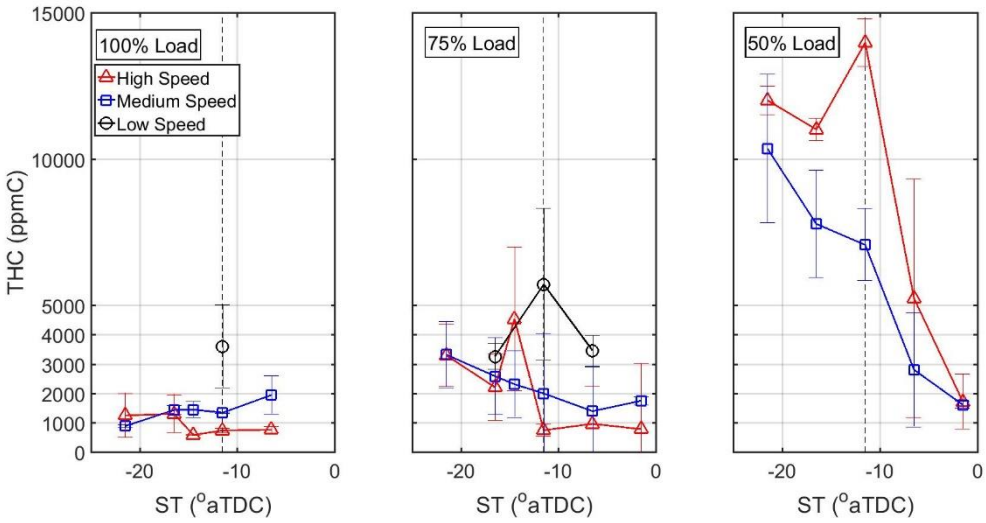

Figure 131: Exhaust THC concentration at different speeds, loads, and spark timings.

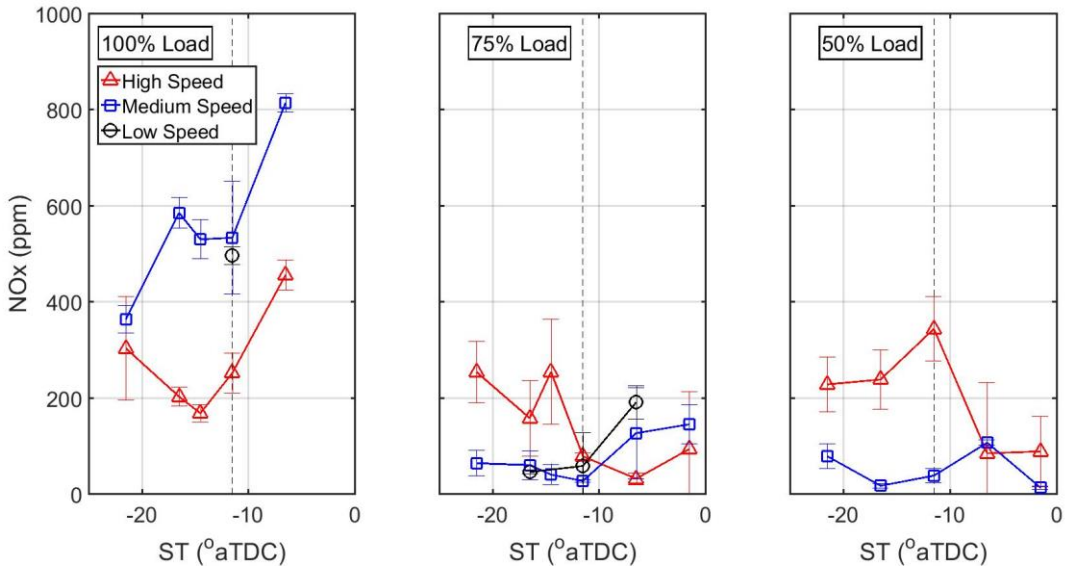

Figure 132: Exhaust NO_x emissions at different engine speeds, loads, and spark timings.

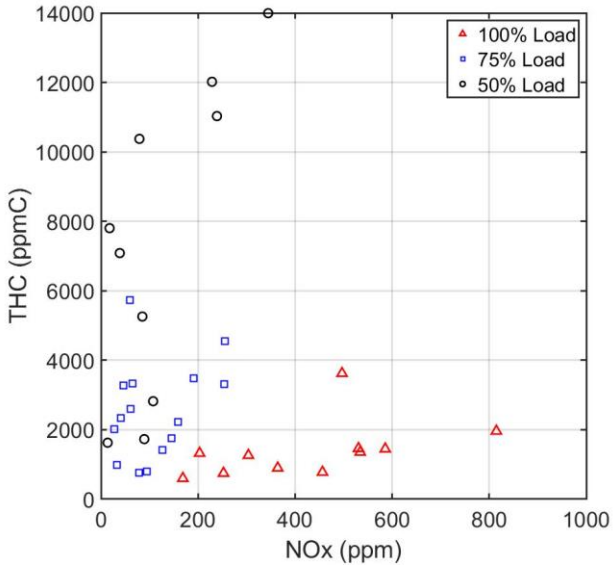

Figure 133: Total hydrocarbons and NO_x emissions showing the tradeoff between the two species.

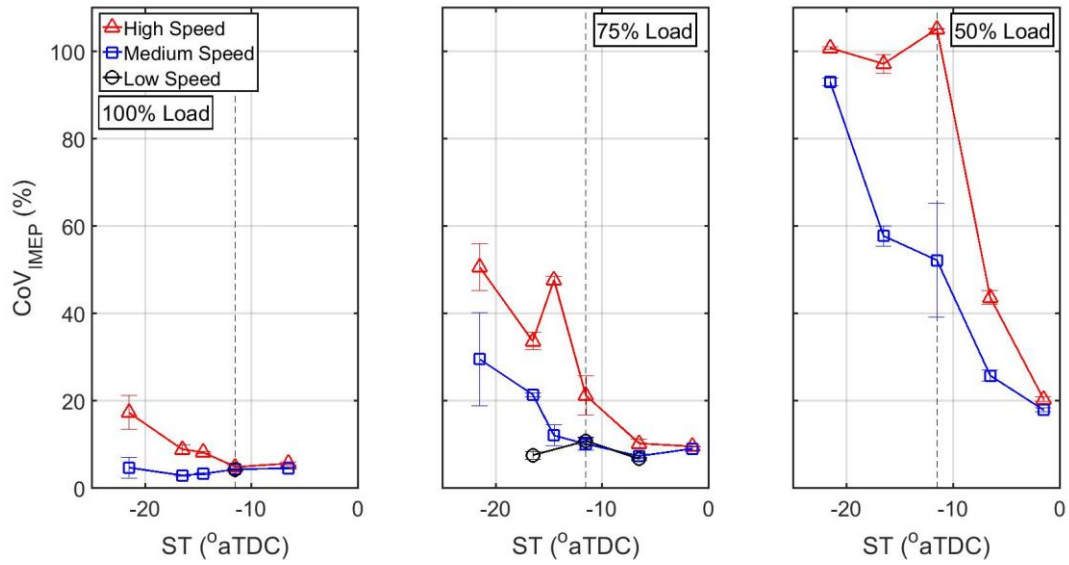

Figure 134: Coefficient of variation of indicated mean effective pressure at different engine speeds, loads, and spark timings.

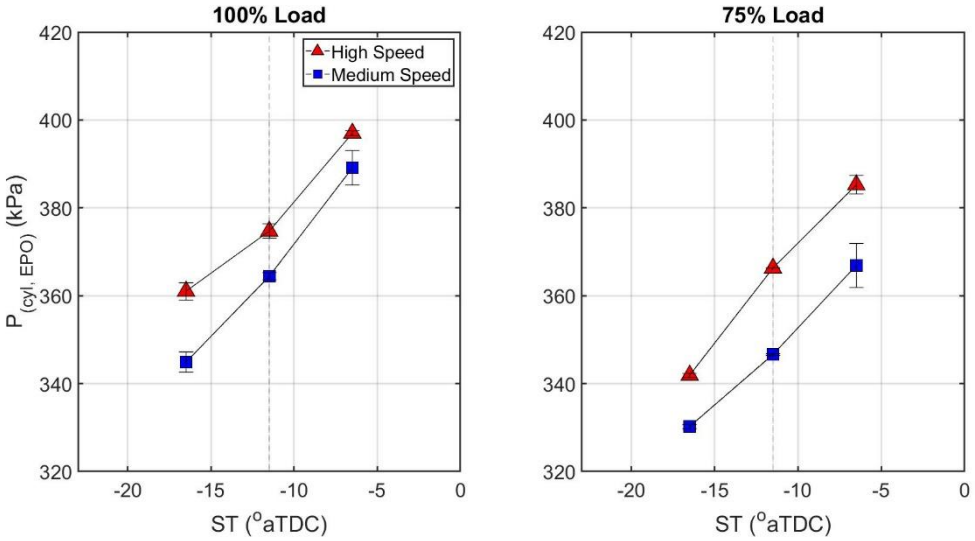

Figure 135: Cylinder pressure at EPO for different engine speeds, loads, and spark timings.

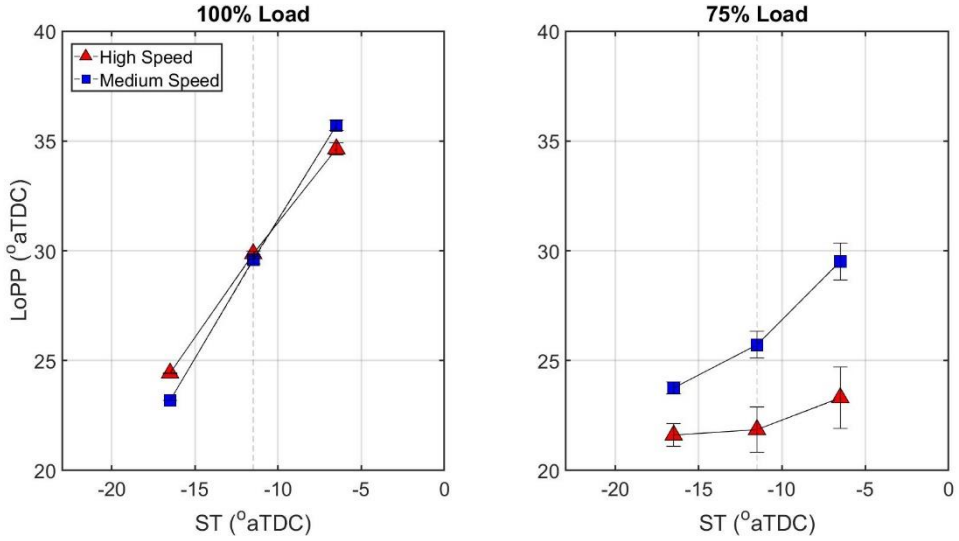

Figure 136: Location of peak cylinder pressure for different engine speeds, loads, and spark timings.

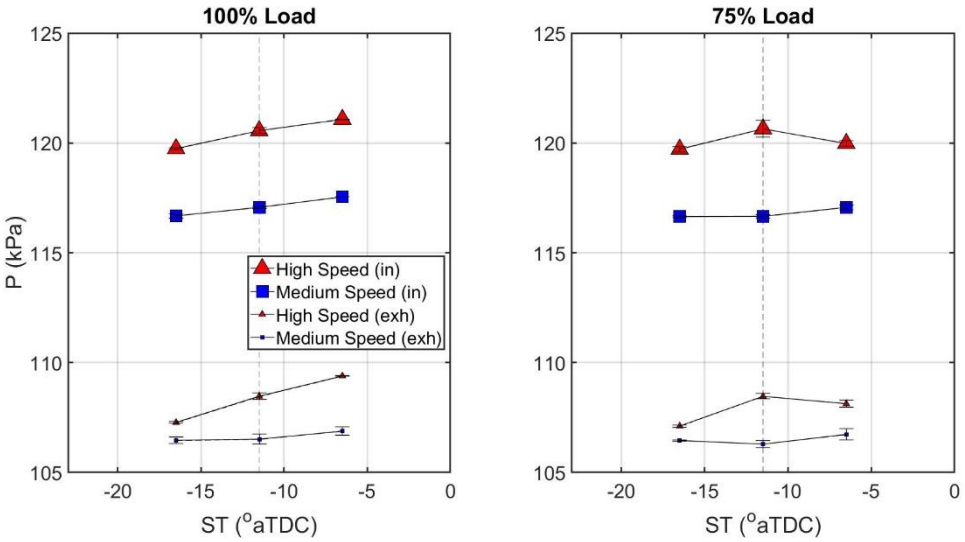

Figure 137: Average intake and exhaust pressures for different engine speeds, loads, and spark timings. Intake pressure is averaged from IPO to IPC. Exhaust pressure is averaged from EPO to EPC.

APPENDIX D: HIGH SPEED EXPERIMENTAL RESULTS

9.1. Sample Results

The following section shows some experimental results to demonstrate the nature of the raw collected data. The data was processed and cleaned before being used for any analysis.

Figure 138 and Figure 139 represent data for the eight high speed parameters on an ensemble averaged basis (thick black curves) for advanced and retarded cases, respectively at 75% load condition. Figure 140 shows time series data for 10 consecutive cycles at the standard operating case (525 RPM, 100 % load, 11.5^{o} BTDC ST). Such data is available for all test cases listed in the experimental test matrix (Table 2).

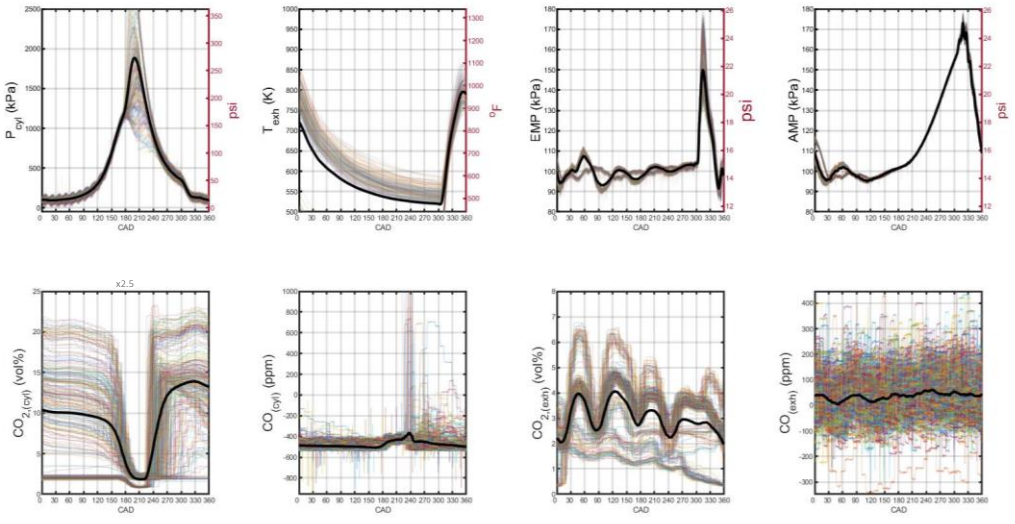

Figure 138: Ensemble averaged high speed data at 75% load, 10 CAD advanced ST, and 525 RPM.

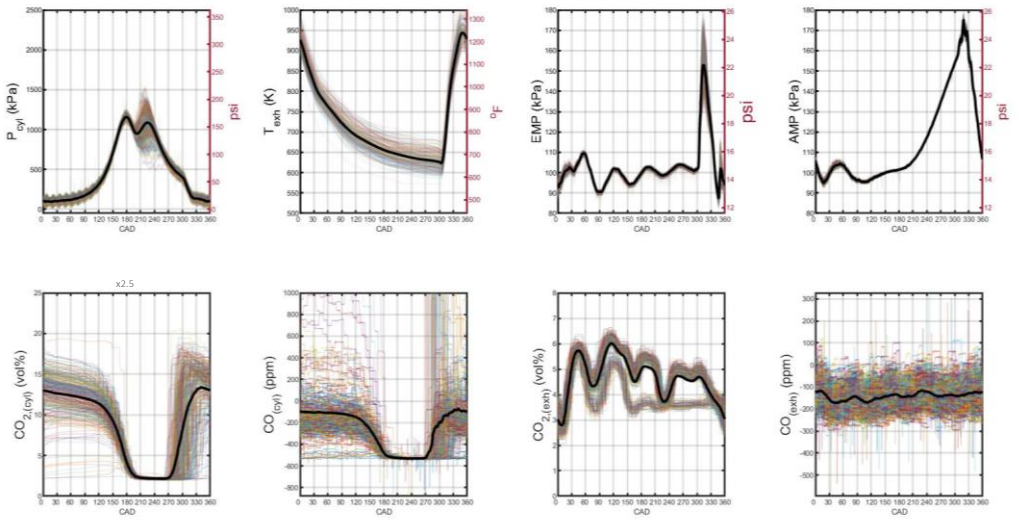

Figure 139: Ensemble averaged high speed data at 75% load, 10 CAD retarded ST, and 525 RPM.

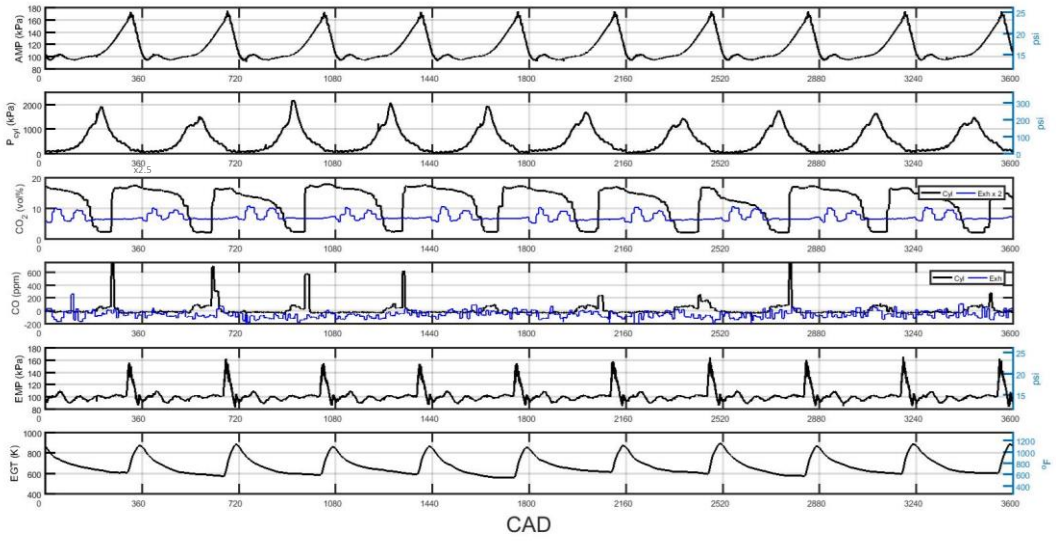

Figure 140: Time-resolved high speed data at 100% load, standard ST, and 525 RPM.

9.2. High speed Exhaust Temperature Results

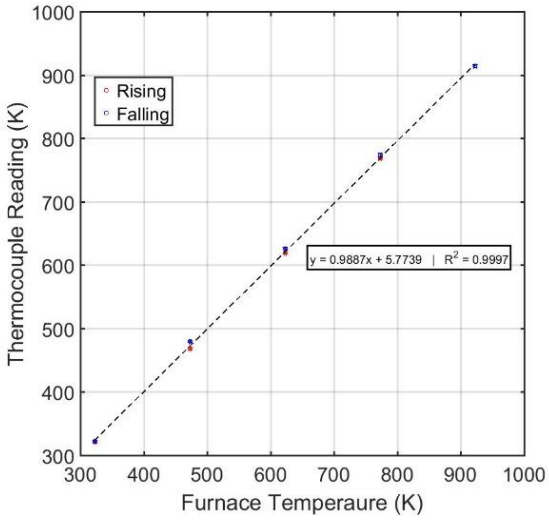

Figure 141: Calibration curve for the high speed thermocouple (TC).

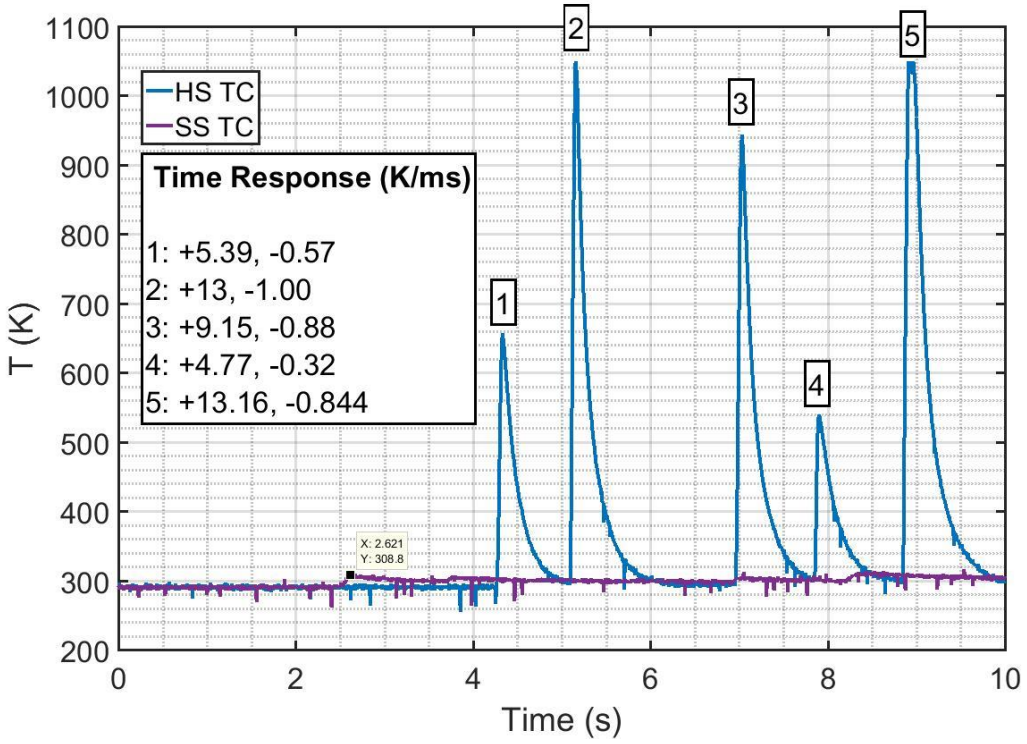

Figure 142: Response of the high speed (HS) TC to a lighter flame being swept to and fro across its tips at ~ 1.5 m/s. 'SS' are asynchronous measurements from a standard slow speed thermocouple.

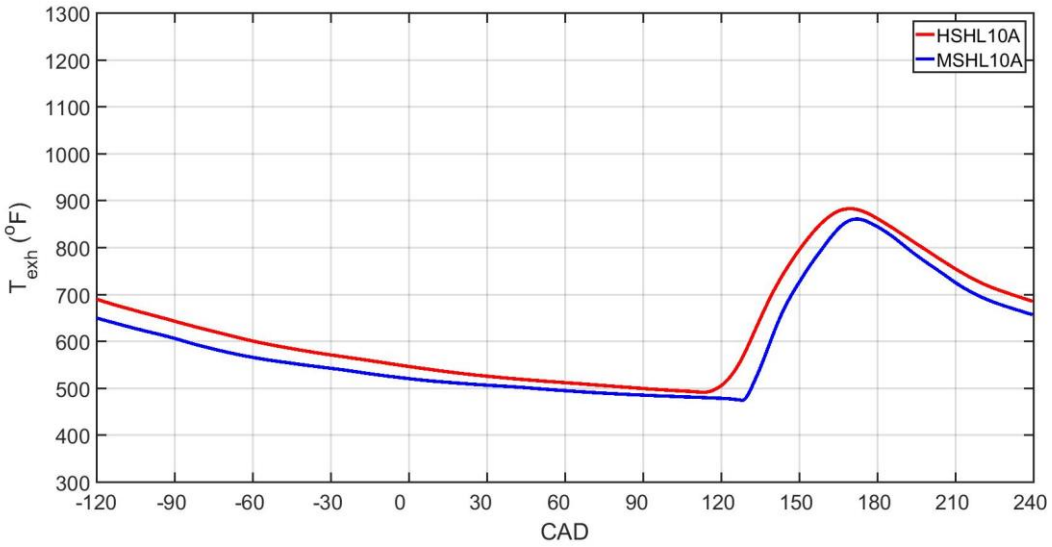
HSHL10A
MSHL10A
T_{exh} (^{o}F)
CAD
1300
1200
1100
1000
900
800
700
600
500
400
300
-120
-90
-60
-30
0
30
60
90
120
150
180
210
240

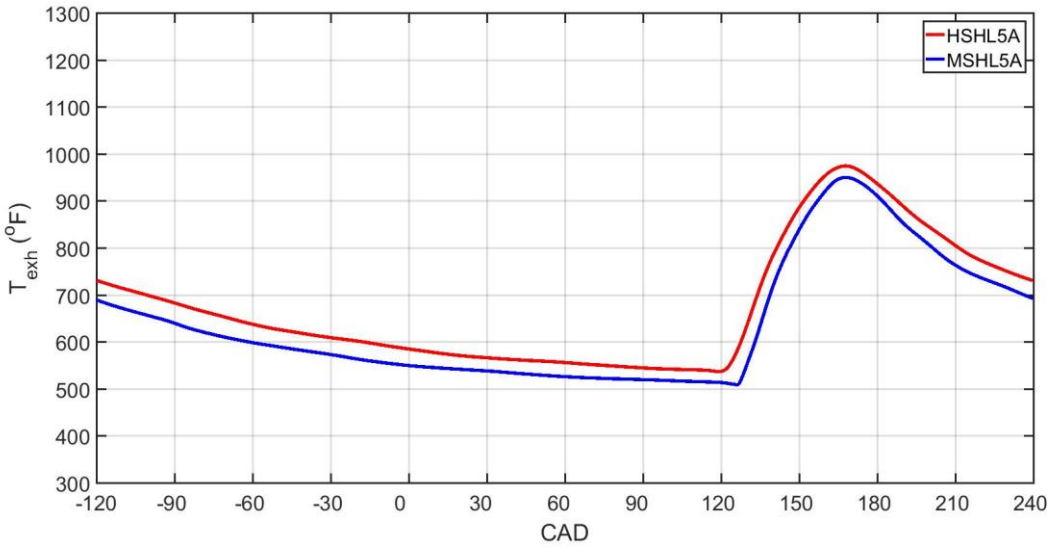
HSHL5A
MSHL5A
T_{exh} (^{o}F)
CAD
1300
1200
1100
1000
900
800
700
600
500
400
300
-120
-90
-60
-30
0
30
60
90
120
150
180
210
240

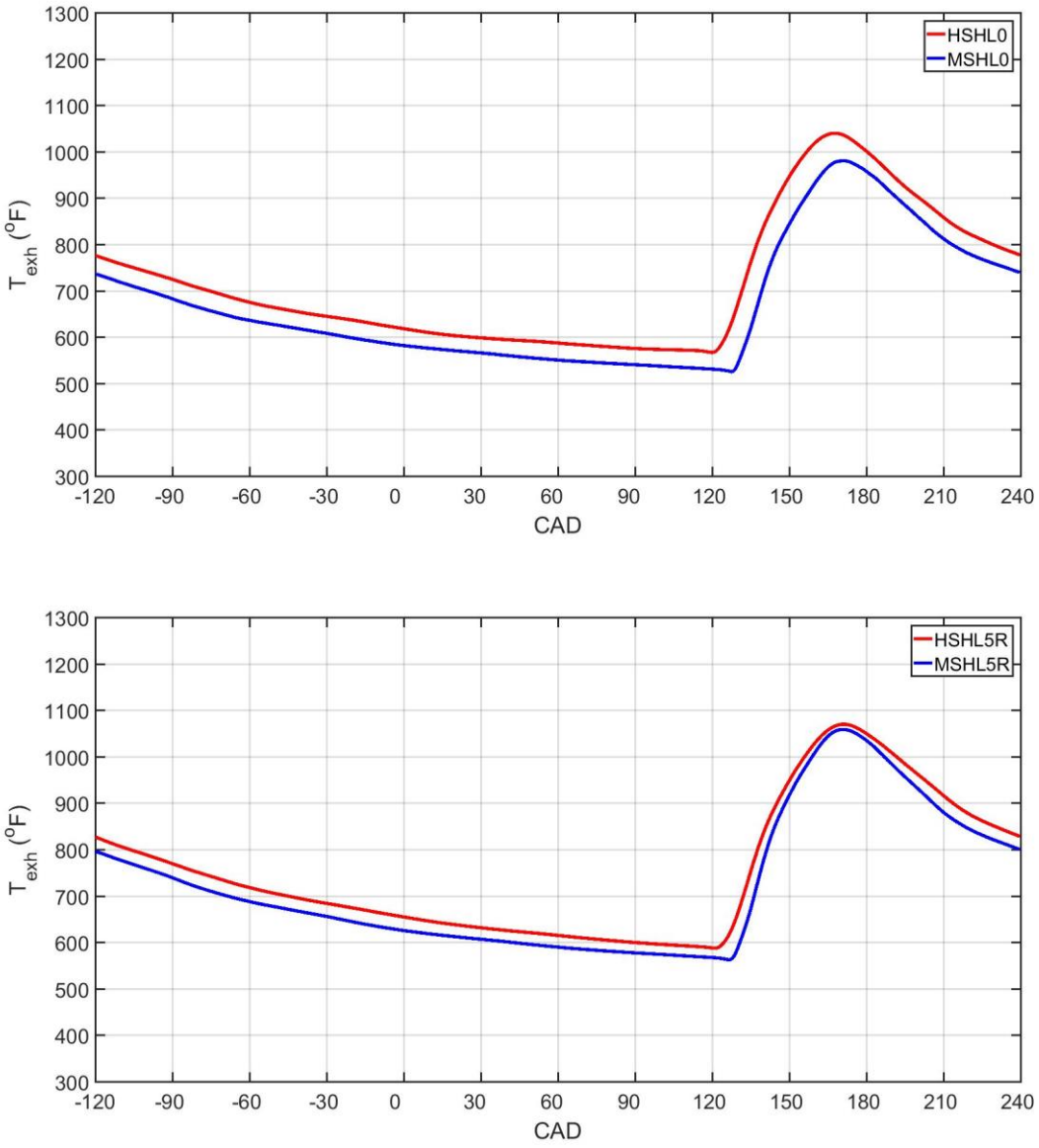

Figure 143: Ensemble averaged high speed exhaust temperature at different engine operating points. 120 CAD is EPO. (Key: HS – high speed, MS – medium speed, HL – high load, TQL – three quarter load, R – retarded, A- advanced)

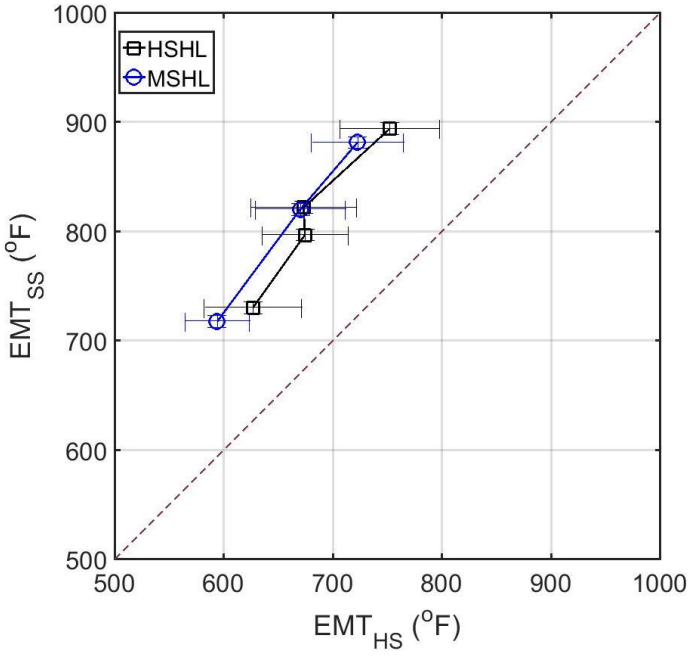

Figure 144: Comparison of slow speed exhaust temperature and high speed exhaust temperature averaged over the entire cycle.

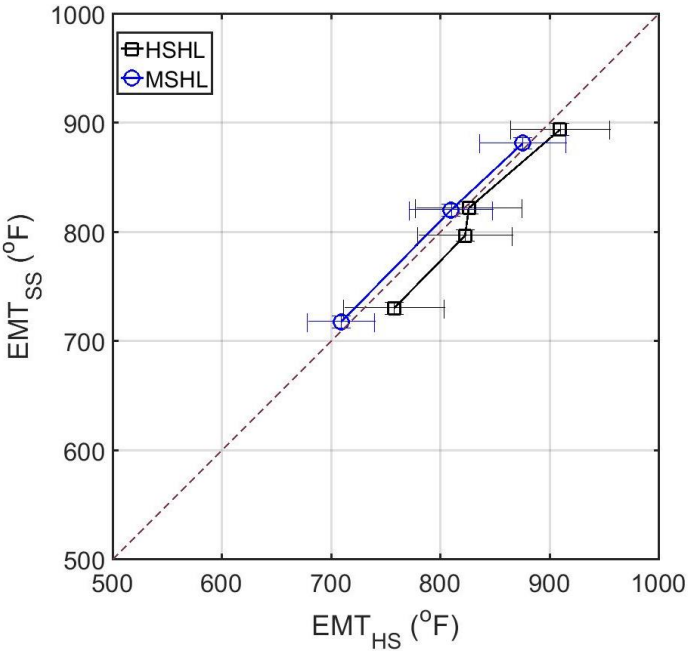

Figure 145: Comparison of slow speed exhaust temperature and high speed exhaust temperature averaged from EPO to EPC.

APPENDIX E: PRESSURE-BASED MASS FLOW CALCULATIONS

Prior to calculating air flow using exhaust O_2 measurement, a pressure-based flow calculation approach was tried. The method did not produce acceptable results and was therefore not pursued further. Details of the method are listed here for the record so that future researchers trying to implement same/similar methods will be aware of the challenges associated with implementing such methods.

Mass flow of air into the cylinder was calculated from experimental air manifold and cylinder pressures using the following gas dynamic equations:

$$\frac{dm}{dt} = \frac{C_D A_R p_o}{\sqrt{RT_o}} \left(\frac{p_T}{p_o}\right)^{\frac{1}{k}} \sqrt{\left\{\frac{2k}{k-1}\left[1 - \left(\frac{p_T}{p_o}\right)^{\frac{k-1}{k}}\right]\right\}}$$

$$\frac{dm}{dt} = \frac{C_D A_R p_o}{\sqrt{RT_o}} (k)^{\frac{1}{2}} \left\{\frac{2}{k+1}\right\}^{\frac{k+1}{2(k-1)}} \quad \text{when} \quad \frac{p_T}{p_o} \leq \left\{\frac{2}{k+1}\right\}^{\frac{k}{(k-1)}}$$

Experimental steady state air manifold temperature was used for the upstream temperature during regular flow and high speed exhaust manifold temperature was used to represent cylinder temperature during backflow. The specific heat ratio was assumed to be 1.4. Discharge coefficients were calculated by matching mass flow calculation results to those obtained from a CFD study on the same engine [80]. The results are shown in Figure 146.

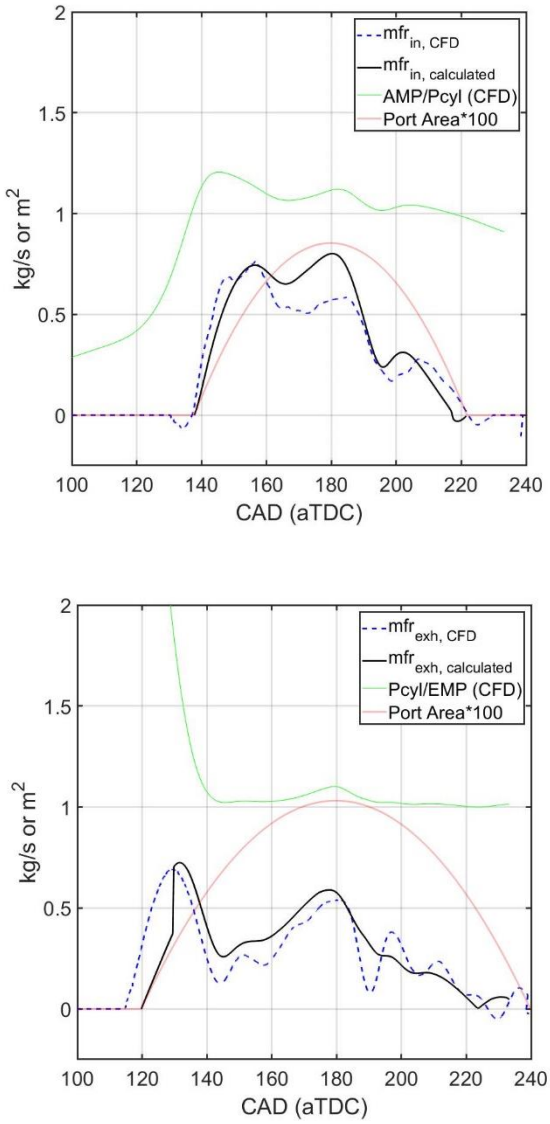

Figure 146: Intake and exhaust flow rates from pressure-based calculations using discharge coefficients of 0.6 (forward) and 0.8 (reverse) compared to CFD results.

The problem encountered with this method was obtaining accurate absolute cylinder pressure, which was needed for accurately calculating air mass flow across the cylinder. The weakest link in this process was the cylinder pressure (P_{cyl}), which was measured by a piezoelectric transducer on a relative basis; and was then converted to

absolute pressure using a datum pressure value. Results from exploratory experiments in which the engine was run unloaded at slow speed (300 to 350 RPM) suggested that the best value to peg P_{cyl} would be the air manifold pressure (AMP) at BDC. AMP was measured using a piezoresistive transducer on an absolute basis. Doing so gave pressure reference values of around 106 kPa, 101 kPa, and 98 kPa for the high, medium, and low speed cases, respectively. This, and the resulting effects on the delivered mass, are shown in Figure 147. The sharp increase in AMP from 450 RPM to 525 RPM leads to an unrealistic decrease in intake mass flows if P_{cyl} is pegged to AMP at BDC. This is because the $AMP_{(BDC)}$ based P_{cyl} pegging exercise results in higher pressures downstream of the intake port during initial portions of the intake process (IPO to BDC).

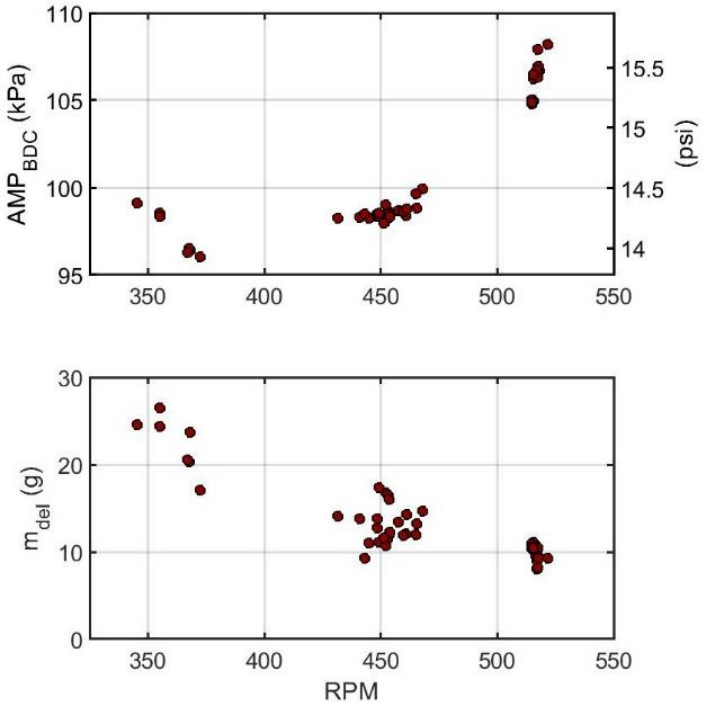

Figure 147: Intake pressure at BDC and calculated air mass delivered per cycle as a function of engine speed.

Because of the uncertainty in obtaining a correct datum for pegging cylinder pressure measurements and, to a lesser extent, the lack of confidence in discharge coefficient values, this air flow calculating approach was abandoned. The choice of upstream temperature was probably a tertiary source of error as well. Figure 148 shows an example of intake and exhaust flow rate calculations performed on a cycle resolved basis.

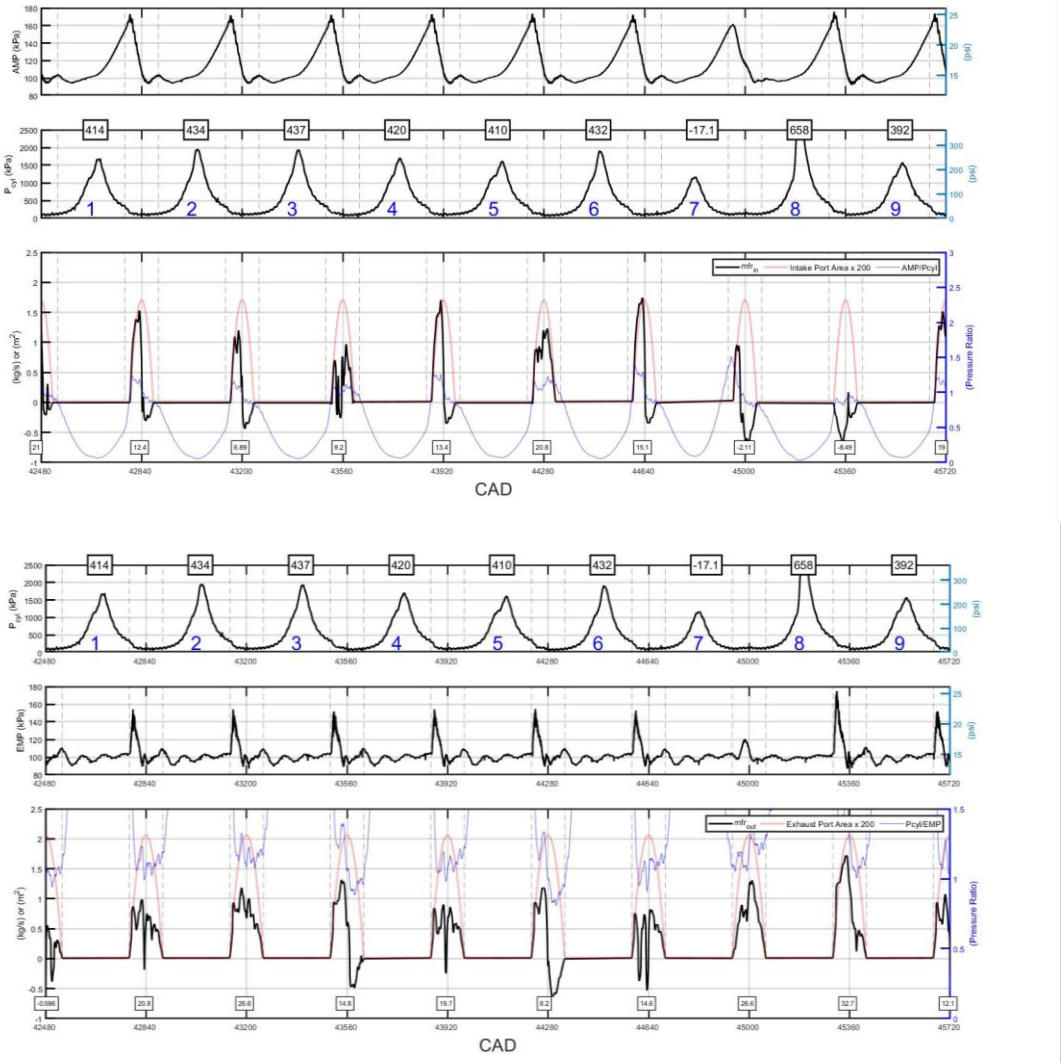

Figure 148: Intake and exhaust mass flow rate results on a cycle resolved basis.

APPENDIX F: UNCERTAINTY ANALYSIS

Rule for combination of errors:

$$Z = F(X1, X2, \dots)$$

$$dZ = \sqrt{\left(\frac{\partial F}{\partial X1}\right)^2 dX1^2 + \left(\frac{\partial F}{\partial X2}\right)^2 dX2^2 + \cdots}$$

Calculating uncertainty in TER:

$$TER = 17.2 \frac{m_{f,trap}}{m_{air,trap}}$$

Using the error combination rule:

$$d(TER) = \sqrt{\left(\frac{17.2}{m_{air,trap}}\right)^2 dm_{f,trap}^2 + \left(\frac{17.2\, m_{f,trap}}{m_{air,trap}^2}\right)^2 dm_{air,trap}^2}$$

The functions (F) used to calculate $d(m_{air,trap})$ and $d(m_{f,trap})$ are listed below.

F1: $m_{f,del\ per\ cycle}(g) = 0.663 \frac{Q_{fuel}(SLPM)}{RPM}$

F2: $m_{f,trap}(g) = m_{f,del\ per\ cycle}$

F3: $m_{air,del\ per\ cycle}(g) = \frac{1770 + 1808\, \Delta P_{in}("H_2O)}{RPM}$

F4: $m_{air,trap}(g) = m_{air,del\ per\ cycle}\, \eta_{trap}$

F5: $m_{res,trap}(g) = TRF\, m_{total,trap}$

The following assumptions are used in the d(TER) calculations with the aforelisted F's:

- All delivered fuel is trapped
- Neglecting air from residuals
- Uncertainty in trapping efficiency is 1%-pt
- Least count of manometer used for air flow measurement is 0.1"H_2O
- Uncertainty in RPM measurement is 3 RPM
- Uncertainty in fuel flow measurement is 4 SLPM
- Uncertainty in TRF is defined by the 95% CI

9.3. Sensitivity Analysis (Scavenging Curve Shape)

The sensitivity of various gas flow parameters (total delivered mass, total trapped mass, TRF, and TER) to the shape of the scavenging curve is studied for the HS-HL-0 case. This is done by perturbing *EngCylScavFunction* sub-model parameters (transition point, anchor point, and shape factor) from a reference value. The reference scavenging profile used is adapted from the hybrid model results by pulling transition and anchor points from it. Results of this analysis are shown in Figure 149 to Figure 151. Scavenging results are found to be more sensitive to changes in shape factor and anchor point compared to transition point changes. This is because changing the transition point minimally affects the scavenging curve shape.

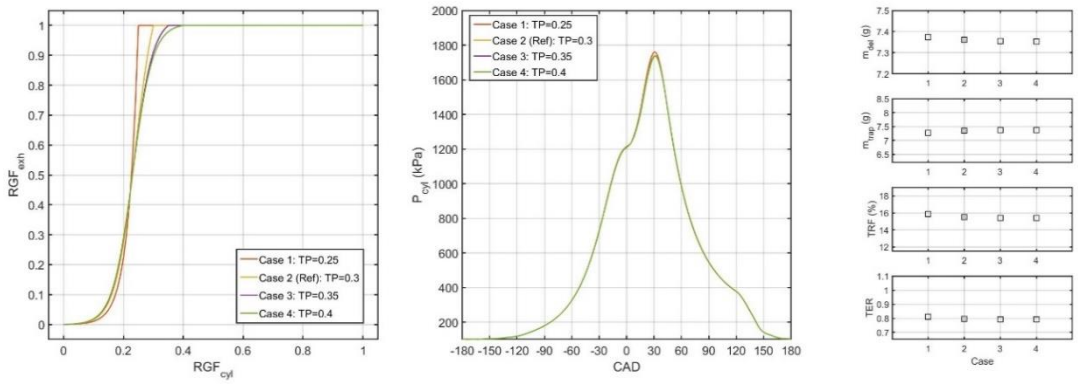

Figure 149: Sensitivity of changing transition point from perfect displacement on engine cylinder pressure and scavenging parameters.

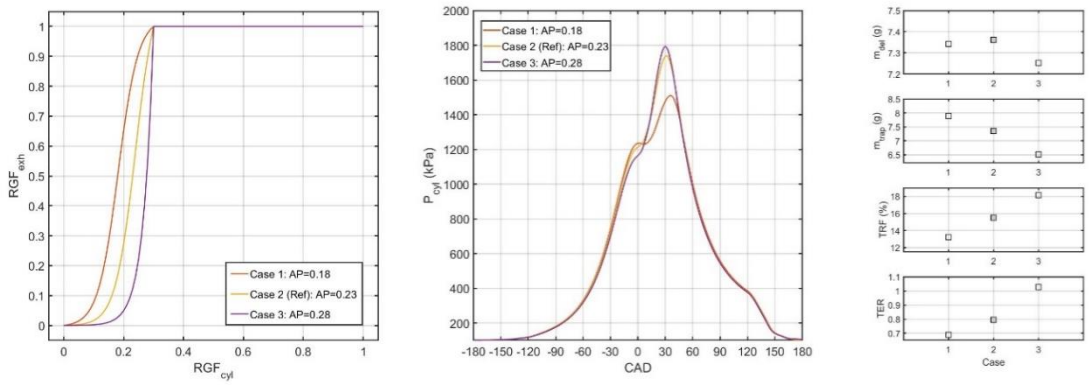

Figure 150: Sensitivity of changing anchor point on engine cylinder pressure and scavenging parameters.

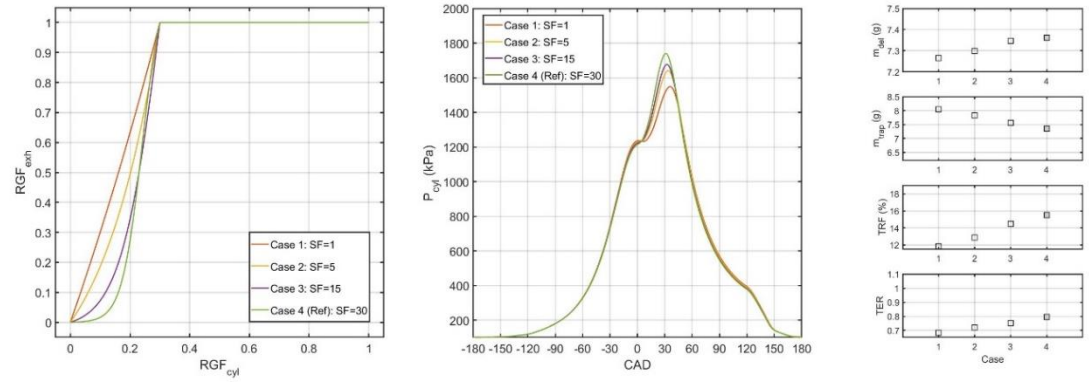

Figure 151: Sensitivity of changing shape factor on engine cylinder pressure and scavenging parameters.

A supplementary sensitivity analysis to changes in IMEP is also presented in Figure 152. It is seen that changes in fueling that consequently change the IMEP can have significant effects on the scavenging results.

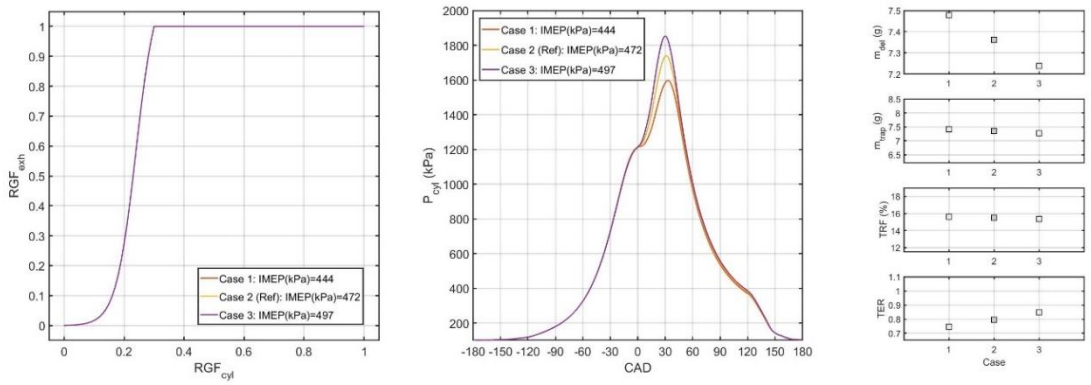

Figure 152: Sensitivity of changing IMEP on engine cylinder pressure and scavenging parameters.

9.4. Comparison with Experimental Results

The following graphs compare some additional experimental and *GT-Power* simulated results. *GT-Power* simulations used the hybrid model derived scavenging curves (Figure 101) with the 'three pressure analysis' solver.

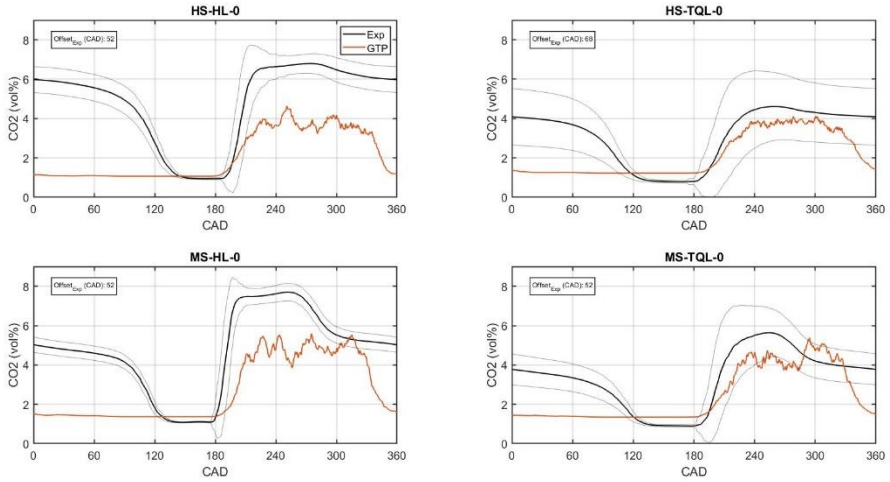

Figure 153: Experimental and GT-Power simulated cylinder CO_2 concentration at standard spark timing. Note that experimental results are obtained from point-based sampling while GT-Power results are bulk gas averages (Approach III).

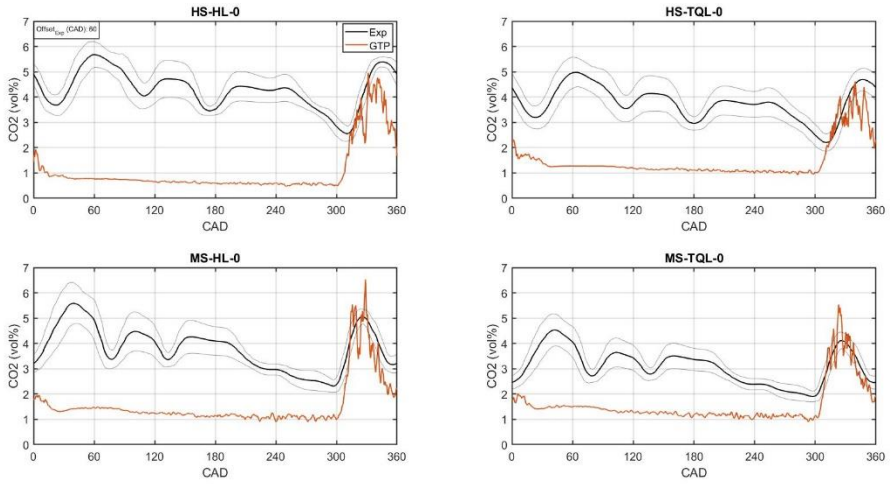

Figure 154: Experimental and GT-Power simulated exhaust CO_2 concentration at standard spark timing. Note that experimental results are obtained from point-based sampling while GT-Power results are bulk gas averages (Approach III).

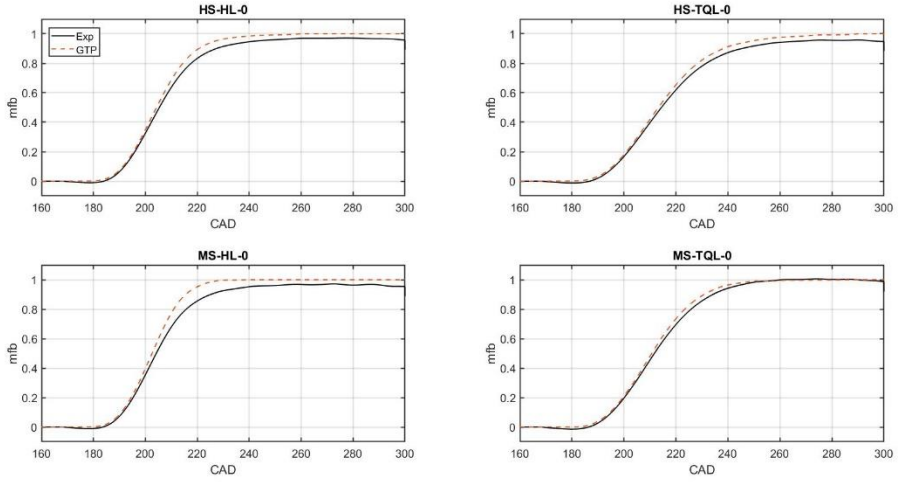

Figure 155: Experimental and GT-Power simulated mass fraction burned profiles at standard spark timing for different speeds and loads (Approach III).

9.5. Additional Analysis

Simulated results for parameters that cannot be easily measured are presented in this section to demonstrate some of the capabilities of *GT-Power* that can be used in future studies to gain insights into the nature of gas exchange in two-stroke engines.

Figure 156 shows the retained cylinder mass during gas exchange (including fuel injection) for the four standard spark timing cases on a time resolved basis. Various mass exchange events can be analyzed using the cylinder mass plot, which can in turn help explain the final trapped mass quantity, e.g. the MS-TQL case has the smallest trapped mass because of a sharp decrease in cylinder mass after IPC. The high exhaust flow that causes this sharp drop can be explained by using cylinder and exhaust pressure results presented in Chapter 6.

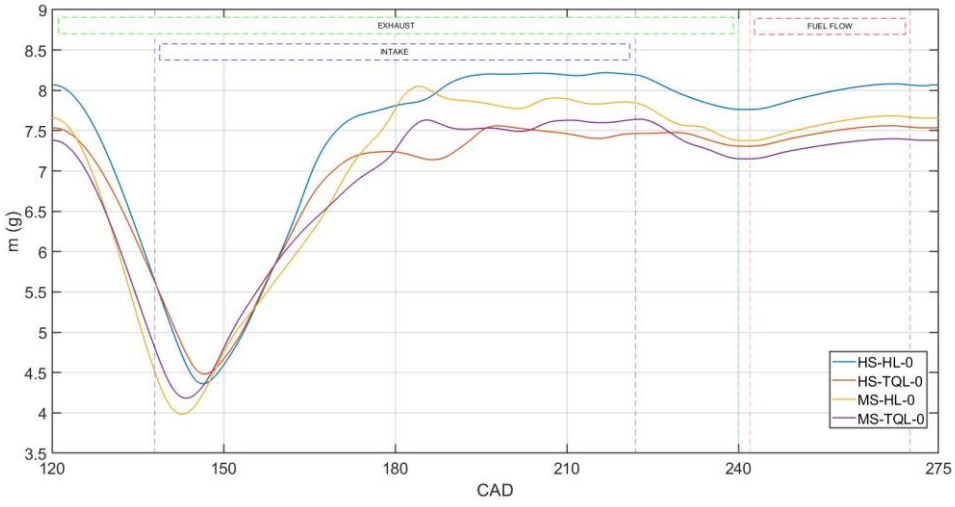

Figure 156: GT-Power simulated cylinder mass during an engine cycle for different speeds and loads at standard spark timing.

The total cylinder mass can be broken down into its residual and non-residual (air and fuel) constituents by using cycle resolved residual gas fraction shown in Figure 157(a). The resulting residual mass is shown in Figure 157(b). It can be seen that the HS-HL-0 case, which was shown to have the highest trapped mass in Figure 156, has the lowest TRF (Figure 157a) and residual mass (Figure 157b) because of a very rapid decay in the residual mass quantity from EPO to BDC, which can be attributed to a strong blowdown pulse and a strong well-timed scavenging pulse. The incident and reflected waves sensed as the exhaust pressure wave are shown separately for the HS-HL-0 case in Figure 158. The strong blowdown peak and the deep scavenging wave valley are evident.

(a) (b)

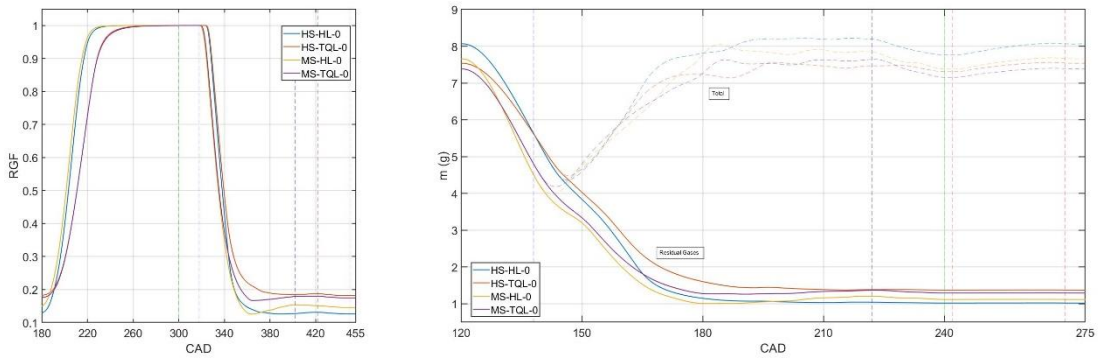

Figure 157: GT-Power simulated (a) residual gas fraction and (b) residual mass in the cylinder during an engine cycle for different speeds and loads at standard spark timing. Dashed lines in (b) show total cylinder mass.

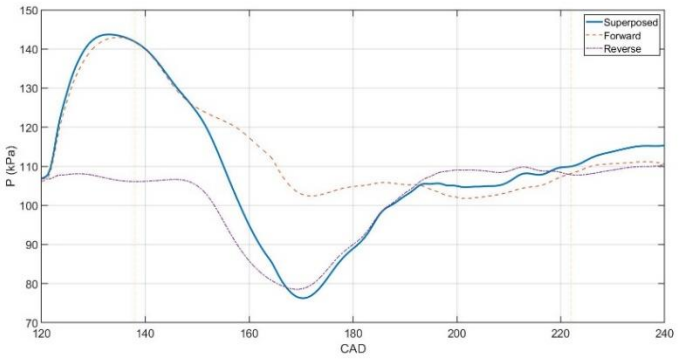

Figure 158: GT-Power simulated incident (forward), reflected (reverse), and superposed exhaust pressure wave at HS-HL-0.

Figure 159(a) shows the average cylinder gas temperature for the four standard spark timing cases during an engine cycle and Figure 159(b) shows the average specific heat ratio. It can be seen that the dominant factor controlling specific heat ratio is its inverse relationship with temperature. Composition effects (e.g. increased dilution levels increase specific heat ratio) are secondary and difficult to discern.

(a) (b)

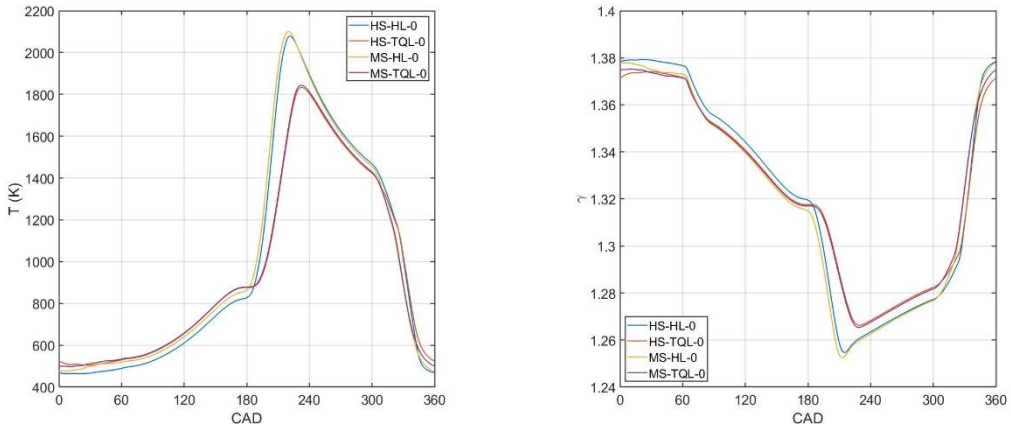

Figure 159: GT-Power simulated cylinder (a) average temperature and (b) specific heat ratio during an engine cycle for different speeds and loads at standard spark timing.

Lastly, Figure 160(a) shows the T-s diagram for the four standard spark timing cases with different events labeled. The compression process from end of fuel injection (EO_{inj}) to TDC is almost isentropic. The entropy decreases slightly because of heat losses to the walls as the cylinder temperature rises during compression. Once combustion starts slightly before TDC, the cylinder gas temperatures increase drastically along with the specific entropy. The sharp rise in specific entropy reflects the highly irreversible nature of combustion which generates a lot of entropy. Specific entropy peaks at the point of peak temperature. After combustion, expansion causes gas temperatures to cool and entropy decreases because wall heat losses transfer entropy from the system. This continues until EPO, after which near-isentropic blowdown takes place until IPO. This observation adds credence to the isentropic blowdown assumption used in the simple scavenging model development. Entropy decreases rapidly beyond IPO as fresh low temperature gases enter the cylinder. Entropy increases slightly from IPC to EPC probably because of entropy generation, and then it rises rapidly (almost isothermally) after EPC during fuel injection because of entropy transfer accompanying fuel. Figure 160(b) shows a magnified version of the fuel injection tail of the T-s diagram.

(a) (b)

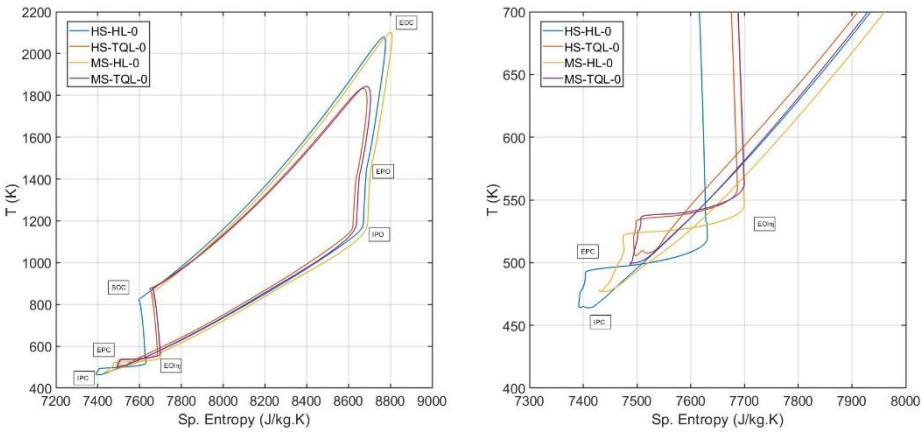

Figure 160: (a) GT-Power simulated T-s diagram for different speeds and loads at standard spark timing. (b) shows a magnified version of the fuel injection loop.